

High-resolution imaging methods in array signal processing

Xenaki, Angeliki; Knudsen, Kim

Publication date:
2015

Document Version
Publisher's PDF, also known as Version of record

[Link back to DTU Orbit](#)

Citation (APA):
Xenaki, A., & Knudsen, K. (2015). High-resolution imaging methods in array signal processing. Kgs. Lyngby: Technical University of Denmark (DTU). (DTU Compute PHD-2015; No. 368).

DTU Library

Technical Information Center of Denmark

General rights

Copyright and moral rights for the publications made accessible in the public portal are retained by the authors and/or other copyright owners and it is a condition of accessing publications that users recognise and abide by the legal requirements associated with these rights.

- Users may download and print one copy of any publication from the public portal for the purpose of private study or research.
- You may not further distribute the material or use it for any profit-making activity or commercial gain
- You may freely distribute the URL identifying the publication in the public portal

If you believe that this document breaches copyright please contact us providing details, and we will remove access to the work immediately and investigate your claim.

Ph.D. Thesis

 **DTU Compute**
Department of Applied Mathematics and Computer Science

High-resolution imaging methods in array signal processing

Angeliki Xenaki

Kgs. Lyngby, 2015



DTU Compute
Department of Applied Mathematics and Computer Science
Technical University of Denmark

Matematiktorvet
Building 303B
2800 Kongens Lyngby, Denmark
Phone +45 4525 3031
compute@compute.dtu.dk
www.compute.dtu.dk

PHD-2015-368
ISSN: 0909-3192



To the memory of Finn Jacobsen

Preface

This thesis was submitted to the Technical University of Denmark (DTU) in partial fulfillment of the requirements for the degree of Doctor of Philosophy (PhD) in Mathematics, Physics and Informatics. The work presented in this thesis was carried out from July 2011 to April 2015, partially at the Scientific Computing section at the Department of Applied Mathematics and Computer Science (DTU Compute, formerly known as DTU Informatics) and partially at the Marine Physical Laboratory at Scripps Institution of Oceanography, University of California San Diego (UCSD). This project has been supervised by Professors Klaus Mosegaard and Peter Gerstoft and Associate Professors Kim Knudsen, Finn Jacobsen and Jonas Brunskog. The project was funded jointly by the Danish National Advanced Technology Foundation (Højteknologifonden), DTU Compute and the Office of Naval Research (ONR) under Grant No. N00014-11-1-0320.

Abstract

The purpose of this study is to develop methods in array signal processing which achieve accurate signal reconstruction from limited observations resulting in high-resolution imaging. The focus is on underwater acoustic applications and sonar signal processing both in active (transmit and receive) and passive (only receive) mode. The study addresses the limitations of existing methods and shows that, in many cases, the proposed methods overcome these limitations and outperform traditional methods for acoustic imaging.

The project comprises two parts; The **first part** deals with computational methods in active sonar signal processing for detection and imaging of submerged oil contamination in sea water from a deep-water oil leak. The submerged oil field is modeled as a fluid medium exhibiting spatial perturbations in the acoustic parameters from their mean ambient values which cause weak scattering of the incident acoustic energy. A high-frequency active sonar is selected to insonify the medium and receive the backscattered waves. High-frequency acoustic methods can both overcome the optical opacity of water (unlike methods based on electromagnetic waves) and resolve the small-scale structure of the submerged oil field (unlike low-frequency acoustic methods). The study shows that high-frequency acoustic methods are suitable not only for large-scale localization of the oil contamination in the water column but also for statistical characterization of the submerged oil field through inference of the spatial covariance of its acoustic parameters.

The **second part** of the project investigates methods that exploit sparsity in order to achieve super-resolution in sound source localization with passive sonars. Sound source localization with sensor arrays involves the estimation of the direction-of-arrival (DOA) of the associated wavefronts from a limited number of observations. Usually, there are only a few sources generating the acoustic wavefield such that DOA estimation is essentially a sparse signal reconstruction problem. Conventional methods for DOA estimation (i.e., beamforming) suffer from resolution limitations related to the physical size and the geometry of the array. DOA estimation methods that are developed up-to-date in order to overcome the resolution limitations of conventional methods involve the estimation or the eigendecomposition of the data cross-spectral matrix. The cross-spectral methods require many snapshots (i.e., observation windows of the recorded wavefield) hence are suitable only for stationary incoherent sources. In this study, the DOA estimation problem is formulated both for single and multiple snapshots in the compressive sensing framework (CS), which achieves sparsity, thus improved resolution, and can be solved efficiently with convex optimization. It is shown that CS has superior performance compared to traditional DOA estimation methods especially under challenging scenarios such as coherent arrivals, single-snapshot data and random array configurations. The high-resolution performance and the robustness of CS in DOA estimation are validated with experimental array data from ocean acoustic measurements.

Resumé

Formålet med dette projekt er at udvikle metoder inden for array signalbehandling, som kan bruges til at opnå en nøjagtig signalrekonstruktion med høj opløsning ud fra begrænsede observationer. Fokus er rettet mod anvendelser inden for undervandsakustik med henblik dels på lokalisering og statistisk karakterisering af svage spredningsområder (aktiv sonar signalbehandling) og dels på lokalisering og monitorering af lydkilder (passiv sonar signalbehandling). Studiet påviser begrænsninger i eksisterende metoder og viser, at de udviklede metoder i mange tilfælde overkommer disse begrænsninger og tillige overgår de traditionelle metoder inden for feltet.

Projektet består af to dele. Den **første del** beskriver, hvordan beregningsmetoder inden for signalbehandling aktiv sonar kan bruges til at lokalisere og observere olieforurening fra et undersøisk olieudslip. Det undersøiske oliefelt modelleres som en perturbation af et omgivende felt, som giver anledning til en svag spredning af en indkommende akustisk bølge. Med højfrekvent aktiv sonar udsendes i mediet en akustisk bølge og den reflekterede spredte bølge måles. Højfrekvente akustiske metoder er gode til for det første at overvinde problemer med vands optiske uigennemsigtighed (modsat de metoder som er baseret på elektromagnetiske bølger) og for det andet at kunne skelne små-skala strukturen i undersøiske olieletter (modsat akustiske lavfrekvensmetoder). Studiet viser, at akustiske højfrekvensmetoder er velegnede ikke blot til lokalisering af olieforurening i vandsøjlen, men også til statistisk beskrivelse af det undersøiske oliefelt.

Den **anden del** af projektet undersøger metoder, der gør brug af sparsitet for at kunne opnå høj-opløselig lokalisering af lydkilden med passiv sonar. Lokalisering af lydkilden med et sensor array omfatter en estimering af ankomstretning (DOA) af de tilhørende bølgefronter fra et begrænset antal observationer. Normalt er der kun få kilder, der genererer det akustiske bølgefelt, således at DOA-estimeringen i bund og grund er et sparse rekonstruktionsproblem. Almindelige metoder til DOA-estimering (fx beamforming) lider under at give en begrænset opløsning afhængig af det anvendte måleudstyrs fysiske størrelse og geometri. De DOA estimeringsmetoder, som er udviklet frem til i dag med henblik på at kunne forbedre opløsningen i de konventionelle metoder, inkluderer bl.a. spektralmatrix-metoder. Disse metoder kræver flere snapshots (dvs. observationsvinduer over det målte bølgefelt), og er kun brugbare i forbindelse med stillestående, adskilte kilder. I dette studie er DOA-estimeringsproblemet beskrevet både for enkelte og flere snapshots i termer af compressed sensing (CS). Det formulerede rekonstruktionsproblem er et konvekst optimeringsproblem, som kan løses effektivt og således bestemme en sparse rekonstruktion (svarende til en forbedret opløsning). Det er vist, at CS har højere performance sammenlignet med traditionelle DOA-estimeringsmetoder, især under udfordrende forhold så som koherens, single-snapshot og tilfældige array-konfigurationer. Den høje opløsning og robustheden af CS i DOA-estimeringer er valideret med eksperimentelle data fra akustiske havmålinger.

Acknowledgments

*‘When you set out for Ithaca
wish that the way is long,
full of adventure, full of knoweledge.’*

-Constantinos Cavafis-

The course towards completing this PhD study was a very valuable experience through which I evolved in many aspects and it would be an omission not to acknowledge the people who contributed to this journey.

First and foremost, I would like to express my gratitude to all my supervisors; I would like to thank Klaus Mosegaard for offering me the opportunity of this exciting PhD project. Special thanks to Peter Gerstoft for his invaluable guidance through all the stages of the project and for the stimulating collaboration, for his hospitality during my external stay at Scripps Institution of Oceanography and for facilitating and encouraging me to ascend the steep hill both of the PhD studies and of La Jolla Shores Drive. I am deeply thankful to Kim Knudsen for his support at the final stage of the PhD and for accepting to take over the administrative burden of my relocation to DTU Compute. I am grateful to Finn Jacobsen who is a constant source of inspiration either present or not and to Jonas Brunskog for his encouraging attitude and constructive comments.

I would like to thank Efren Fernandez-Grande, Olivier Carriere, Ravi Menon and Knud Cordua for the useful discussions and diverse input to the project and for their interest. It has been a great pleasure working with you. I want also to thank William Hodgkiss and Christoph Mecklenbräuker for their useful comments on my papers.

During this PhD project I had the opportunity to work in several groups and university departments which, despite the complicated logistics, gave me the chance to meet many nice people. A very special thanks to all the colleagues and friends in Scientific Computing at DTU Compute, in Acoustic Technology at DTU Electrical Engineering and in the Marine Physical Laboratory at Scripps institution of Oceanography for creating a very friendly and supportive atmosphere and a lively research environment.

Finally, I would like to thank my family for always supporting my choices with trust, facilitating my way and shielding it with love and my friends all over the world for their unconditional love, for all the experiences we shared, for their support in hard times and all the fun in good times. You are always in my heart which eliminates the distance that separates us.

List of symbols

Abbreviations

(I)DFT	(Inverse) Discrete Fourier transform
CBF	Conventional beamforming
CS	Compressive sensing
DOA	Direction-of-arrival
FOCUSS	Focal underdetermined system solver
LASSO	Least absolute shrinkage and selection operator
MAP	Maximum a posteriori
MUSIC	Multiple signal classification
MVDR	Minimum variance distortionless response
RIP	Restricted isometry property
SNR	Signal-to-noise ratio
Sonar	Sound navigation and ranging
ULA	Uniform linear array

Symbols in Part I

ϵ_κ	Compressibility perturbation
ϵ_ρ	Density perturbation
$\hat{\mathbf{r}}$	Unit vector in the direction of \mathbf{r}
κ	Compressibility, [Pa ⁻¹]
\mathbf{r}	Position vector
\mathbf{r}_0	Observation position vector
j	Imaginary unit, $j = \sqrt{-1}$
∇	Gradient/divergence operator for scalars/vectors
ω	Angular frequency, [rad/s]
∂	Partial differential operator
ρ	Density, [kg/m ³]
A	Pressure complex amplitude
c	Speed of sound, [m/s]
g	Free-space Green's function, [Pa]

k	Wavenumber, $k = \omega/c$, [m ⁻¹]
p	Sound pressure, [Pa]
p_i	Incident pressure, [Pa]
p_s	Scattered pressure, [Pa]
R	Scattering region
r	Length of position vector \mathbf{r} , [m]
t	Time, [s]

Symbols in Part II

\cap	Intersection of sets
ϵ	Upper bound for the noise ℓ_2 -norm
λ	Wavelength, [m]
$\ \mathbf{x}\ _0$	ℓ_0 -pseudonorm of a vector \mathbf{x}
$\ \mathbf{x}\ _p$	ℓ_p -norm of a vector \mathbf{x}
Φ	Orthonormal basis matrix
Ψ	Measurement matrix
\mathbf{A}	Sensing matrix
$\mathbf{a}(\theta)$	Steering vector at direction θ
\mathbf{I}_N	Identity matrix, $N \times N$
\mathbf{n}	Additive noise vector
\mathbf{x}	Sparse signal vector/optimization variable
\mathbf{x}^*	Optimal variable of an optimization problem
\mathbf{y}	Measurement vector
\mathcal{D}	Domain of the optimization problem
μ	Regularization parameter
θ	Direction of arrival (angle of incidence), [°]
$\hat{\mathbf{x}}$	Estimate for vector \mathbf{x}
$^{-1}$	Inverse operator
H	Hermitian operator, i.e, conjugate transpose
T	Transpose operator
d	Intersensor spacing, [m]
f_0	Objective (cost) function
$f_i, i = 1, \dots, m$	Inequality constraint functions
$h_j, j = 1, \dots, q$	Equality constraint functions
p^*	Optimal value of an optimization problem

List of figures

2.1	Texture of chemically dispersed oil in the Gulf of Mexico, 2010.	6
2.2	Schematic for backscattering from an inhomogeneous field R	8
2.3	Monostatic configuration for a multibeam echo sounder.	10
3.1	Compressive sensing method for data acquisition of sparse signals.	15
3.2	Schematic of single-pixel imaging demonstrating the principle of compressive sensing.	16
3.3	Geometric visualization of the ℓ_p -norm problem for $0 \leq p \leq 2$	19
3.4	Sound source localization with a uniform linear array.	20
3.5	Data acquisition of sparse signals in array signal processing.	21
3.6	Trade-off between coherence of a structured sensing matrix and basis mismatch.	22

Contents

Preface	iii
Abstract	v
Resumé	vii
Acknowledgments	ix
List of symbols	xi
List of figures	xiii
1 Introduction	1
1.1 Thesis structure	3
2 Part I: Computational methods for detection and imaging of oil in sea water	5
2.1 Background	5
2.1.1 Modeling of oil in sea water	6
2.1.2 Scattering from inhomogeneities	7
2.1.3 Statistical characterization of weak scattering fields with high-frequency acoustics	9
2.2 Contributions	10
2.2.1 Part I: Papers A, B	11
2.3 Perspectives and future work	12
3 Part II: Sparse signal reconstruction for direction-of-arrival estimation	13
3.1 Background	13
3.1.1 Compressive sensing framework	14
3.1.2 Formulation of a convex optimization problem	17
3.1.3 Sparse signal reconstruction	18
3.1.4 DOA estimation	19
3.1.5 Limitations of CS in DOA estimation	21
3.2 Contributions	23
3.2.1 Part II: Papers C-G	24

3.3 Perspectives and future work	24
4 Summary/Conclusion	27
Bibliography	31
Published Journal and Conference Papers	39
A Modeling and detection of oil in sea water	43
B Statistical characterization of weak scattering fields with inverse methods	55
C Compressive beamforming	67
D Sparsity and super-resolution in sound source localization with sensor arrays	81
E Grid-free compressive beamforming	89
Additional Papers	105
F Single and multiple snapshot compressive beamforming	107
G Sparse acoustic imaging with a spherical array	121

CHAPTER 1

Introduction

We use our senses to extract information from the environment and process it as accurately as possible to our advantage, e.g., for protection, to take action or make decisions. For example, our ears function as sensors which detect, filter and process acoustic radiation to determine the sound level, the direction of propagation and the frequency content of the sources that produce it. By extension, array signal processing is developed to infer information about a signal from a propagating wavefield captured by an array of sensors. By deploying a group of transducers in a geometrical configuration forming an array, the propagating wavefield is sampled not only in time but also in space. Then, signal processing aims at combining the sensor outputs in a way that enhances the extraction of information from the recorded wavefield.

Opposed to using a single sensor, array signal processing can achieve signal enhancement over noise. This is due to the fact that a signal appears correlated at all sensors while random noise is statistically independent from sensor to sensor. Thus, the noise can be reduced by averaging the recordings across sensors to improve signal detection. Moreover, array signal processing uses the information of the geometry of the data acquisition system to attribute directionality to the array, allowing to characterize a signal by determining, not only the spectral content of the sources that produce it, but also their number and locations. Similarly, sensor arrays can be used to monitor the position of a source by tracking its signature as it moves in space. Therefore, array signal processing is an active research area in diverse fields, e.g., in electromagnetic, seismic or acoustic imaging. In acoustics, array signal processing is used for visualization of sound fields, identification and localization of noise sources or detection of objects that emit or scatter sound waves. The applications range from environmental acoustics [1] and noise control [2] to non-destructive testing [3], underwater [4] and medical ultrasound imaging [5].

In array signal processing, a problem can be formulated as a filtering or a parameter estimation process [6]. A filtering problem aims to separate the desired signal from noise or interference by allowing the signal to pass unattenuated while rejecting other contributions. Parameter estimation is achieved by minimizing an error function (e.g., the squared mean difference) between a modeled signal and the observed wavefield. The modeled signal is chosen according to prior knowledge about the underlying physical process that generates it. In many problems though, as in Fourier-based spectral analysis, the filtering and the parameter estimation approach yield equivalent results.

The first method developed to achieve spatio-temporal filtering of the wavefield with an array of sensors was beamforming. The conventional (Bartlett) beamformer [7] dates back to the second world war, and is an application of Fourier analysis to spatio-temporally sampled data. Beamforming combines the sensor outputs coherently to electronically steer the array in several focusing directions and measure the output power. The steering directions with maximum power yield the source locations. The conventional beamformer suffers from resolution limitations related to the physical size and the geometry of the array (aperture) regardless of the signal-to-noise ratio (SNR).

Adaptive beamforming [8] was developed to overcome the resolution limitations of the conventional beamformer by minimizing the contributions of noise and other signals arriving from directions other than the focusing one in order to detect closely spaced signal sources. The resolution of adaptive beamformers depends on the array aperture and the SNR. The introduction of subspace-based estimation techniques [9] in array signal processing offered a resolution ability which, in principle, is not limited by the array aperture, provided that the number of the observation windows in the recorded wavefield (snapshots) and the SNR are sufficiently high [10].

This PhD study is concerned with high-resolution methods for acoustic imaging using sensor arrays. It addresses the limitations of existing methods [11] and proposes alternative methods to overcome these limitations. The focus is on sonar signal processing applications both in active (transmit and receive) and passive (only receive) mode.

The study comprises two parts. The first part deals with the statistical characterization of weak scattering fields from monostatic backscattering using high-frequency acoustics with application in the detection and characterization of a contamination area from a submerged oil spill. In a monostatic sonar configuration the transmitter and the receiver are collocated such that the backscattered waves (i.e., the waves reflected back to the direction of incidence) are observed, while weak scattering implies that multiply scattered waves are negligible since only a small fraction of the incident acoustic energy is scattered. The challenge of a deep-water oil leak is that a significant quantity of oil remains in the water column and possibly changes properties. There is a need to quantify the oil settled within the water column and determine its physical properties to assist the oil recovery. High-frequency acoustic methods are promising since they can both overcome the optical opacity of the water and achieve high-resolution imaging. Considering the submerged oil-spill as a random field of spatial heterogeneities in the acoustic parameters in relation to the surrounding medium, a weak scattering approach is used to model the acoustic backscattering. It is shown that a high-frequency active sonar can be used to detect the submerged oil spill and determine its spatial statistics by resolving small-scale structure.

The second part describes the primary purpose of the project which is to adapt the framework of compressive sensing [12] to the context of array signal processing in order to achieve high-resolution acoustic imaging. Compressive sensing proves that a sparse signal (i.e., a signal which can be fully described with only a few parameters) can be recovered efficiently with a number of incoherent measurements which is comparable to the degree of information content in the signal rather than its size. The possibility of dimensionality reduction in the required observations for accurate reconstruction of sparse signals is very useful especially whenever acquiring data is difficult, dangerous or expensive. In acoustic imaging there are usually only a few sources generating the observed wavefield. Exploiting the underlying sparsity, we show that compressive sensing in array signal processing achieves high-resolution sound source localization outperforming the existing methods. Furthermore, most of the existing methods are based on the second-order statistics of the data, i.e., the sample covariance matrix from a number of snapshots [10]. However compressive sensing can achieve high-resolution imaging even with a single snapshot, which is useful for detection of moving sources and multipath arrivals.

1.1 Thesis structure

This PhD thesis is based on a collection of scientific articles published in peer-reviewed scientific journals and international conference proceedings. The remainder of the thesis develops as follows. Chapters 2 and 3 provide a synopsis of the methods investigated in Parts I and II of the project respectively, along with a summary of the corresponding articles and the contributions of this study to the existing literature. Chapter 4 concludes the study with a summary of the results.

Seven papers are included in the attached appendices. Papers A and B are related to Part I, while Papers C-G are related to Part II. The two parts of the thesis with their corresponding papers can be read independently. It is recommended that Papers A-F are read before proceeding to the conclusions chapter.

CHAPTER 2

Part I: Computational methods for detection and imaging of oil in sea water

This chapter places high-frequency acoustic methods in the context of current challenges in underwater acoustic imaging for volume scattering characterization. It provides a summary of the scientific contribution in Papers A and B in relation to the existing literature and suggests future work.

2.1 Background

The high prices of crude oil in the market in connection with the limited number of accessible fossil fuel natural reserves has recently encouraged investments in oil and gas exploration and production offshore and in greater depths. However, the environmental impact of deep-water drilling in the case of an accident is significant as it was indicated by the oil spill of Deepwater Horizon in the Gulf of Mexico in 2010 [13].

Prior to the oil accident of Deepwater Horizon, the presence of oil in the sea was confined at shallow-water owing to either natural processes (e.g. biogenic oil) or human-induced pollution (e.g., oil slicks along shipping routes, accidents from shallow water oil drills). Subsequently, the effort has been focused on monitoring and characterizing oil pollution on the sea surface. Remote sensing methods from satellites and aircrafts, which are based on the interaction between electromagnetic waves and oil or water, are efficient imaging methods of buoyant oil on the sea surface [14, 15].

The challenge of a deep-water oil leak encountered in the case of Deepwater Horizon is that a significant quantity of oil remained in the water column after the cease of the discharge from the wellhead. There are two main reasons explaining the existence of submerged oil [16, 17]. The one is due to a natural process. The oil leaking from the wellhead lost some of the lighter hydrocarbons and changed properties while traveling the long distance to the sea surface. The second reason is the use of undersea dispersants directly on the wellhead decreasing the surface tension of the oil-water interface and causing the oil to decompose into smaller, heavier droplets. Hence, much of the oil which was released into the water, decomposed into stringy formations of viscous material mixed with water which remained trapped far below the sea surface [16, 17].

Assessing the environmental impact, one should note that surface oil is easier to be removed than submerged oil. It is dissipated by naturally occurring physical and biochemical processes such as the effect of wind, waves and microbes which cause the oil to evaporate or degrade. Furthermore, since several methods of detecting surface oil

have been developed, man can accelerate the process of oil dissipation by burning oil or skimming the surface [14].

On the other hand, there are serious environmental implications in the existence of submerged oil in the sea. Oil in deep water persists for long periods since it does not undergo substantial biodegradation [18]. Besides, oil absorbs infrared radiation and re-emits it as thermal energy with implications in global warming [19]. Another major concern of large scale release of oil is its toxicity to marine life [20]. Therefore, it is of interest to determine the physical properties and describe the spatial covariance of the submerged oil in order to monitor the degradation process.

Methods based on electromagnetic waves are inefficient for mapping submerged oil in the sea since the electromagnetic waves attenuate fast when traveling in water. High-frequency acoustic methods are promising since they can both overcome the optical opacity of the water and resolve the small-scale structure of the new forms of oil. Therefore, such methods can be used both to localize submerged oil fields and to characterize them in terms of their second order statistics.

2.1.1 Modeling of oil in sea water

There are indications that the submerged oil extends throughout the water column as elongated formations of viscous material mixed with water and possibly with biological material [16]; see Fig. 2.1.



Figure 2.1: Texture of chemically dispersed oil in the Gulf of Mexico, 2010. Photo from Steve McDonald, TerraSond.

Hence, the submerged oil in the water is modeled as a fluid medium with spatial heterogeneity in the compressibility and density, potentially exhibiting roughness at the interfaces with the water and possibly comprising inclusions of light, compressible gas bubbles. Then, the water column is modeled as a random field of volume inhomogeneities with a region of contamination characterized by a different covariance structure than the rest of the field. The water-contamination interface roughness is modeled as a special case of spatial heterogeneity [21, 22]. Since the existence of submerged oil is controlled

by the ambient density it is a reasonable assumption that the difference in the acoustic parameters between the two fluid media is small causing weak scattering of the incident acoustic energy [4, 23]. The average compressibility and density are assumed constant throughout the field.

In the absence of turbulence and for a short measurement interval, the random field representing the water column is assumed to be spatially stationary and time-invariant. Stationarity can be exploited to develop a numerical method for synthetically generating random fields. We employ a random field generator [24, 25] which supports several covariance models both isotropic and anisotropic [26, 27] and dissociates the random numbers (realizations) and the covariance parameters such that they can be altered either separately or simultaneously. Therefore, the random field generator [28–30] is a flexible tool for modeling a stationary random field with the desired statistics (mean and covariance).

2.1.2 Scattering from inhomogeneities

When an acoustic wave propagates in the marine environment it loses some of its energy due to the interaction with regions or objects which deflect (scatter) or absorb sound. An acoustic wave is scattered, not only by solid objects and discrete inclusions such as bubbles or gas voids, but also by regions characterized by acoustic properties, i.e., compressibility and density, that differ from those of the surrounding medium. Sources of weak scattering (i.e., which scatter only a small fraction of the incident acoustic energy) are the inherent spatial variations in the acoustic properties of the medium due to temperature and/or salinity fluctuations, the irregularities at the ocean interfaces as well as both biological or inanimate material hosted in the marine environment [4, 21, 23].

Suppose there is a region R in the medium characterized by spatial heterogeneity in the compressibility κ_e and density ρ_e relative to the corresponding acoustic parameters of the medium, κ and ρ . Then, the wave equation for the acoustic pressure, derived from the conservation of mass and momentum under adiabatic considerations and distinguishing between the variations of pressure and density caused by the sound wave and the variations of compressibility and density due to the medium inhomogeneity, takes the form [31],

$$\nabla^2 p - \frac{1}{c^2} \frac{\partial^2 p}{\partial t^2} = \frac{1}{c^2} \frac{\partial^2 p}{\partial t^2} \epsilon_\kappa(\mathbf{r}, t) - \nabla (\epsilon_\rho(\mathbf{r}, t) \nabla p), \quad (2.1)$$

where $p = p(\mathbf{r}, t)$ is the acoustic pressure either inside or outside the region R , c is the speed of sound and,

$$\epsilon_\kappa = \begin{cases} \frac{\kappa_e - \kappa}{\kappa} & \text{inside } R \\ 0 & \text{outside } R \end{cases} \quad \epsilon_\rho = \begin{cases} \frac{\rho_e - \rho}{\rho_e} & \text{inside } R \\ 0 & \text{outside } R \end{cases}$$

are the deviations of the compressibility and density, as a function of position \mathbf{r} and time t , relative to their unperturbed mean values.

Assuming time-stationarity, i.e., the fluctuations vary in a statistical manner only as a function of space (which is the case when the region R is a ‘foreign body’ in the medium), the Helmholtz equation for the pressure amplitude can be used,

$$\nabla^2 p + k^2 p = -k^2 \epsilon_\kappa(\mathbf{r}) p - \nabla (\epsilon_\rho(\mathbf{r}) \nabla p), \quad (2.2)$$

where $k = \omega/c$ is the wavenumber and ω is the radial frequency. The harmonic time dependence $e^{j\omega t}$ is implied and neglected for simplicity.

Note that Eq. (2.2) is homogeneous with respect to p . The terms in the right hand side are related to the interaction of the sound wave p and the inhomogeneities in R , thus they can be considered as sources of scattered sound. Specifically, the first term which is related to inhomogeneities in compressibility acts as a pulsating monopole source, while the second term related to density inhomogeneities acts as a dipole source. Nevertheless, they do not introduce new energy into the wavefield.

Applying the Gauss-Green theorem, the differential Helmholtz equation takes the form of the integral equation [31],

$$p(\mathbf{r}_0) = p_i(\mathbf{r}_0) + \int_R (k^2 \epsilon_\kappa(\mathbf{r}) p(\mathbf{r}) - \nabla(\epsilon_\rho(\mathbf{r}) \nabla p(\mathbf{r}))) g(\mathbf{r}_0|\mathbf{r}) d\mathbf{r}, \quad (2.3)$$

where g is the Green's function and p_i is the incident wave which feeds energy into the medium from the boundary representing the inhomogeneous term. Then, the scattered sound pressure p_s observed at \mathbf{r}_0 due to scattering from spatial fluctuations in the acoustic properties of the of the medium within a scattering region R (see Fig. 2.2) is given by the integral [31],

$$p_s(\mathbf{r}_0) = \int_R (k^2 \epsilon_\kappa(\mathbf{r}) p(\mathbf{r}) g(\mathbf{r}_0|\mathbf{r}) + \epsilon_\rho(\mathbf{r}) \nabla p(\mathbf{r}) \nabla g(\mathbf{r}_0|\mathbf{r})) d\mathbf{r}. \quad (2.4)$$

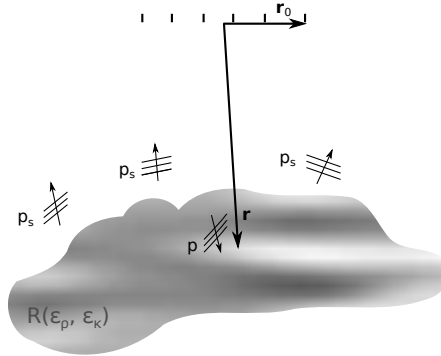


Figure 2.2: Schematic for backscattering from an inhomogeneous field R .

The Green's function describes the sound pressure at an observation point \mathbf{r}_0 due to a unit, simple-harmonic, point source located at \mathbf{r} ,

$$g(\mathbf{r}_0|\mathbf{r}) = \frac{1}{4\pi|\mathbf{r}_0 - \mathbf{r}|} e^{-jk|\mathbf{r}_0 - \mathbf{r}|}. \quad (2.5)$$

For far field radiation, the Fraunhofer approximation for the range term is valid [32],

$$|\mathbf{r}_0 - \mathbf{r}| \approx r - \hat{\mathbf{r}} \cdot \mathbf{r}_0, \quad (2.6)$$

where $r = |\mathbf{r}|$ and $\hat{\mathbf{r}} = \frac{\mathbf{r}}{r}$ is the unit vector in the direction of \mathbf{r} and the Green's function takes the simpler form,

$$g(\mathbf{r}_0|\mathbf{r}) \approx \frac{1}{4\pi r} e^{-jk(r - \hat{\mathbf{r}} \cdot \mathbf{r}_0)}. \quad (2.7)$$

The incident wave which insonifies the region R emanates from a monopole located at the origin of the coordinate system out of the scattering region R ,

$$p_i(\mathbf{r}) = A \frac{e^{-jk r}}{r}, \quad (2.8)$$

where A is the pressure complex amplitude at a distance 1 m from the source.

The integral equation in Eq. (2.4), is exact and valid universally for parameter perturbations of arbitrary size. Discontinuous perturbation can also be handled with Eq. (2.4) since it does not involve gradients of the model parameters [22]. Nevertheless, solving Eq. (2.4) requires exact expressions of the Green's function, g , and the sound pressure, p , inside the scattering region R . This is achieved in only a few special cases (e.g. scattering by spheres) for which the integral equation for the scattered wave can be solved analytically. Alternatively it can be solved by variational methods or approximations [31, 33].

In the case of weak scattering, first-order scattering is assumed thus the Born approximation is applied. The Born approximation implies that the sound pressure inside the scattering region is equal to the incident sound pressure, $p \approx p_i$, neglecting the effect of higher-order scattering [31, 33]. Thus, inserting Eqs. (2.7) and (2.8) into Eq. (2.4) the pressure scattered from inhomogeneities in the acoustic parameters of the medium is,

$$p_s(\mathbf{r}_0) \approx \frac{k^2 A}{4\pi} \int_R \left([\epsilon_\kappa(\mathbf{r}) - \epsilon_\rho(\mathbf{r})] \frac{e^{-jk(2r - \hat{\mathbf{r}} \cdot \mathbf{r}_0)}}{r^2} \right) d\mathbf{r}. \quad (2.9)$$

The density fluctuations can be neglected since they are proportional to the compressibility fluctuations and are less significant in fluid media [33, 34]. Owing to the Born approximation, Eq. (2.9) relates linearly the backscattered pressure and the fluctuations in the acoustic parameters.

2.1.3 Statistical characterization of weak scattering fields with high-frequency acoustics

In an acoustic backscattering model of volume inhomogeneities, a statistical description of the field is more appropriate than a deterministic description due to the complex structure of the inhomogeneities [34, 35]. Besides, a deterministic description of the field has less to offer when the interest is in studying volume reverberation in a medium where there is flow, such as in the water column.

Typically, volume reverberation is described by the statistical distribution of the backscattering strength. The backscattering strength is defined as the ratio of the scattered intensity to the incident intensity per unit volume in dB [4, 23, 34, 36, 37]. This measure is widely used in sonar applications concerned with target detection and identification [38, 39] or with the remote classification of weak scattering mechanisms such as seafloor sedimentation by comparison to known models [23, 40, 41]. The backscattering strength is proportional to the cross spectral density thus related to the statistical properties of the field [38, 41, 42]. However, for narrowband insonification the backscattering strength provides a single measure and additional information for the covariance parameters are required to relate the spatial variation of the scattering field to a covariance model. This study proposes an alternative method to infer the covariance parameters of the scattering field [24, 25].

For acoustic imaging of the weak scattering field representing the water column, active sensing (i.e., a pulse is used to insonify the area of interest) and a monostatic configuration (i.e., the transmitter and the receiver array are collocated) are considered. Specifically, a high-frequency multibeam sonar is chosen as the transmitting and receiving configuration [43]; See Fig. 2.3. Delay-and-sum beamforming [11] is used to impose directivity to the receiving array and time-varied gain (TVG) is applied to compensate for spreading loss and absorption making the received signals independent of the scatterer's distance. The beamformer output contains the contribution of all the field values

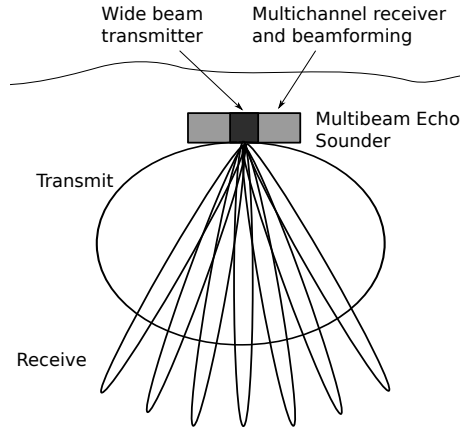


Figure 2.3: Schematic of a monostatic configuration for a multibeam echo sounder in the across-track plane. The transmitter insonifies the medium with a wide beam and beamforming attributes directivity to the receiving hydrophone array to localize the backscattered returns.

on the radial distance of focus weighted by the beampattern. However, the more the beampattern resembles a delta function, the more will the beamformer output be proportional to the field value at the focusing direction. Thus, the parameters of the spatial covariance of a field of volume inhomogeneities can be estimated by the statistics of the beamformer output. For a stationary random process the discrete spatial covariance function can be estimated from a finite number of samples. Therefore, the random field is localized with beamforming and inference of spatial covariance is based on the statistics of the beamforming reconstruction. Nevertheless, the reconstruction is subject to resolution limitations of the sonar configuration. The use of high frequencies, resulting in narrow beamwidths, improves the resolution and allows the detection of small scale characteristics [23, 38–41].

2.2 Contributions

Several authors [21, 22, 44–46] have used the weak scattering approach to model monostatic backscattering from inhomogeneous sediments in the seafloor. Palmese and Trucco [44] incorporate the effect of volume reverberation from the seabed to their model of imaging embedded objects with a 3D monostatic sonar configuration. Li [45] and Li

et al [46] model the monostatic backscattering from three-dimensional volume inhomogeneities in shallow water ocean sediments.

Tang [21] and Ivakin [22] developed independently the theoretical framework for a unified approach to describe weak scattering due to interface roughness and volume inhomogeneities, i.e., spatial fluctuations of the compressibility and density, from ocean sediments. The unified approach is based on the assumption that the roughness can be described as a specific kind of spatial fluctuation around an otherwise horizontal interface. Ivakin [22] further assumes that the weak scattering approach is not restricted to small-scale roughness but it extends to arbitrary roughness as long as the difference in the parameters between the adjacent media is not large. The unified approach in modeling scattering from irregular media facilitates the description of cases where the effect of volume and surface scattering is comparable and potentially coherent.

Acoustic methods based on Doppler velocimetry which have been used [47, 48] to quantify turbulent flow of hydrocarbons are inefficient to quantify the submerged oil since they require knowledge of the exact position of the oil leak. Tracking of the submerged oil is mainly based on fluorescence and dissolved oxygen measurements and low-frequency acoustic [14] or seismic methods [49]. These methods can detect submerged oil plumes but they do not provide information about the spatial distribution of the stringy oil contaminants in the water.

The contribution of the present study [24, 25] comprises:

- The introduction of a random field generator to implement a physical model of the water column with a region of contamination from submerged dispersed oil. The chosen random field generator [28] provides great modeling flexibility as it supports several covariance models and, unlike other methods used in ocean acoustics [45, 46], it allows local perturbations of the modeled random field.
- The application of the unified weak scattering approach in modeling backscattered returns from density and compressibility perturbations in the water column.
- The use of high-frequency acoustic methods to detect the submerged field and infer the parameters of its spatial covariance.
- Traditional methods describe weak scattering fields by comparing the statistical distribution of backscattering strength with known models [23, 40, 41]. We propose an alternative method which allows the description of a stationary scattering field in terms of its second-order statistics without prior knowledge of its spatial covariance.

A summary of the papers related to part I follows.

2.2.1 Part I: Papers A, B

Paper A describes a weak scattering approach for modeling backscattering from inhomogeneous substances, as submerged crude oil in the water column. A random field generator is introduced to implement a physical model of the inhomogeneous media and a high-frequency active sonar is selected to collect the backscattered returns. It is shown that high-frequency acoustics can be used to detect the submerged field and infer the parameters of its spatial covariance.

Paper B investigates an inverse method to describe volume scattering models qualitatively in terms of their statistical properties. It demonstrates that the proposed method

provides robust estimates of the covariance parameters, i.e., variance and characteristic lengths, hence characterization of the scattering field in terms of its second order statistics.

2.3 Perspectives and future work

The developed model indicates that detection and monitoring of oil contamination submerged into the water column is possible with high-frequency acoustic methods. Some suggestions for future research directions follow:

- Tank experiments with different kinds of oil and several oil-dispersant ratios are required to improve the model providing accurate (realistic) values for compressibility and density perturbations.
- Due to lack of relevant experimental data, the experimental validation of the model was not possible, yet it is necessary.
- Adaptation of the model to a more complicated propagation environment, i.e., with non-uniform sound speed profile, would increase the realm of applications.
- Sparse methods [50] for inference of the (sparse) covariance characteristics of the random field could be investigated.

CHAPTER 3

Part II: Sparse signal reconstruction for direction-of-arrival estimation

This chapter provides an overview of the compressive sensing (CS) framework for sparse signal reconstruction with limited data and its application in direction-of-arrival (DOA) estimation with sensor arrays. It highlights the scientific contribution of the conducted research, presented in Papers C, D, E, F and G, in relation to the state of the art at the time of publication and indicates future research directions.

3.1 Background

Many engineering problems involve either the reconstruction of a signal of interest or the estimation of its parameters from a (usually small) number of observations. Often, natural signals are sparse, i.e., they can be described only with a few parameters. Therefore, finding sparse solutions of underdetermined systems of linear equations is of significant importance in signal processing and inverse problems. Compressive sensing [12, 51], also known as compressed sensing [52] or compressive sampling [53, 54], is a method for solving such underdetermined problems assuring very accurate reconstruction. Compressive sensing fuses data compression into data acquisition (hence the name) as described in the following.

CS revolutionized the way we acquire and process information by providing a fundamentally new approach. CS exploits the fact that many signals are inherently sparse in some representation basis, to allow high-resolution signal reconstruction from far fewer linear measurements than the size of the signal (sampling in sub-Nyquist rates). In fact, the number of required measurements is proportional to the sparsity level (i.e., the number of non-zero parameters) rather than the size of the underlying signal, effectively constituting a compression. Since the number of measurements is much smaller than the size of the signal, the resulting problem is underdetermined. The CS framework indicates that, even though sparse signal reconstruction from an underdetermined problem in principle requires a difficult combinatorial search, in practice, it can be solved efficiently with convex optimization (see Sec. 3.1.2).

The idea of approximating an essentially combinatorial problem with a convex one to achieve both high-resolution and computationally tractable sparse signal reconstruction dates back to some early work in geophysics [55, 56] where an ℓ_1 -norm minimization problem is employed to recover spike sequences, corresponding to sediment layer interfaces, from seismic data. Since then, the interest in sparse signal reconstruction with convex optimization appears now and again in several fields concerned both with the theoretical aspects of the method [57] and its applications [58, 59]. Despite these early

promising results, it was the introduction of compressive sensing [52, 60] that revived the interest in sparse signal recovery from limited data.

CS has found applications in a wide range of scientific fields from medical [60, 61] and ultrasound imaging [62], to error correction in channel coding [63], radar detection [64], seismic imaging [65, 66] and image reconstruction [54] to name a few. In ocean acoustics, CS is shown to improve the performance of matched field processing [67, 68], which is a generalized beamforming method for localizing sources in complex environments, and of coherent passive fathometry in inferring the number and depth of sediment layer interfaces [69].

In direction-of-arrival (DOA) estimation (see Sec. 3.1.4), CS achieves high-resolution acoustic imaging [70, 71], outperforming traditional methods [10]. Besides, DOA estimation with CS is reliable even with a single snapshot [72–74] unlike the cross-spectral DOA estimation methods [11], e.g., the minimum variance distortionless response beamformer (MVDR) [8] and the multiple signal classification (MUSIC) [9], which also offer super-resolution.

3.1.1 Compressive sensing framework

CS is a method to include data compression directly into signal acquisition with a single measurement process. Thus CS, in effect, requires a substantially smaller data set than the traditional sampling to provide accurate signal reconstruction under two conditions [12, 51, 53, 75]:

1. sparsity of the underlying signal,
2. sufficient incoherence of the process which maps the underlying signal to the observations so that distinct signals lead to distinct observations.

A concise description of the method follows.

Let $\mathbf{x} \in \mathbb{C}^N$ be an unknown vector representing the underlying signal we aim to reconstruct. Assume that the signal \mathbf{x} is sparse, i.e., it has only K nonzero elements with $K \ll N$. The underlying signal can be either sparse *per se*, e.g., an astronomical image with only a few stars in image processing, or in a more general sense it can be sparse in some domain of representation, e.g., the frequency domain representation of a sinusoidal time signal. Let $\mathbf{y} \in \mathbb{C}^M$ be a vector of measurements linearly related to the signal \mathbf{x} , e.g., time samples of the sinusoidal signal. In the absence of noise, the vectors \mathbf{x} and \mathbf{y} are related by a linear set of equations,

$$\mathbf{y} = \mathbf{A}\mathbf{x}. \quad (3.1)$$

The sensing matrix $\mathbf{A} = \mathbf{\Psi}\mathbf{\Phi}$ is the product of the matrix $\mathbf{\Phi}_{N \times N}$, a basis which transforms the signal from one domain to another (e.g., the identity matrix for originally sparse signals or the inverse discrete Fourier transform (IDFT) for a time-frequency representation), and the matrix $\mathbf{\Psi}_{M \times N}$, which represents the measurement process (e.g., time sampling). The matrix \mathbf{A} is assumed known and fixed, i.e., it does not adapt to the information on the signal \mathbf{x} , and full-rank.

Conventional sampling approaches [76] require a data rate that is at least twice the maximum frequency present in the signal (Nyquist rate) to preserve accurately the information in the signal. In this case, assuming that the maximum frequency in the signal does not exceed $N/2$ Hz, the measurement matrix is $\mathbf{\Psi} = \mathbf{I}_N$, where \mathbf{I}_N is the

$N \times N$ identity matrix. Then, the underlying signal is reconstructed accurately through the inverse transform $\hat{\mathbf{x}} = \mathbf{x} = \mathbf{A}^{-1}\mathbf{y} = \Phi^{-1}\mathbf{y}$.

For sparse signals, the conventional data acquisition rate is much higher than the rate of information in the signal. CS, on the other hand, exploits the inherent sparsity to capture all the information in the signal with only a few random measurements, effectively performing a compression as illustrated in Fig. 3.1. In the CS formulation, the problem in Eq. (3.1) is underdetermined, $M < N$, thus admits an infinite number of solutions. A way of solving this ill-posed problem is constraining the possible solutions with prior information, here by exploiting sparsity.

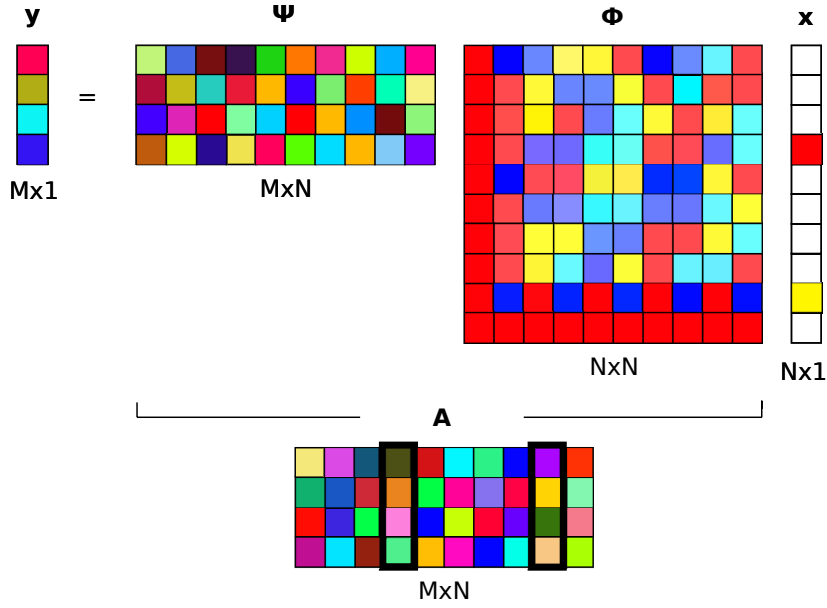


Figure 3.1: Compressive sensing method for data acquisition of sparse signals. The measurement vector \mathbf{y} is a linear combination of the two columns of the sensing matrix \mathbf{A} which correspond to nonzero coefficients of the signal \mathbf{x} . The deterministically random (incoherent) nature of \mathbf{A} allows for accurate reconstruction of the sparse signal \mathbf{x} even though the resulting problem is underdetermined $M < N$, thus ill-posed.

Figure 3.2 demonstrates the principle of compressive sensing with an example from optics, i.e., a single-pixel camera [77]. Assume a $(p \times p)$ -pixel image (arranged in a $(p \times p) = N$ -dimensional vector \mathbf{x}) which is captured and reconstructed from a digital camera. Many images have a sparse representation (only few non-zero coefficients) in some basis Φ (e.g., in the wavelet domain) [53]. Conventional (Nyquist) sampling requires $M = N$ sensors (observations \mathbf{y}) to collect N pixel values ($\Psi = \mathbf{I}_N$) and achieve accurate reconstruction ($\hat{\mathbf{x}} = \mathbf{x} = \Phi^{-1}\mathbf{y}$); see Fig. 3.2(a). A single-pixel camera uses instead a digital array of N micro-mirrors with variable orientations to reflect random portions of the incident light field (corresponding to the initial image) into a single sensor; see Fig. 3.2(b). Each micro-mirror can be oriented independently either towards the sensor (shown as black) or away from it (shown as white) and a random number generator sets the mirror orientations to a pseudorandom pattern for each measurement. Then,

M independent measurements are collected (forming the observation vector \mathbf{y} in this case) while the random orientation of the micromirrors at each measurement assures incoherence of the sensing process (i.e., a deterministically pseudorandom matrix Ψ). The array of micro-mirrors placed between the image and the sensor performs multiplexing allowing efficient image reconstruction through CS (see Sec. 3.1.3).

Concerning data compression, conventional schemes first acquire all the $M = N$ samples and then detect the significant coefficients through a basis transform Φ (e.g., a wavelet transform) which are subsequently saved while the rest are discarded. The image is reconstructed from the compressed data through an inverse transform based only on the retained coefficients [53] (omitted in Fig. 3.2). On the other hand, CS achieves data compression directly in the data acquisition process as it requires only $M < N$, $M \propto K$ observations.

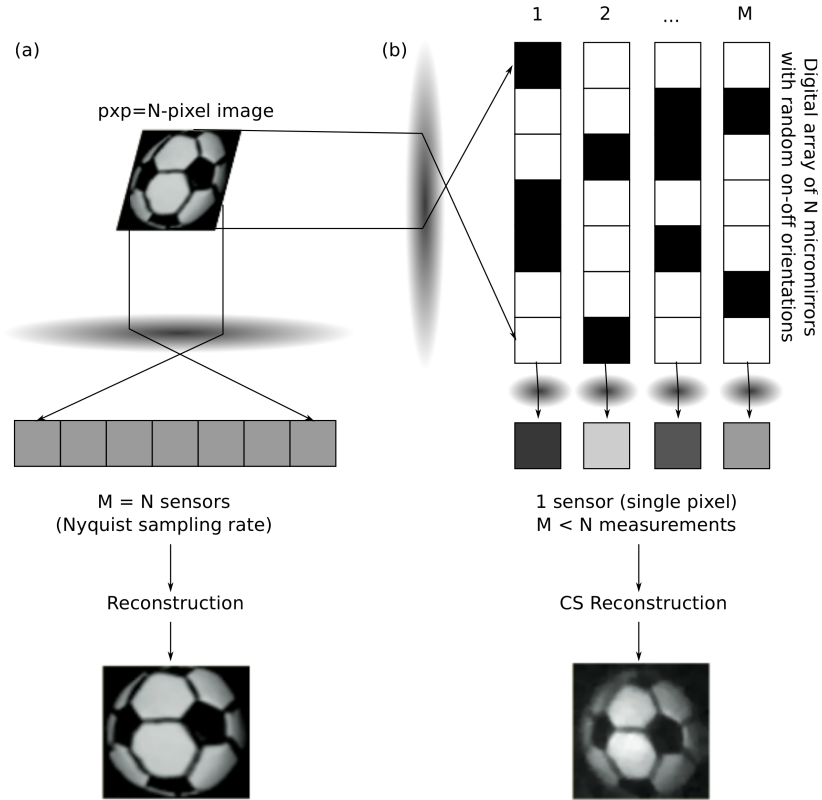


Figure 3.2: Single-pixel imaging demonstrating the principle of compressive sensing. A (64×64) -pixel ($N = 4096$), black-and-white image of a soccer ball is reconstructed through (a) conventional (Nyquist) sampling with $M = N = 4096$ sensors (photodiodes) and (b) CS from $M = 1600$ sequential random measurements with a single-sensor (single-pixel) camera. The example is adapted from Ref. [75].

3.1.2 Formulation of a convex optimization problem

A solution to the problem in Eq. (3.1) is obtained by minimizing an appropriate norm with an optimization procedure. To aid the reader, a short summary of the mathematical definitions of convex optimization problems and of norms follows.

A generic optimization problem has the form [78],

$$\begin{aligned} & \min_{\mathbf{x}} f_0(\mathbf{x}) \\ & \text{subject to} \quad f_i(\mathbf{x}) \leq 0, \quad i = 1, \dots, m \\ & \quad \quad \quad h_j(\mathbf{x}) = 0, \quad j = 1, \dots, q, \end{aligned} \quad (3.2)$$

where $\mathbf{x} \in \mathbb{C}^N$ is the optimization variable, the function $f_0 : \mathbb{C}^N \rightarrow \mathbb{R}$ is the objective (or cost) function, the functions $f_i : \mathbb{C}^N \rightarrow \mathbb{R}$ are the inequality constraint functions and the functions $h_j : \mathbb{C}^N \rightarrow \mathbb{C}$ are the equality constraint functions. The optimization problem (3.2) is convex when f_0, \dots, f_m are convex functions and h_1, \dots, h_q are affine (linear) functions.

The set of points for which the objective and all constraint functions in Eq. (3.2) are defined is called the domain of the optimization problem,

$$\mathcal{D} = \bigcap_{i=0}^m \text{dom} f_i \cap \bigcap_{j=1}^q \text{dom} h_j. \quad (3.3)$$

A point $\tilde{\mathbf{x}} \in \mathcal{D}$ is called feasible if it satisfies the constraints in Eq. (3.2).

The optimal value p^* of the optimization problem (3.2), achieved at the optimal variable \mathbf{x}^* , is,

$$\begin{aligned} p^* &= \inf \{ f_0(\mathbf{x}) \mid f_i(\mathbf{x}) \leq 0, \quad h_j(\mathbf{x}) = 0 \} \\ &= \{ f_0(\mathbf{x}^*) \mid f_i(\mathbf{x}^*) \leq 0, \quad h_j(\mathbf{x}^*) = 0 \}, \end{aligned} \quad (3.4)$$

for all $i = 1, \dots, m$ and $j = 1, \dots, q$.

There are several off-the-shelf toolboxes for disciplined convex optimization [79–82]. In this project, the cvx toolbox is used which is available in the Matlab environment. It uses interior point solvers, which are based on the gradient descent method, to obtain the global solution of a well-defined optimization problem [78].

A function $f : \mathbb{C}^N \rightarrow \mathbb{R}$ is called a norm if it is [78]:

1. nonnegative, i.e., $f(\mathbf{x}) \geq 0$ for all $\mathbf{x} \in \mathbb{C}^N$,
2. definite, i.e., $f(\mathbf{x}) = 0$ only if $\mathbf{x} = \mathbf{0}$,
3. homogeneous, i.e., $f(\alpha \mathbf{x}) = |\alpha| f(\mathbf{x})$ for all $\mathbf{x} \in \mathbb{C}^N$ and $\alpha \in \mathbb{C}$,
4. and satisfies the triangle inequality, i.e., $f(\mathbf{x}_1 + \mathbf{x}_2) \leq f(\mathbf{x}_1) + f(\mathbf{x}_2)$ for all $\mathbf{x}_1, \mathbf{x}_2 \in \mathbb{C}^N$.

The ℓ_p -norm of a vector $\mathbf{x} \in \mathbb{C}^N$ is defined as $\|\mathbf{x}\|_p = \left(\sum_{i=1}^N |x_i|^p \right)^{1/p}$ for $p \geq 1$ and it is a convex function. For example, for $p = 1$ the ℓ_1 -norm is the sum of the absolute values of the vector coefficients and for $p = 2$ the ℓ_2 -norm is the Euclidean distance.

By extension, the ℓ_0 -norm is defined as $\|\mathbf{x}\|_0 = \sum_{i=1}^n 1_{x_i \neq 0}$. Usually, the prefix *pseudo* (ℓ_0 -*pseudonorm*) is used since the ℓ_0 -norm does not fulfill the scaling property, $\|a\mathbf{x}\|_0 = \|\mathbf{x}\|_0 \neq |a| \|\mathbf{x}\|_0$, $a \neq 0$, hence it is not a proper norm.

3.1.3 Sparse signal reconstruction

By definition, a sparse estimate $\hat{\mathbf{x}}$ is obtained by minimizing the ℓ_0 -pseudonorm, which counts the number of non-zero entries in the vector,

$$\min_{\mathbf{x} \in \mathbb{C}^N} \|\mathbf{x}\|_0 \text{ subject to } \mathbf{y} = \mathbf{A}\mathbf{x}. \quad (P_0)$$

However, the minimization problem (P_0) ¹ is a nonconvex combinatorial problem which becomes computationally intractable even for moderate dimensions. The breakthrough of CS came with the proof that for sufficiently sparse signals and sensing matrices with sufficiently incoherent columns [83, 84] the (P_0) problem is equivalent to the (P_1) problem [52, 60, 85],

$$\min_{\mathbf{x} \in \mathbb{C}^N} \|\mathbf{x}\|_1 \text{ subject to } \mathbf{y} = \mathbf{A}\mathbf{x}. \quad (P_1)$$

The ℓ_1 relaxation (P_1) of the (P_0) problem (also known as basis pursuit [86]) is the closest convex optimization problem to (P_0) and can be solved efficiently with convex programming even for large dimensions. Moreover, due to the convexity of the ℓ_1 -norm, the method of minimizing (P_1) converges to the global minimum. Other ℓ_p -norm relaxations of the (P_0) problem for $0 < p < 1$, which also favor sparsity, are nonconvex and convergence to global minima is not guaranteed [59, 81]. However, they can be reformulated in an iterative reweighted convex minimization problem and yield sparse estimates provided proper initialization [59, 71, 87, 88].

For comparison, traditional methods solve the undetermined problem in Eq. (3.1), $M < N$ by seeking the solution with the minimum ℓ_2 -norm through the minimization problem (P_2) ,

$$\min_{\mathbf{x} \in \mathbb{C}^N} \|\mathbf{x}\|_2 \text{ subject to } \mathbf{y} = \mathbf{A}\mathbf{x}. \quad (P_2)$$

The problem (P_2) is convex and has the analytic minimum length solution,

$$\hat{\mathbf{x}} = \mathbf{A}^H (\mathbf{A}\mathbf{A}^H)^{-1} \mathbf{y}. \quad (3.5)$$

It aims to minimize the energy of the underlying signal through the ℓ_2 -norm, rather than its sparsity, hence its solution is non-sparse. Thus, the problem (P_1) has increased performance over (P_2) for sparse signals (at the cost of computational complexity since it does not have an analytic solution) and it can be solved efficiently with convex optimization.

Figure 3.3 depicts the geometry of the ℓ_p -norm minimization problem, for $0 \leq p \leq 2$ constrained to fit the data. To keep the visualization intuitive, an example is considered where the sparse vector $\mathbf{x} \in \mathbb{R}^2$, with a single nonzero element ($\|\mathbf{x}\|_0 = 1$), is to be recovered by $\mathbf{y} \in \mathbb{R}$ linear measurements. Since there are less observations than unknowns, all \mathbf{x} residing on the line $\mathbf{y} = \mathbf{A}\mathbf{x}$ satisfy the constraint. A unique solution is found only by providing additional information about \mathbf{x} . For example, we seek the one with the minimum ℓ_p -norm.

Geometrically, all vectors with ℓ_p -norm less or equal to a value $r \in \mathbb{R}$ are on an ℓ_p -ball with radius r , $\{\mathbf{x} \mid \|\mathbf{x}\|_p \leq r\}$. In \mathbb{R}^2 , the ℓ_2 -ball is a disk while the ℓ_1 -ball is a rhombus. The solution $\hat{\mathbf{x}}$, is the intersection of the measurement line and the smallest ℓ_p -ball. The ℓ_2 -norm optimization problem, Fig. 3.3(d), results almost always in non-sparse solutions due to the isotropy of the ℓ_2 -ball. In contrast, the edginess of the ℓ_p -ball, $0 < p \leq 1$ favors sparse solutions, Fig. 3.3(b),(c), and likely leads to the solution of the ℓ_0 -norm problem, Fig. 3.3(a).

¹The equation labeling (P_p) is used to denote the ℓ_p -norm minimization problem.

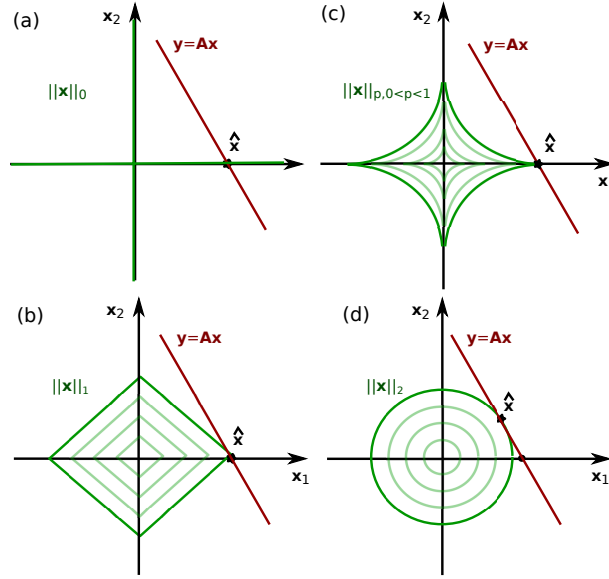


Figure 3.3: Geometric visualization of (a) the ℓ_0 -norm, (b) the ℓ_1 -norm, (c) the $\ell_{<1}$ -norm and (d) the ℓ_2 -norm problem in \mathbb{R}^2 . The solution $\hat{\mathbf{x}}$ is the intersection of the measurement line $\mathbf{y} = \mathbf{A}\mathbf{x}$ and the minimum norm-ball in each case.

The theory extends to noisy measurements and compressible signals (approximately sparse) [89–91] making the framework useful for practical applications. Assuming that the measurements are contaminated with additive noise $\mathbf{n} \in \mathbb{C}^M$ such that $\mathbf{y} = \mathbf{A}\mathbf{x} + \mathbf{n}$ the (P_1) problem is reformulated as,

$$\min_{\mathbf{x} \in \mathbb{C}^N} \|\mathbf{x}\|_1 \text{ subject to } \|\mathbf{A}\mathbf{x} - \mathbf{y}\|_2 \leq \epsilon, \quad (P_1^\epsilon)$$

where ϵ is the noise floor. The solution to (P_1^ϵ) has the minimum ℓ_1 -norm while it fits the data up to the noise level. (P_1^ϵ) can be reformulated in an unconstrained form with the use of Lagrange multipliers,

$$\min_{\mathbf{x} \in \mathbb{C}^N} \|\mathbf{A}\mathbf{x} - \mathbf{y}\|_2^2 + \mu \|\mathbf{x}\|_1, \quad (P_1^\mu)$$

where the regularization parameter μ controls the relative importance between the sparsity of the solution (ℓ_1 -norm term) and the fit to the measurements (ℓ_2 -norm term). The unconstrained problem (P_1^μ) has the form of a least-squares minimization with an ℓ_1 regularization term and it is also known as the least absolute shrinkage and selection operator (LASSO) [58]. The minimizer of (P_1^μ) corresponds to the maximum a posteriori (MAP) estimate in a Bayesian formulation assuming a complex Gaussian likelihood for the data and a Laplace-like prior distribution for the parameters of the underlying signal \mathbf{x} [92].

3.1.4 DOA estimation

The problem of DOA estimation in acoustic imaging refers to the localization of (usually a few) sources from noisy measurements of the wavefield with an array of sensors. For

simplicity, we assume that the waves are locally planar over the array aperture, i.e., the sources are in the far-field of the array, and narrowband processing with a known sound speed. Considering the one-dimensional problem with a uniform linear array (ULA) of sensors, the location of a source is characterized by the direction of arrival of the associated plane wave, $\theta \in [-90^\circ, 90^\circ]$, with respect to the array axis; see Fig. 3.4.

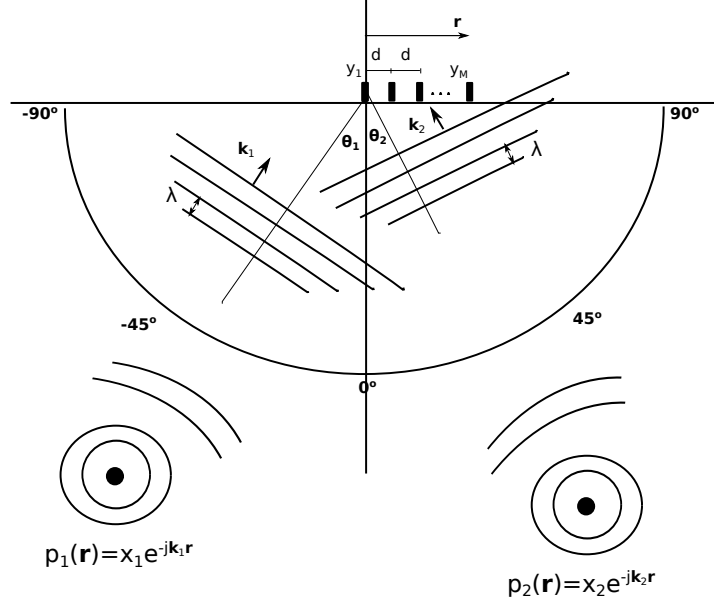


Figure 3.4: Sound source localization with a uniform linear array (ULA). The sources are in the far-field of the array such that the wavefronts, $p(\mathbf{r})$, are locally plane upon arrival. The recorded sound pressure at the array \mathbf{y} is a superposition of plane waves from different directions θ weighted by the complex source amplitudes \mathbf{x} .

The propagation delay from the i th potential source to each of the M array sensors is described by the steering (or replica) vector,

$$\mathbf{a}(\theta_i) = \frac{1}{\sqrt{M}} \left[1, e^{j2\pi \frac{d}{\lambda} \sin \theta_i}, \dots, e^{j2\pi \frac{d}{\lambda} (M-1) \sin \theta_i} \right]^T, \quad (3.6)$$

where λ is the wavelength and d is the intersensor spacing. The normalization $1/\sqrt{M}$, such that $\|\mathbf{a}\|_2 = 1$, is used to simplify the analysis.

Discretizing the half-space of interest, $\theta \in [-90^\circ, 90^\circ]$, into N angular directions the DOA estimation problem can be expressed with the linear model,

$$\mathbf{y} = \mathbf{A}\mathbf{x} + \mathbf{n}, \quad (3.7)$$

where $\mathbf{y} \in \mathbb{C}^M$ is the complex-valued data vector from the measurements at the M sensors, $\mathbf{x} \in \mathbb{C}^N$ is the unknown vector of the complex source amplitudes at all N directions on the angular grid of interest and $\mathbf{n} \in \mathbb{C}^M$ is the additive noise vector. The sensing matrix,

$$\mathbf{A}_{M \times N} = [\mathbf{a}(\theta_1), \dots, \mathbf{a}(\theta_N)], \quad (3.8)$$

maps the source vector \mathbf{x} to the observations \mathbf{y} and has as columns the steering vectors in Eq. (3.6) at all look directions.

The problem of DOA estimation is to recover the source vector $\mathbf{x} \in \mathbb{C}^N$, given the sensing matrix $\mathbf{A}_{M \times N}$ and an observation vector $\mathbf{y} \in \mathbb{C}^M$. Practically, even though there are only a few sources $K < M$ generating the acoustic field, we are interested in a fine resolution on the angular grid to achieve accurate localization such that $M \ll N$ and the problem in Eq. (3.7) is underdetermined. Employing the framework of sparse signal reconstruction, high-resolution DOA estimation is achieved by solving, for example, (P_1^e) .

It is important to note that in DOA estimation, as in many other problems, the sensing matrix $\mathbf{A} = \mathbf{\Psi}\mathbf{\Phi}$ has a structure related to the underlying physical process. Specifically, in array signal processing $\mathbf{\Phi}$ is an IDFT basis between the spatial and the wavenumber domain and $\mathbf{\Psi}$ is a sampling matrix selecting the rows of the IDFT basis corresponding to the positions of the sensors; see Fig. 3.5. This results to a structured matrix \mathbf{A} , namely an oversampled DFT basis, setting limitations in the quality of reconstruction; see Sec. 3.1.5.

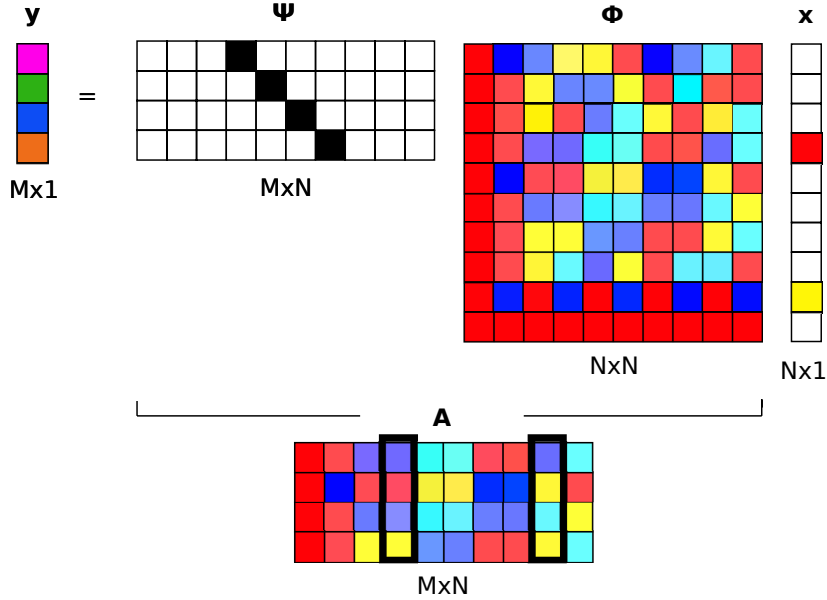


Figure 3.5: Data acquisition of sparse signals in array signal processing resulting in a structured sensing matrix \mathbf{A} . Compare with CS data acquisition in Fig. 3.1.

3.1.5 Limitations of CS in DOA estimation

3.1.5.1 Coherent sensing matrix

To guarantee good performance of CS in parameter estimation, the columns of the sensing matrix should be incoherent as described by the restricted isometry property (RIP) [93, 94]. Note that we use the term incoherent columns to refer to linearly independent vectors in accordance with the terminology in the compressive sensing literature

[12, 51]; not to be confused with the coherence of sound sources or wavefield arrivals. Sufficient incoherence of the sensing matrix is achieved with high-probability with random measurements [52, 63]. In this case, the optimization problems (P_0) and (P_1) are equivalent, resulting in the same unique solution.

In contrast, many problems involve sensing matrices with highly coherent columns thus the study of sparse recovery with a coherent sensing matrix is important [95–97]. In the case of a coherent sensing matrix, uniqueness of the CS solution is not guaranteed as the underdetermined problem becomes extremely ill-posed (i.e., there are more than one solutions with equal ℓ_1 -norm that explain the data). Therefore, the sparse estimate may be offset from the actual solution. An analysis of the performance of CS in relation to the coherence of the sensing matrix \mathbf{A} in DOA estimation is presented in Ref. [71].

3.1.5.2 Basis mismatch

Another limitation is basis mismatch [98] which occurs when the nonzero coefficients of the sparse signal \mathbf{x} do not coincide with the grid due to inadequate discretization. Under basis mismatch, spectral leakage leads to inaccurate reconstruction. Employing finer grids [70, 99] alleviates basis mismatch on the expense of increased computational complexity, especially in large two-dimensional or three-dimensional problems as encountered in seismic imaging for example [65, 66, 100]. More importantly, grid refinement results in increased coherence of the measuring process, which can induce offset in the estimates [71]. A way to overcome basis mismatch is to avoid discretization by solving the minimization problem (P_1^ϵ) in the dual domain [78] and achieve DOA estimation through polynomial rooting [101–104].

The trade-off between coherence of the sensing matrix in DOA estimation and basis mismatch is illustrated in Fig. 3.6.

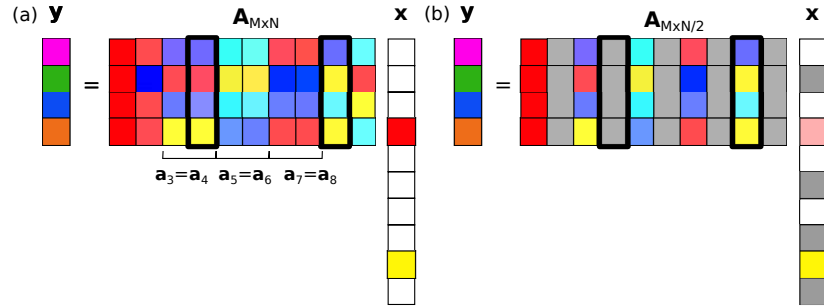


Figure 3.6: Trade-off between coherence of a structured sensing matrix and basis mismatch. (a) Fine discretization of the problem captures all the features of the sparse signal \mathbf{x} but results in an oversampled DFT basis with coherent columns constituting a hopelessly ill-posed inverse problem. (b) Coarse discretization (excluding every second column of \mathbf{A} depicted as grey) reduces the coherence between the columns of the resulting sensing matrix but does not provide the required resolution to capture some features (e.g. the red component) of the sparse signal \mathbf{x} .

3.2 Contributions

Indications of the high-resolution capabilities and the robustness of CS in DOA estimation are presented in Refs. [70, 72, 74]. Malioutov *et al.* [70] study the performance of CS in DOA estimation with respect to noise, source number and coherent arrivals and compare it with the performance of traditional DOA estimation methods both in the single and multiple-snapshot formulation. Their analysis is based on the unconstrained form of the ℓ_1 minimization problem (P_1^μ) and the importance of a good choice of regularization parameter is indicated, yet not systematically studied.

Edelmann and Gaumond [72] compare the single-snapshot sparse signal reconstruction method with conventional beamforming using towed array data. Thus, they validate the superior performance of CS-based reconstruction with experimental results, which is more pronounced with undersampling.

Fortunati *et al.* [74] investigate the statistical performance and the resolution capabilities of CS in single-snapshot DOA estimation with different algorithms and compare it with conventional beamforming. Their results show that CS provides improved accuracy and resolution in DOA estimation which is validated with experimental towed array data from a bistatic sonar configuration.

Furthermore, Refs. [73, 105–107] employ the LASSO formulation (P_1^μ) to express the sparse DOA reconstruction as the MAP estimator in the Bayesian formulation with a complex Gaussian likelihood for the data and a Laplace-like prior distribution for the source amplitudes. Specifically, Refs. [106, 107] study the regularization parameter selection problem in the generalized LASSO formulation [108]. They show that an optimal value for the regularization parameter is indicated by the LASSO path [108, 109] for a given sparsity level.

References [73, 105] are concerned with DOA tracking, i.e., a sequential estimation technique that follows the DOA evolution in time-varying scenarios (e.g. moving sources). They introduce a sequential Bayesian approach imposing a weighted Laplace-like prior to the source amplitudes where the weights (hyperparameters) are updated according to information from previous iterations. Thus, DOA tracking is achieved by single-snapshot processing, yet combining effectively information through multiple snapshots.

Along with the aforementioned research on sparse signal reconstruction for DOA estimation, our contribution [71, 88, 104, 110] comprises:

- The adaptation of the CS theory to narrowband DOA estimation with linear arrays both for single-snapshot and multiple-snapshot processing.
- A systematic analysis of the limitations of CS in DOA estimation in relation to the discretization of the angular grid, the coherence of the sensing matrix, the geometry of the array and the SNR.
- Methods to improve the accuracy in DOA estimation under noise-level uncertainty through a reweighed iterative optimization process.
- Tailoring the optimization theory of primal-dual formulation to DOA estimation thus achieving grid-free sparse reconstruction and overcoming the problem of basis mismatch.
- Demonstration of the high-resolution capabilities of CS-based DOA estimation by comparison with conventional DOA estimation methods.
- Validation of the results with experimental data from ocean acoustic measurements.

A summary of the papers related to part II follows.

3.2.1 Part II: Papers C-G

Paper C demonstrates the robustness of CS in DOA estimation with sensor arrays both with simulations and experimental data from ocean acoustic measurements. It is shown that sparse signal reconstruction outperforms traditional DOA estimation methods providing high-resolution imaging even with coherent arrivals, single-snapshot data and random array geometries. A systematic analysis of the limitations of CS in DOA estimation is introduced. Finally, an iterative reweighted ℓ_1 -norm optimization scheme is proposed to enhance sparsity under noisy conditions.

Paper D investigates the possibility of improving the resolution in sparse signal reconstruction for DOA estimation by solving an ℓ_p -norm minimization problem with $0 < p < 1$. It is shown that, even though the resulting optimization problem is non-convex, it reduces to an iterative reweighted ℓ_2 -norm minimization problem which is convex and has an analytic solution. The focal underdetermined system solver (FOCUSS) algorithm [81] is employed to solve the iterative reweighted ℓ_2 -norm minimization problem.

Paper E provides the theoretical framework for solving the DOA estimation problem as a sparse signal reconstruction in the continuum of the angular spectrum. It demonstrates that by avoiding discretization of the problem, we circumvent basis mismatch resulting in high-resolution sparse DOA reconstruction. The method is shown to overcome limitations of traditional DOA estimation methods.

Paper F expresses the sparse signal reconstruction in DOA estimation as a least-squares minimization problem with an ℓ_1 -norm regularization term. It indicates that in this form the CS solution can be interpreted as the MAP estimate in a statistical Bayesian setting both in the single and multiple-snapshot formulation. A procedure is explained for choosing the regularization parameter to achieve an estimate with the desired sparsity level. It is shown that CS outperforms conventional DOA estimation methods which is validated with experimental data from a multipath shallow water environment.

Paper G investigates the application of sparse signal reconstruction to DOA estimation with spherical arrays. It shows through simulations that CS achieves high-resolution acoustic imaging in spherical array signal processing outperforming traditional methods.

3.3 Perspectives and future work

The present study provides the foundations of sparse reconstruction in DOA estimation and demonstrates the great potential of the method for high-resolution acoustic imaging. These promising results encourage for further research. As the application of CS in DOA estimation is relatively new, there is a number of exciting perspectives:

- The present analysis is limited to linear arrays and one-dimensional sound source localization. Generalization of sparse signal reconstruction to two-dimensional and three-dimensional source localization is of great interest with direct applications in near-field acoustic and seismic imaging. Besides, the study of array configurations other than linear (e.g., spherical arrays as in Paper G) will extend the realm of applications.

- The notion of sparsity in DOA estimation indicates point sources. However, several acoustic scenes involve extended sources, e.g., sources of aeroacoustic noise from wind turbines [111]. Thus, it is important to extend the analysis of sparse signal reconstruction to continuous sources by promoting block sparsity, e.g., through the fused LASSO problem [112].
- Moreover, recovery of non-sparse signals, e.g., by applying sparsity constraints on the second-order statistics of the spatial source distribution [50] rather than on the source distribution *per se*, would make the method more universal.
- Since the underlying mechanism of sound propagation yields highly structured problems (i.e., non-random sensing matrix \mathbf{A}), it is relevant from a computational perspective to investigate convex optimization algorithms tailored for structured problems [113] to improve the reconstruction accuracy and the computational efficiency.
- Supplementary, extensive experimental validation of CS-based DOA estimation in more complex scenarios (e.g., incorporating Doppler shifts for moving sources) would establish the robustness of the method.

CHAPTER 4

Summary/Conclusion

This PhD study investigates methods in array signal processing that achieve high-resolution acoustic imaging. The methods are applied to active sonar signal processing for localization and statistical characterization of weak scattering fields and to passive sonar signal processing for DOA estimation and source tracking.

The study comprises two parts. The first part examines the use of a high-frequency active sonar for detection and statistical characterization of submerged oil contamination in sea water due to an oil spill from a deep-water oil drill (Papers A, B). The water column is modeled as a spatially stationary random field of compressibility and density inhomogeneities, with an area which is characterized by different spatial covariance characteristics, i.e., variance, correlation length and anisotropy. For that reason, an algorithm for synthetically generating stationary, Gaussian random fields is introduced (Paper A). It is demonstrated that the selected random field generator supports a variety of covariance models which can be used to represent different spatial properties of the field, such as isotropy or anisotropy, smoothness or irregularity. What is more, it dissociates the random numbers and the covariance parameters such that they can be altered separately. In addition, this allows for local perturbations of the random field. Therefore, the selected random field generator provides great flexibility in implementing the physical model of an inhomogeneous field with spatial covariance.

Since the existence of submerged oil is controlled by the ambient density, the difference in the acoustic parameters between the oil contamination area and the surrounding medium is considered small. As a result, when insonified with an acoustic wave, the submerged oil field causes weak scattering of the incident acoustic energy. A model is implemented to study the underlying mechanisms of backscattering due to spatial heterogeneity of the medium and predict the backscattering returns (Paper A). A unified approach is adopted to model weak scattering both from volume heterogeneity and interface roughness. The unified approach considers interface roughness as a special case of spatial heterogeneity. Thus, backscattering due to water-oil interface roughness can be successfully integrated to the scattering model from spatial heterogeneity of the acoustic parameters. Scattering from light gas bubbles is also studied and included in the model.

High-frequency acoustic methods are proposed to detect and localize the oil polluted area (Papers A, B). A monostatic active sonar configuration is considered to insonify the medium and receive the backscattered returns. The acoustic map is subject to the resolution limitations of the sonar. Nevertheless, it is shown that high-frequency sonars improve the resolution in the acoustic imaging allowing the detection of small scale structure. A method for inference of spatial covariance parameters, i.e., variance and correlation, is proposed to describe the scattering field in terms of its second-order statistics from the backscattered returns (Papers A, B). It is indicated that high-frequency acoustics provide a quantitative statistical description of the random field which is useful in monitoring the degradation process of the submerged oil contamination.

All in all, the results indicate that high-frequency acoustic methods not only are suitable for large-scale detection of oil contamination in the water column but also allow inference of the spatial covariance parameters resulting in a statistical description of the oil field. However, experimental validation is required to tune the statistical parameters of the random fields and improve the sound propagation model based on the sound speed profile and the geomorphy of the experimental site.

The second part adapts the theory of compressive sensing (CS) to direction-of-arrival (DOA) estimation in passive sonar signal processing, which is the main research topic of the PhD study. Signal acquisition based on CS can be more efficient than traditional sampling for sparse or compressible signals. Consequently, CS requires much fewer measurements than traditional methods for accurate reconstruction when the underlying signal is sparse. The problem of DOA estimation involves inferring the number, the angular direction and the complex amplitude of usually few wavefront arrivals, possibly in the presence of noise, from measurements of the wavefield with an array of sensors. Hence, DOA estimation is essentially a sparse signal reconstruction problem from an undetermined linear system of equations. Exploiting the inherent sparsity, the problem of DOA estimation can be solved in the CS framework, i.e., by solving an ℓ_1 -norm minimization problem with convex optimization, to achieve high-resolution acoustic imaging.

It is demonstrated that CS outperforms the conventional DOA estimation methods (Papers C–G). Specifically, conventional beamforming (CBF), which can be interpreted as an ℓ_2 -norm minimization problem, suffers from low resolution and the presence of side-lobes. Other methods, such as MVDR and MUSIC, overcome the resolution limit of conventional beamforming by exploiting signal information conveyed by the cross-spectral matrix and offer high-resolution DOA maps. However, the performance of cross-spectral methods depends on the eigenvalues of the cross-spectral matrix thus it degrades with few snapshots (observations of the array output), when the cross-spectral matrix is rank deficient, and in the presence of coherent arrivals, when the signal subspace is reduced. CS achieves high-resolution acoustic imaging by promoting sparsity in the reconstructed DOA map even with a single snapshot and coherent arrivals since it utilizes directly the measured pressure and not the cross-spectral matrix. For multiple snapshots, CS assumes a constant sparsity profile to combine information across snapshots (Papers C, F).

The ℓ_1 -norm minimization is a convex problem thus converges to a global minimum. However, the solution to the ℓ_1 -norm minimization problem is often not the sparsest possible, especially with noisy observations. It is demonstrated that the ℓ_1 -norm can be replaced by other sparsity promoting functions to enhance sparsity (Papers C, D). Even though the resulting problem is non-convex, it can be solved with convex optimization as an iterative reweighted ℓ_1 -norm minimization problem. Provided proper initialization, convergence to local minima is avoided.

The limitations of CS in DOA estimation are described by an offset and resolution analysis (Paper C). It is shown that the estimate offset and the resolution of CS are related to the coherence of the sensing matrix and depend on array geometry, frequency, source location and SNR. Nevertheless, these limitations are restricted to the proximity of the direction of the actual arrival while CS has robust performance in most of the angular spectrum.

On a discrete angular grid, the CS reconstruction degrades due to basis mismatch when the DOAs do not coincide with the angular directions on the grid. Basis mismatch can be overcome by formulating the problem in the continuum of the angular spectrum. It is shown that, even though the problem in the continuous formulation

has infinitely many unknowns, it can be solved efficiently over few optimization variables in the dual domain with semidefinite programming (Paper E). Utilizing the dual optimal variables, the DOAs are accurately reconstructed through polynomial rooting. Polynomial rooting is employed in several DOA estimation methods to improve the resolution (Root-MVDR, Root-MUSIC). However, these methods involve the estimation of the cross-spectral matrix hence they require many snapshots and stationary incoherent sources and are suitable only for uniform linear arrays. Grid-free CS is demonstrated not to have these limitations (Paper E).

The ℓ_1 -norm minimization problem in sparse signal reconstruction can be reformulated into a least-squares problem with an ℓ_1 -norm regularization term. This formulation allows the sparse reconstruction method to be interpreted in a Bayesian setting where both the observations and the unknowns are treated as stochastic processes. Assuming a complex Gaussian likelihood for the data and a Laplacian-like prior for the unknown complex parameters, the CS solution is shown to be the maximum a posteriori estimate both in the single and the multiple snapshot case (Paper F). In the ℓ_1 -norm regularized least-squares formulation, the choice of the regularization parameter is crucial as it controls the balance between the sparsity of the estimated solution and the data-fit, determining the quality of the reconstruction. The solution as a function of the regularization parameter follows a piecewise smooth trajectory. It is shown that the singularity points in the solution path are associated with a change in sparsity and can be used to indicate a proper value of the regularization parameter to achieve high-resolution DOA reconstruction (Paper F).

Overall, CS reconstruction in DOA estimation provides high-resolution acoustic imaging even with non-uniform array configurations, single-snapshot data, coherent arrivals and under noisy conditions outperforming conventional DOA estimation methods. This is validated both through simulations and with experimental towed array data from ocean acoustic measurements.

Bibliography

- [1] E. Tiana-Roig, F. Jacobsen, and E. Fernandez-Grande. Beamforming with a circular microphone array for localization of environmental noise sources. *J. Acoust. Soc. Am.*, **128**(6):3535–3542, 2010.
- [2] A. Xenaki, F. Jacobsen, and E. Fernandez-Grande. Improving the resolution of three-dimensional acoustic imaging with planar phased arrays. *J. Sound Vibration*, **331**(8):1939–1950, 2012.
- [3] Y. Fan, B. Tysoe, J. Sim, K. Mirkhani, A. Sinclair, F. Honarvar, H. Sildva, A. Szecket, and R. Hardwick. Nondestructive evaluation of explosively welded clad rods by resonance acoustic spectroscopy. *Ultrasonics*, **41**(5):369–375, 2003.
- [4] X. Lurton. *An Introduction to Underwater Acoustics: Principles and Applications*, chapter 3. Praxis Publishing, Chichester, UK, 2002.
- [5] J. J. Arendt. A model for the propagation and scattering of ultrasound in tissue. *J. Acoust. Soc. Am.*, **89**(1):182–190, 1991.
- [6] D. H. Johnson and D. E. Dudgeon. *Array signal processing: concepts and techniques*, chapter 1–4. Prentice Hall, New Jersey, 1993.
- [7] M. S. Bartlett. Smoothing periodograms from time series with continuous spectra. *Nature*, **161**(4096):686–687, 1948.
- [8] J. Capon. High-resolution frequency-wavenumber spectrum analysis. *Proc. IEEE*, **57**(8):1408–1418, 1969.
- [9] R. Schmidt. Multiple emitter location and signal parameter estimation. *IEEE Trans. Antennas Propag.*, **34**(3):276–280, 1986.
- [10] H. Krim and M. Viberg. Two decades of array signal processing research: the parametric approach. *IEEE Signal Proc. Mag.*, **13**(4):67–94, 1996.
- [11] H. L. Van Trees. *Optimum Array Processing (Detection, Estimation, and Modulation Theory, Part IV)*, chapter 1–10. Wiley-Interscience, New York, 2002.
- [12] M. Elad. *Sparse and redundant representations: from theory to applications in signal and image processing*, pages 1–359. Springer, New York, 2010.
- [13] Deepwater horizon accident and response. <http://www.bp.com/en/global/corporate/gulf-of-mexico-restoration/deepwater-horizon-accident-and-response.html>, April 2015.

- [14] R. L. Crout. Measurements in support of the Deepwater Horizon (MC-252) oil spill response. In *Proceedings of SPIE 8030, Ocean Sensing and Monitoring III*, volume 8030, pages 80300J:1–12, Orlando, FL, 2011. International Society for Optics and Photonics.
- [15] L. Shi, A. Y. Ivanov, M. He, and C. Zhao. Oil spill mapping in the western part of the East China Sea using synthetic aperture radar imagery. *Int. J. Remote Sens.*, **29**(21):6315–6329, 2008.
- [16] M. Schrope. Oil spill: Deep wounds. *Nature*, **472**(7342):152–154, 2011.
- [17] S. A. Socolofsky, E. E. Adams, and C. R. Sherwood. Formation dynamics of sub-surface hydrocarbon intrusions following the Deepwater Horizon blowout. *Geoph. Res. Lett.*, **38**(9), 2011.
- [18] R. Camilli, C.M. Reddy, D.R. Yoerger, B.A.S. Van Mooy, M.V. Jakuba, J.C. Kinsey, C.P. McIntyre, S.P. Sylva, and J.V. Maloney. Tracking hydrocarbon plume transport and biodegradation at Deepwater Horizon. *Science*, **330**(6001):201–204, 2010.
- [19] J.D. Kessler, D.L. Valentine, M.C. Redmond, M. Du, E.W. Chan, S.D. Mendes, E.W. Quiroz, C.J. Villanueva, S.S. Shusta, L.M. Werra, S.A. Yvon-Lewis, and T.C. Weber. A persistent oxygen anomaly reveals the fate of spilled methane in the deep Gulf of Mexico. *Science*, **331**(6015):312–315, 2011.
- [20] A.R. Diercks, R.C. Highsmith, V.L. Asper, D.J. Joung, Z. Zhou, L. Guo, A.M. Shiller, S.B. Joye, A.P. Teske, N. Guinasso, T.L. Wade, and S.E. Lohrenz. Characterization of subsurface polycyclic aromatic hydrocarbons at the Deepwater Horizon site. *Geoph. Res. Lett.*, **37**(20):L20602:1–6, 2010.
- [21] D. Tang. A note on scattering by a stack of rough interfaces. *J. Acoust. Soc. Am.*, **99**(3):1414–1418, 1996.
- [22] A. N. Ivakin. A unified approach to volume and roughness scattering. *J. Acoust. Soc. Am.*, **103**(2):827–837, 1998.
- [23] L. R. LeBlanc, S. G. Schock, DeBruin D. L., M. Jenkins, and L. Munro. High-resolution sonar volume scattering measurements in marine sediments. *J. Acoust. Soc. Am.*, **97**(5):2979–2986, 1995.
- [24] A. Xenaki, P. Gerstoft, and K. Mosegaard. Modeling and detection of oil in sea water. *J. Acoust. Soc. Am.*, **134**(4):2790–2798, 2013.
- [25] A. Xenaki, P. Gerstoft, O. Carriere, and K. Mosegaard. Statistical characterization of weak scattering fields with inverse methods. In *MTS/IEEE Oceans 2013*, pages 1–7, 2013.
- [26] T. Mejer Hansen, K. Skou Cordua, M. Caroline Looms, and K. Mosegaard. SIPPI: A Matlab toolbox for sampling the solution to inverse problems with complex prior information: Part 1-Methodology. *Comput. Geosci.*, 52:470–480, 2013.

- [27] P. Goovaerts. *Geostatistics for Natural Resources Evaluation*, chapter 4.2. Oxford University Press, New York, 1997.
- [28] M. L. Ravalec, B. Noetinger, and L. Y. Hu. The FFT moving average (FFT-MA) generator: An efficient numerical method for generating and conditioning Gaussian simulations. *Math. Geol.*, **32**(6):701–723, 2000.
- [29] M. J. L. Robin, A. L. Gutjahr, E. A. Sudicky, and J. L. Wilson. Cross-correlated random field generation with the direct Fourier transform method. *Water Resour. Res.*, **29**(7):2385–2397, 1993.
- [30] F. Ruan and D. McLaughlin. An efficient multivariate random field generator using the fast Fourier transform. *Adv. Water Resour.*, **21**(5):385–399, 1998.
- [31] P. M. Morse and K. U. Ingard. *Theoretical Acoustics*, chapter 8. International Series in Pure and Applied Physics. McGraw-Hill, New York, 1968.
- [32] V. Murino and A. Trucco. Three-dimensional image generation and processing in underwater acoustic vision. *Proceedings of the IEEE*, **88**(12):1903–1984, 2000.
- [33] L. A. Chernov. *Wave Propagation in a Random Medium*, chapter 4. McGraw-Hill, New York, 1960.
- [34] D. R. Jackson and M. D. Richardson. *High-Frequency Seafloor Acoustics*, chapter 2, 7, 14. Monograph series in underwater acoustics. Springer, New York, 2007.
- [35] A. Turgut. Inversion of bottom/subbottom statistical parameters from acoustic backscatter data. *J. Acoust. Soc. Am.*, **102**(2):833–852, 1997.
- [36] A. N. Ivakin and J-P. Sessarego. High frequency broad band scattering from water-saturated granular sediments: Scaling effects. *J. Acoust. Soc. Am.*, **122**(5):EL165–EL171, 2007.
- [37] H. Medwin and C. S. Clay. *Fundamentals of Acoustical Oceanography*, chapter 9. Academic Press, Boston, 1998.
- [38] A. A. Douglas and A. P. Lyons. Novel physical interpretations of K-distributed reverberation. *IEEE J. Oceanic Eng.*, **27**(4):800–813, 2002.
- [39] A. P. Lyons and A. A. Douglas. Statistical characterization of high-frequency shallow-water seafloor backscatter. *J. Acoust. Soc. Am.*, **106**(1):1307–1315, 1999.
- [40] D. R. Jackson, K. B. Briggs, and M. D. Richardson. Tests of models for high-frequency seafloor backscatter. *IEEE J. Oceanic Eng.*, **21**(4):458–470, 1996.
- [41] A. N. Gavrilov and I. M. Parnum. Fluctuations of seafloor backscatter data from multibeam sonar systems. *IEEE J. Oceanic Eng.*, **35**(2):209–219, 2010.
- [42] N. P. Chotiros. Non-Rayleigh distributions in underwater acoustic reverberation in a patchy environment. *IEEE J. Oceanic Eng.*, **35**(2):236–241, 2010.

- [43] G. Wendelboe, H. Dahl, E. Maillard, and L. Bjorno. Towards a fully calibrated multibeam echosounder. In *Proceedings of Meetings on Acoustics*, volume 17, pages 1836–1843, Edinburgh, UK, 2012.
- [44] M. Palmese and A. Trucco. Acoustic imaging of underwater embedded objects: Signal simulation for three-dimensional sonar instrumentation. *IEEE Trans. Instrum. Meas.*, **55**(4):1339–1347, 2006.
- [45] D. Li. *Modeling of Monostatic Bottom Backscattering from Three-Dimensional Volume Inhomogeneities and Comparisons with Experimental Data*, pages 17–186. Ph.D. dissertation, Mass. Inst. Tech., Cambridge, MA, September 1997.
- [46] D. Li, G. V. Frisk, and D. Tang. Modeling of bottom backscattering from three-dimensional volume inhomogeneities and comparisons with experimental data. *J. Acoust. Soc. Am.*, **109**(4):1384–1397, April 2001.
- [47] R. Camilli, D. Di Iorio, A. Bowen, C. M. Reddy, A. H. Techet, D. R. Yoerger, L. L. Whitcomb, J. S. Seewald, S. P. Sylva, and J. Fenwick. Acoustic measurement of the Deepwater Horizon Macondo well flow rate. *Proc. Natl. Acad. Sci. U.S.A.*, **109**(50):20235–20239, 2012.
- [48] M. K. K. McNutt, R. Camilli, T. J. Crone, G. D. Guthrie, P. A. Hsieh, T. B. Ryerson, O. Savas, and F. Shaffer. Review of flow rate estimates of the Deepwater Horizon oil spill. *Proc. Natl. Acad. Sci. U.S.A.*, **109**(50):20260–20267, 2012.
- [49] J. A. Hildebrand, L. Armi, and P. C. Henkart. Seismic imaging of the water-column deep layer associated with the Deepwater Horizon oil spill. *Geophysics*, **77**(2):11–16, 2012.
- [50] S. Zhong, Q. Wei, and X. Huang. Compressive sensing beamforming based on covariance for acoustic imaging with noisy measurements. *J. Acoust. Soc. Am.*, **134**(5):EL445–EL451, 2013.
- [51] S. Foucart and H. Rauhut. *A mathematical introduction to compressive sensing*, pages 1–589. Springer, New York, 2013.
- [52] D. L. Donoho. Compressed sensing. *IEEE Trans. Inf. Theory*, **52**(4):1289–1306, 2006.
- [53] E. J. Candès and M. B. Wakin. An introduction to compressive sampling. *IEEE Signal Proc. Mag.*, **25**(2):21–30, 2008.
- [54] J. Romberg. Imaging via compressive sampling. *IEEE Signal Proc. Mag.*, **25**(2):14–20, 2008.
- [55] S. Levy and P. Fullagar. Reconstruction of a sparse spike train from a portion of its spectrum and application to high-resolution deconvolution. *Geophysics*, **46**(9):1235–1243, 1981.
- [56] F. Santosa and W. Symes. Linear inversion of band-limited reflection seismograms. *SIAM J. Sci. Stat. Comput.*, **7**(4):1307–1330, 1986.

- [57] D. L. Donoho and P. B. Stark. Uncertainty principles and signal recovery. *SIAM J. Appl. Math.*, **49**(3):906–931, 1989.
- [58] R. Tibshirani. Regression shrinkage and selection via the lasso. *J. Roy. Statist. Soc. Ser. B*, **58**(1):267–288, 1996.
- [59] I. F. Gorodnitsky and B. D. Rao. Sparse signal reconstruction from limited data using FOCUSS: A re-weighted minimum norm algorithm. *IEEE Trans. Signal Process.*, **45**(3):600–616, 1997.
- [60] E. J. Candés, J. Romberg, and T. Tao. Robust uncertainty principles: Exact signal reconstruction from highly incomplete frequency information. *IEEE Trans. Inf. Theory*, **52**(2):489–509, 2006.
- [61] M. Lustig, D. Donoho, and J. M. Pauly. Sparse MRI: The application of compressed sensing for rapid MR imaging. *Magn. Reson. Med.*, **58**(6):1182–1195, 2007.
- [62] N. Wagner, Y. C. Eldar, and Z. Friedman. Compressed beamforming in ultrasound imaging. *IEEE Trans. Signal Process.*, **60**(9):4643–4657, 2012.
- [63] E. J. Candés and T. Tao. Decoding by linear programming. *IEEE Trans. Inf. Theory*, **51**(12):4203–4215, 2005.
- [64] M. A. Herman and T. Strohmer. High-resolution radar via compressed sensing. *IEEE Trans. Signal Process.*, **57**(6):2275–2284, 2009.
- [65] H. Yao, P. Gerstoft, P. M. Shearer, and C. Mecklenbräuker. Compressive sensing of the Tohoku-Oki Mw 9.0 earthquake: Frequency-dependent rupture modes. *Geophys. Res. Lett.*, **38**(20):1–5, 2011.
- [66] H. Yao, P. M. Shearer, and P. Gerstoft. Compressive sensing of frequency-dependent seismic radiation from subduction zone megathrust ruptures. *Proc. Natl. Acad. Sci. U.S.A.*, **110**(12):4512–4517, 2013.
- [67] W. Mantzel, J. Romberg, and K. Sabra. Compressive matched-field processing. *J. Acoust. Soc. Am.*, **132**(1):90–102, 2012.
- [68] P. A. Forero and P. A. Baxley. Shallow-water sparsity-cognizant source-location mapping. *J. Acoust. Soc. Am.*, **135**(6):3483–3501, 2014.
- [69] C. Yardim, P. Gerstoft, W. S. Hodgkiss, and Traer J. Compressive geoacoustic inversion using ambient noise. *J. Acoust. Soc. Am.*, **135**(3):1245–1255, 2014.
- [70] D. Malioutov, M. Çetin, and A. S. Willsky. A sparse signal reconstruction perspective for source localization with sensor arrays. *IEEE Trans. Signal Process.*, **53**(8):3010–3022, 2005.
- [71] A. Xenaki, P. Gerstoft, and K. Mosegaard. Compressive beamforming. *J. Acoust. Soc. Am.*, **136**(1):260–271, 2014.
- [72] G. F. Edelmann and C. F. Gaumond. Beamforming using compressive sensing. *J. Acoust. Soc. Am.*, **130**(4):232–237, 2011.

- [73] C. F. Mecklenbräuker, P. Gerstoft, A. Panahi, and M. Viberg. Sequential Bayesian sparse signal reconstruction using array data. *IEEE Trans. Signal Process.*, **61**(24):6344–6354, 2013.
- [74] S. Fortunati, R. Grasso, F. Gini, M. S. Greco, and K. LePage. Single-snapshot DOA estimation by using compressed sensing. *EURASIP J. Adv. Signal Process.*, **120**(1):1–17, 2014.
- [75] R. G. Baraniuk. Compressive sensing. *IEEE Signal Proc. Mag.*, **24**(4):118–121, 2007.
- [76] J. Proakis and D. Manolakis. *Digital Signal Processing, Principles, Algorithms and Applications*, chapter 5. Prentice Hall, New Jersey, third edition, 1996.
- [77] M. F. Duarte, M. A. Davenport, D. Takhar, J. N. Laska, T. Sun, K. E. Kelly, and R. G. Baraniuk. Single-pixel imaging via compressive sampling. *IEEE Signal Proc. Mag.*, **25**(2):83–91, 2008.
- [78] S. Boyd and L. Vandenberghe. *Convex optimization*, pages 1–684. Cambridge university press, New York, 2004.
- [79] M. A. T. Figueiredo, R. D. Nowak, and S. J. Wright. Gradient projection for sparse reconstruction: Application to compressed sensing and other inverse problems. *IEEE J. Sel. Topics Signal Process.*, **1**(4):586–597, 2007.
- [80] S. J. Wright, R. D. Nowak, and M. A. T. Figueiredo. Sparse reconstruction by separable approximation. *IEEE Trans. Signal Process.*, **57**(7):2479–2493, 2009.
- [81] S. F. Cotter, B. D. Rao, K. Engan, and K. Kreutz-Delgado. Sparse solutions to linear inverse problems with multiple measurement vectors. *IEEE Trans. Signal Process.*, **53**(7):2477–2488, 2005.
- [82] M. Grant and S. Boyd. CVX: Matlab software for disciplined convex programming, version 2.0 beta. <http://cvxr.com/cvx>, September 2013.
- [83] D. L. Donoho and M. Elad. Optimally sparse representation in general (nonorthogonal) dictionaries via l_1 minimization. *Proc. Natl. Acad. Sci. U.S.A.*, **100**(5):2197–2202, 2003.
- [84] R. G. Baraniuk, M. Davenport, R. DeVore, and M. Wakin. A simple proof of the restricted isometry property for random matrices. *Constr. Approx.*, **28**(3):253–263, 2008.
- [85] E. J. Candès and T. Tao. Near-optimal signal recovery from random projections: Universal encoding strategies? *IEEE Trans. Inf. Theory*, **52**(12):5406–5425, 2006.
- [86] S. S. Chen, D. L. Donoho, and M. A. Saunders. Atomic decomposition by basis pursuit. *SIAM J. Sci. Comput.*, **20**(1):33–61, 1998.
- [87] E. J. Candès, M. B. Wakin, and S. Boyd. Enhancing sparsity by reweighted l_1 minimization. *J. Fourier Anal. Appl.*, **14**(5):877–905, 2008.

- [88] A. Xenaki, P. Gerstoft, and K. Mosegaard. Sparsity and super-resolution in sound source localization with sensor arrays. In *2nd Underwater Acoustics Conference and Exhibition*, pages 1–6, 2014.
- [89] J. J. Fuchs. Recovery of exact sparse representations in the presence of bounded noise. *IEEE Trans. Inf. Theory*, **51**(10):3601–3608, 2005.
- [90] D. L. Donoho, M. Elad, and V. N. Temlyakov. Stable recovery of sparse overcomplete representations in the presence of noise. *IEEE Trans. Inf. Theory*, **52**(1):6–18, 2006.
- [91] J. A. Tropp. Just relax: Convex programming methods for identifying sparse signals in noise. *IEEE Trans. Inf. Theory*, **52**(3):1030–1051, 2006.
- [92] T. Park and G. Casella. The bayesian lasso. *J. Amer. Statist. Assoc.*, **103**(482):681–686, 2008.
- [93] E. J. Candès and J. Romberg. Sparsity and incoherence in compressive sampling. *Inverse Probl.*, **23**(3):969–985, 2007.
- [94] E. J. Candès. The restricted isometry property and its implications for compressed sensing. *C. R. Math. Acad. Sci.*, **346**(9):589–592, 2008.
- [95] M. Elad. Optimized projections for compressed sensing. *IEEE Trans. Signal Process.*, **55**(12):5695–5702, 2007.
- [96] C. F. Gaumond and G. F. Edelmann. Sparse array design using statistical restricted isometry property. *J. Acoust. Soc. Am.*, **134**(2):191–197, 2013.
- [97] E. J. Candès, Y. C. Eldar, D. Needell, and P. Randall. Compressed sensing with coherent and redundant dictionaries. *Appl. Comput. Harmon. Anal.*, **31**(1):59–73, 2011.
- [98] Y. Chi, L. L. Scharf, A. Pezeshki, and A. R. Calderbank. Sensitivity to basis mismatch in compressed sensing. *IEEE Trans. Signal Process.*, **59**(5):2182–2195, 2011.
- [99] M. F. Duarte and R. G. Baraniuk. Spectral compressive sensing. *Appl. Comput. Harmon. Anal.*, **35**(1):111–129, 2013.
- [100] W. Fan, P. M. Shearer, and P. Gerstoft. Kinematic earthquake rupture inversion in the frequency domain. *Geophys. J. Int.*, **199**(2):1138–1160, 2014.
- [101] E. J. Candès and C. Fernandez-Granda. Towards a mathematical theory of super-resolution. *Comm. Pure Appl. Math.*, **67**(6):906–956, 2014.
- [102] E. J. Candès and C. Fernandez-Granda. Super-resolution from noisy data. *J. Fourier Anal. Appl.*, **19**(6):1229–1254, 2013.
- [103] G. Tang, B. N. Bhaskar, P. Shah, and B. Recht. Compressed sensing off the grid. *IEEE Trans. Inf. Theory*, **59**(11):7465–7490, 2013.

- [104] A. Xenaki and P. Gerstoft. Grid-free compressive beamforming. *J. Acoust. Soc. Am.*, **137**(4):1923–1935, 2015.
- [105] A. Panahi and M. Viberg. Fast LASSO based DOA tracking. In *4th IEEE International Workshop on Computational Advances in Multi-Sensor Adaptive Processing (CAMSAP)*, pages 397–400. IEEE, 2011.
- [106] A. Panahi and M. Viberg. Fast candidate points selection in the lasso path. *IEEE Signal Proc. Let.*, **19**(2):79–82, 2012.
- [107] C. F. Mecklenbräuker, P. Gerstoft, and E. Zöchmann. Beamforming of the residuals is the LASSO’s dual. submitted to *IEEE Trans. Signal Process.*, 2015.
- [108] R. Tibshirani and J. Taylor. The solution path of the generalized lasso. *Ann. Stat.*, **39**(3):1335–1371, 2011.
- [109] H. Zou, T. Hastie, and R. Tibshirani. On the “degrees of freedom” of the lasso. *Ann. Stat.*, **35**(5):2173–2192, 2007.
- [110] P. Gerstoft, A. Xenaki, and C. F. Mecklenbräuker. Single and multiple snapshot compressive beamforming. submitted to *J. Acoust. Soc. Am.*, March 2015.
- [111] S. Oerlemans, P. Sijtsma, and M. López. Location and quantification of noise sources on a wind turbine. *J. Sound Vibration*, **299**(4):869–883, 2007.
- [112] R. Tibshirani, M. Saunders, S. Rosset, J. Zhu, and K. Knight. Sparsity and smoothness via the fused lasso. *J. Roy. Statist. Soc. Ser. B*, **67**(1):91–108, 2005.
- [113] S. Sra, S. Nowozin, and S. J. Wright, editors. *Optimization for machine learning*, chapter 3. MIT Press, Massachusetts, 2012.

Published Journal and Conference Papers

Part I

PAPER **A**

Modeling and detection of oil in sea water

Authors:

Angeliki Xenaki, Peter Gerstoft and Klaus Mosegaard

Published in:

Journal of the Acoustical Society of America, vol. **134**(4), pp. 2790–2798, 2013.

Modeling and detection of oil in sea water

Angeliki Xenaki^{a)}

Department of Applied Mathematics and Computer Science, Technical University of Denmark, Kgs. Lyngby, 2800 Denmark

Peter Gerstoft

Scripps Institution of Oceanography, University of California San Diego, La Jolla, California 92093-0238

Klaus Mosegaard

Department of Applied Mathematics and Computer Science, Technical University of Denmark, Kgs. Lyngby, 2800 Denmark

(Received 15 April 2013; revised 19 July 2013; accepted 6 August 2013)

The challenge of a deep-water oil leak is that a significant quantity of oil remains in the water column and possibly changes properties. There is a need to quantify the oil settled within the water column and determine its physical properties to assist in the oil recovery. There are currently no methods to map acoustically submerged oil in the sea. In this paper, high-frequency acoustic methods are proposed to localize the oil polluted area and characterize the parameters of its spatial covariance, i.e., variance and correlation. A model is implemented to study the underlying mechanisms of backscattering due to spatial heterogeneity of the medium and predict backscattering returns. An algorithm for synthetically generating stationary, Gaussian random fields is introduced which provides great flexibility in implementing the physical model of an inhomogeneous field with spatial covariance. A method for inference of spatial covariance parameters is proposed to describe the scattering field in terms of its second-order statistics from the backscattered returns. The results indicate that high-frequency acoustic methods not only are suitable for large-scale detection of oil contamination in the water column but also allow inference of the spatial covariance parameters resulting in a statistical description of the oil field.

© 2013 Acoustical Society of America. [<http://dx.doi.org/10.1121/1.4818897>]

PACS number(s): 43.60.Fg, 43.60.Cg [ZHM]

Pages: 2790–2798

I. INTRODUCTION

Prior to the oil accident of the Deepwater Horizon, the presence of oil in the sea was confined at shallow-water owing to either natural processes (e.g., biogenic oil) or human-induced pollution (e.g., oil slicks along shipping routes, blow outs from shallow water oil drills). Subsequently, the effort has been focused on monitoring and characterizing oil pollution on the sea surface. Remote sensing methods from satellites and aircrafts are efficient imaging methods of buoyant oil on the sea surface.^{1,2} The challenge of a deep-water oil leak encountered in the case of the Deepwater Horizon is that a significant quantity of oil remained in the water column after the cease of the discharge from the wellhead^{3,4} with serious environmental implications.^{5–7} Much of the oil which was released into the water decomposed into stringy formations of viscous material which remained trapped, mixed with water, far below the sea surface;^{3,4} see Fig. 1. Even though the mean values of the acoustic parameters, the compressibility, and density, of sea water and oil are approximately equal, weak scattering of acoustic waves (volume reverberation) can be observed in both areas due to random fluctuations of the acoustic parameters from their mean value. It is of interest to determine the

physical properties of the new forms of oil and describe the spatial covariance of the submerged oil in order to monitor the degradation process.

Methods based on electromagnetic waves are inefficient for mapping submerged oil in the sea since the electromagnetic waves attenuate fast when traveling in water. Acoustic methods based on Doppler velocimetry which have been used^{8,9} to quantify turbulent flow of hydrocarbons are inefficient to quantify the submerged oil since they require knowledge of the exact position of the oil leak. Tracking of the submerged oil is mainly based on fluorescence and dissolved oxygen measurements and low-frequency acoustic¹ or seismic methods.¹⁰ These methods can detect submerged oil plumes but they do not provide information about the spatial distribution of the stringy oil contaminants in the water. High-frequency acoustic methods are promising since they can both overcome the optical opacity of the water and resolve the small-scale structure of the new forms of oil. Therefore, such methods can be used both to localize submerged oil fields and to characterize them in terms of their second order statistics.

The submerged oil in the water is modeled as a fluid medium with spatial heterogeneity, potentially exhibiting roughness at the interfaces with the water and possibly comprising inclusions of gas bubbles. Since the existence of submerged oil is controlled by the ambient density it is a reasonable assumption that the difference in the acoustic parameters between the two fluid media is small, producing weak scattering of the incident acoustic energy.^{11,12}

^{a)} Author to whom correspondence should be addressed. Current address: Scripps Institution of Oceanography, University of California San Diego, La Jolla, CA 92093-0238. Electronic mail: anxe@dtu.dk

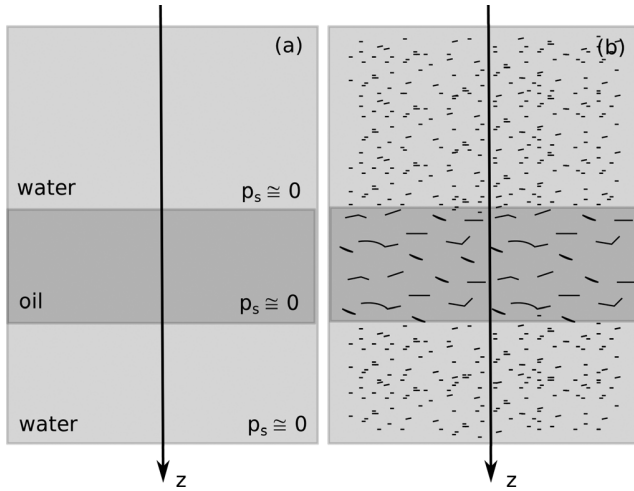


FIG. 1. Schematic for a submerged dispersed oil plume within the water column. (a) The mean values of the acoustic parameters for the two media are approximately equal. (b) Weak scattering can be observed due to random fluctuations of the acoustic parameters from their mean values.

Several authors^{13–17} have used the weak scattering approach to model monostatic backscattering from inhomogeneous sediments in the seafloor. Palmese and Trucco¹³ incorporate the effect of volume reverberation from the seabed to their model of imaging embedded objects with a three-dimensional (3D) monostatic sonar configuration. Li¹⁴ and Li *et al.*¹⁵ model the monostatic backscattering from 3D volume inhomogeneities in shallow water ocean sediments.

Tang¹⁶ and Ivakin¹⁷ developed independently the theoretical framework for a unified approach to describe weak scattering due to interface roughness and volume inhomogeneities, i.e., spatial fluctuations of the compressibility and density, from ocean sediments. The unified approach is based on the assumption that the roughness can be described as a specific kind of spatial fluctuation around an otherwise horizontal interface. Ivakin¹⁷ further assumes that the weak scattering approach is not restricted to small-scale roughness but it extends to arbitrary roughness as long as the difference in the parameters between the adjacent media is not large. The unified approach in modeling scattering from irregular media facilitates the description of cases where the effect of volume and surface scattering is comparable and potentially coherent.

In this paper the weak scattering approach is applied for modeling the backscattered returns from inhomogeneous substances in the water column. A random field generator is introduced to implement a physical model of the inhomogeneous media and high-frequency active sonar is selected to collect the backscattered returns. Relative to methods used in ocean acoustics,^{14,15} the random field generator¹⁸ allows local perturbations of the modeled random field.

It is shown that high-frequency acoustics can be used to detect the submerged field and infer the parameters of its spatial covariance. Traditional methods describe weak scattering fields by comparing the statistical distribution of backscattering strength with known models.^{12,19,20} An alternative method is proposed which allows the description of a stationary scattering field in terms of its second-order statistics without prior knowledge of its spatial covariance.

II. SCATTERING FROM INHOMOGENEITIES

Since the focus of this work is on modeling volume scattering, we undertake the derivation of the scattered pressure due to a region R in the medium with spatial heterogeneity in the acoustic parameters. The derivation follows the analysis by Morse and Ingard.²¹

Assuming time-stationarity, the Helmholtz equation for the scattered acoustic pressure p due to inhomogeneities in the acoustic parameters is given by

$$\nabla^2 p + k^2 p = -k^2 \epsilon_\kappa(\mathbf{r})p - \text{div}(\epsilon_\rho(\mathbf{r})\text{grad } p), \quad (1)$$

where $k = \omega/c$ is the wavenumber, $\omega = 2\pi f$ is the radial frequency, c is the speed of sound, and

$$\epsilon_\kappa = \begin{cases} \frac{\kappa_e - \kappa}{\kappa} & \text{inside } R \\ 0 & \text{outside } R, \end{cases} \quad \epsilon_\rho = \begin{cases} \frac{\rho_e - \rho}{\rho_e} & \text{inside } R \\ 0 & \text{outside } R \end{cases}$$

are the deviations of the model parameters, namely, of the compressibility and density, relative to their unperturbed mean values, κ and ρ , respectively. The fluctuations vary in a statistical manner as a function of space.

Applying the Gauss-Green theorem, the Helmholtz equation takes the form of the integral equation,

$$\begin{aligned} p(\mathbf{r}_0) &= p_i(\mathbf{r}_0) \\ &+ \int_R (k^2 \epsilon_\kappa(\mathbf{r})p(\mathbf{r}) - \nabla(\epsilon_\rho(\mathbf{r})\nabla p(\mathbf{r}))) g(\mathbf{r}_0|\mathbf{r})d\mathbf{r} \\ &= p_i(\mathbf{r}_0) + \int_R (k^2 \epsilon_\kappa p g + \epsilon_\rho \nabla p \nabla g)d\mathbf{r}, \end{aligned} \quad (2)$$

where g is the Green's function and p_i is the incident wave. The Green's function describes the sound pressure at an observation point \mathbf{r}_0 due to a point source located at \mathbf{r} and is given by

$$g(\mathbf{r}_0|\mathbf{r}) = \frac{1}{4\pi|\mathbf{r}_0 - \mathbf{r}|} e^{-ik|\mathbf{r}_0 - \mathbf{r}|}. \quad (3)$$

The time convention $e^{i\omega t}$ is implied and neglected for simplicity. For far field radiation the Green's function takes the form in Eq. (4), where $r = |\mathbf{r}|$,

$$g(\mathbf{r}_0|\mathbf{r}) = \frac{1}{4\pi r} e^{-ik|\mathbf{r}_0 - \mathbf{r}|}. \quad (4)$$

The incident wave insonifies the region R . It emanates from a monopole located at the origin of the coordinate system out of the scattering region R and is given by Eq. (5),

$$p_i(\mathbf{r}) = A \frac{e^{-ikr}}{r}, \quad (5)$$

where A is the pressure amplitude at a distance 1 m from the source, k is the wavenumber of the incident wave, and r denotes the location of the insonified point.

The integral equation, Eq. (2), is exact and valid universally for parameter perturbations of arbitrary size.

Discontinuous perturbation can also be handled with Eq. (2) since it does not involve gradients of the model parameters.¹⁷ Nevertheless, solving Eq. (2) requires exact expressions of the Green's function and the sound pressure inside the scattering region R . The integral equation for the scattered wave can be solved analytically only for a few special cases (e.g., scattering by spheres). Alternatively it can be solved by variational methods or approximations.^{21,22}

In the case of weak scattering, first-order scattering is assumed, thus Born's approximation is applied. Born's approximation implies that the sound pressure inside the scattering region is equal to the incident sound pressure neglecting the effect of higher-order scattering.^{21,22}

The sound pressure observed at a remote position \mathbf{r}_0 due to scattering from inhomogeneities in the acoustic parameters located at \mathbf{r} within a region R is determined by inserting Eqs. (4) and (5) into Eq. (2). In a monostatic configuration and assuming that the Born approximation is valid the scattered sound pressure is given by²¹

$$p_s(\mathbf{r}_0) = \frac{k^2 A}{4\pi} \int_R \left((\epsilon_\kappa(\mathbf{r}) - \epsilon_\rho(\mathbf{r})) \frac{e^{-ik(|\mathbf{r}_0 - \mathbf{r}| + r)}}{r^2} \right) d\mathbf{r}. \quad (6)$$

III. RANDOM FIELD GENERATOR

There are indications that the submerged oil extends throughout the water column as elongated formations of viscous material mixed with water and possibly with biological material.³ Since the spatial distribution of scatterers due to dispersed oil varies in a complex way it is reasonable to model it as a random field of compressibility and density perturbations of the background medium with specified statistical properties.

In the absence of turbulence and for a short measurement interval, the random field is assumed to be spatially stationary and time-invariant. Stationarity can be exploited to develop a numerical method for synthetically generating random fields.

A. Methods for generating random fields

The term random field generator refers to an algorithm which utilizes uncorrelated normally distributed random numbers to generate more complex random fields with specific spatial covariance characteristics.^{18,23,24} In principle, the algorithm generates a stationary random field, ϵ , by adding a convolution of a random Gaussian field, n , with a decomposition of the underlying covariance function, w , to the mean value, m ,

$$\epsilon = m + w * n. \quad (7)$$

Several statistical methods have been proposed for synthetically generating random fields which differ in the implementation of the convolution in Eq. (7). Using the Cholesky decomposition of the covariance matrix,^{25,26} the convolution is calculated by multiplying the lower triangular matrix by a vector of random uncorrelated numbers. The moving average (MA) method^{27,28} offers an alternative implementation

of the covariance decomposition. In this method, the covariance function is expressed as a convolution product of two mirror symmetric functions. The function resulting from the decomposition of the covariance function is further convolved with a set of uncorrelated random numbers on the field grid. The drawback of this method is that it is generally difficult to determine the decomposition function.^{18,27,28}

Spectral methods perform the convolution in the spectral domain using the fast Fourier transform (FFT) algorithm.^{14,15,23,24} The spectral methods are based on the fact that, for a stationary random field, the Fourier transform connects the covariance function, $C(\mathbf{h})$, with its spectral equivalent, the power spectrum, $S(\mathbf{k})$, where \mathbf{h} and \mathbf{k} are vectors denoting the lag and spectral distance, respectively,^{29,30}

$$\begin{aligned} C(\mathbf{h}) &= \langle \epsilon(\mathbf{r}) \epsilon(\mathbf{r} + \mathbf{h}) \rangle \\ S(\mathbf{k}) &= \int_{-\infty}^{\infty} C(\mathbf{h}) e^{-i2\pi \mathbf{k} \mathbf{h}} d\mathbf{h}. \end{aligned} \quad (8)$$

Since a convolution in the spatial domain is equivalent to a product in the spectral domain and the Fourier transform of a real and even function is also a real and even function, the decomposition of the power spectrum is symmetric and can be calculated by its square root. Thus, the spectral methods generate random fields subject to specific covariance characteristics by multiplying the square root of the power spectrum by a set of complex Gaussian numbers, $N \sim \mathcal{CN}(0, 1)$, where $\mathcal{CN}(0, 1)$ denotes the standard complex normal distribution. Spectral methods perform the computations efficiently due to the FFT algorithm. However, equidistant grids are required. Besides, care should be taken on the selection of the random numbers generated in the spectral domain to obtain real-valued fields in the spatial domain.^{14,15,18,23,24}

B. The FFT-MA generator

The numerical method used herein to generate discrete, stationary, random fields for the perturbations is called the fast Fourier transform-moving average (FFT-MA).¹⁸ The FFT-MA method combines the advantages of the spectral methods and of the MA approach. It performs the computations in the spectral domain using the efficient FFT algorithm while preserving the generation of the random numbers in the spatial domain as in the MA framework,

$$\epsilon(\mathbf{r}) = m(\mathbf{r}) + F^{-1} \{ \sqrt{S(\mathbf{k})} F\{n(\mathbf{r})\} \}. \quad (9)$$

Briefly, the steps of the FFT-MA random field generator algorithm involve:

- (1) Calculation of the discrete covariance function $C(\mathbf{h})$ on a spatial grid with spacing at least half of the characteristic length in each direction; see Sec. III C. It is important to perform the discretization symmetrically to obtain a real and even covariance function. Zero-padding at least to the extent of a characteristic length is required to avoid wrap-around effects.
- (2) Generation of Gaussian random numbers from the standard normal distribution on the spatial grid $n(\mathbf{r}) \sim \mathcal{N}(0, 1)$.

- (3) Fourier transform $C(\mathbf{h})$ and $n(\mathbf{r})$ to obtain the power spectrum $S(\mathbf{k})$ and the spectral representation of the random numbers $N(\mathbf{k})$, respectively. Since $C(\mathbf{h})$ is real and even, $S(\mathbf{k})$ is real and even as well.
- (4) Computation of the square root of the power spectral density as in spectral methods $G(\mathbf{k}) = \sqrt{S(\mathbf{k})}$.
- (5) Inverse Fourier transforms the product $G(\mathbf{k})N(\mathbf{k})$ giving the convolution product $g(\mathbf{r}) * n(\mathbf{r})$.
- (6) Generation of the random field $\epsilon(\mathbf{r}) = m(\mathbf{r}) + g(\mathbf{r}) * n(\mathbf{r})$ according to the MA framework.

Compared to spectral methods the generation of the random numbers in the spatial domain allows local perturbations which will practically affect the field values on the grid to the extent of the correlation length. This is not possible in spectral methods where changing a random number in the spectral domain affects the whole spatial domain. Similar to the spectral methods, the FFT-MA algorithm requires regular grids in each direction (i.e., equidistant spacing) in the spatial domain.

C. Covariance models

The implemented FFT-MA algorithm can generate one-dimensional (1D), two-dimensional (2D), or 3D random fields with a Gaussian, Eq. (10), exponential, Eq. (11), or spherical, Eq. (12), covariance,^{31,32}

$$C(h) = \sigma^2 e^{-3h^2/l^2}, \quad (10)$$

$$C(h) = \sigma^2 e^{-3h/l}, \quad (11)$$

$$C(h) = \begin{cases} \sigma^2 \left(1 - \left(\frac{3}{2} \frac{h}{l} - \frac{1}{2} \left(\frac{h}{l} \right)^3 \right) \right) & \text{if } h \leq l \\ 0 & \text{if } h > l, \end{cases} \quad (12)$$

where $h = |\mathbf{h}|$ is the lag distance (isotropic case), $\sigma^2 = C(0)$ is the variance, and l is the characteristic length. The spherical covariance function becomes zero at a distance equal to the characteristic length. The Gaussian and exponential covariance functions reach the zero value asymptotically and have decayed by 95% at a distance equal to the characteristic length.

Figure 2 compares the three covariance models in the isotropic case. For short lag distances near the origin the

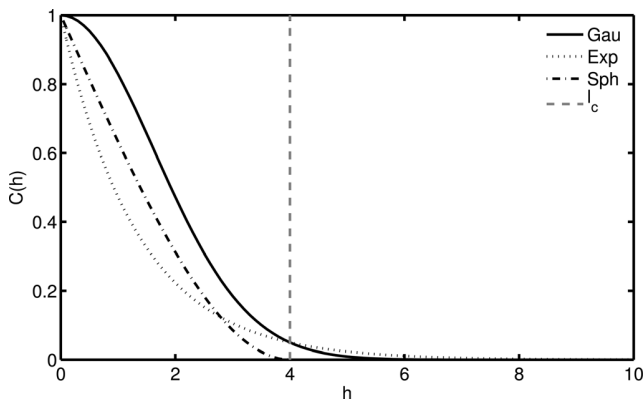


FIG. 2. 1D Gaussian (full line), exponential (dotted line), and spherical (dashed line) covariance functions as a function of the lag distance h . The variance is $\sigma^2 = 1$ and the characteristic length is $l = 4$.

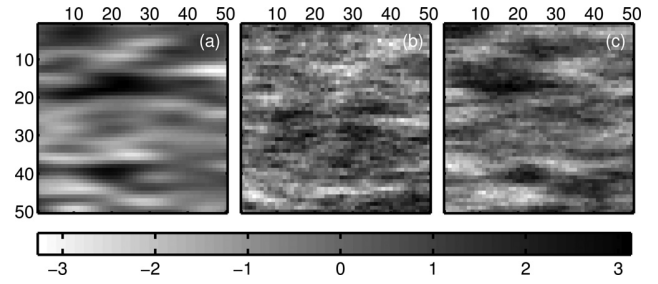


FIG. 3. Realizations of 2D anisotropic random fields with (a) Gaussian, (b) exponential, and (c) spherical covariance on a grid of 50×50 pixels. The mean field is $m = 0$ with variance $\sigma^2 = 1$, major characteristic length $l_{\max} = 20$ pixels in the horizontal direction and anisotropy factor (the ratio of the minor to the major characteristic length) 0.2 for all models.

Gaussian model has a parabolic behavior, suitable for modeling regular phenomena due to the smooth decay, while the exponential and the spherical model decay linearly.³²

In the multidimensional case, the implemented FFT-MA algorithm can generate fields with geometric anisotropy as well.³¹ In this case, the characteristic length is direction-dependent. A linear coordinate transformation involving a rotation and a scaling is used to include anisotropy in the expressions of Eqs. (10)–(12).³²

D. Examples

A variety of covariance models can be used to determine the spatial properties of the generated field. In modeling this gives flexibility in representing different qualities of the field as smoothness or irregularity, isotropy or anisotropy. Figure 3 shows realizations of 2D anisotropic random fields with Gaussian, exponential, and spherical covariance. The field with a Gaussian covariance exhibits smooth characteristics while the field with an exponential covariance is more irregular.

The random numbers and the covariance parameters are dissociated and can be altered either separately or simultaneously. This is possible since the generating field is Gaussian and the resulting field is a linear transformation of the Gaussian field. The separation of the random and covariance parameters gives great flexibility which is useful for inverse methods. Figure 4 shows realizations of 2D anisotropic fields with Gaussian covariance generated by retaining the set of random numbers and altering the characteristic length. As the

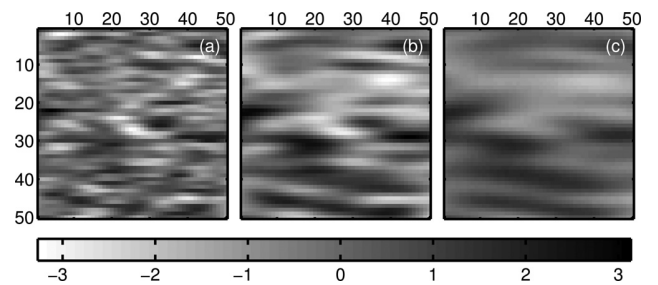


FIG. 4. Perturbation of covariance parameters only. Realizations of 2D anisotropic random fields with Gaussian covariance on a grid of 50×50 pixels. The mean field is $m = 0$ with variance $\sigma^2 = 1$ and anisotropy factor 0.2 in all cases. The major characteristic length is occurring in the horizontal direction and is (a) $l_{\max} = 10$, (b) $l_{\max} = 20$, and (c) $l_{\max} = 30$ pixels.

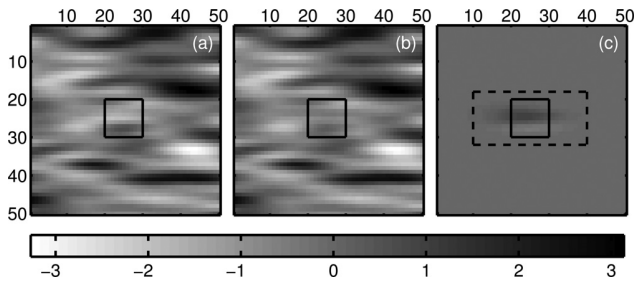


FIG. 5. Local alteration of the random numbers. (a) and (b) realizations of 2D anisotropic random fields with Gaussian covariance, mean $m = 0$, variance $\sigma^2 = 1$, major characteristic length $l_{\max} = 20$ pixels in the horizontal direction and anisotropy factor 0.2. The realization in (b) is generated by the same set of random numbers except from a window of 10×10 pixels (black square) where the random numbers are locally perturbed. (c) The difference between the realizations in (a) and (b). The region of perturbation augmented by the characteristic length in each direction is marked with a dashed rectangle.

characteristic length increases the spatial features are merged to larger formations but they appear at the same location.

The ability not only to alter the set of random numbers separately from the covariance parameters but also to perform local alterations is the main improvement of the FFT-MA algorithm with respect to spectral methods. This is due to the generation of random numbers in the spatial domain. Figure 5 exhibits the effect of a local alteration of the random set.

In conclusion, the FFT-MA algorithm provides an efficient and flexible method for implementing physical models of random fields.

IV. MODELING AND DETECTION OF VOLUME INHOMOGENEITIES

The random field generator and the propagation model are the necessary tools in simulating backscattered returns from weak scatterers. After choosing a receiving configuration, the backscattered returns are post-processed using beamforming to localize the scattering region from the received signals.

Active sensing (i.e., a pulse is used to insonify the area of interest) and a monostatic configuration (i.e., the transmitter and the receiver array are collocated) are considered here. A multibeam sonar is chosen as the transmitting and receiving configuration.

Following the specifications in Ref. 33, the considered transmitter emits a 200 kHz narrowband sinusoidal signal. The pulse is gated with a Hamming window of $120 \mu\text{s}$ length incorporating 24 periods. The duration of the transmitted pulse, T_s , dictates the range resolution, $\Delta r = cT_s/2$. The source level is 200 dB re $1 \mu\text{Pa}$ at 1 m. The transmitter has a directivity pattern characterized by constant response within an angle of 140° in the across-track plane and a much narrower opening angle of 2° in the along-track plane.

The receiver comprises $N_m = 256$ hydrophones arranged in a uniform linear array (ULA) with $d_m = 1.6$ mm spacing. Delay-and-sum beamforming with Hamming weighting is applied³⁴ to impose directivity to the receiving array. The sound speed profile is assumed constant. The half-power beam width defines the angular resolution of the beamformer. The beam width at broadside is $\sin^{-1}[0.886(\lambda/N_md_m)] \approx 1^\circ$ with uniform weighting³⁴ and 1.4° with Hamming weighting. Even

though Hamming weighting degrades the angular resolution of the beamformer, it is chosen since it significantly suppresses the maximum sidelobe level from -13 dB with uniform weighting to -43 dB.

Sound attenuation due to dissipation in sea water is accounted for by introducing an imaginary part to the acoustic wavenumber.¹¹ The absorption coefficient is calculated according to the Francois-Garrison equation.^{35,36} The attenuation is attributed to absorption from pure water and from the chemical relaxation of magnesium sulfate which is the main absorption mechanism at frequencies within the range of 10 to 500 kHz. The absorption coefficient is $\alpha = 50$ dB/km for salinity 35 ppm, temperature 6° , pH 8, depth 50 m, and frequency 200 kHz, corresponding to a sound speed of 1470 m/s. Even though the absorption for the oil contaminants is expected to be larger, the excess of attenuation is neglected since the sound propagates mainly into sea water.

Dynamic focusing is considered to relate the focusing distance with the travel time ($r = ct/2$), resulting in an infinite depth of field.^{37,38} Time-varied gain (TVG) is applied to compensate for spreading loss and absorption making the received signals independent of the scatterer's distance. This corresponds to multiplication of the received signals, p_r , with a range dependent function $f(r) = r^2 e^{2\alpha r}$. In the presence of additive ambient noise, $p_r = p_s + n$, the application of TVG to the received signals is expected to amplify not only the signal, the scattered pressure p_s , but also the noise with increasing range. Nevertheless, ambient noise is neglected since the scattered pressure, Eq. (6), is much higher than additive noise in the received signal due to the high source level and the high-frequency considered.

Since the transmitter of the sonar has a narrow directivity pattern in the along-track plane, only the 2D across-track plane is modeled. The model grid extends horizontally from $x = -100$ to 100 m and vertically from $z = 0.5$ to 100 m with spacing $dx = dz = 0.05$ m in both directions. The beamforming grid spans from $\theta = -70^\circ$ to 70° with spacing $d\theta = 1.4^\circ$ and from $r = 0.5$ to 100 m radially with spacing $dr = 0.1$ m. A range dependent correction, $1/r d\theta dr$, is applied to the reconstructed values on the beamforming grid to compensate for the increasing width of the grid cells with increasing range. The beamformer values are interpolated to the model grid after the reconstruction. The resolution cells become wider as the $|x|$ and z values increase resulting in lower resolution for distant locations. The range resolution is constant and equal to 0.1 m.

For acquiring a 3D image, a planar array is required, increasing the complexity of the processing. In this case sparse arrays is an option.³⁹

A. Volume heterogeneity

A 2D field of volume inhomogeneities is considered representing the water column with a region of contamination characterized by a different covariance structure than the rest of the field.³ The average compressibility and density are constant throughout the field.

It is often assumed that the compressibility fluctuations are proportional to density fluctuations with a position-

independent proportionality factor.¹⁹ Besides, compressibility fluctuations are larger than density fluctuations in fluids.²² Therefore, only compressibility fluctuations are considered in the model of volume reverberation.

The selection of the parameters is somehow arbitrary due to lack of experimental information. For the pure water region an isotropic Gaussian covariance model [Eq. (10)] is selected with variance $\sigma_\kappa^2 = 0.001$ and characteristic length $l = 0.1$ m. The contaminated region is expected to have a higher viscosity and present layering due to oil/water interface tension.⁴⁰ Therefore, an anisotropic spherical covariance model is selected for the contaminated region with variance $\sigma_\kappa^2 = 0.01$, major characteristic length $l_{\max} = 2$ m occurring in the horizontal direction and minor characteristic length $l_{\min} = 0.5$ m occurring in the vertical direction. Figures 6(a) and 6(b) show the insonified area and the beamformer output.

Figures 6(c) and 6(d) show another case where the inhomogeneous fields in the two regions differ only in the characteristic lengths. Namely, the pure water region is described by an isotropic Gaussian covariance model with variance

$\sigma_\kappa^2 = 0.01$ and characteristic length $l = 0.1$ m. The contaminated region is described by an anisotropic Gaussian covariance model with variance $\sigma_\kappa^2 = 0.01$, major characteristic length $l_{\max} = 2$ m occurring in the horizontal direction and minor characteristic length $l_{\min} = 0.5$ m occurring in the vertical direction.

B. Surface roughness

Based on the unified formulation^{16,17} scattering from surface roughness is modeled as a special case of spatial heterogeneity. Equation (6) is used to calculate the scattered pressure attributed to surface roughness. In this case the covariance characteristics of the roughness at the interfaces are described by a 1D Gaussian covariance model with a variance of $\sigma^2 = 0.01$ and a characteristic length of $l = 0.1$ m.

Figure 7 shows the insonified area in the case of two distinct anomalous interfaces and the beamformer output.

C. Small gas bubbles

Exact formulas can be derived for the scattered pressure from spheres owing to their simple geometry. When the wavelength is long relative to the diameter of the sphere, the Born approximation is valid and the expressions can be simplified for simple scattering. The focus here is on light compressible spheres like gas bubbles in water or oil, for which the compressibility is larger, $\kappa_g > \kappa$, and the density is much smaller, $\rho_g \ll \rho$, than the corresponding values of the ambient fluid. Following Ref. 21, the scattered pressure at \mathbf{r}_0 due to a gas sphere at \mathbf{r} with radius a smaller than the wavelength of the insonifying wave is approximated by

$$p_s(\mathbf{r}_0) = A \frac{e^{ikr}}{r} \left(\frac{1}{3} k^2 a^3 \left(\frac{\kappa_g}{\kappa} + 3 \right) \right). \quad (13)$$

Figure 8 shows the beamformed backscattered returns from 10^3 bubbles with radius $a = 0.5$ mm randomly distributed within the observation grid. The ratio of compressibilities is $\kappa_g/\kappa = 10^4$ since the compressibility of water is on

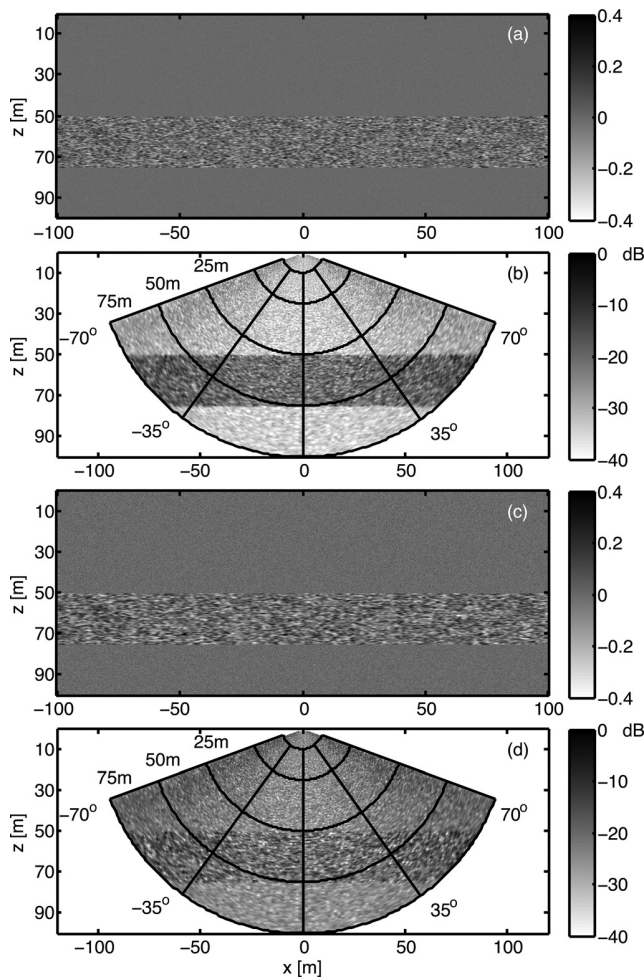


FIG. 6. (a) and (c) 2D fields of compressibility fluctuations in the water column and (b) and (d) the corresponding beamforming reconstructions. The contamination extends over 50 to 75 m depth characterized by a different covariance structure than the rest of the field. (c) and (d) The two fields differ only in the characteristic lengths.

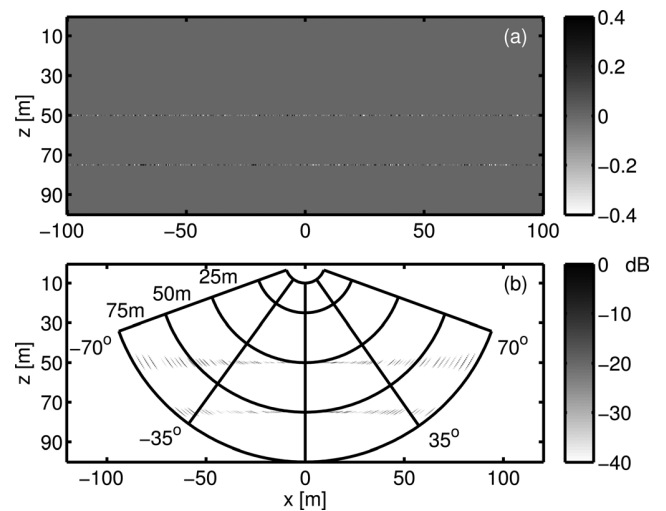


FIG. 7. (a) 2D field with two rough surfaces at 50 and 75 m, respectively, and (b) the beamforming reconstruction.

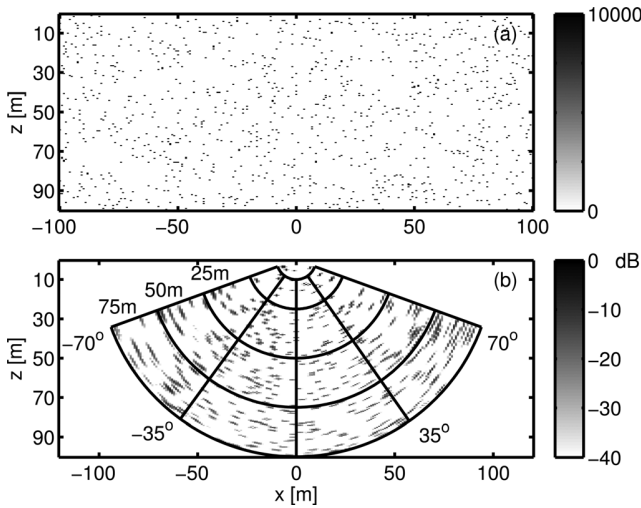


FIG. 8. (a) 2D field with randomly distributed small gas bubbles and (b) the beamforming reconstruction.

the order of $\kappa \simeq 10^{-10} \text{ Pa}^{-1}$ and of air is on the order of $\kappa_g \simeq 10^{-6} \text{ Pa}^{-1}$.

V. INFERENCE OF SPATIAL COVARIANCE PARAMETERS

In an acoustic backscattering model of volume inhomogeneities, a statistical description of the field is more appropriate than a deterministic description due to the complex structure of the inhomogeneities.^{30,41} Besides, a deterministic description of the field has less to offer when the interest is in studying volume reverberation in a medium where there is flow, such as in the water column.

Typically, volume reverberation is described by the statistical distribution of the backscattering strength. The backscattering strength is defined as the ratio of the scattered intensity to the incident intensity per unit volume in dB.^{11,12,30,42,43} This measure is widely used in sonar applications concerned with target detection and identification^{44,45} or with the remote classification of weak scattering mechanisms such as seafloor sedimentation by comparison to known models.^{12,19,20} The backscattering strength is proportional to the cross spectral density thus related to the statistical properties of the field.^{20,44,46} However, for narrowband measurements the backscattering strength provides a single measure and additional information for covariance parameters are required to relate the spatial variation of the scattering field to a covariance model. Herein, an alternative method is proposed to infer the covariance parameters of the scattering field directly from the beamforming reconstruction without using prior knowledge on the spatial covariance.

Using the Fraunhofer approximation, the range in the phase term of the far field expression of the Green's function [Eq. (4)] can be approximated by the first-order terms of a second-order binomial expansion,³⁷

$$|\mathbf{r}_0 - \mathbf{r}| \approx r - \hat{\mathbf{r}} \cdot \mathbf{r}_0, \quad (14)$$

where $r = |\mathbf{r}|$ and $\hat{\mathbf{r}} = \mathbf{r}/r$ is the unit vector in the direction of the scatterer's location.

After application of dynamic focusing and TVG (compensating for the r^2 attenuation term), the signals received at the horizontal sensor locations, $\mathbf{x}_q = [\mathbf{q} - (N_m - 1/2)]d_m$, $\mathbf{q} = [0, 1, \dots, N_m - 1]$, according to Eq. (6) are

$$\begin{aligned} \mathbf{p}_q(r) &\propto \sum_{\theta} \epsilon_{\kappa}(\theta, r) e^{-ik(2r - \mathbf{x}_q \sin(\theta))} \\ &\propto e^{-ik2r} \sum_{\theta} \epsilon_{\kappa}(\theta, r) \mathbf{v}(\theta), \end{aligned} \quad (15)$$

where r is the radial distance of focus and $\mathbf{v}(\theta) = e^{ik\mathbf{x}_q \sin(\theta)}$.

Applying conventional beamforming with Hamming weighting to the received signals, the beam associated with the steering angle θ_f at radial distance r is

$$b_f(\theta_f, r) = (\mathbf{w}_H \odot \mathbf{v}(\theta_f))^{\dagger} \cdot \mathbf{p}_q(r), \quad (16)$$

where \mathbf{w}_H is the vector of the Hamming weights, † denotes conjugate transpose, and \odot denotes element-wise multiplication.

Introducing the beam pattern as a function of the arrival angle θ when the array is steered at θ_f ,³⁴

$$B_H(\theta, \theta_f) = (\mathbf{w}_H \odot \mathbf{v}(\theta_f))^{\dagger} \cdot \mathbf{v}(\theta), \quad (17)$$

the beam $b_f(\theta_f, r)$ is expressed as

$$b_f(\theta_f, r) = e^{-ik2r} \sum_{\theta} \epsilon_{\kappa}(\theta, r) B_H(\theta, \theta_f). \quad (18)$$

Thus the beamformer output normalized by the maximum value in the beamforming reconstruction is connected to the field values as

$$b_{\text{out}}(\theta_f, r) = \frac{\left| \sum_{\theta} \epsilon_{\kappa}(\theta, r) B_H(\theta, \theta_f) \right|^2}{\max_{(\theta_f, r)} \left| \sum_{\theta} \epsilon_{\kappa}(\theta, r) B_H(\theta, \theta_f) \right|^2} \quad (19)$$

or

$$b(\theta_f, r) = \sqrt{b_{\text{out}}} = \frac{\left| \sum_{\theta} \epsilon_{\kappa}(\theta, r) B_H(\theta, \theta_f) \right|}{\max_{(\theta_f, r)} \left| \sum_{\theta} \epsilon_{\kappa}(\theta, r) B_H(\theta, \theta_f) \right|}. \quad (20)$$

According to Eq. (20), the square root of the beamformer output at a point on the beamforming grid contains the contribution of all the field values on the radial distance of focus, $\epsilon_{\kappa}(\theta, r)$, weighted by the beam pattern. However, the more the beam pattern resembles a delta function, the more the square root of the beamformer output, $b(\theta_f, r)$, will be proportional to the corresponding field value, $\epsilon_{\kappa}(\theta_f, r)$. Thus, the parameters of the spatial covariance of a field of volume inhomogeneities can be estimated by the statistics of the square root of the beamforming output.

For a stationary random process, u , the discrete spatial covariance function can be estimated from a finite number of samples, N , as⁴⁷

$$\hat{C}(\eta) = \frac{1}{N} \sum_{i=1}^{N-\eta} (u_{i+\eta} - \bar{u})(u_i - \bar{u}), \quad (21)$$

where $\eta = 0, 1, \dots, N-1$, $\bar{u} = 1/N \sum_{i=1}^N u_i$ is the sample mean and denotes an estimate.

For a 2D field the sample covariance estimate is

$$\hat{C}(h_x, h_z) = \frac{1}{N_x N_z} \sum_{i=1}^{N_x-\xi} \sum_{j=1}^{N_z-\zeta} (b_c(x_i + h_x, z_j + h_z) - \bar{b}_c)(b_c(x_i, z_j) - \bar{b}_c), \quad (22)$$

where N_x, N_z denote the number of sample grid points in the x and z directions, dx, dz are the corresponding grid spacings, $\xi = 0, 1, \dots, N_x-1$, $\zeta = 0, 1, \dots, N_z-1$ and $h_x = \xi dx$, $h_z = \zeta dz$ are the lag distances in the x and z directions, respectively.

In order to obtain the beamformer values on the sample grid in Cartesian coordinates, $b_c(x, z)$, interpolation is used based on the nearest neighbor method.

Covariance sample estimates are calculated for the field in Fig. 6(b). The sampling window has dimensions $N_x dx = 10$ m ($dx = 0.05$ m) in the x direction and $N_z dz = 1$ m ($dz = 0.05$ m) in the z direction. The sampling window is chosen such that it exceeds the correlation lengths in each direction and that it is small enough to examine areas where the resolution cells have approximately the same size, thus fulfill the condition of spatial stationarity. Additional averaging over 20 beamforming reconstructions is used to improve the statistical estimate. Since the covariance is expected to be non-negative, only non-negative values are used.

Figures 9 and 10 show examples of covariance estimation when sampled at the contaminated region characterized by an anisotropic, spherical covariance model and at the sea water region characterized by an isotropic, Gaussian covariance model, respectively. The specific samples are centered to the grid where the beamformer resolution is 1.2 m in the x

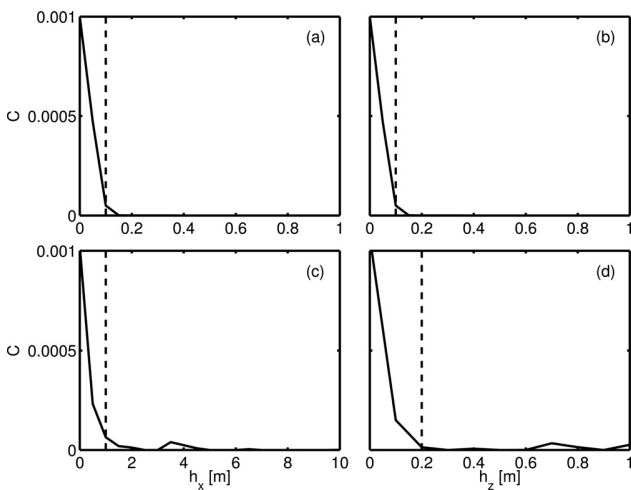


FIG. 9. (a) and (b) True and (c) and (d) reconstructed covariance function for the region characterized by an anisotropic, spherical covariance model with variance $\sigma_k^2 = 0.01$, major characteristic length $l_{\max} = 2$ m in the x direction and minor characteristic length $l_{\min} = 0.5$ m in the z direction. The dashed lines denote the characteristic lengths in each case.

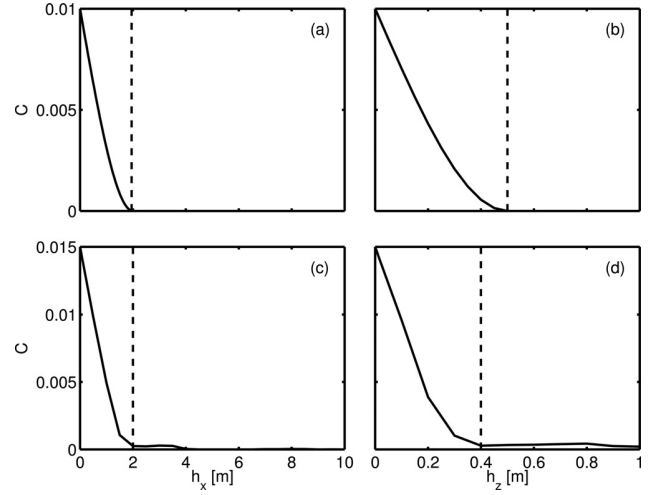


FIG. 10. (a) and (b) True and (c) and (d) reconstructed covariance function for the region characterized by an isotropic, Gaussian covariance model with variance $\sigma_k^2 = 0.001$, and characteristic length $l = 0.1$ m. The dashed lines denote the characteristic lengths in each case.

direction (due to beam width) and 0.1 m in the z direction (due to time-gating). Specifically, the sampling windows extend from -5 to 5 m in the x direction and from 52.5 to 53.5 m and 48.5 to 49.5 m, respectively, in the z direction. The theoretical [Figs. 9(a), 9(b), 10(a), and 10(b)] and estimated [Figs. 9(c), 9(d), 10(c), and 10(d)] covariance functions are compared in the direction both of the major and the minor characteristic length for the two fields. The variance corresponds to the maximum value of the covariance function at zero lag. The characteristic length corresponds to the lag where the covariance function has decayed by at least 95% and is denoted by a dashed line in each case.

For the contaminated region (Fig. 9) the sample covariance provides good estimates of the characteristic lengths in both directions since the characteristic lengths exceed the resolution. Contrary, at the sea-water region (Fig. 10) the characteristic length is smaller than the resolution in the x direction of the beamformer, thus the estimate does not reflect the actual values of the parameter but rather the resolution limits; note the scale difference on the h_x axis.

VI. CONCLUSION

Detection and characterization of submerged oil in the sea water is studied with a model of backscattering from volume inhomogeneities. The physical model for the submerged oil is represented as a random field of compressibility fluctuations which exhibits stationary spatial correlation. A random field generator based on the FFT-MA approach is introduced to implement the physical model. The proposed algorithm provides great flexibility in different modeling scenarios. An active, high-frequency, monostatic sonar is selected to insonify the medium and collect the backscattered returns. The random field is localized with beamforming and inference of spatial covariance is based on the statistics of the beamforming reconstruction.

The simulation results indicate that inference of the spatial covariance parameters is possible with high-frequency

acoustics, providing a quantitative statistical description of the random field. Nevertheless, the reconstructions are subject to resolution limitations of the sonar. The use of high frequencies, resulting in narrow beam widths, improves the resolution and allows the detection of small scale characteristics. On the other hand, the use of high frequencies requires challenging sonar designs with high power demands, since high-frequency sound attenuates fast when propagating in the water, and small interelement spacing.

- ¹R. L. Crout, "Measurements in support of the Deepwater Horizon (MC-252) oil spill response," in *Proceedings of SPIE8030, Ocean Sensing and Monitoring III*, Vol. 8030, International Society for Optics and Photonics, Orlando, FL (2011).
- ²L. Shi, A. Y. Ivanov, M. He, and C. Zhao, "Oil spill mapping in the western part of the East China Sea using synthetic aperture radar imagery," *Int. J. Remote Sens.* **29**, 6315–6329 (2008).
- ³M. Schrope, "Oil spill: Deep wounds," *Nature* **472**, 152–154 (2011).
- ⁴S. A. Socolofsky, E. E. Adams, and C. R. Sherwood, "Formation dynamics of subsurface hydrocarbon intrusions following the Deepwater Horizon blowout," *Geophys. Res. Lett.* **38**, 1–6 (2011).
- ⁵R. Camilli, C. Reddy, D. Yoerger, B. Van Mooy, M. Jakuba, J. Kinsey, C. McIntyre, S. Sylva, and J. Maloney, "Tracking hydrocarbon plume transport and biodegradation at Deepwater Horizon," *Science* **330**, 201–204 (2010).
- ⁶J. Kessler, D. Valentine, M. Redmond, M. Du, E. Chan, S. Mendes, E. Quiroz, C. Villanueva, S. Shusta, L. Werra, S. Yvon-Lewis, and T. Weber, "A persistent oxygen anomaly reveals the fate of spilled methane in the deep Gulf of Mexico," *Science* **331**, 312–315 (2011).
- ⁷A. Diercks, R. Highsmith, V. Asper, D. Joung, Z. Zhou, L. Guo, A. Shiller, S. Joye, A. Teske, N. Guinasso, T. Wade, and S. Lohrenz, "Characterization of subsurface polycyclic aromatic hydrocarbons at the Deepwater Horizon site," *Geophys. Res. Lett.* **37**, 1–6 (2010), doi:10.1029/2010GL045046.
- ⁸R. Camilli, D. Di Iorio, A. Bowen, C. M. Reddy, A. H. Techet, D. R. Yoerger, L. L. Whitcomb, J. S. Seewald, S. P. Sylva, and J. Fenwick, "Acoustic measurement of the Deepwater Horizon Macondo well flow rate," *Proc. Natl. Acad. Sci. U.S.A.* **109**, 20235–20239 (2012).
- ⁹M. K. K. McNutt, R. Camilli, T. J. Crone, G. D. Guthrie, P. A. Hsieh, T. B. Ryerson, O. Savas, and F. Shaffer, "Review of flow rate estimates of the Deepwater Horizon oil spill," *Proc. Natl. Acad. Sci. U.S.A.* **109**, 20260–20267 (2012).
- ¹⁰J. A. Hildebrand, L. Armi, and P. C. Henkart, "Seismic imaging of the water-column deep layer associated with the Deepwater Horizon oil spill," *Geophysics* **77**, 11–16 (2012).
- ¹¹X. Lurton, *An Introduction to Underwater Acoustics: Principles and Applications* (Praxis Publishing, Chichester, UK, 2002).
- ¹²L. R. LeBlanc, S. G. Schock, D. L. DeBruin, M. Jenkins, and L. Munro, "High-resolution sonar volume scattering measurements in marine sediments," *J. Acoust. Soc. Am.* **97**, 2979–2986 (1995).
- ¹³M. Palmese and A. Trucco, "Acoustic imaging of underwater embedded objects: Signal simulation for three-dimensional sonar instrumentation," *IEEE Trans. Instrum. Meas.* **55**, 1339–1347 (2006).
- ¹⁴D. Li, "Modeling of monostatic bottom backscattering from three-dimensional volume inhomogeneities and comparisons with experimental data," Ph.D. dissertation, Massachusetts Institute of Technology, Cambridge, MA, 1997, pp. 17–186.
- ¹⁵D. Li, G. Frisk, and D. Tang, "Modeling of bottom backscattering from three-dimensional volume inhomogeneities and comparisons with experimental data," *J. Acoust. Soc. Am.* **109**, 1384–1397 (2001).
- ¹⁶D. Tang, "A note on scattering by a stack of rough interfaces," *J. Acoust. Soc. Am.* **99**, 1414–1418 (1996).
- ¹⁷A. Ivakin, "A unified approach to volume and roughness scattering," *J. Acoust. Soc. Am.* **103**, 827–837 (1998).
- ¹⁸M. L. Ravalec, B. Noetinger, and L. Y. Hu, "The FFT moving average (FFT-MA) generator: An efficient numerical method for generating and conditioning Gaussian simulations," *Math. Geol.* **32**, 701–723 (2000).
- ¹⁹D. R. Jackson, K. B. Briggs, and M. D. Richardson, "Tests of models for high-frequency seafloor backscatter," *IEEE J. Ocean. Eng.* **21**, 458–470 (1996).
- ²⁰A. N. Gavrilov and I. M. Parnum, "Fluctuations of seafloor backscatter data from multibeam sonar systems," *IEEE J. Ocean. Eng.* **35**, 209–219 (2010).
- ²¹P. M. Morse and K. U. Ingard, *Theoretical Acoustics*, International Series in Pure and Applied Physics (McGraw-Hill, New York, 1968), Chap. 8.
- ²²L. A. Chernov, *Wave Propagation in a Random Medium* (McGraw-Hill, New York, 1960), Chap. 4.
- ²³M. J. L. Robin, A. L. Gutjahr, E. A. Sudicky, and J. L. Wilson, "Cross-correlated random field generation with the direct Fourier transform method," *Water Resour. Res.* **29**, 2385–2397 (1993), doi:10.1029/93WR00386.
- ²⁴F. Ruan and D. McLaughlin, "An efficient multivariate random field generator using the fast Fourier transform," *Adv. Water Resour.* **21**, 385–399 (1998).
- ²⁵F. Alabert, "The practice of fast conditional simulations through the LU decomposition of the covariance matrix," *Math. Geol.* **19**, 369–386 (1987).
- ²⁶M. Davis, "Production of conditional simulations via the LU triangular decomposition of the covariance matrix," *Math. Geol.* **19**, 91–98 (1987).
- ²⁷A. G. Journel, "Geostatistics for conditional simulation of ore bodies," *Econ. Geol.* **69**, 673–687 (1974).
- ²⁸D. S. Oliver, "Moving averages for Gaussian simulation in two and three dimensions," *Math. Geol.* **27**, 939–960 (1995).
- ²⁹J. Bendat and A. Piersol, *Random Data: Analysis and Measurement Procedures* (Wiley, Hoboken, NJ, 2011), Vol. 729, Chap. 5.
- ³⁰D. R. Jackson and M. D. Richardson, *High-Frequency Seafloor Acoustics*, Monograph Series in Underwater Acoustics (Springer, New York, 2007), Chap. 2.
- ³¹T. M. Hansen, K. S. Cordua, M. C. Looms, and K. Mosegaard, "SIPPI: A MATLAB toolbox for sampling the solution to inverse problems with complex prior information: Part 1-Methodology," *Comput. Geosci.* **52**, 470–480 (2013).
- ³²P. Goovaerts, *Geostatistics for Natural Resources Evaluation* (Oxford University Press, New York, 1997), Chap. 4.2.
- ³³G. Wendelboe, H. Dahl, E. Maillard, and L. Bjorno, "Towards a fully calibrated multibeam echo sounder," in *Proceedings of Meetings on Acoustics*, Edinburgh, UK, 2012, Vol. 17, pp. 1836–1843.
- ³⁴H. Van Trees, *Optimum Array Processing (Detection, Estimation, and Modulation Theory, Part IV)* (Wiley-Interscience, New York, 2002), Chaps. 2 and 3.
- ³⁵R. E. Francois and G. R. Garrison, "Sound absorption based on ocean measurements. Part I: Pure water and magnesium sulfate contributions," *J. Acoust. Soc. Am.* **72**, 896–907 (1982).
- ³⁶R. E. Francois and G. R. Garrison, "Sound absorption based on ocean measurements. Part II: Boric acid contribution and equation for total absorption," *J. Acoust. Soc. Am.* **72**, 1879–1890 (1982).
- ³⁷V. Murino and A. Trucco, "Three-dimensional image generation and processing in underwater acoustic vision," *Proc. IEEE* **88**, 1903–1984 (2000).
- ³⁸V. Murino and A. Trucco, "Underwater 3D imaging by FFT dynamic focusing beamforming," in *Proceedings of ICIP-94, IEEE International Conference*, Austin, TX (1994), Vol. 1, pp. 890–894.
- ³⁹A. Trucco, M. Palmese, and S. Repetto, "Devising an affordable sonar system for underwater 3-D vision," *IEEE Trans. Instrum. Meas.* **57**, 2348–2354 (2008).
- ⁴⁰P. De Gennes and C. Taupin, "Microemulsions and the flexibility of oil/water interfaces," *J. Phys. Chem.* **86**, 2294–2304 (1982).
- ⁴¹A. Turgut, "Inversion of bottom/subbottom statistical parameters from acoustic backscatter data," *J. Acoust. Soc. Am.* **102**, 833–852 (1997).
- ⁴²A. N. Ivakin and J.-P. Sessarego, "High frequency broad band scattering from water-saturated granular sediments: Scaling effects," *J. Acoust. Soc. Am.* **122**, EL165–EL171 (2007).
- ⁴³H. Medwin and C. S. Clay, *Fundamentals of Acoustical Oceanography* (Academic Press, Boston, 1998), Chap. 9.
- ⁴⁴A. A. Douglas and A. P. Lyons, "Novel physical interpretations of K-distributed reverberation," *IEEE J. Ocean. Eng.* **27**, 800–813 (2002).
- ⁴⁵A. P. Lyons and A. A. Douglas, "Statistical characterization of high-frequency shallow-water seafloor backscatter," *J. Acoust. Soc. Am.* **106**, 1307–1315 (1999).
- ⁴⁶N. P. Chotiros, "Non-Rayleigh distributions in underwater acoustic reverberation in a patchy environment," *IEEE J. Ocean. Eng.* **35**, 236–241 (2010).
- ⁴⁷G. M. Jenkins and D. G. Watts, *Spectral Analysis and its Applications* (Holden-Day, San Francisco, CA, 1968), Chap. 5, pp. 171–189.

PAPER **B**

Statistical characterization of weak scattering fields with inverse methods

Authors:

Angeliki Xenaki, Peter Gerstoft, Olivier Carriere and Klaus Mosegaard

Published in:

Proceedings of Oceans 2013, San Diego, CA, USA, 2013.

Statistical characterization of weak scattering fields with inverse methods

Angeliki Xenaki^{*†}, Peter Gerstoft[†], Olivier Carriere[†] and Klaus Mosegaard^{*}

^{*}Department of Applied Mathematics and Computer Science, Technical University of Denmark, 2800 Kgs. Lyngby, Denmark

[†]Scripps Institution of Oceanography, University of California San Diego, La Jolla, CA 92093-0238, USA

Abstract—In an acoustic backscattering model of a stationary field of volume inhomogeneities, a stochastic description of the field is more useful than a deterministic description due to the complex nature of the field. A method based on linear inversion is developed to infer information about the statistical properties of the scattering field from the obtained cross-spectral matrix.

I. INTRODUCTION

Determination of the statistical properties of volume reverberation is crucial for dictating the level of false alarm in the design of detection methods [1], [2] and for correlating the acoustic return to the characteristics of known sediments in remote sediment classification [3]–[5]. Hence, substantial effort has been focused on modeling weak scattering [6]–[9]. High-frequency active sonars provide high-resolution measurements and improve volume backscattering models by means of detection of small scale structure as individual scatterers play a more important role in determining scattering parameters [1]–[5].

Herein, the weak scattering approach is applied for studying the backscattering from inhomogeneous substances in the water column and specifically for the characterization of submerged oil from a deep-water oil leak. In such cases, there are indications that a significant quantity of oil remains submerged and extends throughout the water column as elongated formations of viscous material mixed with water and possibly with biological material [10], [11]. Since the existence of submerged oil is controlled by the ambient density, the difference in the acoustic parameters between the two fluid media is small producing weak scattering of the incident acoustic energy [3], [12]. The submerged oil in the water is modeled as a fluid medium exhibiting spatial heterogeneity. A random field generator [13] is used to implement a physical model of the inhomogeneous medium and a high-frequency active sonar is selected to collect the backscattered returns.

Typically, volume reverberation is described by the statistical distribution of the backscattering strength, which is defined as the ratio of the scattered intensity to the incident intensity per unit volume in dB [3], [12], [14]–[16]. The backscattering strength is proportional to the cross spectral density of the scattering field thus related to its statistical properties such as variance and correlation length [1], [5], [17]. However, for narrowband measurements the backscattering strength provides a single measure and additional information for covariance parameters are required to relate the spatial variation of the scattering field to a covariance function.

A method is developed which allows to describe volume scattering models quantitatively in terms of their statistical

properties. Determining the correlation function of the field parameters directly with inverse methods gives a better measure of the volume reverberation statistical characteristics.

The theory of Toeplitz matrices [18] is employed to study the stability of the solution and thus the quality of the reconstruction.

II. FORWARD PROBLEM

A. Scattering from inhomogeneities

The scattered sound pressure p_s observed at a remote position \mathbf{r}_0 due to scattering from spatial fluctuations of the compressibility $\epsilon_\kappa(\mathbf{r})$ and density $\epsilon_\rho(\mathbf{r})$ of the medium within a scattering region R (see Fig. 1) is given by the integral equation [19],

$$p_s(\mathbf{r}_0) = \int_R (k^2 \epsilon_\kappa(\mathbf{r}) p(\mathbf{r}) - \nabla [\epsilon_\rho(\mathbf{r}) \nabla p(\mathbf{r})]) g(\mathbf{r}_0 | \mathbf{r}) d\mathbf{r}, \quad (1)$$

where k is the wavenumber, $p(\mathbf{r})$ is the wave insonifying the scatterer located at \mathbf{r} and $g(\mathbf{r}_0 | \mathbf{r}) = \frac{1}{4\pi|\mathbf{r}_0 - \mathbf{r}|} e^{-ik|\mathbf{r}_0 - \mathbf{r}|}$ is the free-space Green's function which describes the sound pressure at an observation point \mathbf{r}_0 due to a point source at \mathbf{r} . The harmonic time dependence $e^{i\omega t}$ is implied and neglected for simplicity. The compressibility and density fluctuations are normalized to their mean values, $\epsilon_\kappa(\mathbf{r}) = \frac{\delta\kappa(\mathbf{r})}{\langle\kappa\rangle}$, $\epsilon_\rho(\mathbf{r}) = \frac{\delta\rho(\mathbf{r})}{\langle\rho\rangle}$, thus are dimensionless quantities.

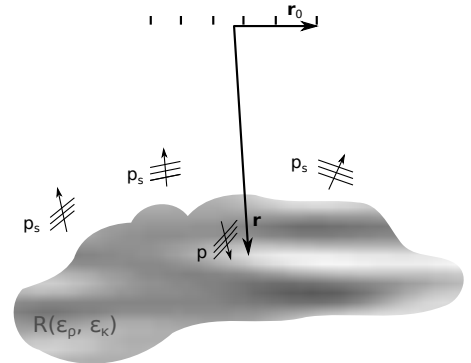


Fig. 1. Schematic for backscattering from an inhomogeneous field R .

For far field radiation, the Fraunhofer approximation for the range term is valid [20],

$$|\mathbf{r}_0 - \mathbf{r}| \approx r - \hat{\mathbf{r}} \cdot \mathbf{r}_0, \quad (2)$$

where $r = |\mathbf{r}|$ and $\hat{\mathbf{r}} = \frac{\mathbf{r}}{r}$ is the unit vector in the direction of \mathbf{r} and the Green's function takes the simpler form,

$$g(\mathbf{r}_0|\mathbf{r}) \approx \frac{1}{4\pi r} e^{-ik(r - \hat{\mathbf{r}} \cdot \mathbf{r}_0)}. \quad (3)$$

The incident wave which insonifies the region R emanates from a monopole located at the origin of the coordinate system out of the scattering region R ,

$$p_i(\mathbf{r}) = A \frac{e^{-ikr}}{r}, \quad (4)$$

where A is the pressure amplitude at a distance 1 m from the source and r denotes the range of the insonified point.

Assuming weak scattering, the Born approximation applies, $p \approx p_i$. Thus, inserting Eqs. (3) and (4) in Eq. (1) the pressure scattered from inhomogeneities in the acoustic parameters of the medium is,

$$p_s(\mathbf{r}_0) \approx \frac{k^2 A}{4\pi} \int_R \left([\epsilon_\kappa(\mathbf{r}) - \epsilon_\rho(\mathbf{r})] \frac{e^{-ik(2r - \hat{\mathbf{r}} \cdot \mathbf{r}_0)}}{r^2} \right) d\mathbf{r}. \quad (5)$$

The density fluctuations are neglected henceforth since they are proportional to the compressibility fluctuations and are less significant in fluid media [15], [21].

Owing to the Born approximation, Eq. (5) relates linearly the backscattered pressure and the fluctuations in the acoustic parameters and can be discretized and rearranged in a matrix-vector formulation.

B. Discretization of the propagation model

An active sonar in a monostatic configuration (the transmitter and receiver array are collocated) is assumed. The transmitter emits a narrowband high-frequency pulse and is supposed to have a narrow directivity pattern in the along-track plane, thus the monochromatic case is considered and only the 2D across-track plane is modeled. The receiver comprises sensors arranged in a uniform linear array centered at the origin of the coordinate system such that the sensors locations are $x_s = (s - \frac{N_s+1}{2})d_s$, $s = 1, 2, \dots, N_s$, where N_s is the number of sensors with interelement spacing d_s . Hence $\hat{\mathbf{r}}_j \cdot \mathbf{r}_0 = x_s \sin(\theta_j)$ in Eq. (2), where θ_j is the angle between the z -axis and the j^{th} scatterer.

For reasons that will become apparent in the following, the model parameters are discretized on a 2D grid equidistantly spaced in $\sin(\theta)$ and r . To simplify the notation, the variable $u = \sin(\theta)$ is introduced such that $\hat{\mathbf{r}}_j \cdot \mathbf{r}_0 = x_s u_j$.

Dynamic focusing is used to relate the focusing distance with the arrival time [20], [22]. The scattered pressure at the sensor located at x_s at the focusing range r_l is,

$$p_s(x_s, r_l) = \frac{k^2 A}{4\pi} \frac{e^{-ik2r_l}}{r_l^2} \frac{dr}{r_l} \sum_j^{N_u} \epsilon_\kappa(u_j, r_l) e^{ikx_s u_j} r_l du. \quad (6)$$

The forward problem can be written in a matrix formulation,

$$\mathbf{d} = \mathbf{G}\mathbf{m} + \mathbf{n}, \quad (7)$$

where \mathbf{d} is the $N \times 1$ vector comprising the acquired data (the scattered returns possibly contaminated with additive noise described by the $N \times 1$ vector \mathbf{n}), \mathbf{G} is the $N \times M$ linear forward matrix and \mathbf{m} is the $M \times 1$ vector of model parameters, namely the compressibility fluctuations.

More analytically, Table I shows the model parameters arranged on the 2D grid, where N_u is the number of arrival directions and N_r is the number of focusing depths. The total number of model parameters is $M = N_r N_u$.

TABLE I. MODEL GRID.

m_1	m_2	\dots	m_{N_u}
m_{N_u+1}	m_{N_u+2}	\dots	m_{2N_u}
\vdots	\vdots	\ddots	\vdots
$m_{(N_r-1)N_u+1}$	$m_{(N_r-1)N_u+2}$	\dots	$m_{N_r N_u}$

The vector \mathbf{m} of the model parameters is formed by stacking the rows of the model grid,

$$\mathbf{m}_{M \times 1} = \begin{bmatrix} \epsilon_\kappa(u_1, r_1) \\ \vdots \\ \epsilon_\kappa(u_{N_u}, r_1) \\ \epsilon_\kappa(u_1, r_2) \\ \vdots \\ \epsilon_\kappa(u_{N_u}, r_2) \\ \vdots \\ \epsilon_\kappa(u_1, r_{N_r}) \\ \vdots \\ \epsilon_\kappa(u_{N_u}, r_{N_r}) \end{bmatrix} = \begin{bmatrix} m_1 \\ \vdots \\ m_{N_u} \\ m_{N_u+1} \\ \vdots \\ m_{2N_u} \\ \vdots \\ m_{(N_r-1)N_u+1} \\ \vdots \\ m_{N_r N_u} \end{bmatrix}. \quad (8)$$

Herein, it is assumed that the model parameters are normally distributed with zero mean value and covariance matrix \mathbf{C}_m such that $\mathbf{m} \sim N(0, \mathbf{C}_m)$. Realizations of the field of model parameters are obtained with a random field generator [13].

The data vector comprises the scattered pressure at each sensor x_s , $s = 1, 2, \dots, N_s$ at each focusing range r_l , $l = 1, 2, \dots, N_r$ (total number of elements $N = N_s N_r$) and additive noise,

$$\mathbf{d}_{N \times 1} = \begin{bmatrix} d_1 \\ d_2 \\ \vdots \\ d_N \end{bmatrix} = \begin{bmatrix} p_s(x_1, r_1) \\ \vdots \\ p_s(x_{N_s}, r_1) \\ p_s(x_1, r_2) \\ \vdots \\ p_s(x_{N_s}, r_2) \\ \vdots \\ p_s(x_1, r_{N_r}) \\ \vdots \\ p_s(x_{N_s}, r_{N_r}) \end{bmatrix} + \begin{bmatrix} n_1 \\ n_2 \\ \vdots \\ n_N \end{bmatrix}. \quad (9)$$

The noise is assumed to be complex Gaussian with zero mean and covariance matrix \mathbf{C}_n such that $\mathbf{n} \sim CN(0, \mathbf{C}_n)$. The noise covariance matrix is diagonal with the diagonal elements equal to the noise variance σ_n^2 . An estimate of the noise variance can be obtained by performing measurements with the sonar in passive mode, prior to the insonification of the field.

Due to dynamic focusing, the forward matrix has a range-dependent structure,

$$\mathbf{G}(r_l)_{N_s \times N_u} \propto \frac{e^{-ik2r_l}}{r_l} \begin{bmatrix} e^{ikx_1 u_1} & \dots & e^{ikx_1 u_{N_u}} \\ e^{ikx_2 u_1} & \dots & e^{ikx_2 u_{N_u}} \\ \vdots & \ddots & \vdots \\ e^{ikx_{N_s} u_1} & \dots & e^{ikx_{N_s} u_{N_u}} \end{bmatrix}. \quad (10)$$

The matrix $\mathbf{G}(r_l)$ contains the propagation phase shifts between all N_s sensors on the ULA positioned at x_s , $s = 1, 2, \dots, N_s$ and all N_u arrival directions u_j , $j = 1, 2, \dots, N_u$ at the focusing distance r_l .

The total $\mathbf{G}_{N \times M}$ matrix, where $N = N_s N_r$, $M = N_u N_r$, is a block matrix which is constructed by the direct sum of $\mathbf{G}(r_l)$ for $l = 1, 2, \dots, N_r$.

$$\mathbf{G}_{N \times M} = \begin{bmatrix} \mathbf{G}(r_1) & \mathbf{0} & \dots & \mathbf{0} \\ \mathbf{0} & \mathbf{G}(r_2) & \dots & \mathbf{0} \\ \vdots & \vdots & \ddots & \vdots \\ \mathbf{0} & \mathbf{0} & \dots & \mathbf{G}(r_{N_r}) \end{bmatrix}. \quad (11)$$

III. INVERSE PROBLEM

Generally, in a medium where there is flow as in the water column, the scattering field will not be static so a deterministic description has less to offer. Considering that $\mathbf{m} \sim N(0, \mathbf{C}_m)$ and $\mathbf{n} \sim CN(0, \mathbf{C}_n)$, the data \mathbf{d} are complex Gaussian $\mathbf{d} \sim CN(0, \mathbf{C}_d)$ with zero mean and covariance matrix \mathbf{C}_d such that,

$$\mathbf{C}_d = \mathbf{G} \mathbf{C}_m \mathbf{G}^H + \mathbf{C}_n, \quad (12)$$

Inversion of Eq. (12) with the least-squares approach yields,

$$\hat{\mathbf{C}}_m = \mathbf{G}^+ [\mathbf{C}_d - \mathbf{C}_n] (\mathbf{G}^+)^H, \quad (13)$$

where $^+$ denotes generalized inverse.

Assuming that the random field of model parameters is stationary, the model covariance matrix, \mathbf{C}_m , has a Toeplitz structure determined by the covariance function. As the model parameters which are more than a characteristic length apart (defined as the lag distance where the covariance function has decayed by 95%) are practically uncorrelated, the dimensions of the problem is significantly reduced [23] when the interest is in solving for the model covariance function and not for the model parameters *per se*. Therefore, herein we are concerned with the overdetermined problem, that is $N > M$.

IV. EIGENVALUE STRUCTURE OF THE FORWARD OPERATOR

The stability of the solution in Eq. (13) is examined through the singular values of the matrix \mathbf{G} . The blocks comprising the matrix \mathbf{G} differ only in a proportionality factor; see Eq. (10). Since the singular values of a block matrix are the combined singular values of its blocks, it is sufficient to examine the singular value structure of $\mathbf{G}(r_l)$. In the overdetermined case, where $N > M$ and thus according to Eq. (11) $N_s > N_u$, the singular values of $\mathbf{G}(r_l)$ are the square roots of the eigenvalues of $\mathbf{G}^H(r_l) \mathbf{G}(r_l)$,

$$\mathbf{G}^H(r_l) \mathbf{G}(r_l)_{N_u \times N_u} \propto \frac{1}{r_l^2} \begin{bmatrix} N_s & \dots & \sum_{s=1}^{N_s} e^{-ikx_s(u_1 - u_{N_u})} \\ \sum_{s=1}^{N_s} e^{-ikx_s(u_2 - u_1)} & \dots & \sum_{s=1}^{N_s} e^{-ikx_s(u_2 - u_{N_u})} \\ \vdots & \vdots & \vdots \\ \sum_{s=1}^{N_s} e^{-ikx_s(u_{N_u} - u_1)} & \dots & N_s \end{bmatrix} \quad (14)$$

The matrix $\mathbf{G}^H(r_l) \mathbf{G}(r_l)$ is Hermitian Toeplitz for equidistant spacing in u , such that $u_i - u_j = d_u(i - j)$, $i, j = 1, 2, \dots, N_u$; see Eq. (14). In this case, it is completely specified by the elements on the first row. The elements on the first row are samples from the periodic sinc function,

$$\begin{aligned}
f(u) &= \sum_{s=1}^{N_s} e^{-ikx_s u} \\
&= \sum_{s=1}^{N_s} e^{-ikd_s \left(s - \frac{N_s+1}{2}\right) u} \\
&= e^{-ikd_s \left(\frac{1-N_s}{2}\right) u} \sum_{s=1}^{N_s} e^{-ikd_s (s-1) u} \\
&= e^{-ikd_s \left(\frac{1-N_s}{2}\right) u} \frac{1 - e^{-ikd_s N_s u}}{1 - e^{-ikd_s u}} \\
&= e^{-i\pi \frac{d_s}{\lambda} (1-N_s) u} \frac{e^{-i\pi N_s \frac{d_s}{\lambda} u} 2i \sin\left(\pi N_s \frac{d_s}{\lambda} u\right)}{e^{-i\pi \frac{d_s}{\lambda} u} 2i \sin\left(\pi \frac{d_s}{\lambda} u\right)} \\
&= \frac{\sin\left(\pi N_s \frac{d_s}{\lambda} u\right)}{\sin\left(\pi \frac{d_s}{\lambda} u\right)} = \frac{\sin\left(\pi W u\right)}{\sin\left(\pi \frac{W}{N_s} u\right)},
\end{aligned} \tag{15}$$

where $W = N_s \frac{d_s}{\lambda}$, such that,

$$\left[\mathbf{G}^H(r_l) \mathbf{G}(r_l) \right]_{ij} \propto \frac{1}{r_l^2} \frac{\sin(\pi W d_u |i-j|)}{\sin(\pi \frac{W}{N_s} d_u |i-j|)} \tag{16}$$

The generating function $f(u)$ can be related to the beam-pattern. As shown in Fig. 2, the zeros of the function occur at $u = q \frac{1}{W}$ for $q \in \{\mathbb{Z} - pN_s\}$ and $p \in \mathbb{Z}$. The function is bounded by the maximum arrival direction of interest $u_{max} \leq 1$. Since the function $f(u)$ is periodic with period $\frac{\lambda}{d_s}$, the condition $\frac{\lambda}{2d_s} > u_{max}$ should be fulfilled to avoid aliasing.

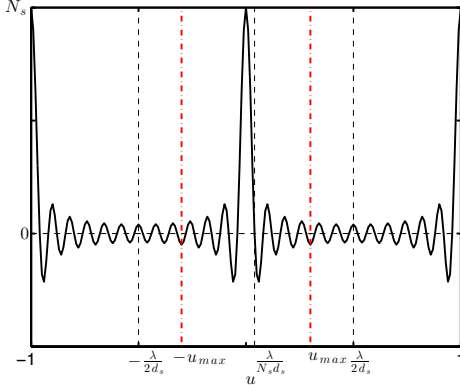


Fig. 2. The sinc periodic function $\frac{\sin(\pi \frac{N_s d_s}{\lambda} u)}{\sin(\pi \frac{d_s}{\lambda} u)}$ as a function of u .

The eigenvalue structure of Toeplitz matrices can be deduced by relating the properties of Toeplitz matrices to those of their simpler special case, the circulant matrices. These two types of matrices are equivalent in an asymptotic sense and this is shown to imply that their eigenvalues among other characteristics behave similarly. The eigenvalues of circulant matrices can be found exactly as the Fourier transform of the elements in the first row [18], [24]. Since u is bounded, $|u| \leq u_{max} \leq 1$, the corresponding Toeplitz matrix is of finite order and is shown in [24] that asymptotically its eigenvalues

are samples of the Fourier spectrum of the series connected with the Toeplitz structure.

Assuming $\frac{\lambda}{2d_s} > u_{max}$ the eigenvalues are determined by the Fourier transform of the sampled truncated sinc function. Figure 3 shows the effect of the grid (sampling) spacing d_u on the eigenvalues of the matrix $\mathbf{G}^H \mathbf{G}$ for fixed frequency and receiving array configuration (fixed W). In case of oversampling when $d_u < \frac{1}{W}$ there will be zero eigenvalues and the matrix $\mathbf{G}^H \mathbf{G}$ will be rank deficient [25]. Otherwise, when $d_u \geq \frac{1}{W}$, the matrix $\mathbf{G}^H \mathbf{G}$ is full rank. The higher the frequency and/or the longer the receiving array, the finer the resolution that can be achieved in terms of d_u . Note that fewer sensors can be used with larger interelement spacing without altering the total length of the array as long as the condition $\frac{\lambda}{2d_s} > u_{max}$ is satisfied.

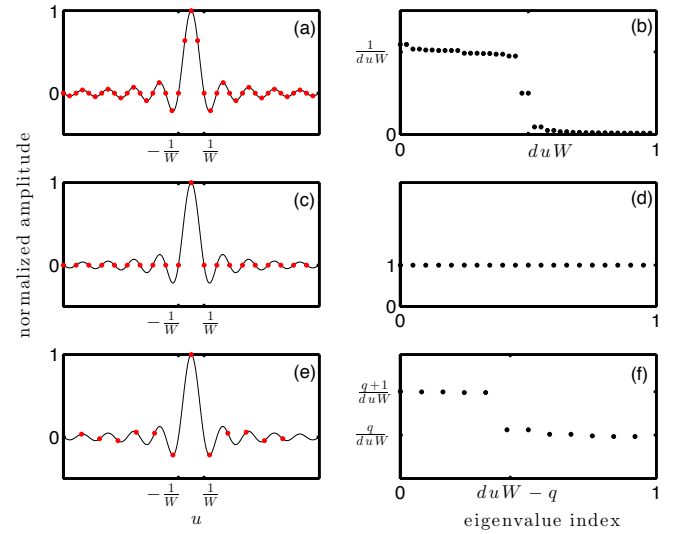


Fig. 3. (a), (c), (e) Sampled truncated sinc function and (b), (d), (f) the corresponding eigenvalue spectrum expressed as a function of the eigenvalue index defined as the ratio $\frac{\# \text{eigenvalue}}{\# \text{total eigenvalues}}$ to provide comparable results. Effect of the sampling distance d_u on the eigenvalues of the matrix $\mathbf{G}^H \mathbf{G}$ for fixed W (frequency and array configuration). (a)-(b) Oversampling $d_u < \frac{1}{W}$, (c)-(d) critical sampling $d_u = \frac{1}{W}$ and (e)-(f) undersampling $d_u > \frac{1}{W}$, $\{q \in \mathbb{N} | q < W d_u < q + 1\}$.

A. Regularization by truncated SVD

In case of oversampling, $d_u < \frac{1}{W}$ (Fig. 3 (a)-(b)), the matrix $\mathbf{G}^H \mathbf{G}$ will have zero eigenvalues and regularization needs to be applied. Due to the specific rectangular distribution of the eigenvalues (Fig. 3 (b)), the truncated SVD (TSVD) method is chosen. The truncation parameter is chosen as the width $d_u W$ of the rectangular distribution.

V. SIMULATION RESULTS

A synthetic example is build to demonstrate the method. An active monostatic sonar is considered with a uniform linear array comprising $N_s = 256$ sensors with interelement spacing $d_s = 1.6$ mm. The field is insonified by a narrowband 200 kHz source. The duration of the pulse is 120 μ s corresponding to a range resolution of 0.1 m ($c = 1500$ m/s) [26].

A 2D field of compressibility fluctuations is considered, representing a region of oil contamination within the water column. The contaminated region is expected to have higher viscosity than the surrounding seawater and present layering due to interface tension [27]. The field is assumed stationary with a zero mean value characterized by an anisotropic Gaussian covariance function with variance $\sigma_\kappa^2 = 0.01$ and characteristic lengths 2 m in x -direction and 0.5 m in z -direction [28]. The variance is the value of the covariance function at zero lag and the characteristic lengths are the lag distances where the covariance function has decayed by 95%.

Naturally, the field of model parameters exhibits stationarity in the Cartesian coordinate system. However, confining the insonified area within an opening angle $[-15^\circ, 15^\circ]$ the curvature is negligible, thus $d_u \approx d_\theta \approx \frac{d_x}{r}$ and $d_r \approx d_z$. The longer the focusing distance, the coarser is the resolution in terms of d_x .

Figure 4 shows a realization of the Gaussian anisotropic field of the model parameters, i.e. the compressibility fluctuations. The considered area is located at the far field of the receiving array and it is confined such that the approximations $d_u \approx d_\theta \approx \frac{d_x}{r}$ and $d_r \approx d_z$ are valid while exceeding the characteristic lengths in both directions. The discretization of the field is chosen so that it complies with the range resolution of the system, $dz = 0.1m$, and that $duW = \frac{dx}{z}W \approx 1$. The latter condition assures that the matrix involved in the inversion is full rank while at the same time giving the finest resolution possible under the full rank condition (see Fig. 3 (c)-(d)).

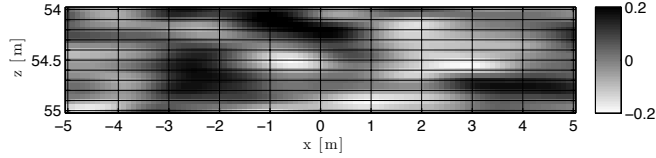


Fig. 4. A realization of the random field of compressibility fluctuations with a Gaussian anisotropic covariance function. The 2D discretization grid is chosen so that $duW = \frac{dx}{z}W \approx 1$ and $dz = 0.1m$ according to the range resolution of the system.

The data covariance matrix is calculated from an ensemble average from 500 pings and additive Gaussian noise is assumed $n \sim \mathcal{CN}(0, 0.01)$. Figure 5 shows the actual model covariance matrix and the result of the least-square inversion (Eq. (13)).

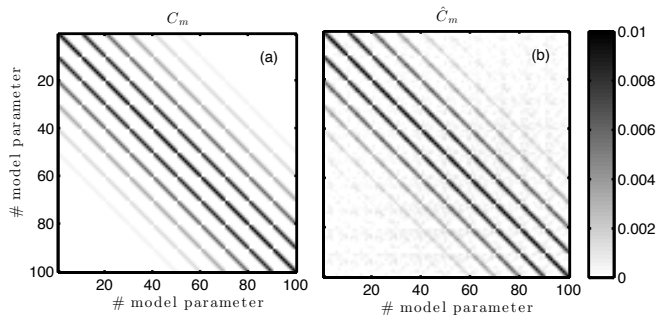


Fig. 5. (a) True and (b) reconstructed model covariance matrix.

Since the field of model parameters is spatially stationary, the model covariance matrix is symmetric block Toeplitz with

the covariance function as the generating function. Thus the covariance function can be deduced from the elements in the first row of the covariance matrix. In order to improve the estimate, the covariance function is calculated by averaging the elements across the blocks in the diagonals and across the diagonals in each block of the covariance matrix.

Figure 6 shows the true and reconstructed covariance function and the characteristic lengths. Due to the ordering of the model parameters on the model vector, the first N_u elements of the covariance function, connected by a red line in Fig. 6 (a), are related to the covariance in u -dimension while the elements $[1 : N_u : M]$, connected by a green line in Fig. 6 (a), are related to the covariance in r -dimension. Since $d_u \approx \frac{d_x}{r}$ and $d_r \approx d_z$, the covariance can be expressed in the x and z -direction as a function of the lag distances $h_x = [0 : N_u - 1]d_u r$ and $h_z = [0 : N_r - 1]d_r$ respectively.

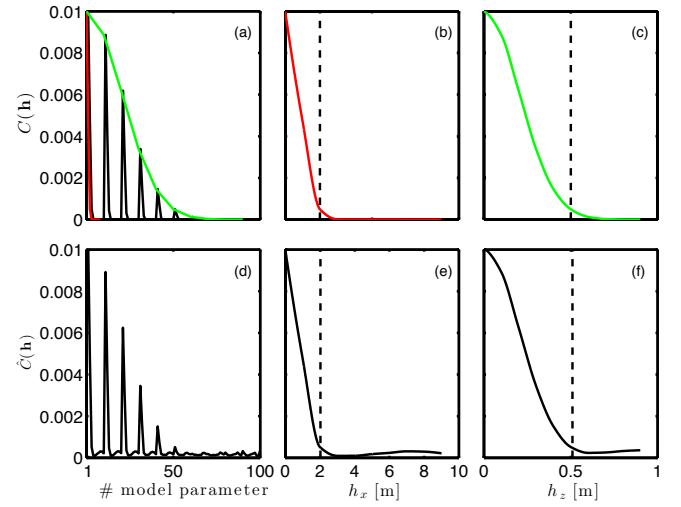


Fig. 6. (a)-(c) True and (d)-(f) reconstructed model covariance function as a function of the lag-distance h_x ((b), (e)) and h_z ((c), (f)) in x and z -direction respectively. The characteristic lengths are denoted by dashed lines in each case.

The results in Figs. 5 and 6 show that the method of least-squares inversion gives robust estimates of the covariance function of the stationary field of model parameters in case that the matrix to be inverted is full rank. Therefore, this method allows the characterization of a stationary field of compressibility fluctuations in terms of its second-order statistics without requiring the determination of the total field.

A. Effect of the number of pings

Figure 7 shows the estimates for the variance, the characteristic length in the x -direction and the characteristic length in z -direction in relation to the number of pings. All the estimates have converged to their true values after averaging over 300 pings.

B. Effect of the regularization by truncated SVD

The synthetic example in Sec. V demonstrates that the inference of the model covariance function is very robust in case that the matrix to be inverted is full rank. Nevertheless, a finer discretization of the model field in an attempt to achieve

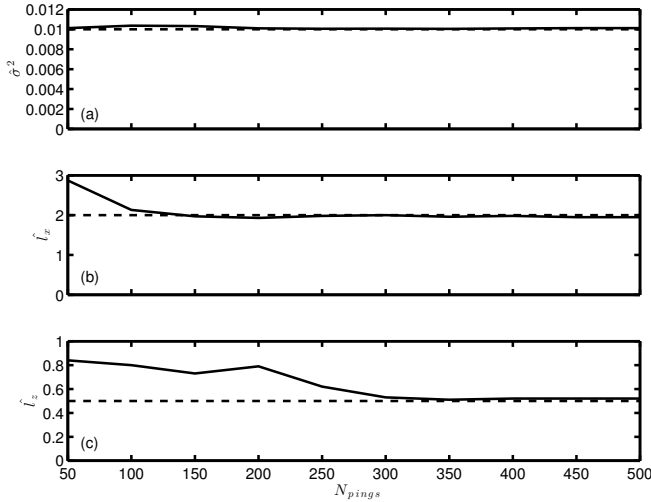


Fig. 7. Estimates of the covariance parameters: (a) variance, (b) characteristic length in x -direction, (c) characteristic length in z -direction as a function of averaging over a number of pings. The dashed lines denote the true value in each case.

finer resolution would result in a rank deficient matrix; see Fig. 3 (a)-(b). Therefore, regularization is required to solve the inverse problem.

Figure 8 shows the estimates for the variance, the characteristic length in the x -direction and the characteristic length in z -direction in relation to the truncation parameter which is the width $d_u W$ of the rectangle distribution in Fig. 3 (b). The smaller is the discretization step d_u , the smaller is also the ratio of the number of contributing eigenvalues to the total number of eigenvalues degrading the estimation of the covariance parameters.

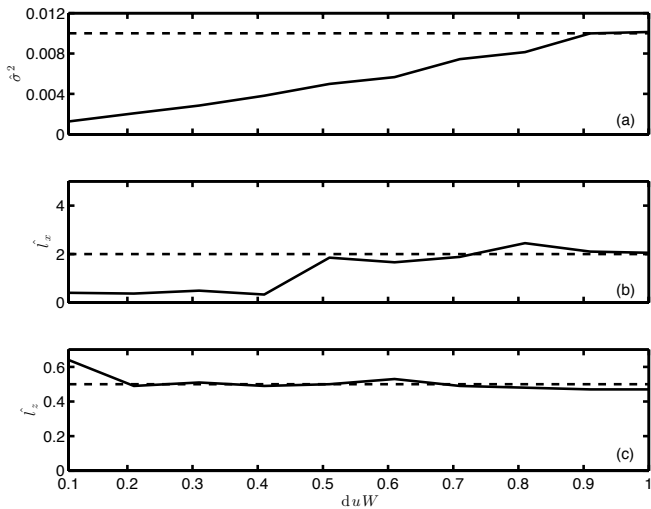


Fig. 8. Estimates of the covariance parameters: (a) variance, (b) characteristic length in x -direction, (c) characteristic length in z -direction with the truncated SVD method. The dashed lines denote the true value in each case.

VI. CONCLUSION

For stationary scattering fields the method of covariance inference allows significant reduction of the dimensions of

the problem. The method provides robust estimates of the covariance parameters, i.e. variance and characteristic lengths, hence characterization of the scattering field in terms of its second-order statistics. The spatial resolution achieved is determined by the characteristics of the sonar configuration, namely the frequency of the insonifying source and the length of the receiving array. An attempt to exceed the resolution limits for a given sonar configuration by regularization of the inverse problem, degrades significantly the accuracy of the estimates of the covariance parameters.

ACKNOWLEDGMENT

This work has been supported by the Danish National Advanced Technology Foundation, Otto Moensteds Fond, Julie von Müllens Fond, Niels Bohr Fond and Oticon Fond.

REFERENCES

- [1] A. A. Douglas and A. P. Lyons, "Novel physical interpretations of K-distributed reverberation," *IEEE J. Oceanic Eng.*, vol. **27**, no. 4, pp. 800–813, 2002.
- [2] A. P. Lyons and A. A. Douglas, "Statistical characterization of high-frequency shallow-water seafloor backscatter," *J. Acoust. Soc. Am.*, vol. **106**, no. 1, pp. 1307–1315, 1999.
- [3] L. R. LeBlanc, S. G. Schock, D. D. L., M. Jenkins, and L. Munro, "High-resolution sonar volume scattering measurements in marine sediments," *J. Acoust. Soc. Am.*, vol. **97**, no. 5, pp. 2979–2986, 1995.
- [4] D. R. Jackson, K. B. Briggs, and M. D. Richardson, "Tests of models for high-frequency seafloor backscatter," *IEEE J. Oceanic Eng.*, vol. **21**, no. 4, pp. 458–470, 1996.
- [5] A. N. Gavrilov and I. M. Parnum, "Fluctuations of seafloor backscatter data from multibeam sonar systems," *IEEE J. Oceanic Eng.*, vol. **35**, no. 2, pp. 209–219, 2010.
- [6] P. Hines, "Theoretical model of acoustic backscatter from a smooth seabed," *J. Acoust. Soc. Am.*, vol. **88**, pp. 324–334, 1990.
- [7] T. Yamamoto, "Acoustic scattering in the ocean from velocity and density fluctuations in the sediments," *J. Acoust. Soc. Am.*, vol. **99**, no. 2, pp. 866–879, 1996.
- [8] K. LePage and H. Schmidt, "Spectral integral representations of monostatic backscattering from three-dimensional distributions of sediment volume inhomogeneities," *J. Acoust. Soc. Am.*, vol. **113**, no. 2, pp. 789–799, 2003.
- [9] A. Turgut, "Inversion of bottom/subbottom statistical parameters from acoustic backscatter data," *J. Acoust. Soc. Am.*, vol. **102**, no. 2, pp. 833–852, 1997.
- [10] M. Schroepe, "Oil spill: Deep wounds," *Nature*, vol. **472**, no. 7342, pp. 152–154, 2011.
- [11] S. A. Socolofsky, E. E. Adams, and C. R. Sherwood, "Formation dynamics of subsurface hydrocarbon intrusions following the Deepwater Horizon blowout," *Geoph. Res. Lett.*, vol. **38**, no. 9, 2011.
- [12] X. Lurton, *An Introduction to Underwater Acoustics: Principles and Applications*. Chichester, UK: Praxis Publishing, 2002, ch. 3.
- [13] M. L. Ravalec, B. Noetinger, and L. Y. Hu, "The FFT moving average (FFT-MA) generator: An efficient numerical method for generating and conditioning Gaussian simulations," *Math. Geol.*, vol. **32**, no. 6, pp. 701–723, 2000.
- [14] A. N. Ivakin and J.-P. Sessarego, "High frequency broad band scattering from water-saturated granular sediments: Scaling effects," *J. Acoust. Soc. Am.*, vol. **122**, no. 5, pp. EL165–EL171, 2007.
- [15] D. R. Jackson and M. D. Richardson, *High-Frequency Seafloor Acoustics*, ser. Monograph series in underwater acoustics. New York: Springer, 2007, ch. 2, 7, 14.
- [16] H. Medwin and C. S. Clay, *Fundamentals of Acoustical Oceanography*. Boston: Academic Press, 1998, ch. 9.
- [17] N. P. Chotiros, "Non-Rayleigh distributions in underwater acoustic reverberation in a patchy environment," *IEEE J. Oceanic Eng.*, vol. **35**, no. 2, pp. 236–241, 2010.

- [18] R. M. Gray, *Toeplitz and Circulant Matrices: A Review*. Found.Trends. Comm. Inf. Theory, 2006, vol. 2, pp. 155–239.
- [19] P. M. Morse and K. U. Ingard, *Theoretical Acoustics*, ser. International Series in Pure and Applied Physics. New York: McGraw-Hill, 1968, ch. 8.
- [20] V. Murino and A. Trucco, “Three-dimensional image generation and processing in underwater acoustic vision,” *Proceedings of the IEEE*, vol. 88, no. 12, pp. 1903–1984, 2000.
- [21] L. A. Chernov, *Wave Propagation in a Random Medium*. New York: McGraw-Hill, 1960, ch. 4.
- [22] V. Murino and A. Trucco, “Underwater 3D imaging by FFT dynamic focusing beamforming,” in *Proceedings ICIP-94, IEEE International Conference*, vol. 1, Austin, TX, 1994, pp. 890–894.
- [23] S. Dosso, P. Nielsen, and M. Wilmut, “Data error covariance in matched-field geoacoustic inversion,” *J. Acoust. Soc. Am.*, vol. 119, no. 1, pp. 208–219, 2006.
- [24] R. M. Gray, “On the asymptotic eigenvalue distribution of Toeplitz matrices,” *IEEE Trans. Inf. Theory*, vol. 18, no. 6, pp. 725–730, 1972.
- [25] R. Menon, P. Gerstoft, and W. S. Hodgkiss, “Asymptotic eigenvalue density of noise covariance matrices,” *IEEE Trans. Signal Process.*, vol. 60, no. 7, pp. 3415–3424, 2012.
- [26] G. Wendelboe, H. Dahl, E. Maillard, and L. Bjorno, “Towards a fully calibrated multibeam echosounder,” in *Proceedings of Meetings on Acoustics*, vol. 17, Edinburgh, UK, 2012, pp. 1836–1843.
- [27] P. De Gennes and C. Taupin, “Microemulsions and the flexibility of oil/water interfaces,” *J. Phys. Chem.*, vol. 86, no. 13, pp. 2294–2304, 1982.
- [28] P. Goovaerts, *Geostatistics for Natural Resources Evaluation*. New York: Oxford University Press, 1997, ch. 4.2.

Part II

PAPER C

Compressive beamforming

Authors:

Angeliki Xenaki, Peter Gerstoft and Klaus Mosegaard

Published in:

Journal of the Acoustical Society of America, vol. **136**(1), pp. 260–271, 2014.

Compressive beamforming

Angeliki Xenaki^{a)} and Peter Gerstoft

Scripps Institution of Oceanography, University of California San Diego, La Jolla, California 92093-0238

Klaus Mosegaard

Department of Applied Mathematics and Computer Science, Technical University of Denmark, Kongens Lyngby, 2800 Denmark

(Received 5 February 2014; revised 10 May 2014; accepted 21 May 2014)

Sound source localization with sensor arrays involves the estimation of the direction-of-arrival (DOA) from a limited number of observations. Compressive sensing (CS) solves such underdetermined problems achieving sparsity, thus improved resolution, and can be solved efficiently with convex optimization. The DOA estimation problem is formulated in the CS framework and it is shown that CS has superior performance compared to traditional DOA estimation methods especially under challenging scenarios such as coherent arrivals and single-snapshot data. An offset and resolution analysis is performed to indicate the limitations of CS. It is shown that the limitations are related to the beampattern, thus can be predicted. The high-resolution capabilities and the robustness of CS are demonstrated on experimental array data from ocean acoustic measurements for source tracking with single-snapshot data. © 2014 Acoustical Society of America.

[<http://dx.doi.org/10.1121/1.4883360>]

PACS number(s): 43.60.Pt, 43.60.Jn, 43.60.Fg [ZHM]

Pages: 260–271

I. INTRODUCTION

The problem of direction-of-arrival (DOA) estimation with sensor arrays, encountered in electromagnetic, acoustic and seismic imaging, is to infer the number and the location of (usually few) sources possibly in the presence of noise from measurements of the wavefield with an array of sensors. Conventional beamforming¹ is the simplest traditional method for DOA estimation, though it is characterized by low resolution. Other methods² developed to overcome the resolution limit of conventional beamforming have degraded performance under noisy conditions, coherent sources and few snapshots.

The compressive sensing (CS) framework asserts that the underlying *sparse* signals can be reconstructed from very few measurements by solving a convex minimization problem. Exploiting the inherent sparsity of the underlying signal, CS outperforms traditional methods which aim to minimize the energy of the reconstructed signal resulting in low-resolution, non-sparse solutions. The convex formulation of CS offers computational efficiency compared to other sparsity promoting methods.

CS (Refs. 3 and 4) has found applications in a wide range of scientific fields from medical^{5,6} and ultrasound imaging,⁷ to error correction in channel coding,⁸ radar detection,⁹ seismic imaging^{10,11} and image reconstruction¹² to name a few. In ocean acoustics, CS is shown to improve the performance of matched field processing,¹³ which is a generalized beamforming method for localizing sources in complex environments, and of coherent passive fathometry in inferring the number and depth of sediment layer interfaces.¹⁴

Indications of the super-resolution (i.e., finer resolution than conventional beamforming) and robustness of CS in DOA estimation are also presented in Refs. 15 and 16. Malioutov *et al.*¹⁵ study the performance of CS in DOA estimation with respect to noise, source number and coherence. Edelmann and Gaumond¹⁶ compare CS with conventional beamforming using towed array data and show that the CS has superior performance, which is more pronounced with undersampling.

We demonstrate the robustness of CS in sound source localization with sensor arrays, especially with coherent arrivals, single-snapshot data and random array geometries. A systematic analysis of offset and resolution is introduced. It is shown that the limitations of the method depend on the array geometry, the frequency, the location of the actual sources and the relative noise level and that they can be predicted from the beampattern.

Moreover, we investigate an iterative reweighed optimization process^{17–19} for more accurate localization combined with a level-correction post-processing step to significantly improve the reconstruction. The superiority of CS in terms of accurate localization, improved resolution and artifact reduction is demonstrated on source tracking from experimental single-snapshot data from ocean acoustic measurements.

In the following, vectors are represented by bold lowercase letters and matrices by bold uppercase letters. The transpose and Hermitian (i.e., conjugate transpose) operators are denoted by T and H , respectively. The l_p -norm of a vector $\mathbf{x} \in \mathbb{C}^n$ is defined as $\|\mathbf{x}\|_p = (\sum_{i=1}^n |x_i|^p)^{1/p}$. By extension, the l_0 -norm is defined as $\|\mathbf{x}\|_0 = \sum_{i=1}^n 1_{x_i \neq 0}$.

II. SPARSE RECONSTRUCTION WITH COMPRESSIVE SENSING

Many engineering problems involve either the reconstruction of a signal of interest or the estimation of its

^{a)} Author to whom correspondence should be addressed. Current address: Department of Applied Mathematics and Computer Science, Technical University of Denmark, Kongens Lyngby, 2800 Denmark. Electronic mail: anxe@dtu.dk

parameters from a (usually small) number of observations. Compressive sensing, also known as compressed sensing²⁰ or compressive sampling,²¹ is a method for solving such underdetermined problems assuring very accurate reconstruction under two conditions:^{3,21,22}

- (1) sparsity of the underlying signal,
- (2) sufficient incoherence of the process which maps the underlying signal to the observations.

A concise description of the method follows.

Let $\mathbf{x} \in \mathbb{C}^N$ be an unknown vector representing the underlying signal we aim to reconstruct. The signal \mathbf{x} is sparse, i.e., it has only K nonzero elements with $K \ll N$. An example of such a sparse signal is the frequency domain representation of a sinusoidal time signal. Let $\mathbf{y} \in \mathbb{C}^M$ be a vector of measurements linearly related to the signal \mathbf{x} , e.g., time samples of the sinusoidal signal. In the absence of noise, the vectors \mathbf{x} and \mathbf{y} are related by a linear set of equations, $\mathbf{y} = \mathbf{A}\mathbf{x}$. The sensing matrix $\mathbf{A} = \mathbf{\Psi}\mathbf{\Phi}$ is the product of the matrix $\mathbf{\Phi}_{N \times N}$, which transforms the signal from one domain to another [e.g., the inverse discrete Fourier transform (IDFT) for a time-frequency representation], and the matrix $\mathbf{\Psi}_{M \times N}$, which represents the measurement process (e.g., time sampling).

The matrix \mathbf{A} is assumed known and fixed (it does not adapt to the information on the signal \mathbf{x}). In the case that $M < N$, the problem is underdetermined and does not have a unique solution. A way of solving this ill-posed problem is constraining the possible solutions with prior information, here by exploiting sparsity.

By definition, sparsity can be imposed on \mathbf{x} by minimizing the l_0 -norm, which counts the number of non-zero entries in the vector, leading to the minimization problem (P_0),

$$\min_{\mathbf{x} \in \mathbb{C}^N} \|\mathbf{x}\|_0 \text{ subject to } \mathbf{y} = \mathbf{A}\mathbf{x}. \quad (P_0)$$

However, the minimization problem (P_0) is a nonconvex combinatorial problem which becomes computationally intractable even for moderate dimensions. The breakthrough of CS came with the proof that for sufficiently sparse signals and sensing matrices with sufficiently incoherent columns^{23,24} the (P_0) problem is equivalent to the (P_1) problem,^{5,20,25}

$$\min_{\mathbf{x} \in \mathbb{C}^N} \|\mathbf{x}\|_1 \text{ subject to } \mathbf{y} = \mathbf{A}\mathbf{x}. \quad (P_1)$$

The l_1 relaxation (P_1) of the (P_0) problem (also known as basis pursuit²⁶) is the closest convex optimization problem to (P_0) and can be solved efficiently even for large dimensions. Moreover, due to the convexity of the l_1 -norm, the method of minimizing (P_1) converges to the global minimum. Other l_p -norm relaxations of the (P_0) problem for $0 < p < 1$, which also favor sparsity, are nonconvex and convergence to global minima is not guaranteed.^{17,27}

For comparison, traditional methods solve the underdetermined problem $\mathbf{y} = \mathbf{A}_{M \times N}\mathbf{x}$, $M < N$ by seeking the solution with the minimum l_2 -norm through the minimization problem (P_2),

$$\min_{\mathbf{x} \in \mathbb{C}^N} \|\mathbf{x}\|_2 \text{ subject to } \mathbf{y} = \mathbf{A}\mathbf{x}. \quad (P_2)$$

The problem (P_2) is convex and has the analytic minimum length solution,

$$\hat{\mathbf{x}} = \mathbf{A}^H(\mathbf{A}\mathbf{A}^H)^{-1}\mathbf{y}. \quad (1)$$

It aims to minimize the energy of the signal through the l_2 -norm, rather than its sparsity, hence its solution is non-sparse. Thus, the problem (P_1) has increased performance over (P_2) for sparse signals (at the cost of computational complexity since it does not have an analytic solution) and it can be solved efficiently with convex optimization.

Figure 1 depicts the geometry of the l_p -norm minimization problem, for $p = 0, 1, 2$ constrained to fit the data. To keep the visualization intuitive, an example is considered where the sparse vector $\mathbf{x} \in \mathbb{R}^2$, with a single nonzero element ($\|\mathbf{x}\|_0 = 1$), is to be recovered by $\mathbf{y} \in \mathbb{R}$ linear measurements. Since there are less measurements than unknowns, all \mathbf{x} residing on the line $\mathbf{y} = \mathbf{A}\mathbf{x}$ satisfy the constraint. A unique solution is found only by providing additional information about \mathbf{x} . For example, we seek the one with the minimum l_p -norm [by solving either (P_0), (P_1), (P_2)].

Geometrically, all vectors with l_p -norm less or equal to a value $r \in \mathbb{R}$ are on an l_p -ball with radius r , $\{\mathbf{x} \mid \|\mathbf{x}\|_p \leq r\}$. In \mathbb{R}^2 , the l_2 -ball is a disk while the l_1 -ball is a rhombus. The solution \mathbf{x} is the intersection of the measurement line and the smallest l_p -ball. The l_2 -norm optimization problem, Fig. 1(c), results almost always in non-sparse solutions due to the curvature of the l_2 -ball. In contrast, the edginess of the l_1 -ball favors sparse solutions, Fig. 1(b), and likely leads to the solution of the l_0 -norm problem, Fig. 1(a).

The theory extends to noisy measurements and compressible signals (approximately sparse)²⁸ making the framework useful for practical applications. Assuming that the measurements are contaminated with additive noise $\mathbf{n} \in \mathbb{C}^M$ such that $\mathbf{y} = \mathbf{A}\mathbf{x} + \mathbf{n}$ the (P_1) problem is reformulated as

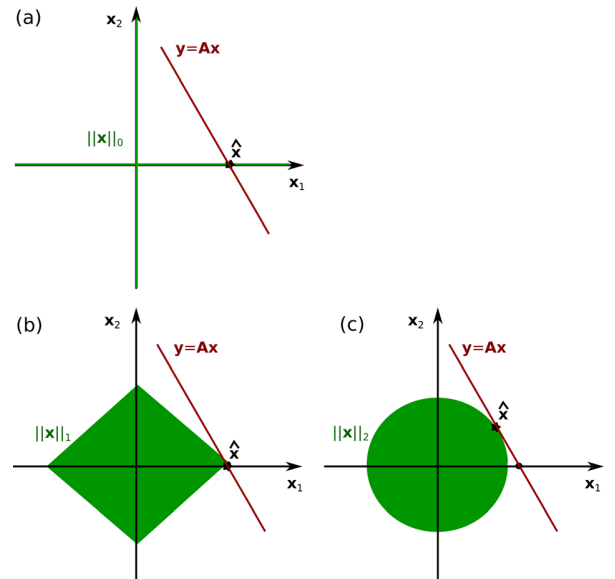


FIG. 1. (Color online) Geometric visualization of (a) the l_0 -norm, (b) the l_1 -norm, and (c) the l_2 -norm problem in \mathbb{R}^2 . The solution $\hat{\mathbf{x}}$ is the intersection of the measurement line $\mathbf{y} = \mathbf{A}\mathbf{x}$ and the minimum norm-ball in each case.

$$\min_{\mathbf{x} \in \mathbb{C}^N} \|\mathbf{x}\|_1 \text{ subject to } \|\mathbf{A}\mathbf{x} - \mathbf{y}\|_2 \leq \epsilon, \quad (P_1^\epsilon)$$

where ϵ is an upper bound for the noise norm, such that $\|\mathbf{n}\|_2 \leq \epsilon$. The solution to (P_1^ϵ) has the minimum l_1 -norm while it fits the data up to the noise level. (P_1^ϵ) can be reformulated in an unconstrained form with the use of Lagrange multipliers,

$$\min_{\mathbf{x} \in \mathbb{C}^N} \|\mathbf{A}\mathbf{x} - \mathbf{y}\|_2^2 + \eta \|\mathbf{x}\|_1. \quad (P_1^\eta)$$

The regularization parameter η controls the relative importance between the sparsity of the solution (l_1 -norm term) and the fit to the measurements (l_2 -norm term).

Herein, we use the cvx toolbox for disciplined convex optimization which is available in the MATLAB environment. It uses interior point solvers to obtain the global solution of a well-defined optimization problem.^{29–31}

III. COMPRESSIVE SENSING FOR DOA ESTIMATION

In this section, we apply the CS for DOA estimation and compare it with widely used localization methods, namely, conventional (delay-and-sum) beamforming (CBF), minimum variance distortionless response (MVDR) beamforming, and the multiple signal classification (MUSIC) method.^{2,32} The focus is on obtaining the accurate locations of the sources rather than their amplitudes since the amplitudes can be adjusted in a further step after the locations are recovered (see Sec. V).

In the following, the sound speed and the geometry of the array are assumed known. We further assume that the sources are in the farfield of the array (i.e., plane waves), the processing is narrowband and the problem is confined in two dimensions (2D) with a linear array of sensors and the sources residing in the plane of the array. These assumptions only serve simplicity. CS, as the other localization methods, is universal and can be extended to three-dimensions (3D) and arrays with arbitrary (but known) geometry, as random arrays.

The location of a source is characterized by the direction of arrival of the associated plane wave $\theta \in [-90^\circ, 90^\circ]$ with respect to the array axis. The propagation delay from the i th potential source to each of the array sensors is described by the steering (or replica) vector,

$$\mathbf{a}(\theta_i) = \frac{1}{\sqrt{M}} e^{j(2\pi/\lambda)\mathbf{r} \sin \theta_i}, \quad (2)$$

where λ is the wavelength and $\mathbf{r} = [r_1, \dots, r_M]^T$ comprises the sensor locations. The normalization $1/\sqrt{M}$, such that $\|\mathbf{a}\|_2 = 1$, is to simplify the analysis.

To infer the unknown number and locations, θ , of the sources, the problem of DOA estimation is formulated as a spatial spectrum estimation problem where the source locations are estimated from the received signal \mathbf{y} .

Let the unknown vector $\mathbf{x} \in \mathbb{C}^N$ comprise the source amplitudes at all directions $\theta \in [-90^\circ, 90^\circ]$ on the grid of interest. Let $\mathbf{y} \in \mathbb{C}^M$ be the vector of wavefield

measurements at the M sensors. Practically, we are interested in a fine resolution on the angular grid, thus $M < N$. The sensing matrix is formed by the steering vectors at all potential source directions as its columns,

$$\mathbf{A}_{M \times N} = [\mathbf{a}(\theta_1), \dots, \mathbf{a}(\theta_N)]. \quad (3)$$

It is the product of a matrix, Ψ , representing the spatial sampling of the wavefield at the sensor locations and an IDFT basis, Φ , connecting the dimensionless spatial domain of the sensor locations *per* wavelength, \mathbf{r}/λ , and the DOA domain in terms of $\sin \theta$.

In the presence of additive noise $\mathbf{n} \in \mathbb{C}^M$, the measurement vector is described by

$$\mathbf{y} = \mathbf{A}\mathbf{x} + \mathbf{n}. \quad (4)$$

In the following, the noise is generated as independent and identically distributed complex Gaussian. The array signal-to-noise ratio (SNR) for a single snapshot is used, defined as $\text{SNR} = 20 \log_{10}(\|\mathbf{A}\mathbf{x}\|_2/\|\mathbf{n}\|_2)$. The choice of the array SNR, which determines the noise l_2 -norm $\|\mathbf{n}\|_2 = \|\mathbf{A}\mathbf{x}\|_2 10^{-\text{SNR}/20}$, serves the analytic study of the (P_1^ϵ) problem.

A. CBF

The CBF (Ref. 1) is the simplest source localization method. The method combines the sensor outputs coherently to enhance the signal at a specific look direction from the ubiquitous noise, yielding the estimate

$$\hat{\mathbf{x}} = \mathbf{A}^H \mathbf{y}. \quad (5)$$

It can be seen as a solution, Eq. (1), to the l_2 -norm minimization problem (P_2) with the simplifying assumption $\mathbf{A}\mathbf{A}^H = \mathbf{I}_M$. The CBF is robust to noise but suffers from low resolution and the presence of sidelobes. The spatial resolution at each look direction, θ_i , $i = 1, \dots, N$, is indicated by the beampattern, $|\mathbf{A}^H \mathbf{a}(\theta_i)|$, i.e., the i th column of $|\mathbf{A}^H \mathbf{A}|$ ($|\cdot|$ is the elementwise absolute value).

The CBF power spectrum is

$$P_{\text{CBF}}(\theta) = \mathbf{a}(\theta)^H \hat{\mathbf{R}}_y \mathbf{a}(\theta), \quad (6)$$

where $\hat{\mathbf{R}}_y = (1/L) \sum_{l=1}^L \mathbf{y}_l \mathbf{y}_l^H$ is the cross-spectral matrix from L snapshots (i.e., observations of \mathbf{y} at a particular frequency). CBF is robust to noise and can be used even with single snapshot data ($L = 1$) but suffers from low resolution and the presence of sidelobes.

B. MVDR beamformer

The MVDR weight vector³³ is obtained by minimizing the output power of the beamformer under the constraint that the signal from the look direction, θ , remains undistorted,

$$\min_{\mathbf{w}} \mathbf{w}^H \hat{\mathbf{R}}_y \mathbf{w} \text{ subject to } \mathbf{w}^H \mathbf{a}(\theta) = 1, \quad (7)$$

resulting in the optimal weight vector

$$\mathbf{w}_{\text{MVDR}}(\theta) = \frac{\hat{\mathbf{R}}_y^{-1} \mathbf{a}(\theta)}{\mathbf{a}(\theta)^H \hat{\mathbf{R}}_y^{-1} \mathbf{a}(\theta)}. \quad (8)$$

The regularized inverse $(\hat{\mathbf{R}}_y + \beta \mathbf{I}_M)^{-1}$ with regularization parameter β is used instead of $\hat{\mathbf{R}}_y^{-1}$, whenever the cross-spectral matrix is rank deficient. The MVDR beamformer power spectrum is

$$P_{\text{MVDR}}(\theta) = \mathbf{w}_{\text{MVDR}}(\theta)^H \hat{\mathbf{R}}_y \mathbf{w}_{\text{MVDR}}(\theta). \quad (9)$$

C. MUSIC

MUSIC (Ref. 34) is based on the eigendecomposition of the cross-spectral matrix and the separation of the signal and the noise subspaces,

$$\hat{\mathbf{R}}_y = \hat{\mathbf{U}}_s \hat{\mathbf{\Lambda}}_s \hat{\mathbf{U}}_s^H + \hat{\mathbf{U}}_n \hat{\mathbf{\Lambda}}_n \hat{\mathbf{U}}_n^H. \quad (10)$$

The signal eigenvectors, $\hat{\mathbf{U}}_s$, corresponding to the largest eigenvalues, $\hat{\mathbf{\Lambda}}_s$, are in the same subspace as the steering vectors, Eq. (2), while the noise eigenvectors, $\hat{\mathbf{U}}_n$, are orthogonal to the subspace of the steering vectors thus $\mathbf{a}(\theta)^H \hat{\mathbf{U}}_n = 0$.

MUSIC uses the orthogonality between the signal and the noise subspaces to locate the maxima in the spectrum,

$$P_{\text{MUSIC}}(\theta) = \frac{1}{\mathbf{a}(\theta)^H \hat{\mathbf{U}}_n \hat{\mathbf{U}}_n^H \mathbf{a}(\theta)}. \quad (11)$$

Both MVDR and MUSIC overcome the resolution limit of the conventional beamformer by exploiting signal information conveyed by the cross-spectral matrix. However, their performance depends on the eigenvalues of the cross-spectral matrix thus it degrades with few snapshots, when the cross-spectral matrix is rank deficient, and in the presence of coherent sources, when the signal subspace is reduced (Chap. 9 in Ref. 32). CS does not have these limitations as it utilizes directly the measured pressure y .

D. Compressive sensing

Usually, there are only few sources $K \ll N$ present and a sparse solution \mathbf{x} can be obtained which honors the data, Eq. (4), using the l_1 -norm for sparsity and the l_2 -norm for noise (P_1^ϵ).

CS for DOA estimation as the solution to the problem (P_1^ϵ) is formulated for a single snapshot. Figure 2(a) compares CBF and CS in the case of a single snapshot. Given a good choice of ϵ , that is $\epsilon = \|\mathbf{n}\|_2$ for the single snapshot case, CS locates the two sources correctly while CBF cannot resolve them as separate due to their proximity. The CS resolution limitations in relation to the SNR and the choice of ϵ are discussed in Secs. IV F and V, respectively.

To compare CS with other methods which involve the cross-spectral matrix, we formulate the method under the multiple snapshots scenario. For L snapshots, the measurement matrix is $\mathbf{Y} = \mathbf{A}\mathbf{X} + \mathbf{N}$, where \mathbf{Y} and \mathbf{N} are $M \times L$ matrices and \mathbf{X} has dimensions $N \times L$.

For moving sources, it befits to solve one optimization problem for each snapshot sequentially, resulting in a sparse

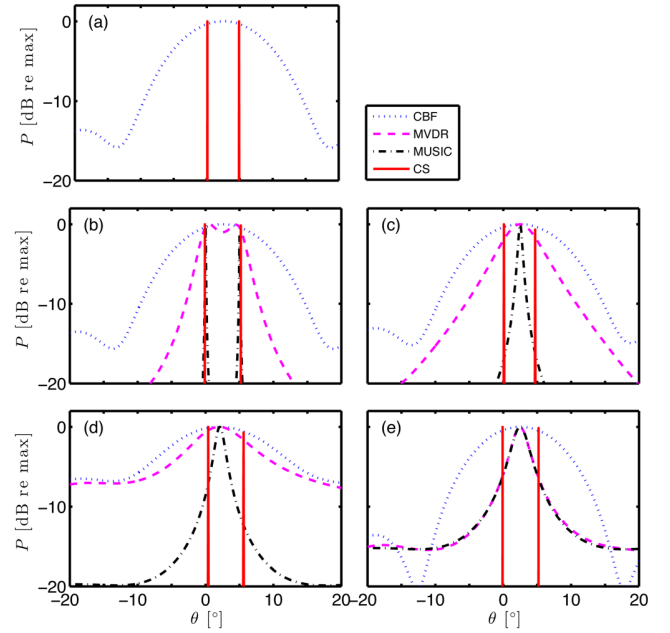


FIG. 2. (Color online) DOA estimation from L snapshots for two equal-strength sources at 0° and 5° with a uniform linear array with $M = 8$ sensors and spacing $d/\lambda = 1/2$. (a) CBF and CS for uncorrelated sources with SNR = 20 dB and one snapshot, $L = 1$. CBF, MVDR, MUSIC, and CS for uncorrelated sources with (b) SNR = 20 dB and $L = 50$, (c) SNR = 20 dB and $L = 4$, (d) SNR = 0 dB and $L = 50$, and (e) for correlated sources with SNR = 20 dB and $L = 50$. The array SNR is for one snapshot.

solution for each snapshot.³⁵ For stationary sources, a way to combine the multiple snapshots is by minimizing the l_1 -norm of the vector \mathbf{x}_2 resulting from calculating the l_2 -norm of the row vectors in \mathbf{X} (see Ref. 15 for details),

$$\min \|\mathbf{x}_2\|_1 \text{ subject to } \|\mathbf{A}\mathbf{X} - \mathbf{Y}\|_2 \leq \epsilon. \quad (12)$$

Figures 2(b)–2(e) compare the CBF, MVDR, MUSIC, and CS methods for DOA estimation. The noise bound, ϵ , is used both as a regularization parameter for the regularized inverse of the cross-spectral matrix in the case of snapshot-starved data, i.e., $L < M$, in MVDR and as a separation limit between the signal and noise subspace eigenvalues in MUSIC.

CBF fails to discern the two closely spaced sources. MVDR and MUSIC provide high resolution under high array SNR and uncorrelated sources but their performance degrades significantly under snapshot-starved data, correlated sources, and noisy conditions. CS resolves the two sources with high resolution in all cases and indicates the applicability of the method in detection of coherent arrivals (such as multipath arrivals) and when a limited number of snapshots is available.

In the following, the CS formulation for a single snapshot is used except at the end of Sec. VI.

IV. LIMITATIONS

CS offers super-resolution due to the sparsity constraint imposed by the minimization of the l_1 -norm of the signal. However, as all DOA estimation methods, it also has limitations. In this section, we analyze the performance of CS in DOA estimation in terms of the discretization of the angular space, the coherence of the sensing matrix and the SNR.

A. Basis mismatch

The fundamental assumption in CS is the sparsity of the underlying signal in the basis of representation, \mathbf{A} . However, a mismatch between the assumed and the actual basis may cause the signal to appear as incompressible. One such example is the mismatch of a DFT basis in FFT beamforming due to inadequate discretization of the DOA domain. When the sources do not coincide with the points on the selected angular grid (particularly in the case of moving sources), the signal might not appear sparse in the selected DFT basis due to spatial spectral leakage. Since the fundamental assumption of sparsity is violated, the CS reconstruction might have poor performance under basis mismatch. An analysis of the sensitivity of CS to basis mismatch is found in Ref. 36.

Herein, we assume that the problem is discretized densely enough to avoid basis mismatch and we study the limitations of CS due to a coherent basis.

B. Coherent or redundant basis

To guarantee good performance of the CS in parameter estimation, the columns of the sensing matrix should be incoherent, i.e., sufficiently uncorrelated.²⁸ In this case, the optimization problems (P_0) and (P_1) are equivalent, resulting in the same unique solution.

Random matrices with Gaussian independent and identically distributed entries are ideal sensing matrices in CS due to their very low coherence.^{8,20} Monajemi *et al.*³⁷ extend the utility of CS to cases which involve some types of deterministic sensing matrices.

Many problems involve sensing matrices with highly coherent columns. A common example is when \mathbf{A} is an over-sampled DFT basis. Sparse recovery with a coherent sensing matrix is important.^{38,39} To achieve low coherence, Elad⁴⁰ proposes an optimized selection of the columns of \mathbf{A} , Gaumond and Edelmann³⁸ examine using a random (or optimized) array in DOA estimation, and Candès *et al.*³⁹ apply the sparsity constraint to the beamformed solution.

In the following, we provide the relevant measures of coherence of the sensing matrix \mathbf{A} in DOA estimation and analyze the performance of CS in relation to this.

C. Coherence measures

An intuitive measure of correlation between any two columns of \mathbf{A} is its mutual coherence defined as^{3,4}

$$\mu(\mathbf{A}) = \max_{i \neq j} \mathbf{G}_{ij}, \quad (13)$$

where \mathbf{G}_{ij} denotes the element in the i th row and j th column of the absolute Gram matrix,

$$\mathbf{G} = |\mathbf{A}^H \mathbf{A}|. \quad (14)$$

The elements of \mathbf{G} are the inner products of the corresponding l_2 -norm normalized columns of \mathbf{A} , Eq. (2), thus are equal to the cosine of the angle between them.

Another measure of correlation of \mathbf{A} is the restricted isometry property (RIP) which is described by the restricted isometry constants.^{23,24} The s th restricted isometry constant δ_s of a matrix $\mathbf{A} \in \mathbb{C}^{M \times N}$ with l_2 -norm normalized columns is the smallest non-negative number such that

$$(1 - \delta_s) \|\mathbf{x}\|_2^2 \leq \|\mathbf{A}\mathbf{x}\|_2^2 \leq (1 + \delta_s) \|\mathbf{x}\|_2^2, \quad (15)$$

for all s -sparse vectors $\mathbf{x} \in \mathbb{C}^N$. The matrix \mathbf{A} satisfies the RIP of order s if $\delta_s \in (0, 1)$. It is more informative to prove the RIP of order $2s$ since $\delta_{2s} < 1$ yields $\|\mathbf{A}(\mathbf{x} - \mathbf{x}')\|_2^2 > 0$ for every s -sparse $\mathbf{x} \neq \mathbf{x}'$, $\mathbf{x}, \mathbf{x}' \in \mathbb{C}^N$ assuring that distinct s -sparse signals correspond to distinct measurement vectors, $\mathbf{y} \neq \mathbf{y}'$.⁴

Let \mathbf{A}_S be a submatrix composed by any set $S \subset N$ of normalized columns of \mathbf{A} with cardinality $\text{card}(S) \leq s$. The condition (15) implies that the Gram matrix $\mathbf{G}_S = \mathbf{A}_S^H \mathbf{A}_S$ has its eigenvalues in the interval $[1 - \delta_s, 1 + \delta_s]$ and if $\delta_s \in (0, 1)$ then \mathbf{G}_S has full rank.²⁴ It follows that $\delta_1 = 0$, $\delta_2 = \mu$, and, since the sequence of restricted isometry constants is non-decreasing,⁴ $\delta_{s>2} \geq \mu$. Therefore, the simple measure of mutual coherence, Eq. (13), usually suffices as an indicator of coherence.

D. Coherence of the sensing matrix in DOA estimation

The sensing matrix $\mathbf{A} = [\mathbf{a}(\theta_1), \dots, \mathbf{a}(\theta_N)]$ is formed by the column steering vectors on an angular grid of $i = 1, \dots, N$ DOAs, $\theta_i \in [-90^\circ, 90^\circ]$; see Eq. (2). Hence, from Eq. (14), the columns or equivalently the rows of \mathbf{G} represent the beampattern for the corresponding focusing direction (see Sec. III A).

The mutual coherence of the sensing matrix \mathbf{A} , i.e., the maximum off-diagonal element in \mathbf{G} [see Eq. (13)], is determined by the frequency, the geometry of the array and the discretization of the angular space. To demonstrate this, we study a uniform linear array (ULA) with $\mathbf{r} = [0 : M - 1]d$ for simplicity. In this case,

$$(\mathbf{A}^H \mathbf{A})_{N \times N} = \frac{1}{M} \begin{bmatrix} M & \dots & \sum_{q=0}^{M-1} e^{j2\pi q(d/\lambda)(\sin \theta_1 - \sin \theta_N)} \\ \sum_{q=0}^{M-1} e^{j2\pi q(d/\lambda)(\sin \theta_2 - \sin \theta_1)} & \dots & \sum_{q=0}^{M-1} e^{j2\pi q(d/\lambda)(\sin \theta_2 - \sin \theta_N)} \\ \vdots & \vdots & \vdots \\ \sum_{q=0}^{M-1} e^{j2\pi q(d/\lambda)(\sin \theta_N - \sin \theta_1)} & \dots & M \end{bmatrix} \quad (16)$$

hence the elements of \mathbf{G} are sampled from the periodic sinc function $f(x)$,

$$f(x) = \frac{1}{M} \left| \sum_{q=0}^{M-1} e^{j2\pi q(d/\lambda)x} \right| = \frac{1}{M} \left| \frac{\sin\left(\pi M \frac{d}{\lambda} x\right)}{\sin\left(\pi \frac{d}{\lambda} x\right)} \right|, \quad (17)$$

such that

$$\mathbf{G}_{ij} = \frac{1}{M} \left| \frac{\sin\left(\pi M \frac{d}{\lambda} (\sin \theta_i - \sin \theta_j)\right)}{\sin\left(\pi \frac{d}{\lambda} (\sin \theta_i - \sin \theta_j)\right)} \right|.$$

Figures 3(a), 3(b) and 3(c), 3(d) show the matrix \mathbf{G} (i.e., the beampattern) as a function of $\sin \theta$ and θ , respectively. When the DOA grid is formed so that $\sin \theta_i = i[\lambda/(Md)]$ or, equivalently, $\theta_i = \sin^{-1}i[\lambda/(Md)]$, where $i = 0, 1, \dots, M-1$ (*), the columns of \mathbf{A} form an orthonormal system, i.e., $\mu(\mathbf{A}) = 0$. In this case, \mathbf{A} is square and Fig. 3(e) shows the corresponding $\mathbf{G} = \mathbf{I}_{M=N}$.

To achieve super-resolution, a finer grid is required resulting in a nonorthonormal sensing matrix \mathbf{A} . Since the row and the column rank of a matrix are equal, a sensing matrix in an underdetermined problem has linearly

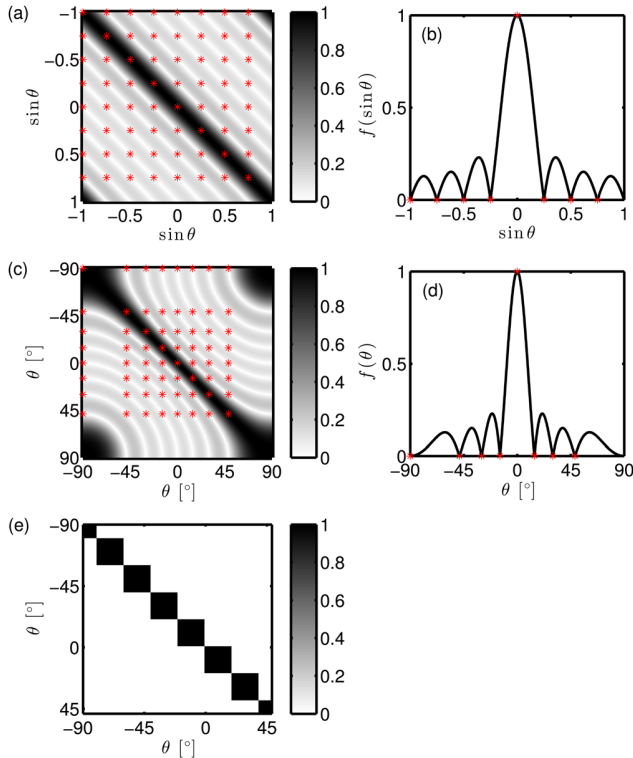


FIG. 3. (Color online) Gram matrix \mathbf{G} in (a) $\sin \theta$ and (c) θ space for a ULA with $M = 8$ sensors and $d/\lambda = 1/2$. Corresponding beampattern at broadside in (b) $\sin \theta$ and (d) θ space. Discretization of the DOA grid (*) such that $\sin \theta_i = i[\lambda/(Md)]$, $i = 0, \dots, M-1$ (a), (b) or, equivalently, $\theta_i = \sin^{-1}i[\lambda/(Md)]$, $i = 0, \dots, M-1$ (c), (d) leads to (e) an orthonormal Gram matrix ($\mu = 0$).

dependent columns. The degree of the linear dependency of the columns of \mathbf{A} is reflected in the coherence.

Figure 4 depicts the Gram matrix for an oversampled DFT (fine angular grid) for three array configurations with the same number of sensors. Grating lobes appear within the visible area when the array spacing is $d/\lambda > 1/2$, Figs. 4(b) and 4(e). A simple way to decrease the coherence of the representation while keeping the number of sensors small is to employ random arrays which lack periodicity, Figs. 4(c) and 4(f).

E. Offset and coherence

In the case of a coherent sensing matrix, uniqueness of the CS solution is not guaranteed (Sec. IV C) thus the DOA of the CS solution, $\hat{\theta}$, may be offset from the actual DOA, θ , resulting in erroneous localization, $\hat{\theta} - \theta \neq 0$. In the absence of spatial aliasing, the coherence of \mathbf{A} is mostly limited to the proximity of the actual directions and it is dependent on the grid spacing relative to the aperture in terms of wavelength. Thus, the maximum CS offset, $\max|\hat{\theta} - \theta|$, is related to the beampattern and the SNR and can be predicted.

Reformulating the constraint in the optimization problem (P_1^c) by denoting the true solution as \mathbf{x}_s ,

$$\begin{aligned} \|\mathbf{A}\mathbf{x} - \mathbf{y}\|_2 &= \|\mathbf{A}\mathbf{x} - (\mathbf{A}\mathbf{x}_s + \mathbf{n})\|_2 \\ &= \|\mathbf{A}(\mathbf{x} - \mathbf{x}_s) - \mathbf{n}\|_2 \leq \epsilon, \end{aligned} \quad (18)$$

and applying the reverse triangle inequality, $\| \|\mathbf{u}\|_2 - \|\mathbf{v}\|_2 \| \leq \|\mathbf{u} - \mathbf{v}\|_2$, where \mathbf{u}, \mathbf{v} are generic vectors, yields

$$\begin{aligned} \|\mathbf{A}(\mathbf{x} - \mathbf{x}_s)\|_2 - \|\mathbf{n}\|_2 &\leq \|\mathbf{A}(\mathbf{x} - \mathbf{x}_s) - \mathbf{n}\|_2 \leq \epsilon, \\ -\epsilon &\leq \|\mathbf{A}(\mathbf{x} - \mathbf{x}_s)\|_2 - \|\mathbf{n}\|_2 \leq \epsilon, \\ 0 &\leq \|\mathbf{A}(\mathbf{x} - \mathbf{x}_s)\|_2 \leq 2\epsilon. \end{aligned} \quad (19)$$

Thus, all vectors \mathbf{x} for which the error norm satisfies $0 \leq \|\mathbf{A}(\mathbf{x} - \mathbf{x}_s)\|_2 \leq 2\epsilon$ are possible solutions to the (P_1^c) problem.

To demonstrate the relation of the CS offset to the mutual coherence of the sensing matrix (i.e., the δ_2 isometry constant; see Sec. IV C) and the SNR we assume that \mathbf{x}_s and \mathbf{x} each have a single nonzero element, x_s at θ_j and x at θ_i , respectively, such that $\|\mathbf{x}_s\|_0 = 1$, $\|\mathbf{x}\|_0 = 1$ which yields,

$$\|\mathbf{A}(\mathbf{x} - \mathbf{x}_s)\|_2 = \|x\mathbf{a}_i - x_s\mathbf{a}_j\|_2^2 \leq 2\epsilon, \quad (20)$$

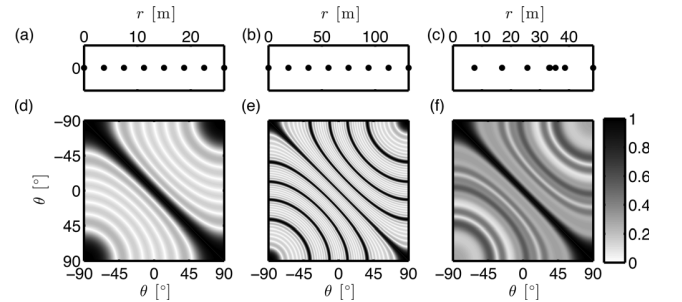


FIG. 4. Array configurations with $M = 8$ sensors at $\lambda = 7.5$ m for a ULA with (a) $d/\lambda = 1/2$, (b) $d/\lambda = 5/2$, (c) a random array. (d)–(f) The corresponding Gram matrices.

where the notation for the steering vectors is simplified such that $\mathbf{a}(\theta_i) = \mathbf{a}_i$.

The optimal value of x which minimizes the error norm $q(x) = \|\mathbf{x}\mathbf{a}_i - x_s\mathbf{a}_j\|_2^2 = x^H x - x^H x_s \mathbf{a}_i^H \mathbf{a}_j - x_s^H x \mathbf{a}_j^H \mathbf{a}_i + x_s^H x_s$ for every θ_i, θ_j is the solution to $\partial q(x)/\partial x = 0$,

$$x = x_s \mathbf{a}_i^H \mathbf{a}_j. \quad (21)$$

Inserting the value for x from Eq. (21) into Eq. (20),

$$\|(\mathbf{a}_i^H \mathbf{a}_j) \mathbf{a}_i - \mathbf{a}_j\|_2 \leq 2\rho, \quad (22)$$

where $\rho = \|\mathbf{n}\|_2 / \|\mathbf{A}\mathbf{x}_s\|_2 = \epsilon/|x_s| = 10^{-\text{SNR}/20}$ is the relative noise level dictated by the SNR. Therefore, the CS DOA, θ_i , may be offset from the true, θ_j , within a region where,

$$\mathbf{G}_{ij} \geq \begin{cases} \sqrt{1 - 4\rho^2}, & \rho < \frac{1}{2}, \\ 0, & \rho \geq \frac{1}{2}. \end{cases} \quad (23)$$

In other words, the SNR sets a coherence limit, $\sqrt{1 - 4\rho^2}$, for the steering vectors, \mathbf{a} , below which accurate DOA reconstruction with CS is not guaranteed. For SNR lower than 6 dB ($\rho \geq \frac{1}{2}$), Eq. (23) yields $\mathbf{G}_{ij} \geq 0$, hence CS may erroneously localize the source at any angle.

Figure 5 depicts the reconstructed DOA and the estimate offset for one source for DOA 0° – 90° . Figure 5(c) shows a detail from Fig. 5(b) towards endfire superimposed to the values of the error norm at the optimal x up to 2ρ , Eq. (22). Even though the CS error is determined by the specific noise realization, the offset region can be identified where $\mathbf{G}_{ij} \geq \sqrt{1 - 4\rho^2}$ and is more pronounced towards endfire where the steering vectors are more correlated.

F. Resolution and coherence

The resolution limit of a DOA estimation method is determined by the minimum required angular separation of

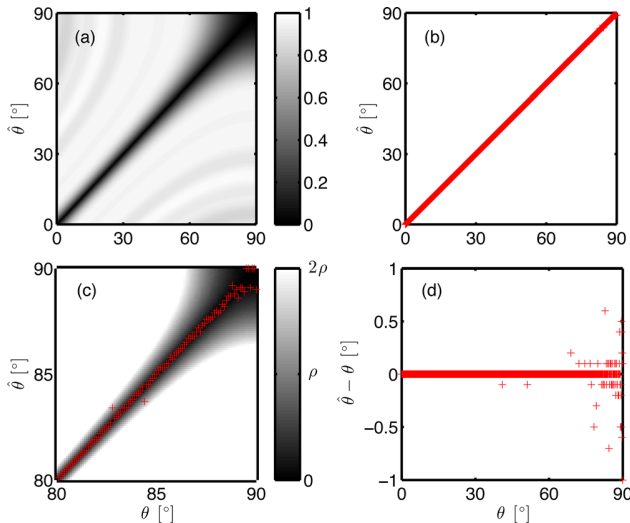


FIG. 5. (Color online) (a) Error norm $\|(\mathbf{a}_i^H \mathbf{a}_j) \mathbf{a}_i - \mathbf{a}_j\|_2$, Eq. (22), for the random array in Fig. 4(c), angular grid spacing 0.1° and SNR = 40 dB ($\rho = 0.01$). (b) Reconstructed DOA. (c) Detail (80° – 90°) from showing the reconstructed DOA in (b) and the error norm in (a) for values up to 2ρ . (d) Offset of the CS solution for one source in relation to the actual DOA.

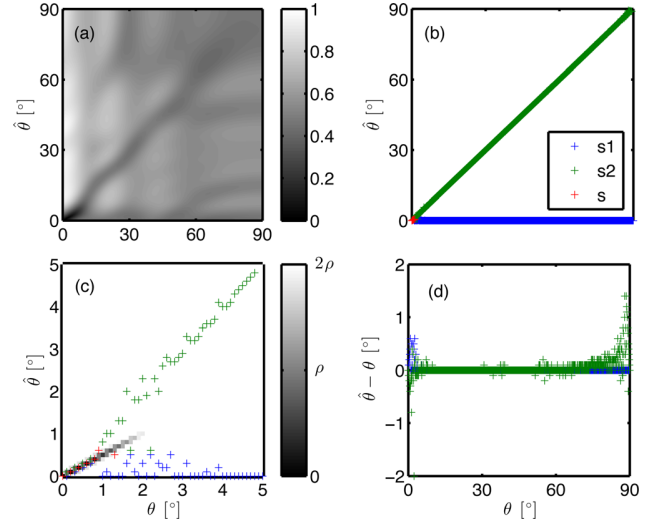


FIG. 6. (Color online) (a) Error norm $\|\mathbf{a}_k^H (\mathbf{a}_i + \mathbf{a}_j) \mathbf{a}_k - \mathbf{a}_i - \mathbf{a}_j\|_2$, Eq. (26), for the random array in Fig. 4(c), angular grid spacing 0.1° and SNR = 40 dB ($\rho = 0.01$). (b) Reconstructed DOAs. (c) Detail (0° – 5°) from showing the reconstructed DOAs in (b) and the error norm in (a) for values up to 2ρ . (d) Estimate offset for a source at 0° and a source at 0° – 90° .

two sources to be resolved as separate. In this section, the CS resolution limit is discussed in relation to the coherence of the sensing matrix and the SNR.

Let the true solution, \mathbf{x}_s , comprise two sources at θ_i and θ_j . The two sources may not be resolved as separate by CS whenever a solution, \mathbf{x} , with only one source at θ_k is possible, i.e., when the error norm $0 \leq \|\mathbf{A}(\mathbf{x} - \mathbf{x}_s)\|_2 \leq 2\epsilon$ while $\|\mathbf{x}_s\|_1 = \|\mathbf{x}\|_1$.

To analyze this we let the two sources in the vector \mathbf{x}_s have equal strength, $x_s/2$, the one with DOA at $\theta_i = 0^\circ$ (Fig. 6) or $\theta_i = 90^\circ$ (Fig. 7) and the other at θ_j moving from 0° to 90° , while the vector \mathbf{x} comprises one source at θ_k with strength x , moving from 0° to 90° . Following Eq. (20),

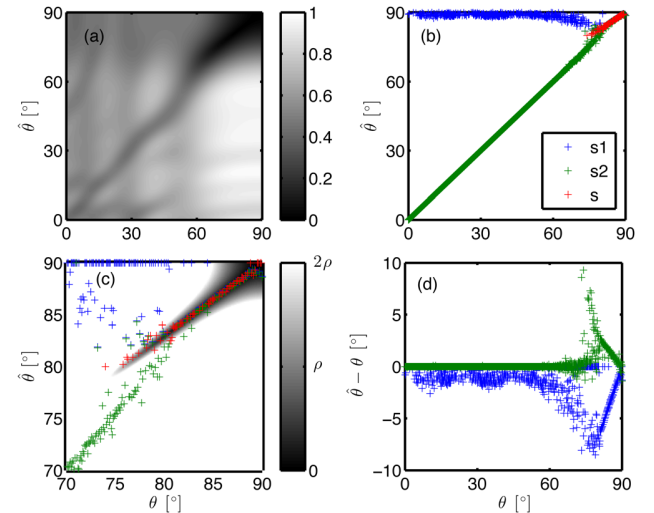


FIG. 7. (Color online) (a) Error norm $\|\mathbf{a}_k^H (\mathbf{a}_i + \mathbf{a}_j) \mathbf{a}_k - \mathbf{a}_i - \mathbf{a}_j\|_2$, Eq. (26), for the random array in Fig. 4(c), angular grid spacing 0.1° and SNR = 40 dB ($\rho = 0.01$). (b) Reconstructed DOAs. (c) Detail (70° – 90°) from showing the reconstructed DOAs in (b) and the error norm in (a) for values up to 2ρ . (d) Estimate offset for a source at 90° and a source at 0° – 90° .

$$\|\mathbf{A}(\mathbf{x} - \mathbf{x}_s)\|_2^2 = \left\| x\mathbf{a}_k - \frac{x_s}{2}\mathbf{a}_i - \frac{x_s}{2}\mathbf{a}_j \right\|_2^2 \leq 2\epsilon. \quad (24)$$

Similar to Eq. (21), the optimal value of the x is

$$x = x_s \frac{\mathbf{a}_k^H (\mathbf{a}_i + \mathbf{a}_j)}{2}, \quad (25)$$

and Eq. (24) yields

$$\frac{1}{2} \|\mathbf{a}_k^H (\mathbf{a}_i + \mathbf{a}_j) \mathbf{a}_k - \mathbf{a}_i - \mathbf{a}_j\|_2 \leq 2\rho. \quad (26)$$

In contrast to Eq. (23), there is no simple expansion of Eq. (26) in terms of \mathbf{G} .

The resolution analysis is depicted in Figs. 6 and 7 at broadside and endfire, respectively, for the random array in Fig. 4(c). The two sources are possibly resolved as one when the angular separation of the sources is less than 2° at broadside and up to 15° at endfire.

Figure 8 shows the angular resolution limit of CS for two sources near broadside, Figs. 8(a) and 8(b), and near endfire, Figs. 8(c) and 8(d) as a function of SNR and compares it with the half-power (-3 dB) beamwidth.

V. SPARSITY AND ESTIMATED NOISE LEVEL

A basic assumption in CS is sparsity of the signal in the representation basis. In the presence of noise, the solution to (P_1) is non-sparse but still a sparse solution can be found instead by solving (P_1^ϵ) or (P_1^η) equivalently. However, when the data noise level $\|\mathbf{n}\|_2$ is unknown, the solution to both (P_1^ϵ) and (P_1^η) depends on the estimated noise level. By underestimating the noise, i.e., ϵ in (P_1^ϵ) or η in (P_1^η) , the CS solution may appear as less sparse than the actual solution. On the other hand, overestimating the noise may cause the CS solution to be too sparse, for example by eliminating sources of smaller strength.

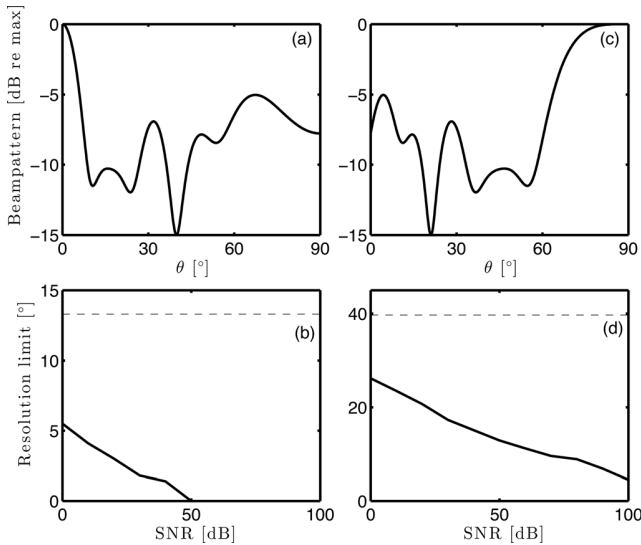


FIG. 8. CS resolution limit for two sources. Beam pattern at (a) broadside and (b) endfire for the random array in Fig. 4(c). Resolution limit versus SNR at (b) broadside and (d) endfire. The half-power beamwidth (dashed line) is indicated in both cases.

In the case that the noise level is not explicitly known, we propose using an underestimated (low) noise level, to assure that all the nonzero components of the solution are captured, and enhance sparsity by reweighing the l_1 -norm iteratively in the convex optimization procedure.^{17,18} After detecting the source locations in the solution with reweighed l_1 -norm minimization, the source amplitudes can be rectified with a level correction step.

A. Reweighed l_1 minimization

The l_1 -norm minimization (P_1^ϵ) is a convex problem and converges to a global minimum. However, the solution to (P_1^ϵ) is not necessarily the sparsest feasible. To enhance sparsity, a reweighed l_1 minimization problem can be solved instead.

The method solves iteratively the weighed l_1 -norm minimization problem (see the Appendix for details),

$$\min_{\mathbf{x} \in \mathbb{C}^N} \|\mathbf{W}\mathbf{x}\|_1 \text{ subject to } \|\mathbf{A}\mathbf{x} - \mathbf{y}\|_2 \leq \epsilon, \quad (P_1^w)$$

where \mathbf{W} is a diagonal weight matrix. Initially, all the weights are 1 leading to the problem (P_1^ϵ) . After the first estimate \mathbf{x} , the weights are updated as

$$w_i = \frac{1}{|\hat{x}_i| + \xi} \quad (27)$$

and the problem (P_1^w) is solved again. The parameter $\xi > 0$ ensures that a null coefficient in the current estimate does not suppress a nonzero coefficient in the next iteration. It should be on the order of the smallest expected source amplitude. The algorithm iterates until a stable estimate is reached, i.e., $\hat{\mathbf{x}}^{k+1} = \hat{\mathbf{x}}^k$, where

$$|w_i x_i|^{k+1} = \begin{cases} \frac{|x_i|}{|x_i| + \xi} \approx 1, & |x_i| > 0, \\ 0, & x_i = 0, \end{cases} \quad (28)$$

thus it has converged (usually one or two iterations suffice).

The weights in Eq. (27) are large for small coefficients, $|x_i|$, and vice versa. Therefore, the smaller coefficients, as indicated by the current solution, are amplified by the weighing, Eq. (27), thus are penalized more in the minimization (P_1^w) .

Figure 9 shows the process of reweighing the l_1 -norm minimization problem. The solution to (P_1^ϵ) with $\epsilon = 0.8\|\mathbf{n}\|_2$, Fig. 9(a), appears less sparse than the actual solution due to the lower noise level. Overestimating the noise level, Fig. 9(b), erroneously favors very sparse solutions suppressing the weakest source in the estimated solution. Figures 9(c) and 9(d) show the solution to (P_1^w) with $\epsilon = 0.8\|\mathbf{n}\|_2$ after the first and second iteration, respectively. Reweighing the l_1 -norm results in a more sparse solution compared to (P_1^ϵ) even though the noise level is underestimated. The (P_1^w) leads to the actual solution already from the first iteration thus the computational burden is not increased significantly compared to (P_1^ϵ) .

B. Level correction

The sparse solution to (P_1^w) can be further improved with level correction. Retaining only the columns in \mathbf{A} which

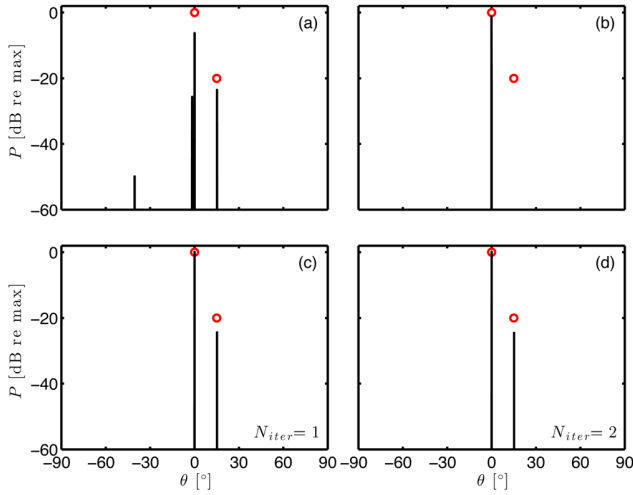


FIG. 9. (Color online) Enhancing sparsity by reweighted l_1 minimization. Two sources at $[0^\circ, 15^\circ]$ with SNR $[20, 0]$ dB, respectively, are detected by measurements on the random linear array in Fig. 4(c). The solution to the (P_1^*) with (a) underestimated noise level $\epsilon = 0.8\|\mathbf{n}\|_2$, (b) overestimated noise level $\epsilon = 2\|\mathbf{n}\|_2$, and the solution to the (P_1^*) with $\epsilon = 0.8\|\mathbf{n}\|_2$ after the (c) first and (d) second iteration.

correspond to peaks in the solution, \mathbf{A}_a , we solve the over-determined problem,^{35,41}

$$\hat{\mathbf{x}}_a = \mathbf{A}_a^+ \mathbf{y}, \quad (29)$$

where the plus sign denotes pseudo-inverse of a matrix, to obtain the source level for just the active indexes.

Figure 10 compares the solutions from CBF, CS, reweighted CS and reweighted CS with level correction. CBF fails to detect the weakest source due to the high sidelobe levels even though the separation of the two sources exceeds half of the mainlobe width. The two sources are localized with high resolution with CS and the estimate is more accurate with reweighted CS. Further processing for level correction gives very good reconstruction.

VI. EXPERIMENTAL RESULTS

To demonstrate the high-resolution capabilities and the robustness of CS in DOA estimation, the method is applied

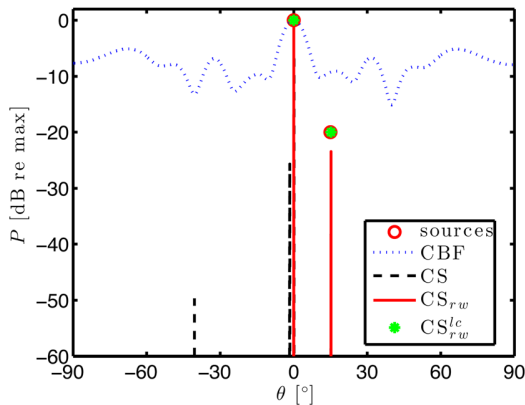


FIG. 10. (Color online) DOA estimation with CBF, CS, reweighted CS and reweighted CS with level correction with the random linear array in Fig. 4(c), for two sources at $[0^\circ, 15^\circ]$ and SNR $[20, 0]$ dB, respectively.

to ocean acoustic measurements for source tracking from single snapshot data and is compared with CBF. More elaborate techniques, such as, for example, multi-rate adaptive beamforming⁴² or post-processing with the method of sub-band peak energy detection,⁴³ would provide cleaner reconstruction than CBF by exploiting information from several snapshots. The main interest is to show the performance of CS as a non-adaptive technique and in challenging scenarios of few snapshots (or even a single one) thus we compare CS simply with CBF.

The data are from the long range acoustic communications (LRAC) experiment⁴⁴ collected from a towed horizontal uniform linear array from 10:00–10:30 UTC on 16 September 2010 in the NE Pacific. The array has $M = 64$ sensors, with intersensor spacing $d = 3$ m, Fig. 11(a), and was towed at 3.5 knots at 200 m depth. The data were acquired with a sampling frequency of 2000 Hz and the record is divided in 4 s non-overlapping snapshots. Each snapshot is Fourier transformed with 2^{13} samples.

Figure 11(b) shows the scaled Gram matrix \mathbf{G} at frequency $f = 125$ Hz ($d/\lambda = 1/4$) for a DOA grid $[-90^\circ:1^\circ:90^\circ]$. The 1° grid spacing is considered sufficient to avoid basis mismatch in this case since a finer grid would not improve the results. The data are post-processed with CBF, CS, and iterative reweighted CS with level correction

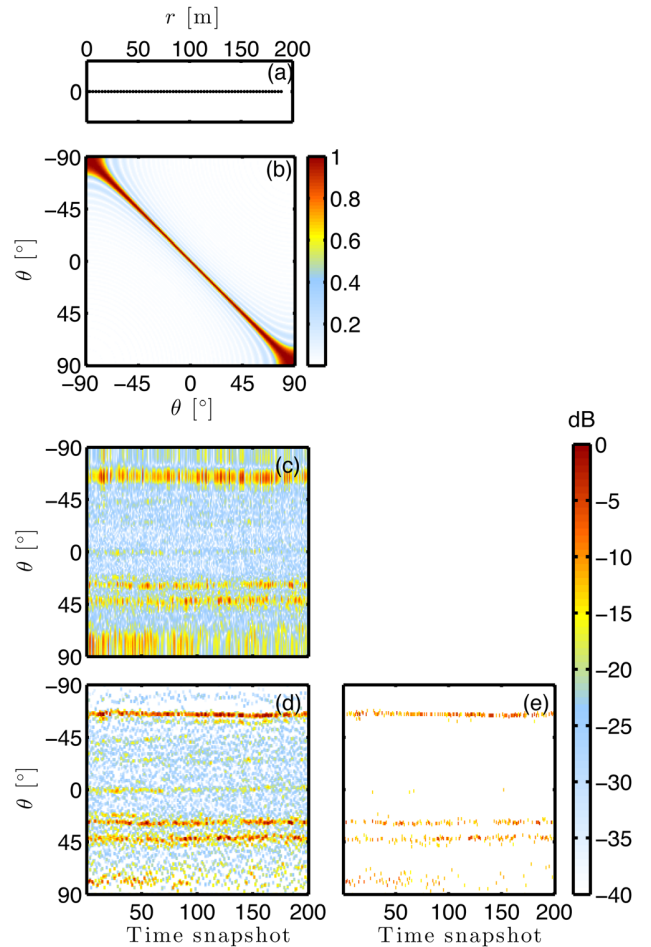


FIG. 11. (Color online) Data from LRAC: (a) Array geometry, (b) Gram matrix \mathbf{G} , (c) CBF, (d) CS, (e) reweighted CS with level correction.

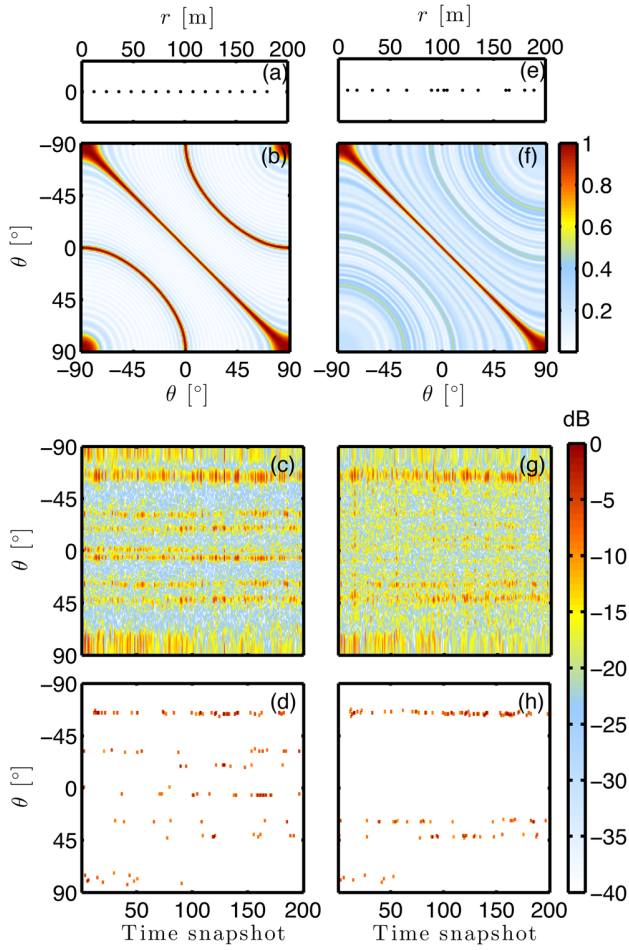


FIG. 12. (Color online) Data from LRAC: (a)–(d) $M = 16$ arranged in a ULA, (e)–(h) $M = 16$ arranged in a random linear array. (a), (e) Array configurations; (b), (d) corresponding Gram matrix; (c), (g) CBF; (d), (h) reweighted CS with level correction.

in Figs. 11(c)–11(e). The unconstrained (P_1^η) formulation of CS is used here with $\eta = 1$.

The beamformer output, Fig. 11(c), indicates the presence of three stationary sources at around 45° , 30° , and -65° . The two arrivals at 45° and 30° are attributed to distant transiting ships, even though a record of ships in the area was not kept. The broad arrival at -65° is from the towship R/V Melville. The CBF map suffers from low resolution and artifacts due to sidelobes and noise. The CS map provides high resolution, Fig. 11(d). The reconstruction is further improved with one iteration of reweighted CS with level correction, Fig. 11(e), which eliminates the noisy artifacts.

The same data set is processed by reducing the sensors by a factor of 4 to $M = 16$ for a ULA with $d/\lambda = 1$, Figs. 12(a)–12(d), and a random array, Figs. 12(e)–12(h). Both array configurations, Figs. 12(a) and 12(e), have the same aperture as the original array hence the same resolution. In the case of the ULA with $d/\lambda = 1$, grating lobes appear in the visible area, Fig. 12(b), resulting in spurious sources in both CBF, Fig. 12(c), and CS, Fig. 12(d). In the case that the sensors are selected randomly, there are no grating lobes in the beam pattern, Fig. 12(f), thus spurious sources do not appear. The increased level of sidelobes in this case degrades the CBF map, Fig. 12(g). In contrast, CS, Fig. 12(h), results in a clean map with accurate localization of

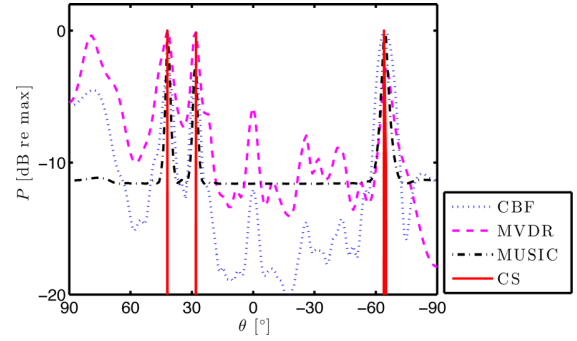


FIG. 13. (Color online) Data from LRAC: Combining the 200 snapshots and processing with CBF, MVDR, MUSIC, and reweighted CS with level correction. The ULA array with $M = 64$ sensors and $d/\lambda = 1/4$ is used.

the three sources. The robustness of CS even with a limited number of sensors indicates the possibility of using arrays with fewer sensors (reducing the cost, exceeding the design frequency) without a significant reconstruction degradation as long as the configuration is random.

Assuming the sources are adequately stationary, the 200 snapshots are combined to compare the CS method with CBF, MVDR, and MUSIC (see Sec. III). The superior performance of CS in terms of resolution and sidelobe levels is depicted in Fig. 13.

VII. CONCLUSION

Source localization with sensor arrays is a sparse signal reconstruction problem which can be efficiently solved with compressive sensing (CS). The offset and resolution analysis indicates that the CS has robust performance in most of the angular spectrum. The CS estimate offset in DOA estimation is related to the coherence of the sensing matrix \mathbf{A} and is restricted to the proximity of the actual source location. Similarly, the resolution of CS is determined by the coherence of \mathbf{A} and depends on array geometry, frequency, source location, and SNR.

CS achieves high-resolution in DOA estimation by promoting sparse solutions. It can distinguish between coherent arrivals, as multipath, since it does not involve the array cross-spectral matrix and can be used even with single-snapshot data outperforming traditional DOA estimation methods. Furthermore, CS can be used with (arbitrary) random array configurations allowing great flexibility in the context of sound source localization.

ACKNOWLEDGMENT

This work was supported by the Office of Naval Research, under Grant No. N00014-11-1-0320.

APPENDIX: REWEIGHTED l_1 MINIMIZATION

To enhance sparsity, the l_1 -norm of a vector, $\mathbf{x} \in \mathbb{C}^N$, can be replaced by other sparsity promoting functions such as, $J(\mathbf{x}) = \sum_{i=1}^N \ln(|x_i| + \xi)$, resulting in the optimization problem,

$$\min_{\mathbf{x} \in \mathbb{C}^N} J(\mathbf{x}) \text{ subject to } \|\mathbf{A}\mathbf{x} - \mathbf{y}\|_2 \leq \epsilon, \quad (P_J^\epsilon)$$

instead of the problem (P_1^ϵ).

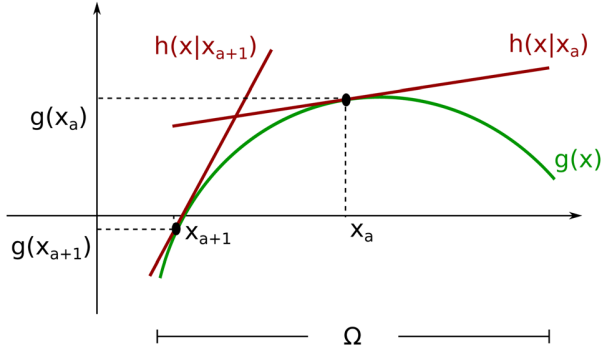


FIG. 14. (Color online) Schematic showing the majorization-minimization procedure for minimizing a concave function.

However, the function $J(\mathbf{x})$ is concave and its minimization is achieved by a majorization-minimization approach⁴⁵ rather than a convex minimization as with the l_1 -norm (P_1^w).

In principle, minimizing a concave function $g(\mathbf{x})$, $\mathbf{x} \in \Omega$, with the majorization-minimization framework involves the following steps (see Fig. 14):

- (1) Majorize $g(\mathbf{x})$ at \mathbf{x}_a with a convex function $h(\mathbf{x}|\mathbf{x}_a)$ such that for $\mathbf{x} \in \Omega$,

$$\begin{aligned} h(\mathbf{x}_a|\mathbf{x}_a) &= g(\mathbf{x}_a), \\ h(\mathbf{x}|\mathbf{x}_a) &\geq g(\mathbf{x}). \end{aligned} \quad (\text{A1})$$

- (2) Minimize the convex function $h(\mathbf{x}|\mathbf{x}_a)$ with respect to $\mathbf{x} \in \Omega$,

$$h(\mathbf{x}_{a+1}|\mathbf{x}_a) = \min_{\mathbf{x} \in \Omega} h(\mathbf{x}|\mathbf{x}_a), \quad (\text{A2})$$

which also assures a descent for the concave function $g(\mathbf{x})$ as

$$g(\mathbf{x}_{a+1}) \leq h(\mathbf{x}_{a+1}|\mathbf{x}_a) \leq h(\mathbf{x}_a|\mathbf{x}_a) = g(\mathbf{x}_a). \quad (\text{A3})$$

- (3) Replace steps (1) and (2) until convergence.

For a differentiable concave function $g(\mathbf{x})$, $\mathbf{x} \in \Omega$, a majorization function can be found easily by definition through the derivative

$$g(\mathbf{x}) \leq g(\mathbf{x}_a) + \nabla g(\mathbf{x}|\mathbf{x}_a) (\mathbf{x} - \mathbf{x}_a), \quad (\text{A4})$$

and minimized such that

$$h(\mathbf{x}_{a+1}|\mathbf{x}_a) = \min_{\mathbf{x} \in \Omega} h(\mathbf{x}|\mathbf{x}_a) = \min_{\mathbf{x} \in \Omega} \nabla g(\mathbf{x}|\mathbf{x}_a) \mathbf{x}. \quad (\text{A5})$$

Therefore, the minimization problem (P_1^c) can be recast in an iterative convex optimization procedure, such that at the $(k+1)$ iteration,

$$\begin{aligned} \min_{\mathbf{x} \in \mathbb{C}^N} \nabla J(\mathbf{x}|\hat{\mathbf{x}}_k) \mathbf{x} \text{ subject to } \|\mathbf{A}\mathbf{x} - \mathbf{y}\|_2 \leq \epsilon, \\ \min_{\mathbf{x} \in \mathbb{C}^N} \sum_{i=1}^N \frac{1}{|\hat{x}_{i,k}| + \xi} |x_i| \text{ subject to } \|\mathbf{A}\mathbf{x} - \mathbf{y}\|_2 \leq \epsilon, \end{aligned} \quad (\text{A6})$$

where $\hat{\mathbf{x}}_k$ is the estimated solution at iteration k . The minimization problem (P_1^c) is equivalent to the iterative weighed l_1 -norm minimization problem (P_1^w),

$$\min_{\mathbf{x} \in \mathbb{C}^N} \|\mathbf{W}\mathbf{x}\|_1 \text{ subject to } \|\mathbf{A}\mathbf{x} - \mathbf{y}\|_2 \leq \epsilon, \quad (P_1^w)$$

where \mathbf{W} is a diagonal weight matrix with elements $w_i = 1/|\hat{x}_i| + \xi$ determined by the solution of the previous iteration $\hat{\mathbf{x}}$. The weight matrix, \mathbf{W} , is initialized with the identity matrix, \mathbf{I}_N , and the parameter $\xi > 0$ is used to prevent infinite-valued weights.

¹D. H. Johnson and D. E. Dudgeon, *Array Signal Processing: Concepts and Techniques* (PRT Prentice Hall, Englewood Cliffs, NJ, 1993), pp. 1–512.

²H. Krim and M. Viberg, “Two decades of array signal processing research: the parametric approach,” *IEEE Signal Process. Mag.* **13**, 67–94 (1996).

³M. Elad, *Sparse and Redundant Representations: From Theory to Applications in Signal and Image Processing* (Springer, New York, 2010), pp. 1–359.

⁴S. Foucart and H. Rauhut, *A Mathematical Introduction to Compressive Sensing* (Springer, New York, 2013), pp. 1–589.

⁵E. J. Candès, J. Romberg, and T. Tao, “Robust uncertainty principles: Exact signal reconstruction from highly incomplete frequency information,” *IEEE Trans. Inf. Theory* **52**, 489–509 (2006).

⁶M. Lustig, D. Donoho, and J. M. Pauly, “Sparse MRI: The application of compressed sensing for rapid MR imaging,” *Magn. Reson. Med.* **58**, 1182–1195 (2007).

⁷N. Wagner, Y. C. Eldar, and Z. Friedman, “Compressed beamforming in ultrasound imaging,” *IEEE Trans. Signal Process.* **60**, 4643–4657 (2012).

⁸E. J. Candès and T. Tao, “Decoding by linear programming,” *IEEE Trans. Inf. Theory* **51**, 4203–4215 (2005).

⁹M. A. Herman and T. Strohmer, “High-resolution radar via compressed sensing,” *IEEE Trans. Signal Process.* **57**, 2275–2284 (2009).

¹⁰H. Yao, P. Gerstoft, P. M. Shearer, and C. Mecklenbräuker, “Compressive sensing of the Tohoku-Oki Mw 9.0 earthquake: Frequency-dependent rupture modes,” *Geophys. Res. Lett.* **38**, 1–5, doi:10.1029/2011GL049223 (2011).

¹¹H. Yao, P. M. Shearer, and P. Gerstoft, “Compressive sensing of frequency-dependent seismic radiation from subduction zone megathrust ruptures,” *Proc. Natl. Acad. Sci. U.S.A.* **110**, 4512–4517 (2013).

¹²J. Romberg, “Imaging via compressive sampling,” *IEEE Signal Process. Mag.* **25**, 14–20 (2008).

¹³W. Mantzel, J. Romberg, and K. Sabra, “Compressive matched-field processing,” *J. Acoust. Soc. Am.* **132**, 90–102 (2012).

¹⁴C. Yardim, P. Gerstoft, W. S. Hodgkiss, and J. Traer, “Compressive geoaoustic inversion using ambient noise,” *J. Acoust. Soc. Am.* **135**, 1245–1255 (2014).

¹⁵D. Malioutov, M. Çetin, and A. S. Willsky, “A sparse signal reconstruction perspective for source localization with sensor arrays,” *IEEE Trans. Signal Process.* **53**, 3010–3022 (2005).

¹⁶G. F. Edelmann and C. F. Gaumond, “Beamforming using compressive sensing,” *J. Acoust. Soc. Am.* **130**, EL232–EL237 (2011).

¹⁷I. F. Gorodnitsky and B. D. Rao, “Sparse signal reconstruction from limited data using FOCUSS: A re-weighted minimum norm algorithm,” *IEEE Trans. Signal Process.* **45**, 600–616 (1997).

¹⁸E. J. Candès, M. B. Wakin, and S. Boyd, “Enhancing sparsity by reweighted l_1 minimization,” *J. Fourier Anal. Appl.* **14**, 877–905 (2008).

¹⁹T. Yardibi, J. Li, P. Stoica, M. Xue, and A. B. Baggeroer, “Source localization and sensing: A nonparametric iterative adaptive approach based on weighted least squares,” *IEEE Trans. Aerosp. Electron. Syst.* **46**, 425–443 (2010).

²⁰D. L. Donoho, “Compressed sensing,” *IEEE Trans. Inf. Theory* **52**, 1289–1306 (2006).

²¹E. J. Candès and M. B. Wakin, “An introduction to compressive sampling,” *IEEE Signal Proc. Mag.* **25**, 21–30 (2008).

²²R. G. Baraniuk, “Compressive sensing,” *IEEE Signal Proc. Mag.* **24**, 118–121 (2007).

²³E. J. Candès, “The restricted isometry property and its implications for compressed sensing,” *C. R. Math. Acad. Sci.* **346**, 589–592 (2008).

²⁴R. G. Baraniuk, M. Davenport, R. DeVore, and M. Wakin, “A simple proof of the restricted isometry property for random matrices,” *Constr. Approx.* **28**, 253–263 (2008).

- ²⁵E. J. Candès and T. Tao, "Near-optimal signal recovery from random projections: Universal encoding strategies?," *IEEE Trans. Inf. Theory* **52**, 5406–5425 (2006).
- ²⁶S. S. Chen, D. L. Donoho, and M. A. Saunders, "Atomic decomposition by basis pursuit," *SIAM J. Sci. Comput.* **20**, 33–61 (1998).
- ²⁷S. F. Cotter, B. D. Rao, K. Engan, and K. Kreutz-Delgado, "Sparse solutions to linear inverse problems with multiple measurement vectors," *IEEE Trans. Signal Process.* **53**, 2477–2488 (2005).
- ²⁸J. A. Tropp, "Just relax: Convex programming methods for identifying sparse signals in noise," *IEEE Trans. Inf. Theory* **52**, 1030–1051 (2006).
- ²⁹M. Grant and S. Boyd, "CVX: Matlab software for disciplined convex programming, version 2.0 beta," <http://cvxr.com/cvx> (Last viewed February 3, 2013).
- ³⁰M. Grant and S. Boyd, "Graph implementations for nonsmooth convex programs," in *Recent Advances in Learning and Control, Lecture Notes in Control and Information Sciences*, edited by V. Blondel, S. Boyd, and H. Kimura (Springer-Verlag, London, 2008), pp. 95–110.
- ³¹S. Boyd and L. Vandenberghe, *Convex Optimization* (Cambridge University Press, New York, 2004), pp. 1–684.
- ³²H. Van Trees, *Optimum Array Processing (Detection, Estimation, and Modulation Theory, Part IV)* (Wiley-Interscience, New York, 2002), Chaps. 1–10.
- ³³J. Capon, "High-resolution frequency-wavenumber spectrum analysis," *Proc. IEEE* **57**, 1408–1418 (1969).
- ³⁴R. Schmidt, "Multiple emitter location and signal parameter estimation," *IEEE Trans. Antennas Propag.* **34**, 276–280 (1986).
- ³⁵C. F. Mecklenbräuker, P. Gerstoft, A. Panahi, and M. Viberg, "Sequential Bayesian sparse signal reconstruction using array data," *IEEE Trans. Signal Process.* **61**, 6344–6354 (2013).
- ³⁶Y. Chi, L. L. Scharf, A. Pezeshki, and A. R. Calderbank, "Sensitivity to basis mismatch in compressed sensing," *IEEE Trans. Signal Process.* **59**, 2182–2195 (2011).
- ³⁷H. Monajemi, S. Jafarpour, M. Gavish, Stat 330/CME 362 Collaboration, and D. L. Donoho, "Deterministic matrices matching the compressed sensing phase transitions of Gaussian random matrices," *Proc. Natl. Acad. Sci. U.S.A.* **110**, 1181–1186 (2013).
- ³⁸C. F. Gaumond and G. F. Edelmann, "Sparse array design using statistical restricted isometry property," *J. Acoust. Soc. Am.* **134**, EL191–EL197 (2013).
- ³⁹E. J. Candès, Y. C. Eldar, D. Needell, and P. Randall, "Compressed sensing with coherent and redundant dictionaries," *Appl. Comput. Harmon. Anal.* **31**, 59–73 (2011).
- ⁴⁰M. Elad, "Optimized projections for compressed sensing," *IEEE Trans. Signal Process.* **55**, 5695–5702 (2007).
- ⁴¹S. J. Wright, R. D. Nowak, and M. A. T. Figueiredo, "Sparse reconstruction by separable approximation," *IEEE Trans. Signal Process.* **57**, 2479–2493 (2009).
- ⁴²H. Cox, "Multi-rate adaptive beamforming (MRABF)," in *Sensor Array and Multichannel Signal Processing Workshop* (IEEE, Cambridge, MA, 2000), pp. 306–309.
- ⁴³M. Bono, B. Shapo, P. McCarty, and R. Bethel, "Subband energy detection in passive array processing," DTIC Document, Texas University–Austin Applied Research Labs (2000).
- ⁴⁴H. C. Song, S. Cho, T. Kang, W. S. Hodgkiss, and J. R. Preston, "Long-range acoustic communication in deep water using a towed array," *J. Acoust. Soc. Am.* **129**, EL71–EL75 (2011).
- ⁴⁵D. R. Hunter and K. Lange, "A tutorial on MM algorithms," *Am. Stat.* **58**, 30–37 (2004).

PAPER D

Sparsity and super-resolution in sound source localization with sensor arrays

Authors:

Angeliki Xenaki, Peter Gerstoft and Klaus Mosegaard

Published in:

Proceedings of 2nd Underwater Acoustics Conference and Exhibition, Rhodes, Greece, 2014.

SPARSITY AND SUPER-RESOLUTION IN SOUND SOURCE LOCALIZATION WITH SENSOR ARRAYS

Angeliki Xenaki^{a,b}, Peter Gerstoft^b and Klaus Mosegaard^a

^aDepartment of Applied Mathematics and Computer Science, Technical University of Denmark, 2800 Kgs. Lyngby, Denmark

^bMarine Physical Laboratory, Scripps Institution of Oceanography, University of California San Diego, La Jolla, California 92093-0238

Corresponding author: Angeliki Xenaki, Technical University of Denmark, Elektrovej, Building 327, 2800 Kgs. Lyngby, Denmark, email: anxe@dtu.dk

Abstract: *Sound source localization with sensor arrays involves the estimation of the direction-of-arrival (DOA) from a limited number of observations. Compressive sensing (CS) is a method for solving such undetermined problems which achieves simultaneously sparsity, thus super-resolution, and computational speed. We formulate the DOA estimation as a sparse signal reconstruction problem and show that methods which exploit sparsity have superior performance compared to traditional methods for DOA estimation. To demonstrate the high-resolution capabilities and the robustness of CS and other sparsity promoting optimization techniques in DOA estimation, the methods are applied to experimental data from underwater acoustic measurements in the challenging scenario of source tracking from single snapshot data.*

Keywords: *Sparsity, compressive sensing, direction of arrival (DOA) estimation, sensor arrays*

1. INTRODUCTION

The problem of direction-of-arrival (DOA) estimation with sensor arrays is to infer the number and the location of (usually few) sound sources possibly in the presence of noise from measurements of the wavefield with an array of sensors. Conventional beamforming [1] is the simplest traditional method for DOA estimation, though it is characterized by low resolution. Other methods [1], developed to overcome the resolution limit of conventional beamforming, have degraded performance under noisy conditions, coherent sources and sample-starved data.

The compressive sensing (CS) framework [2] asserts that signals can be reconstructed from very few measurements as long as the signals are sparse and can be done with computationally efficient methods by solving a convex minimization problem with linear programming. CS and other sparsity promoting methods outperform traditional methods which aim to minimize the energy of the signal resulting in low-resolution, non-sparse solutions.

2. SPARSITY AND COMPRESSIVE SENSING

For simplicity, we formulate the DOA estimation problem assuming that the sources are in the far field of the array (i.e. plane waves), the processing is narrowband and the problem is confined in two dimensions (2D) with a linear array of sensors with known geometry.

Let $\mathbf{x} \in C^N$ be an unknown vector comprising the source strengths at all directions $\theta \in [-90^\circ, 90^\circ]$ relative to the array axis on the angular grid of interest. Usually, there are only few sources $K \ll N$ present, resulting in a sparse \mathbf{x} . Let $\mathbf{y} \in C^M$ be the vector of the wavefield measurements at the M sensors linearly related to the signal \mathbf{x} , such that in the absence of noise,

$$\mathbf{y} = \mathbf{A}_{M \times N} \mathbf{x}. \quad (1)$$

The sensing matrix \mathbf{A} is formed by concatenating the steering vectors,

$$\mathbf{a}(\theta_k) = \frac{1}{\sqrt{M}} e^{j \frac{2\pi}{\lambda} \mathbf{r} \sin \theta_k}, \text{ at all potential source directions } \mathbf{A} = [\mathbf{a}(\theta_1), \dots, \mathbf{a}(\theta_N)], \text{ where } \lambda$$

is the wavelength and $\mathbf{r} = [r_1, \dots, r_M]^T$ the sensor locations.

Practically, we are interested in a fine resolution on the angle grid, thus $M < N$ and the problem (1) is underdetermined. A way of solving this ill-posed problem is to constrain the possible solutions with prior information.

Traditional methods impose a minimum l_2 -norm constraint on the solution and solve (1) through the minimization problem,

$$\min_{\mathbf{x} \in C^N} \|\mathbf{x}\|_2 \text{ subject to } \mathbf{y} = \mathbf{A} \mathbf{x}. \quad (P_2)$$

The convex problem (P₂) aims to minimize the energy of the signal rather than its sparsity, resulting in a non-sparse solution, $\hat{\mathbf{x}} = \mathbf{A}^H (\mathbf{A} \mathbf{A}^H)^{-1} \mathbf{y}$. Beamforming is based on the l_2 -norm method with the simplifying assumption, $\mathbf{A} \mathbf{A}^H = \mathbf{I}_M$, such that, $\hat{\mathbf{x}} = \mathbf{A}^H \mathbf{y}$.

By definition, sparsity can be imposed on the vector \mathbf{x} by minimizing the l_0 -norm $\|\mathbf{x}\|_0 = \sum_{i=1}^N 1_{x_i \neq 0}$, which counts the number of non-zero entries in the vector, leading to the minimization problem (P₀),

$$\min_{\mathbf{x} \in \mathbb{C}^N} \|\mathbf{x}\|_0 \text{ subject to } \mathbf{y} = \mathbf{A} \mathbf{x}. \quad (\text{P}_0)$$

However, the minimization problem (P₀) is a non-convex combinatorial problem, which becomes computationally intractable even for moderate dimensions. The breakthrough of CS came with the proof that for sufficiently sparse signals and sensing matrices with sufficiently incoherent columns the (P₀) problem is equivalent to the (P₁) problem [3],

$$\min_{\mathbf{x} \in \mathbb{C}^N} \|\mathbf{x}\|_1 \text{ subject to } \mathbf{y} = \mathbf{A} \mathbf{x}, \quad (\text{P}_1)$$

where the l_0 -norm is replaced with the l_1 -norm. The l_1 relaxation (P₁) of the (P₀) problem is the closest convex optimization problem to (P₀) and can be solved efficiently with linear programming [4] even for large dimensions.

For noisy measurements, $\mathbf{y} = \mathbf{A} \mathbf{x} + \mathbf{n}$, where $\mathbf{n} \in \mathbb{C}^M$ is additive noise with bounded norm $\|\mathbf{n}\|_2 \leq \varepsilon$, the (P₁) problem is reformulated as [5],

$$\min_{\mathbf{x} \in \mathbb{C}^N} \|\mathbf{x}\|_1 \text{ subject to } \|\mathbf{A} \mathbf{x} - \mathbf{y}\|_2 \leq \varepsilon. \quad (\text{P}_1^\varepsilon)$$

The solution to (P₁^ε) has the minimum l_1 -norm while it fits the data up to the noise level.

CS offers super-resolution due to the sparsity constraint and computational efficiency due to convex relaxation of the l_0 -norm optimization problem. However, as all DOA estimation methods, it has also limitations. A performance analysis of CS in DOA estimation, in terms of the discretization of the angular space, the coherence of the sensing matrix and the signal to noise ratio (SNR), is carried out in [6].

3. ENHANCING SPARSITY

The l_1 -norm of a vector \mathbf{x} is a convex function hence the optimization problem (P₁^ε) converges to a global minimum. However, the solution to (P₁^ε) is not necessarily the sparsest feasible. To enhance sparsity, the l_1 -norm of the vector $\mathbf{x} \in \mathbb{C}^N$ can be

replaced by other sparsity promoting functions such as the l_p -norm, $\|\mathbf{x}\|_p = \left(\sum_{i=1}^N |x_i|^p \right)^{1/p}$, with $0 < p < 1$ [7]; see Fig.1.

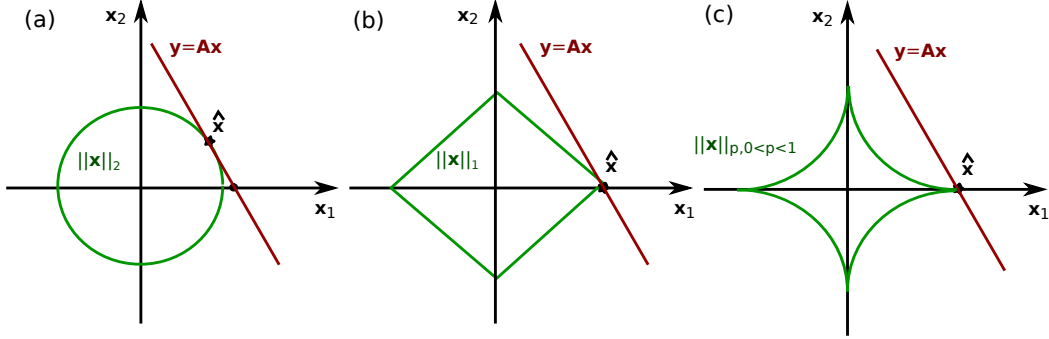


Fig.1: Geometric visualization of (a) the l_2 -norm, (b) the l_1 -norm and (c) the l_p -norm problem with $0 < p < 1$ in R^2 . The solution $\hat{\mathbf{x}}$ is the intersection of the measurement line $\mathbf{y} = \mathbf{A}\mathbf{x}$ and the minimum norm-ball in each case. The l_2 -norm constraint leads to non-sparse solutions, while the l_p -norm, $0 < p \leq 1$, constraint promotes sparse solutions.

Nevertheless, $G(\mathbf{x})$ is a concave function and it can be minimized by a majorization-minimization approach rather than a convex minimization as with the l_1 -norm.

Concisely, minimizing a function $f(x), x \in \Omega$ with the majorization-minimization framework involves finding a convex function $g(x|x_a), x \in \Omega$ which majorizes $f(x)$, such that $g(x|x_a) \geq f(x)$ and $g(x_a|x_a) = f(x_a)$, and then minimizing the function $g(x|x_a)$ with respect to $x \in \Omega$ resulting in $g(x_{a+1}|x_a) = \min_{x \in \Omega} g(x|x_a)$. This procedure assures a descent for $f(x), x \in \Omega_s$, since $f(x_{a+1}) \leq g(x_{a+1}|x_a) \leq g(x_a|x_a) = f(x_a)$. Repeating this process iteratively until convergence results in minimization of the concave function $f(x), x \in \Omega$.

For a differentiable concave function $f(x), x \in \Omega$ a majorization function can be easily found through the derivative $f(x) \leq f(x_0) + \nabla f(x_0)(x - x_0)$ and minimized such that $\min_{x \in \Omega} g(x|x_0) = \min_{x \in \Omega} \nabla f(x_0)x$ (the constant terms are ignored as they don't affect the optimization).

Following the aforementioned analysis, the minimization of a concave function subject to constraints can be recast in an iterative convex minimization problem.

For example, the FOCUSS algorithm [7] minimizes the concave function

$$G(\mathbf{x}) = \sum_{i=1}^N |x_i|^p \text{ with } 0 < p < 1. \text{ Using the transformation } h_i = x_i^2 \geq 0 \text{ yields } G(\mathbf{h}) = \sum_{i=1}^N h_i^{\frac{p}{2}}$$

and $\nabla G(\mathbf{h}|\mathbf{h}_k) = \frac{p}{2} \sum_{i=1}^N h_{i,k}^{\frac{p}{2}-1}$. Thus in the $k+1$ iteration the function to be minimized is

$\nabla G(\mathbf{h} | \mathbf{h}_k) \mathbf{h} = \frac{p}{2} \sum_{i=1}^N h_{i,k}^{\frac{p-1}{2}} h_i$ or equivalently $\frac{p}{2} \sum_{i=1}^N \left(\hat{x}_{i,k}^2 \right)^{\frac{p-1}{2}} \left(x_i^2 \right) = \frac{p}{2} \|\mathbf{W}_k \mathbf{x}\|_2^2$. The matrix $\mathbf{W}_k = \text{diag} \left(\left(\hat{x}_{i,k} \right)^{\frac{p-1}{2}} \right)$ is diagonal with elements related to the solution of the previous iteration, $\hat{\mathbf{x}}_k$, resulting in the iterative l_2 -norm convex minimization problem,

$$\min_{\mathbf{x} \in \mathbb{C}^N} \|\mathbf{W}_k \mathbf{x}\|_2^2 \text{ subject to } \|\mathbf{A} \mathbf{x} - \mathbf{y}\|_2 \leq \varepsilon. \quad (\mathbf{P}_{2,w}^\varepsilon)$$

Reformulating $(\mathbf{P}_{2,w}^\varepsilon)$ in an unconstrained form with the use of Lagrange multipliers,

$$\min_{\mathbf{x} \in \mathbb{C}^N} \|\mathbf{W}_k \mathbf{x}\|_2^2 + \eta \|\mathbf{A} \mathbf{x} - \mathbf{y}\|_2^2, \quad (\mathbf{P}_{2,w}^\eta)$$

the solution can be found analytically in each iteration, $\hat{\mathbf{x}}_{k+1} = \mathbf{W}_k^H \mathbf{W}_k \mathbf{A}^H \left(\mathbf{A} \mathbf{W}_k^H \mathbf{W}_k \mathbf{A}^H + \eta \mathbf{I}_M \right)^{-1} \mathbf{y}$.

Even though the problem is not convex and convergence to the global minimum is not guaranteed, initialization with the l_2 -norm solution such that $\mathbf{W}_0 = \mathbf{I}_N$ usually suffices (at least in the context of DOA estimation) to assure that $(\mathbf{P}_{2,w}^\varepsilon)$ does not get trapped in local minima.

4. EXPERIMENTAL RESULTS

The high-resolution capabilities and the robustness of the sparsity promoting framework in DOA estimation, is demonstrated on ocean acoustic measurements for source tracking from single snapshot data. Specifically, the data is from the long range acoustic communications (LRAC) experiment collected from a towed horizontal uniform linear array from 10:00-10:30 UTC on 16 September 2010 in the NE Pacific. The array has $M=64$ sensors, with intersensor spacing $d=3\text{m}$ and was towed at 3.5 knots at 200m depth. The data were acquired with a sampling frequency of 2000Hz and the record is divided in 4s non-overlapping snapshots. Each snapshot is Fourier transformed with 2^{13} samples.

Figure 2 shows the reconstruction with CBF, CS and l_p -norm minimization, with $p=0.8$, at frequency $f=125\text{Hz}$ ($d/\lambda = 1/4$) for a DOA grid $[-90:1:90]^\circ$. The beamformer output indicates the presence of three sources at around 45° , 30° and -65° . The two arrivals at 45° and 30° are attributed to distant transiting ships. The broad arrival at -65° is from the towship R/V Melville. The beamforming map suffers from low resolution and artifacts due to sidelobes. The CS provides high resolution imaging, which is further improved by enhancing sparsity with $l_{0.8}$ -norm minimization.

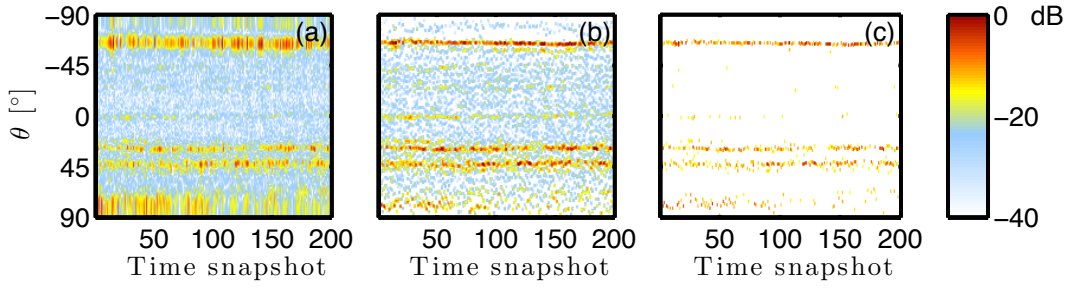


Fig.2: Data from LRAC: (a) conventional beamforming, (b) CS with l_1 -norm minimization (implemented with CVX [4]), (c) CS with $l_{0.8}$ -norm minimization (implemented with FOCUSS [7])

5. CONCLUSION

Sound source localization with sensor arrays is essentially a sparse signal reconstruction problem, which can be efficiently solved with CS or other sparsity promoting optimization procedures providing high-resolution reconstruction in DOA estimation.

REFERENCES

- [1] **Krim H., Viberg M.**, “Two decades of array signal processing research: the parametric approach”, *IEEE Signal Proc. Mag.*, 13, pp. 67-94, 1996.
- [2] **Baraniuk R. G.**, “Compressive sensing”, *IEEE Signal Proc. Mag.*, 24, pp. 118-121, 2007.
- [3] **Candes E. J., Romberg J., Tao T.**, “Robust uncertainty principles: Exact signal reconstruction from highly incomplete frequency information”, *IEEE Trans. Inf. Theory*, 52, pp. 489-509, 2006.
- [4] **Grant M., Boyd S.**, “CVX: Matlab software for disciplined convex programming, version 2.0 beta”, <http://cvxr.com/cvx>, 2013.
- [5] **Donoho D. L., Elad M., Temlyakov V. N.**, “Stable recovery of sparse overcomplete representations in the presence of noise”, *IEEE Trans. Inf. Theory*, 52, pp. 6-18, 2006.
- [6] **Xenaki A., Gerstoft P., Mosegaard K.**, “Compressive beamforming”, *J. Acoust. Soc. Am.*, in press, 2014.
- [7] **Cotter S. F., Rao B. D., Engan K., Kreutz-Delgado K.**, “Sparse solutions to linear inverse problems with multiple measurement vectors”, *IEEE Trans. Signal Process.*, 53, pp. 2477-2488, 2005.

PAPER **E**

Grid-free compressive beamforming

Authors:

Angeliki Xenaki and Peter Gerstoft

Published in:

Journal of the Acoustical Society of America, vol. **137**(4), pp. 1923–1935, 2015.

Grid-free compressive beamforming

Angeliki Xenaki^{a)}

Department of Applied Mathematics and Computer Science, Technical University of Denmark, Kgs. Lyngby 2800, Denmark

Peter Gerstoft

Scripps Institution of Oceanography, University of California San Diego, La Jolla, California 92093-0238

(Received 5 November 2014; revised 3 February 2015; accepted 2 March 2015)

The direction-of-arrival (DOA) estimation problem involves the localization of a few sources from a limited number of observations on an array of sensors, thus it can be formulated as a sparse signal reconstruction problem and solved efficiently with compressive sensing (CS) to achieve high-resolution imaging. On a discrete angular grid, the CS reconstruction degrades due to basis mismatch when the DOAs do not coincide with the angular directions on the grid. To overcome this limitation, a continuous formulation of the DOA problem is employed and an optimization procedure is introduced, which promotes sparsity on a continuous optimization variable. The DOA estimation problem with infinitely many unknowns, i.e., source locations and amplitudes, is solved over a few optimization variables with semidefinite programming. The grid-free CS reconstruction provides high-resolution imaging even with non-uniform arrays, single-snapshot data and under noisy conditions as demonstrated on experimental towed array data.

© 2015 Acoustical Society of America. [<http://dx.doi.org/10.1121/1.4916269>]

[ZHM]

Pages: 1923–1935

I. INTRODUCTION

Sound source localization with sensor arrays involves the estimation of the direction-of-arrival (DOA) of (usually a few) sources from a limited number of observations. Compressive sensing^{1,2} (CS) is a method for solving such underdetermined problems with a convex optimization procedure which promotes sparse solutions.

Solving the DOA estimation as a sparse signal reconstruction problem with CS, results in robust, high-resolution acoustic imaging,^{3–6} outperforming traditional methods⁷ for DOA estimation. Furthermore, in ocean acoustics, CS is shown to improve the performance of matched field processing,^{8,9} which is a generalized beamforming method for localizing sources in complex environments (e.g., shallow water), and of coherent passive fathometry in inferring the number and depth of sediment layer interfaces.¹⁰

One of the limitations of CS in DOA estimation is basis mismatch¹¹ which occurs when the sources do not coincide with the look directions due to inadequate discretization of the angular spectrum. Under basis mismatch, spectral leakage leads to inaccurate reconstruction, i.e., estimated DOAs deviating from the actual ones. Employing finer grids^{3,12} alleviates basis mismatch at the expense of increased computational complexity, especially in large two-dimensional or three-dimensional problems as encountered in seismic imaging, for example.^{13–15}

To overcome basis mismatch, we formulate the DOA estimation problem in a continuous angular spectrum and introduce a sparsity promoting measure for general signals, the atomic norm.¹⁶ The atomic norm minimization problem,

which has infinitely many unknowns, is solved efficiently over few optimization variables in the dual domain with semidefinite programming.¹⁷ Utilizing the dual optimal variables, we show that the DOAs are accurately reconstructed through polynomial rooting. It is demonstrated that grid-free CS gives robust, high-resolution reconstruction also with non-uniform arrays and noisy measurements, exhibiting great flexibility in practical applications.

Polynomial rooting is employed in several DOA estimation methods to improve the resolution. However, these methods involve the estimation of the cross-spectral matrix hence they require many snapshots and stationary incoherent sources and are suitable only for uniform linear arrays (ULA).¹⁸ Grid-free CS is demonstrated not to have these limitations.

Finally, we process acoustic data¹⁹ from measurements in the North-East (NE) Pacific with grid-free CS and demonstrate that the method provides high-resolution acoustic imaging even with single-snapshot data.

In this paper, vectors are represented by bold lowercase letters and matrices by bold uppercase letters. The symbols T , H denote the transpose and the Hermitian (i.e., conjugate transpose) operator, respectively, on vectors and matrices. The symbol $*$ denotes simple conjugation. The generalized inequality $\mathbf{X} \succeq 0$ denotes that the matrix \mathbf{X} is positive semi-definite. The ℓ_p -norm of a vector $\mathbf{x} \in \mathbb{C}^n$ is defined as $\|\mathbf{x}\|_p = (\sum_{i=1}^n |x_i|^p)^{1/p}$. By extension, the ℓ_0 -norm is defined as $\|\mathbf{x}\|_0 = \sum_{i=1}^n 1_{x_i \neq 0}$. The paper makes heavy use of convex optimization theory; for a summary see Appendix A.

II. DISCRETE DOA ESTIMATION

The DOA estimation problem involves the localization of usually a few sources from measurements on an array of

^{a)} Author to whom correspondence should be addressed. Electronic mail: anxe@dtu.dk

sensors. For simplicity, we assume that the sources are in the far-field of the array, such that the wavefield impinging on the array consists of a superposition of plane waves, that the processing is narrowband and the sound speed is known. Moreover, we consider the one-dimensional problem with a uniform linear array of sensors and the sources residing in the plane of the array.

The location of a source is characterized by the direction of arrival of the associated plane wave, $\theta \in [-90^\circ, 90^\circ]$, with respect to the array axis. The propagation delay from the i th potential source to each of the M array sensors is described by the steering (or replica) vector

$$\mathbf{a}(\theta_i) = e^{j2\pi(d/\lambda)[0, \dots, M-1]^T \sin \theta_i}, \quad (1)$$

where λ is the wavelength and d is the intersensor spacing.

Discretizing the half-space of interest, $\theta \in [-90^\circ, 90^\circ]$, into N angular directions the DOA estimation problem is expressed in a matrix-vector formulation

$$\mathbf{y} = \mathbf{A}\mathbf{x}, \quad (2)$$

where $\mathbf{y} \in \mathbb{C}^M$ is the vector of the wavefield measurements at the M sensors, $\mathbf{x} \in \mathbb{C}^N$ is the unknown vector of the complex source amplitudes at all N directions on the angular grid of interest, and \mathbf{A} is the sensing matrix which maps the signal to the observations

$$\mathbf{A}_{M \times N} = [\mathbf{a}(\theta_1), \dots, \mathbf{a}(\theta_N)]. \quad (3)$$

In the presence of additive noise $\mathbf{n} \in \mathbb{C}^M$, the measurement vector is described by

$$\mathbf{y} = \mathbf{A}\mathbf{x} + \mathbf{n}. \quad (4)$$

The noise is generated as independent and identically distributed complex Gaussian. The array signal-to-noise ratio (SNR) for a single-snapshot is used in the simulations, defined as $\text{SNR} = 20 \log_{10}(\|\mathbf{A}\mathbf{x}\|_2 / \|\mathbf{n}\|_2)$, which determines the noise ℓ_2 -norm, $\|\mathbf{n}\|_2 = \|\mathbf{A}\mathbf{x}\|_2 10^{-\text{SNR}/20}$.

A. Sparse signal reconstruction

Practically, we are interested in a fine resolution on the angular grid such that $M < N$ and problem (2) is underdetermined. A way to solve this ill-posed problem is to constrain the possible solutions with prior information.

Traditional methods solve the underdetermined problem (2) by seeking the solution with the minimum ℓ_2 -norm which fits the data as described by the minimization problem

$$\min_{\mathbf{x} \in \mathbb{C}^N} \|\mathbf{x}\|_2 \text{ subject to } \mathbf{y} = \mathbf{A}\mathbf{x}. \quad (5)$$

The minimization problem (5) is convex with analytic solution, $\hat{\mathbf{x}} = \mathbf{A}^H(\mathbf{A}\mathbf{A}^H)^{-1}\mathbf{y}$. However, it aims to minimize the energy of the signal rather than its sparsity, hence the resulting solution is non-sparse.

Conventional beamforming²⁰ (CBF) is the simplest source localization method and it is based on the ℓ_2 -norm method with the simplifying condition $\mathbf{A}\mathbf{A}^H = \mathbf{I}_M$. CBF

combines the sensor outputs coherently to enhance the signal at a specific look direction from the ubiquitous noise yielding the solution

$$\hat{\mathbf{x}}_{\text{CBF}} = \mathbf{A}^H \mathbf{y}. \quad (6)$$

CBF is robust to noise but suffers from low resolution and the presence of sidelobes.

A sparse solution \mathbf{x} is preferred by minimizing the ℓ_0 -norm leading to the minimization problem

$$\min_{\mathbf{x} \in \mathbb{C}^N} \|\mathbf{x}\|_0 \text{ subject to } \mathbf{y} = \mathbf{A}\mathbf{x}. \quad (7)$$

However, the minimization problem (7) is a non-convex combinatorial problem which becomes computationally intractable even for moderate dimensions. The breakthrough of compressive sensing^{1,2} (CS) came with the proof that for sufficiently sparse signals, $K \ll N$, $K < M$, and sensing matrices with sufficiently incoherent columns the minimization problem (7) is equivalent to the minimization problem

$$\min_{\mathbf{x} \in \mathbb{C}^N} \|\mathbf{x}\|_1 \text{ subject to } \mathbf{y} = \mathbf{A}\mathbf{x}, \quad (8)$$

where the ℓ_0 -norm is replaced with the ℓ_1 -norm. The problem (8) is the closest convex optimization problem to problem (7) and can be solved efficiently by convex optimization even for large dimensions.²¹

For noisy measurements Eq. (4), the constraint in Eq. (8) becomes $\|\mathbf{y} - \mathbf{A}\mathbf{x}\|_2 \leq \epsilon$, where ϵ is the noise floor, i.e., $\|\mathbf{n}\|_2 \leq \epsilon$. Then, the solution is²²

$$\hat{\mathbf{x}}_{\text{CS}} = \underset{\mathbf{x} \in \mathbb{C}^N}{\text{argmin}} \|\mathbf{x}\|_1 \text{ subject to } \|\mathbf{y} - \mathbf{A}\mathbf{x}\|_2 \leq \epsilon, \quad (9)$$

which has the minimum ℓ_1 -norm while it fits the data up to the noise level.

Herein, we use the cvx toolbox for disciplined convex optimization which is available in the Matlab environment. It uses interior point solvers to obtain the global solution of a well-defined optimization problem.²³ Interior point methods solve an optimization problem with linear equality and inequality constraints by transforming it to a sequence of simpler linear equality constrained problems which are solved iteratively with the Newton's method (iterative gradient descent method) increasing the accuracy of approximation at each step.²⁴

B. Basis mismatch

CS offers improved resolution due to the sparsity constraint and it can be solved efficiently with convex optimization. However, CS performance in DOA estimation is limited by the coherence of the sensing matrix \mathbf{A} (see Ref. 5), described by the restricted isometry property,²⁵ and by basis mismatch^{11,12} due to inadequate discretization of the angular grid. Herein, we demonstrate a way to overcome the limitation of basis mismatch by solving the ℓ_1 -minimization problem on a grid-free, continuous spatial domain.

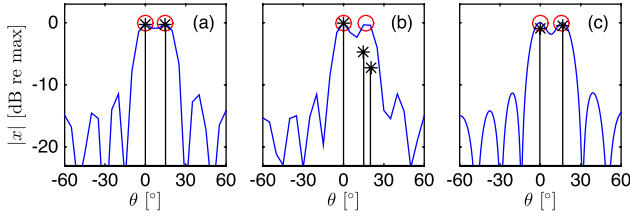


FIG. 1. (Color online) CS performance in DOA estimation in terms of the discretization of the angular space. A standard ULA is used with $M = 8$ sensors, $d/\lambda = 1/2$ and $\text{SNR} = 20$ dB. CBF and CS (*) reconstruction of two sources (a) at 0° and 15° on a grid $[-90^\circ : 5^\circ : 90^\circ]$, (b) at 0° and 17° on a grid $[-90^\circ : 5^\circ : 90^\circ]$, and (c) at 0° and 17° on a grid $[-90^\circ : 1^\circ : 90^\circ]$.

The fundamental assumption in CS is the sparsity of the underlying signal in the basis of representation, i.e., the sensing matrix \mathbf{A} . However, when the sources do not match with the selected angular grid, the signal might not appear sparse in the selected discrete Fourier transform basis.¹¹ Figure 1 shows the degradation of CS performance under basis mismatch due to inadequate discretization of the DOA domain in fast Fourier transform beamforming.

To increase the precision of the CS reconstruction, Malioutov *et al.*³ and Duarte and Baraniuk¹² propose an adaptive grid refinement. The adaptive grid refinement aims at improving the resolution of CS reconstruction without significant increase in the computational complexity by first detecting the regions where sources are present on a coarse grid and then refining the grid locally only at these regions. Grid refinement is an intuitive way of circumventing basis mismatch. However, the problem of basis mismatch is avoided only if the problem is solved in a continuous setting, particularly for moving sources.

III. CONTINUOUS DOA ESTIMATION

In the continuous approach, the K -sparse signal, x , is expressed as

$$x(t) = \sum_{i=1}^K x_i \delta(t - t_i), \quad (10)$$

where $x_i \in \mathbb{C}$ is the complex amplitude of the i th source, $t_i = \sin \theta_i$ is its support, i.e., the corresponding DOA, on the continuous sine spectrum $\mathbb{T} = [-1, 1]$ (with $T \subset \mathbb{T}$ the set of the DOAs of all K sources) and $\delta(t)$ is the Dirac delta function.

The sound pressure received at the m th sensor is expressed as a superposition of plane waves from all possible directions on the continuous sine spectrum \mathbb{T} ,

$$y_m = \int_{-1}^1 x(t) e^{j2\pi(d/\lambda)(m-1)t} dt = \sum_{i=1}^K x_i e^{j2\pi(d/\lambda)(m-1)t_i}, \quad (11)$$

and the measurement vector of the sensor array is

$$\mathbf{y}_{M \times 1} = \mathcal{F}_M x, \quad (12)$$

where \mathcal{F}_M is a linear operator (inverse Fourier transform) which maps the continuous signal x to the observations $\mathbf{y} \in \mathbb{C}^M$.

In the presence of additive noise, $\mathbf{n} \in \mathbb{C}^M$, the measurement vector is described by

$$\mathbf{y} = \mathcal{F}_M x + \mathbf{n}, \quad (13)$$

similarly to Eq. (4).

IV. GRID-FREE SPARSE RECONSTRUCTION

To solve the underdetermined problem (12) [or equivalently problem (13)] in favor of sparse solutions, we describe an optimization procedure which promotes sparsity on a continuous optimization variable.

A. Atomic norm

In the discrete formulation (4) of the DOA estimation problem, the prior information about the sparse distribution of sources is imposed through the ℓ_1 -norm of the vector \mathbf{x} to obtain sparse estimates (9). By extension, in the continuous formulation (13), we introduce the atomic norm,¹⁶ $\|\cdot\|_{\mathcal{A}}$, as a sparsity promoting measure for the continuous signal $x(t)$ in Eq. (10) defined as

$$\|x\|_{\mathcal{A}} = \sum_{i=1}^K |x_i|. \quad (14)$$

In other words, the atomic norm is a measure for continuous signals equivalent to the ℓ_1 -norm (which is defined only on vector spaces). Hence, the atomic norm is a convex function which promotes sparsity in a general framework. For a discrete grid the atomic norm corresponds to the ℓ_1 -norm.

To clarify the analogy between the ℓ_1 -norm and the atomic norm and justify the term *atomic*, consider that the vector $\mathbf{x} \in \mathbb{C}^N$ can be interpreted as a linear combination of N unit vectors. The unit vectors, in this case, are the smallest units, or *atoms*, in which the vector \mathbf{x} can be decomposed into. The ℓ_1 -norm is the sum of the absolute values of the weights of this linear combination of atoms.²⁴

Analogously, the continuous signal (10) can be interpreted as a linear combination of K delta functions $\delta(t - t_i)$, serving as atoms for the continuous signal $x(t)$ and the atomic norm is the sum of the absolute values of the weights of the linear combination of these atoms.¹⁶ Even though there are infinitely many atoms in the continuous case, only few of those, $K < M$, constitute the signal and the sum in Eq. (14) is finite.

B. Primal problem

Utilizing the convex measure of the atomic norm, the DOA estimation in the continuous angular space is solved with the sparsity promoting minimization problem,

$$\min_x \|x\|_{\mathcal{A}} \text{ subject to } \mathbf{y} = \mathcal{F}_M x. \quad (15)$$

Since the optimization variable x is a continuous parameter, the primal problem (15) is infinite dimensional and cannot be solved as such. It is possible to approximate the continuous variable x on a discrete grid and solve the ℓ_1 -norm optimization problem (8). This would increase the computational

complexity significantly when the discretization step is reduced to improve precision. An alternative to this, is to gradually refine the discretization step.³ However, we show that by solving the dual problem instead, there is no need to employ a discrete approximation of the continuous variable, x .

C. Dual problem

To formulate the dual problem to problem (15) (see Appendix A for details), we construct the Lagrangian by making the explicit equality constraints, $\mathbf{y} = \mathcal{F}_M x$, implicit in the objective function,

$$L(x, \mathbf{c}) = \|x\|_{\mathcal{A}} + \text{Re}[\mathbf{c}^H(\mathbf{y} - \mathcal{F}_M x)], \quad (16)$$

where $\mathbf{c} \in \mathbb{C}^M$ is the vector of dual variables.

The dual function $g(\mathbf{c})$ is the infimum, i.e., the greatest lower bound, of the Lagrangian, $L(x, \mathbf{c})$, over the primal optimization variable x ,

$$\begin{aligned} g(\mathbf{c}) &= \inf_x L(x, \mathbf{c}) \\ &= \text{Re}[\mathbf{c}^H \mathbf{y}] + \inf_x (\|x\|_{\mathcal{A}} - \text{Re}[\mathbf{c}^H \mathcal{F}_M x]). \end{aligned} \quad (17)$$

To evaluate the second term in Eq. (17) we note that for every x_i , $\text{Re}[(\mathbf{c}^H \mathcal{F}_M)_i x_i] = \text{Re}[(\mathcal{F}_M^H \mathbf{c})_i^H x_i] = |(\mathcal{F}_M^H \mathbf{c})_i| |x_i| \cos \phi_i$, where ϕ_i is the angle between x_i and $(\mathcal{F}_M^H \mathbf{c})_i$. Then,

$$\begin{aligned} |x_i| - \text{Re}[(\mathcal{F}_M^H \mathbf{c})_i^H x_i] &= |x_i| [1 - |(\mathcal{F}_M^H \mathbf{c})_i| \cos \phi_i] \\ &\geq |x_i| [1 - |(\mathcal{F}_M^H \mathbf{c})_i|]. \end{aligned} \quad (18)$$

The lower bound in Eq. (18) is non-negative if $|\mathcal{F}_M^H \mathbf{c}|$ is less than one, $\max_i |(\mathcal{F}_M^H \mathbf{c})_i| \leq 1$, and the infimum is zero. Otherwise, $|x_i| [1 - |(\mathcal{F}_M^H \mathbf{c})_i|] < 0$ and the infimum is attained at $-\infty$. Hence, the dual function is

$$g(\mathbf{c}) = \begin{cases} \text{Re}[\mathbf{c}^H \mathbf{y}], & \|\mathcal{F}_M^H \mathbf{c}\|_{\infty} \leq 1 \\ -\infty, & \text{otherwise.} \end{cases} \quad (19)$$

From Eq. (18), $|x_i| [1 - |(\mathcal{F}_M^H \mathbf{c})_i| \cos \phi_i] = 0$ at the infimum, which for every $x_i \neq 0$ yields $|(\mathcal{F}_M^H \mathbf{c})_i| \cos \phi_i = 1$, i.e., $|(\mathbf{c}^H \mathcal{F}_M)_i| = 1$ and $\phi_i = 0$, as both $|(\mathbf{c}^H \mathcal{F}_M)_i| \leq 1$ and $\cos \phi_i \leq 1$. Thus, for $x_i \neq 0$, $(\mathcal{F}_M^H \hat{\mathbf{c}})_i$ is a unit vector in the direction of x_i ,

$$\begin{aligned} (\mathcal{F}_M^H \hat{\mathbf{c}})_i &= x_i / |x_i|, \quad x_i \neq 0, \\ |\mathcal{F}_M^H \hat{\mathbf{c}}_i| &< 1, \quad x_i = 0. \end{aligned} \quad (20)$$

Maximizing the dual function (19) constitutes the dual problem

$$\max_{\mathbf{c} \in \mathbb{C}^M} \text{Re}[\mathbf{c}^H \mathbf{y}] \text{ subject to } \|\mathcal{F}_M^H \mathbf{c}\|_{\infty} \leq 1. \quad (21)$$

Since the primal problem (15) is convex with linear equality constraints (A11), strong duality holds assuring that the maximum of the dual problem (21) is equal to the minimum of the primal problem.

The dual problem (21) selects a vector $\mathbf{c} \in \mathbb{C}^M$ which is maximally aligned with the measurement vector $\mathbf{y} \in \mathbb{C}^M$ while

its beamformed amplitude $|\mathcal{F}_M^H \mathbf{c}|$ is bounded by unity across the whole angular spectrum. At the angular direction corresponding to the DOA of an existing source, the beamformed dual vector (20) is equal to the normalized source amplitude.

D. Dual problem using semidefinite programming

The dual problem (21) is a semi-infinite programming problem with a finite number of optimization variables, $\mathbf{c} \in \mathbb{C}^M$, and infinitely many inequality constraints, which is still intractable.

Define the dual polynomial

$$H(z) = \mathcal{F}_M^H \mathbf{c} = \sum_{m=0}^{M-1} c_m z^m = \sum_{m=0}^{M-1} c_m e^{-j[2\pi(d/\lambda)t]m}. \quad (22)$$

Note that $\mathcal{F}_M^H \mathbf{c}$ is a trigonometric polynomial (B1), of the variable $z(t) = e^{-j2\pi(d/\lambda)t}$, $t \in \mathbb{T}$, with the dual variables $\mathbf{c} = [c_0, \dots, c_{M-1}]^T$ as coefficients and degree $M-1$.

The inequality constraint in Eq. (21) implies that the dual polynomial has amplitude uniformly bounded for all $t \in \mathbb{T}$; see Eq. (B7). Making use of the approximation in Eq. (B6) for bounded trigonometric polynomials, the constraint in Eq. (21) can be replaced with finite dimensional linear matrix inequalities. Thus, the dual problem is solved with semidefinite programming,^{23,24} i.e., a convex optimization problem where the inequality constraints are linear matrix inequalities with semidefinite matrices

$$\begin{aligned} \max_{\mathbf{c}, \mathbf{Q}} \text{Re}(\mathbf{c}^H \mathbf{y}) \text{ subject to } & \begin{bmatrix} \mathbf{Q}_{M \times M} & \mathbf{c}_{M \times 1} \\ \mathbf{c}_{1 \times M}^H & 1 \end{bmatrix} \succeq 0, \\ \sum_{i=1}^{M-j} \mathbf{Q}_{i,i+j} &= \begin{cases} 1, & j=0 \\ 0, & j=1, \dots, M-1. \end{cases} \end{aligned} \quad (23)$$

The number of optimization variables of the dual problem (23) is $(M+1)^2/2$ equal to half the number of elements of the Hermitian matrix in the inequality constraint. Thus, a problem with infinitely many unknown parameters, Eq. (15), is solved over a few optimization variables.

E. Support detection through the dual polynomial

Strong duality assures that by solving the dual problem (21), or equivalently Eq. (23), we obtain the minimum of the primal problem (15). However, the dual problem provides an optimal dual vector, $\hat{\mathbf{c}}$, but not the primal solution, \hat{x} . Since the corresponding dual polynomial, $H(z) = \mathcal{F}_M^H \hat{\mathbf{c}}$, has the properties in Eq. (20), the support \hat{T} of the primal solution \hat{x} can be estimated by locating the angular directions t_i where the amplitude of the dual polynomial is one (i.e., the angular directions at the maxima of the beamformed dual vector),

$$|H(z)| \leq 1, \quad \forall t \in \mathbb{T} \rightarrow \begin{cases} |H[z(t_i)]| = 1, & t_i \in \hat{T} \\ |H[z(t)]| < 1, & t \in \mathbb{T} \setminus \hat{T}. \end{cases} \quad (24)$$

Following Appendix B 4, this is done by locating the roots of the non-negative polynomial which lie on the unit circle $|z| = 1$ (see also Sec. VIII B),

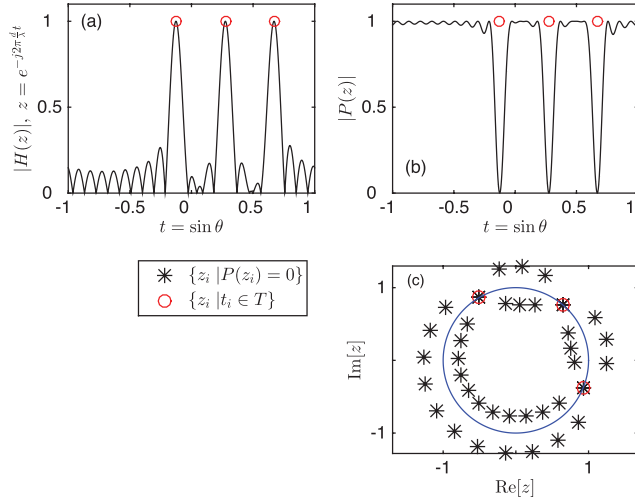


FIG. 2. (Color online) Support detection through the dual polynomial. A ULA is used with $M = 21$ sensors and $d/\lambda = 1/2$ to localize three sources with support set $T = [-0.126, 0.275, 0.67]$. (a) The dual polynomial $|H(z)|$. (b) The non-negative polynomial $P(z)$. (c) The support T is estimated by the angle of the roots, z_i , of $P(z)$ for which $|z_i| = 1$.

$$P(z) = 1 - R(z) = 1 - \sum_{m=-(M-1)}^{M-1} r_m z^m, \quad (25)$$

where $R(z) = H(z)H(z)^H = |H(z)|^2$ with coefficients $r_m = \sum_{l=0}^{M-1-m} \hat{c}_l \hat{c}_{l+m}^*$, $m \geq 0$ and $r_{-m} = r_m^*$, i.e., the autocorrelation of $\hat{\mathbf{c}}$.

Note that the polynomial of degree $2(M-1)$,

$$P_+(z) = z^{M-1}P(z) = (1 - r_0)z^{M-1} - \sum_{m=-(M-1), m \neq 0}^{M-1} r_m z^{(m+M-1)}, \quad (26)$$

which has only positive powers of the variable z , has the same roots as $P(z)$, besides the trivial root $z = 0$. Thus, the support \hat{T} of $\hat{\mathbf{x}}$, i.e., the DOAs of the sources, is recovered by locating the roots of $P_+(z)$ on the unit circle (see Fig. 2),

$$\hat{T} = \left\{ t_i = \frac{\lambda}{2\pi d} \arg z_i \mid P_+(z_i) = 0, |z_i| = 1 \right\}. \quad (27)$$

F. Reconstruction of the primal solution \mathbf{x}

Once the support is recovered by locating the roots of the polynomial in Eq. (26) that lie on the unit circle (27), the source amplitudes [the complex weights in Eq. (10)] are recovered from

$$\hat{\mathbf{x}}_{\text{CS}_{\text{dual}}} = \mathbf{A}_T^+ \mathbf{y}, \quad (28)$$

where $^+$ denotes the pseudoinverse of \mathbf{A}_T with columns $\mathbf{a}(t_i) = e^{j2\pi(d/\lambda)[0, \dots, M-1]^T t_i}$ for $t_i \in \hat{T}$.

Figure 3 shows the DOA estimation with grid-free CS following the procedure described in this section (see Appendix C for a MATLAB implementation). The dual polynomial attains unit amplitude, $|H(z)| = 1$, at the support of the

solution, i.e., the DOAs of the existing sources; see Fig. 3(a). Figure 3(b) compares the grid-free CS (28) and the CBF reconstruction in DOA estimation. The grid-free CS offers very accurate localization, while CBF is characterized by low resolution. Moreover, CBF fails to detect the weak source at 15.962° since it is totally masked by the sidelobes.

V. MAXIMUM RESOLVABLE DOAS

The maximum number of resolvable DOAs with grid-free CS is determined by the maximum number of roots of $P_+(z)$ in Eq. (26) which can be on the unit circle, $|z| = 1$. Since the coefficients of the polynomial $P_+(z)$ are conjugate symmetric around the term z^{M-1} , the roots appear in pairs at the same angular direction t_l , one inside the unit circle, $z_{\text{in}} = r_l e^{-j2\pi(d/\lambda)t_l}$ at radius $r_l < 1$, and the other outside of the unit circle $z_{\text{out}} = (1/r_l) e^{-j2\pi(d/\lambda)t_l} = 1/(z_{\text{in}})^H$. This implies that the roots on the unit circle have double multiplicity. The polynomial $P_+(z)$ has in total $2(M-1)$ roots, as determined by its degree. Hence, there are at most $M-1$ (double) roots on the unit circle.

The necessary condition for the dual polynomial (24) to satisfy the condition $|H(z)| < 1$ for some $t \in \mathbb{T}$, thus avoid the non-informative case of a constant dual polynomial, is that the number of sources should not exceed^{17,26}

$$K_{\max} = \left\lfloor \frac{M-1}{2} \right\rfloor, \quad (29)$$

where $\lfloor \cdot \rfloor$ is the largest integer not greater than the argument. In other words, at least half of the (paired) $M-1$ roots should lie off the unit circle alternating with the roots on the unit circle leading to the bound (29).

For positive source amplitudes, $x_i \in \mathbb{R}_+$, the condition (29) is sufficient and no separation condition is required for the resolvable sources.²⁶ However, for complex amplitudes, $x_i \in \mathbb{C}$, the sources are resolved uniquely only if the corresponding DOAs are separated by at least,^{17,27}

$$\min_{t_i, t_j \in \mathbb{T}} |t_i - t_j| = \frac{\lambda}{Md}, \quad (30)$$

where $|t_i - t_j|$ is a wrap-around distance meaning that we identify the points $-1, 1$, in $\mathbb{T} = [-1, 1]$.

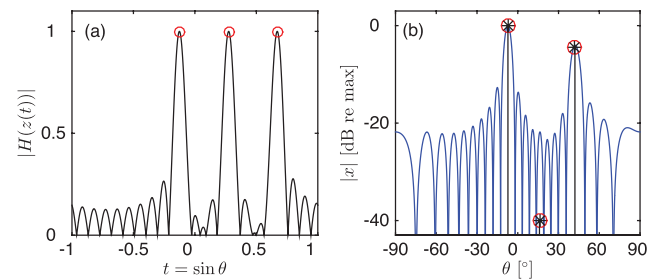


FIG. 3. (Color online) Grid-free sparse reconstruction. A standard ULA is used with $M = 21$ sensors and $d/\lambda = 1/2$ to localize three sources (\circ) at $\theta = [-7.2385^\circ, 15.962^\circ, 42.0671^\circ]$ with amplitudes $|x| = [1, 0.01, 0.6]$. (a) The dual polynomial. (b) Reconstruction with grid-free CS ($*$) and CBF.

The minimum separation condition (30) is a consequence of the coherence of the sensing process which is related to the beampattern; see Sec. IVD in Ref. 5. To guarantee a well-posed sparse signal reconstruction, it is required that the columns of the inverse Fourier operator \mathcal{F}_M , the steering vectors (1), are sufficiently uncorrelated. The continuous formulation (12) implies that adjacent steering vectors are in arbitrarily close directions, hence fully coherent. However, the requirement (30) inhibits closely spaced (i.e., highly correlated) steering vectors, hence prevents the sparse reconstruction problem from being too ill-posed due to coherence.

Figure 4 shows the reconstruction for the maximum number of sources possible. For positive source amplitudes, $x_i \in \mathbb{R}_+$, the bound (29) suffices to ensure a unique solution. Grid-free CS achieves super-resolution even for DOAs in general position; see Figs. 4(a)–4(b). Inserting an additional source at 71.81° , thus exceeding the maximum number of resolvable sources (29), results in a non-informative dual polynomial, $|H(z)| \approx 1$, for all $t \in \mathbb{T}$, Fig. 4(c), and inaccurate reconstruction where only seven out of the 11 sources are resolved, Fig. 4(d). For complex source amplitudes, $x_i \in \mathbb{C}$, an additional constraint (30) on the minimum

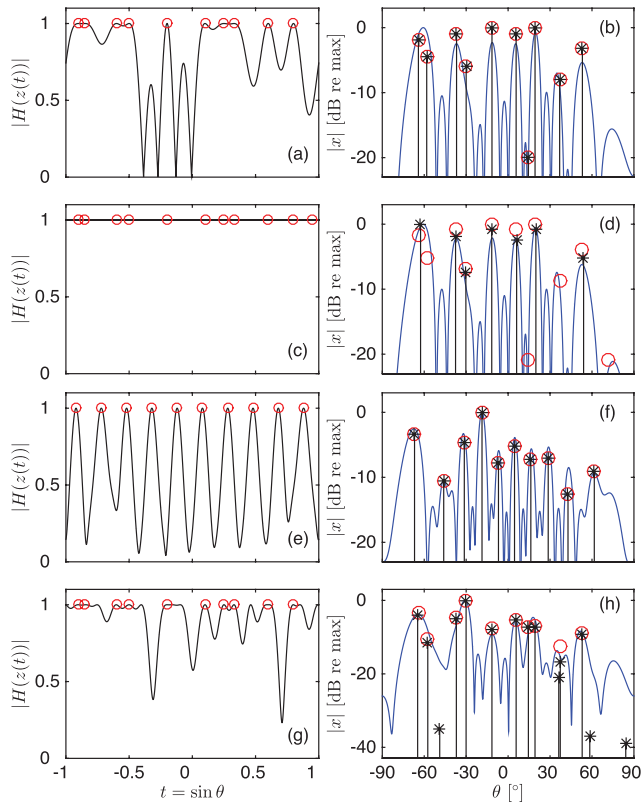


FIG. 4. (Color online) Grid-free sparse reconstruction. A ULA is used with $M = 21$ sensors and $d/\lambda = 1/2$ to localize the possible maximum number of sources (\circ), $\lfloor (M-1)/2 \rfloor = 10$. (a) The dual polynomial and (b) reconstruction with grid-free CS ($*$) and CBF for sources with positive amplitudes, $x_{10,\mathbb{R}} = [0.8, 0.6, 0.9, 0.5, 1, 0.9, 0.1, 1, 0.4, 0.7]$. (c) The dual polynomial and (d) reconstruction for 11 sources with positive amplitudes, $x_{11,\mathbb{R}} = [x_{10,\mathbb{R}}, 0.1]$. (e) The dual polynomial and (f) reconstruction for sources with complex amplitudes, $x_{10,\mathbb{C}} = x_{10,\mathbb{R}} + i[-1.6, 0.5, -1.3, -2.6, 0.4, -1.2, -1.2, -0.6, -0.5, 0.6]$, separated by the condition (30). (g) The dual polynomial and (h) reconstruction for sources with complex amplitudes, $x_{10,\mathbb{C}}$, but locations violating the condition (30).

separation of DOAs is required along with the bound on the number of sources (29) to ensure a unique solution, Figs. 4(e)–4(f). Violating the minimum separation condition, the CS DOA estimation becomes extremely ill-posed due to the coherence of the underlying steering vectors resulting in inaccurate reconstruction characterized by the presence of spurious sources, Figs. 4(g)–4(h).

VI. NON-UNIFORM ARRAYS

The method is also applicable to non-uniform arrays, constructed by randomly choosing sensors from a standard ULA configuration, by adding an additional constraint in the optimization problem (23).²⁷ The additional constraint ensures that coefficients of the dual polynomial corresponding to inactive sensors on the ULA, $c_{m_{\text{null}}}$, are annihilated.

The dual problem in a semidefinite programming formulation (23) is augmented with an additional constraint and takes the form

$$\begin{aligned} \max_{\mathbf{c}, \mathbf{Q}} \quad & \text{Re}(\mathbf{c}^H \mathbf{y}) \quad \text{subject to} \quad \begin{bmatrix} \mathbf{Q}_{M \times M} & \mathbf{c}_{M \times 1} \\ \mathbf{c}_{1 \times M}^H & 1 \end{bmatrix} \succeq 0, \\ & \sum_{i=1}^{M-j} \mathbf{Q}_{i,i+j} = \begin{cases} 1, & j=0 \\ 0, & j=1, \dots, M-1, c_{m_{\text{null}}} = 0. \end{cases} \end{aligned} \quad (31)$$

Figure 5 shows the DOA estimation with grid-free CS and compares it with the CBF reconstruction in the case of a random array. Even though CBF performance degrades significantly due to the increased sidelobe levels introduced by the random array and the strong source towards endfire, CS still offers exact reconstruction.

VII. GRID-FREE RECONSTRUCTION WITH NOISE

The problem of grid-free DOA estimation with CS extends to noisy measurements making the framework useful for practical applications. Assuming that the measurements [Eq. (13)] are contaminated with additive noise $\mathbf{n} \in \mathbb{C}^M$, such that $\|\mathbf{n}\|_2 \leq \epsilon$, the atomic norm minimization problem (15) is reformulated as²⁸

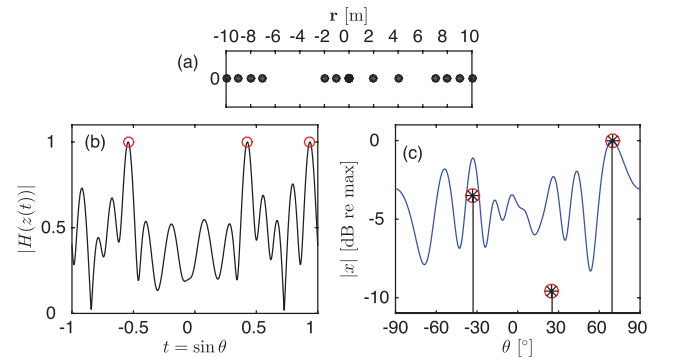


FIG. 5. (Color online) Grid-free sparse reconstruction. (a) A random array constructed by randomly selecting $M = 13$ sensors out of a standard ULA with 21 sensors and $d/\lambda = 1/2$. The sources (\circ) are at $\theta = [-32.8881^\circ, 25.2773^\circ, 69.3903^\circ]$ with amplitudes $|x| = [0.67, 0.33, 1]$. (b) The dual polynomial. (c) Reconstruction with grid-free CS ($*$) and CBF.

$$\min_x \|x\|_{\mathcal{A}} \text{ subject to } \|\mathbf{y} - \mathcal{F}_M x\|_2 \leq \epsilon. \quad (32)$$

To solve the infinite dimensional primal problem (32) we formulate the equivalent dual problem (see Appendix D)

$$\max_{\mathbf{c}} \text{Re}(\mathbf{c}^H \mathbf{y}) - \epsilon \|\mathbf{c}\|_2 \text{ subject to } \|\mathcal{F}_M^H \mathbf{c}\|_{\infty} \leq 1, \quad (33)$$

and we replace the infinite-dimensional constraints with finite matrix inequalities,

$$\begin{aligned} \max_{\mathbf{c}, \mathbf{Q}} \text{Re}(\mathbf{c}^H \mathbf{y}) - \epsilon \|\mathbf{c}\|_2 \text{ subject to } & \begin{bmatrix} \mathbf{Q}_{M \times M} & \mathbf{c}_{M \times 1} \\ \mathbf{c}_{1 \times M}^H & 1 \end{bmatrix} \succeq 0, \\ \sum_{i=1}^{M-j} \mathbf{Q}_{i,i+j} = & \begin{cases} 1, & j = 0 \\ 0, & j = 1, \dots, M-1. \end{cases} \end{aligned} \quad (34)$$

Problem (34) is a convex optimization problem which can be solved efficiently with semidefinite programming²³ to obtain an estimate for the coefficients, $\mathbf{c} \in \mathbb{C}^M$, of the dual polynomial. The support of the solution, i.e., the DOAs of the existing sources is found by locating the points where the dual polynomial has unit amplitude following the methodology in Sec. IVE. Once the support is recovered the source amplitudes are estimated by solving a discrete overdetermined problem, Eq. (28).

Figure 6 shows the DOA estimation for three sources with grid-free CS when the array measurements are contaminated with additive noise [Eq. (13)] such that SNR = 20 dB. Grid-free CS improves significantly the resolution in the reconstruction compared to CBF, even though some weak spurious sources appear as artifacts due to the noise in the measurements.

VIII. DOA ESTIMATION WITH POLYNOMIAL ROOTING

Polynomial rooting can increase performance and achieve super-resolution in several DOA estimation methods, such as the minimum variance distortionless response (MVDR) beamformer, the multiple signal classification (MUSIC) method and the minimum-norm method. All these methods involve the estimation or the eigendecomposition of the cross-spectral matrix both in their spectral and root version.

The cross-spectral matrix estimated from L snapshots (i.e., observations of \mathbf{y} at a particular frequency) is defined as

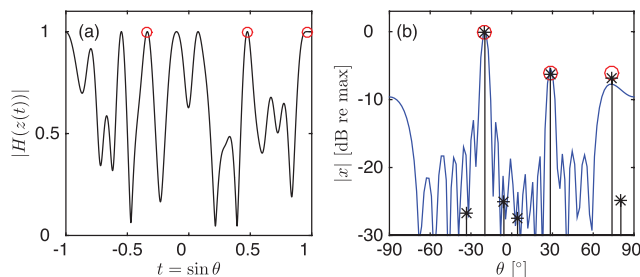


FIG. 6. (Color online) Grid-free sparse reconstruction. A ULA is used with $M = 21$ sensors and $d/\lambda = 1/2$ to localize three sources (○) at $\theta = [-19.6942^\circ, 28.3594^\circ, 73.9457^\circ]$ with amplitudes $|x| = [0.6, 0.3, 0.3]$. (a) The dual polynomial. (b) Reconstruction with grid-free CS (*) and CBF. The SNR is 20dB.

$$\hat{\mathbf{C}}_y = \frac{1}{L} \sum_{l=1}^L \mathbf{y}_l \mathbf{y}_l^H. \quad (35)$$

The eigendecomposition of the cross-spectral matrix separates the signal and the noise subspaces

$$\hat{\mathbf{C}}_y = \hat{\mathbf{U}}_s \hat{\mathbf{\Lambda}}_s \hat{\mathbf{U}}_s^H + \hat{\mathbf{U}}_n \hat{\mathbf{\Lambda}}_n \hat{\mathbf{U}}_n^H, \quad (36)$$

where $\hat{\mathbf{U}}_s$ comprises the signal eigenvectors, which correspond to the largest eigenvalues $\hat{\mathbf{\Lambda}}_s$, and $\hat{\mathbf{U}}_n$ comprises the noise eigenvectors. The signal eigenvectors are in the same subspace as the steering vectors (1), while the noise eigenvectors are orthogonal to the subspace of the steering vectors, thus $\mathbf{a}(\theta)^H \hat{\mathbf{U}}_n = \mathbf{0}$.

A. Spectral version of DOA estimation methods

MVDR (Ref. 29) aims to minimize the output power of the beamformer under the constraint that the signal from the look direction remains undistorted. The MVDR beamformer power spectrum is

$$P_{\text{MVDR}}(\theta) = \frac{1}{\mathbf{a}(\theta)^H \hat{\mathbf{C}}_y^{-1} \mathbf{a}(\theta)}. \quad (37)$$

MUSIC (Ref. 30) uses the orthogonality between the signal and the noise subspace to locate the maxima in the spectrum

$$P_{\text{MUSIC}}(\theta) = \frac{1}{\mathbf{a}(\theta)^H \hat{\mathbf{U}}_n \hat{\mathbf{U}}_n^H \mathbf{a}(\theta)}. \quad (38)$$

The minimum-norm is also an eigendecomposition based method but, unlike MUSIC which utilizes all noise eigenvectors, it uses a single vector, $\mathbf{v} = [v_0, \dots, v_{M-1}]^T$, which resides in the noise subspace [compare with the dual vector $\hat{\mathbf{c}}$ Eq. (20) which resides in the signal subspace] such that

$$\mathbf{a}(\theta_i)^H \mathbf{v} = 0, \quad i = 1, \dots, K, \quad (39)$$

where K is the number of sources.

All the noise subspace eigenvectors, i.e., the columns of $\hat{\mathbf{U}}_n$ have the property in Eq. (39). However, if the vector \mathbf{v} is chosen as a linear combination of the noise subspace eigenvectors the algorithm tends to be more robust.^{18,31,32}

The minimum-norm method selects a vector, \mathbf{v} , in the noise subspace with minimum ℓ_2 -norm and unit first element, $v_0 = 1$. The vector \mathbf{v} can be constructed from the noise eigenvectors as³¹

$$\mathbf{v} = \hat{\mathbf{U}}_n \mathbf{d}^H / \|\mathbf{d}\|_2^2, \quad (40)$$

where the vector \mathbf{d} is the first row of $\hat{\mathbf{U}}_n$. Equivalently, the vector \mathbf{v} can be constructed from the signal eigenvectors as

$$\mathbf{v} = \hat{\mathbf{U}}_s \frac{\mathbf{b}^H}{1 - \|\mathbf{b}\|_2^2}, \quad (41)$$

where the vector \mathbf{b} is the first row of $\hat{\mathbf{U}}_s$.

The minimum-norm spectrum is

$$P_{\min\text{-norm}}(\theta) = \frac{1}{\mathbf{a}(\theta)^H \mathbf{v} \mathbf{v}^H \mathbf{a}(\theta)}. \quad (42)$$

B. Root version of DOA estimation methods

The root version of the DOA estimation methods is based on the fact that for ULAs the null spectrum has the form of the trigonometric polynomial in Eq. (B2) with $\omega = 2\pi(d/\lambda) \sin \theta$ (since $\sin \theta \in [-1, 1]$, then for a standard ULA $\omega \in [-\pi, \pi]$). Thus, evaluating the spectrum is equivalent to evaluating the roots of the polynomial on the unit circle.³³

More analytically, let $N(\theta) = \mathbf{a}(\theta)^H \mathbf{\Psi} \mathbf{a}(\theta)$ be the null spectrum, such that the spectrum is $S(\theta) = N(\theta)^{-1}$. For MVDR, $\mathbf{\Psi} = \hat{\mathbf{C}}_y^{-1}$ (Ref. 18, p. 1147), for MUSIC, $\mathbf{\Psi} = \hat{\mathbf{U}}_n \hat{\mathbf{U}}_n^H$ (Ref. 18, p. 1159) and for the minimum-norm method, $\mathbf{\Psi} = \mathbf{v} \mathbf{v}^H$ (Ref. 18, p. 1163). Then

$$\begin{aligned} N(\theta) &= \sum_{m=0}^{M-1} \sum_{n=0}^{M-1} e^{-j2\pi m(d/\lambda) \sin \theta} \Psi_{mn} e^{-j2\pi n(d/\lambda) \sin \theta} \\ &= \sum_{l=-(M-1)}^{M-1} \psi_l e^{-j2\pi l(d/\lambda) \sin \theta}, \\ N(z) &= \sum_{l=-(M-1)}^{M-1} \psi_l z^{-l}, \end{aligned} \quad (43)$$

where $\psi_l = \sum_{m=-n=l} \Psi_{mn}$ is the sum of the elements of the Hermitian matrix $\mathbf{\Psi}$ along the l th diagonal and $z = e^{j2\pi(d/\lambda) \sin \theta}$.

The set of DOAs, \hat{T} , is estimated from the roots of the polynomial $N(z)$, or equivalently the polynomial $N_+(z) = z^{M-1} N(z)$, which lie on the unit circle, $z_i = e^{j \arg(z_i)}$ as

$$\hat{T} = \left\{ \sin \theta_i = \frac{\lambda}{2\pi d} \arg z_i \mid N_+(z_i) = 0, |z_i| = 1 \right\}. \quad (44)$$

After the support is recovered, the amplitudes can be estimated through an overdetermined problem as in Eq. (28).

Even though the root forms of DOA estimation methods have, often, more robust performance than the corresponding spectral forms,³⁴ they require a regular array geometry to form a trigonometric polynomial and detect its roots behavior. To achieve a robust estimate of the cross-spectral matrix many snapshots are required, $L > M$, i.e., stationary sources. Furthermore, eigendecomposition based methods fail to discern coherent arrivals. Forward/backward smoothing techniques^{35,36} can be employed to mitigate this problem and make eigendecomposition based methods suitable for identification of coherent sources as well, but they still require a regular array geometry and an increased number of sensors.

IX. EXPERIMENTAL RESULTS

The high-resolution capabilities of sparse signal reconstruction methods, i.e., CS for DOA estimation, and the robustness of grid-free sparse reconstruction even under

noisy conditions and with random array configurations are demonstrated on ocean acoustic measurements. The interest is on single-snapshot reconstruction for source tracking and the results are compared with CBF.

The data set is from the long range acoustic communications (LRAC) experiment¹⁹ recorded from 10:00–10:30 UTC on 16 September 2010 in the NE Pacific and is the same as in Ref. 5 to allow comparison of the results. The data are from a horizontal uniform linear array towed at 3.5 knots at 200 m depth. The array has $M = 64$ sensors, with intersensor spacing $d = 3$ m. The data were acquired with a sampling frequency of 2000 Hz and the record is divided in 4 s non-overlapping snapshots. Each snapshot is Fourier transformed with 2^{13} samples.

The data are post-processed with CBF and CS on a discrete DOA grid $[-90^\circ : 1^\circ : 90^\circ]$ as well as grid-free CS at frequency $f = 125$ Hz ($d/\lambda = 1/4$). To facilitate the comparison of the results, the grid-free CS reconstruction is also presented on the grid $[-90^\circ : 1^\circ : 90^\circ]$ by rounding the estimated DOAs to the closest integer angle and using the maximum power within each bin. The results are depicted in Fig. 7 both with all $M = 64$ sensors active, Figs. 7(a)–7(d) and by retaining only $M = 16$ sensors active in a non-uniform

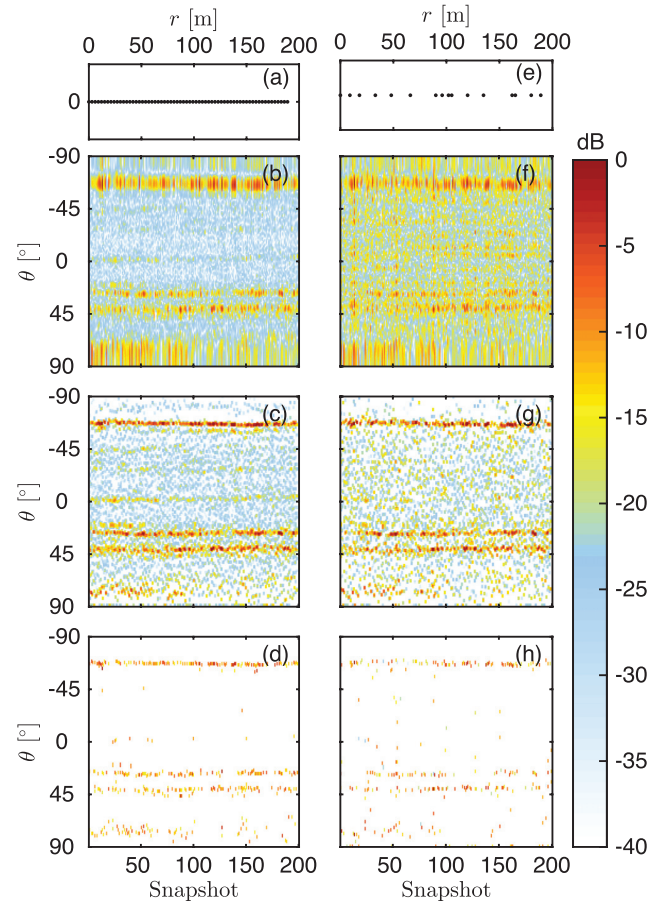


FIG. 7. (Color online) Data from LRAC. (a) Uniform array with $M = 64$ sensors and the corresponding (b) CBF, (c) CS on a discrete grid, $[-90^\circ : 1^\circ : 90^\circ]$, and (d) grid-free CS reconstruction. (e) Non-uniform array with $M = 16$ sensors and the corresponding (f) CBF, (g) CS on a discrete grid and (h) grid-free CS reconstruction.

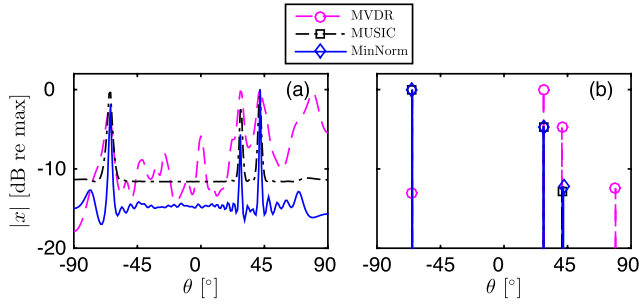


FIG. 8. (Color online) Data from LRAC, combining the 200 snapshots to estimate the cross-spectral matrix and processing with MVDR, MUSIC, and the minimum-norm method. (a) Spectral version and (b) root version. The ULA with $M = 64$ sensors and $d/\lambda = 1/4$ is used.

configuration, Figs. 7(e)–7(h). Both array configurations, Figs. 7(a) and 7(e), have the same aperture thus the same resolution.

The CBF map (6) in Fig. 7(b) indicates the presence of three stationary sources at around 45° , 30° , and -65° . The two arrivals at 45° and 30° are attributed to distant transiting ships, even though a record of ships in the area was not kept. The broad arrival at -65° is from the tow ship R/V Melville. The CBF map suffers from low resolution and artifacts due to sidelobes and noise. The CS reconstruction (9) [$\epsilon = 3.5$, Fig. 7(c)] results in improved resolution in the localization of the three sources by promoting sparsity and significant reduction of artifacts in the map. The grid-free CS solution (28), Fig. 7(d), provides high resolution and further artifact reduction due to polynomial rooting.

Retaining only $1/4$ of the sensors on the array in a non-uniform configuration degrades the resolution of CBF due to increased sidelobe levels, Fig. 7(f). However, both CS on a discrete DOA grid, Fig. 7(g), and grid-free CS, Fig. 7(h), provide high-resolution DOA estimation without a significant reconstruction degradation.

The single-snapshot processing, Fig. 7, indicates that the sources are adequately stationary. Therefore, the 200 snapshots can be combined to estimate the cross-spectral matrix (35) and employ cross-spectral methods for DOA estimation. Figure 8(a) compares the power spectra of MVDR (37), MUSIC (38), and the minimum-norm method (42) and Fig. 8(b) the corresponding root versions.

The root versions of cross-spectral methods, especially the root MUSIC and the root minimum-norm method, provide improved resolution compared to the corresponding spectral forms. However, the root cross-spectral methods require both many snapshots (i.e., stationary sources) for a robust estimate of the cross-spectral matrix and uniform arrays. Grid-free CS does not have these limitations.

X. CONCLUSION

DOA estimation with sensor arrays is a sparse signal reconstruction problem which can be solved with CS. Discretization of the problem involves a compromise between the quality of reconstruction and the computational complexity, especially for high-dimensional problems. Grid-free CS assures that the sparsity promoting optimization

problem in CS can be solved in the dual domain with semi-definite programming even when the unknowns are infinitely many. Grid-free CS achieves high-resolution DOA estimation through the polynomial rooting method.

In contrast to established DOA estimation methods, CS provides high-resolution acoustic imaging even with non-uniform array configurations and robust performance under noisy measurements and single-snapshot data. Finally, the grid-free CS has the same performance both with coherent and incoherent, stationary or moving sources while other DOA estimation methods based on polynomial rooting fail to discern coherent arrivals and have degraded resolution for moving sources as they require many snapshots.

ACKNOWLEDGMENTS

This work was supported by the Office of Naval Research, under Grant No. N00014-11-1-0320.

APPENDIX A: CONVEX OPTIMIZATION PROBLEMS

This section summarizes the basic notions and formulations encountered in convex optimization problems, as presented analytically in Ref. 24.

1. Primal problem

A generic optimization problem has the form

$$\begin{aligned} \min_{\mathbf{x}} f_0(\mathbf{x}) \\ \text{subject to } f_i(\mathbf{x}) \leq 0, \quad i = 1, \dots, m \\ h_j(\mathbf{x}) = 0, \quad j = 1, \dots, q, \end{aligned} \quad (\text{A1})$$

where $\mathbf{x} \in \mathbb{C}^N$ is the optimization variable, the function $f_0 : \mathbb{C}^N \rightarrow \mathbb{R}$ is the objective (or cost) function, the functions $f_i : \mathbb{C}^N \rightarrow \mathbb{R}$ are the inequality constraint functions and the functions $h_j : \mathbb{C}^N \rightarrow \mathbb{C}$ are the equality constraint functions. The optimization problem (A1) is convex when f_0, \dots, f_m are convex functions and h_1, \dots, h_q are affine (linear) functions.

The set of points for which the objective and all constraint functions in Eq. (A1) are defined is called the domain of the optimization problem

$$\mathcal{D} = \bigcap_{i=0}^m \text{dom } f_i \cap \bigcap_{j=1}^q \text{dom } h_j. \quad (\text{A2})$$

A point $\tilde{\mathbf{x}} \in \mathcal{D}$ is called feasible if it satisfies the constraints in Eq. (A1).

The optimal value p^* of the optimization problem (A1), achieved at the optimal variable \mathbf{x}^* , is

$$\begin{aligned} p^* &= \inf \{f_0(\mathbf{x}) \mid f_i(\mathbf{x}) \leq 0, h_j(\mathbf{x}) = 0\} \\ &= \{f_0(\mathbf{x}^*) \mid f_i(\mathbf{x}^*) \leq 0, h_j(\mathbf{x}^*) = 0\}, \end{aligned} \quad (\text{A3})$$

for all $i = 1, \dots, m$ and $j = 1, \dots, q$.

2. The Lagrangian

The Lagrangian, L , of an optimization problem is obtained by augmenting the objective function with a weighted sum of the constraint functions. The Lagrangian of the generic optimization problem (A1) is

$$L(\mathbf{x}, \boldsymbol{\lambda}, \mathbf{v}) = f_0(\mathbf{x}) + \sum_{i=1}^m \lambda_i f_i(\mathbf{x}) + \operatorname{Re} \left[\sum_{j=1}^q \nu_j h_j(\mathbf{x}) \right], \quad (\text{A4})$$

where λ_i is the Lagrange multiplier associated with the i th inequality constraint, $f_i(\mathbf{x}) \leq 0$, and ν_j is the Lagrange multiplier associated with the j th equality constraint, $h_j(\mathbf{x}) = 0$. The vectors $\boldsymbol{\lambda} \in \mathbb{R}^m$ and $\mathbf{v} \in \mathbb{C}^q$ are the dual variables of the problem (A1).

3. The dual function

The dual function of the problem (A1) is the minimum value of the Lagrangian (A5) over $\mathbf{x} \in \mathcal{D}$ for $\boldsymbol{\lambda} \in \mathbb{R}^m$ and $\mathbf{v} \in \mathbb{C}^q$,

$$g(\boldsymbol{\lambda}, \mathbf{v}) = \inf_{\mathbf{x} \in \mathcal{D}} L(\mathbf{x}, \boldsymbol{\lambda}, \mathbf{v}). \quad (\text{A5})$$

Since the dual function is the pointwise infimum of a family of affine functions of $(\boldsymbol{\lambda}, \mathbf{v})$, it is concave, even when problem (A1) is not convex.

The dual function (A5) yields lower bounds on the optimal value p^* Eq. (A3) for any $\boldsymbol{\lambda} \succeq 0$ (where \succeq represents componentwise inequality) and any \mathbf{v} ,

$$g(\boldsymbol{\lambda}, \mathbf{v}) \leq p^*, \quad (\text{A6})$$

since $g(\boldsymbol{\lambda}, \mathbf{v}) = \inf_{\mathbf{x} \in \mathcal{D}} L(\mathbf{x}, \boldsymbol{\lambda}, \mathbf{v}) \leq L(\tilde{\mathbf{x}}, \boldsymbol{\lambda}, \mathbf{v}) \leq f_0(\tilde{\mathbf{x}})$ for every feasible point $\tilde{\mathbf{x}}$.

4. Dual problem

The dual function (A5) gives a lower bound on the optimal value p^* of the optimization problem (A1), which depends on the dual variables $(\boldsymbol{\lambda}, \mathbf{v})$ with $\boldsymbol{\lambda} \succeq 0$; see Eq. (A6). The best lower bound, i.e., the lower bound with the greatest value, is obtained through the optimization problem

$$\max_{\boldsymbol{\lambda}, \mathbf{v}} g(\boldsymbol{\lambda}, \mathbf{v}) \text{ subject to } \boldsymbol{\lambda} \succeq 0, \quad (\text{A7})$$

which is the dual problem to the optimization problem (A1).

The dual problem (A7) is a convex optimization problem, since the objective function to be maximized is concave and the constraints are convex, irrespectively whether the primal problem (A1) is convex or not.

5. Weak duality

The optimal value d^* of the dual problem (A7), achieved at the dual optimal variables $(\boldsymbol{\lambda}^*, \mathbf{v}^*)$ is

$$d^* = \sup \{g(\boldsymbol{\lambda}, \mathbf{v}) \mid \boldsymbol{\lambda} \succeq 0\} = \{g(\boldsymbol{\lambda}^*, \mathbf{v}^*) \mid \boldsymbol{\lambda}^* \succeq 0\}. \quad (\text{A8})$$

The dual maximum d^* is the best lower bound on the minimum of the primal problem (A3), which can be obtained from the Lagrange dual function. The inequality

$$d^* \leq p^*, \quad (\text{A9})$$

holds even if the primal problem (A1) is non-convex and is called weak duality.

The non-negative difference $p^* - d^*$ is called the duality gap for the optimization problem (A1), since it gives the gap between the minimum of the primal problem and the maximum of the dual problem.

6. Slater's condition and strong duality

When the duality gap, $p^* - d^*$, is zero, strong duality holds characterized by the equality

$$d^* = p^*. \quad (\text{A10})$$

Strong duality holds when the optimization problem (A1) is convex and there exists a strictly feasible point, i.e., the inequality constraints hold with strict inequalities. The constraint qualification which implies strong duality for convex problems is called Slater's condition,

$$\begin{aligned} f_i(\mathbf{x}) &< 0, \quad i = 1, \dots, m, \\ \mathbf{A}_{q \times N} \mathbf{x} &= \mathbf{y}. \end{aligned} \quad (\text{A11})$$

When the primal problem is convex and Slater's condition holds there exist a dual feasible $(\boldsymbol{\lambda}^*, \mathbf{v}^*)$ such that $g(\boldsymbol{\lambda}^*, \mathbf{v}^*) = d^* = p^*$, i.e., the optimal value of the primal problem can be obtained by solving the dual problem.

The Slater's condition holds also with a weaker constraint qualification, when some of the inequality constraint functions, f_1, \dots, f_k , are affine (instead of convex)

$$\begin{aligned} f_i(\mathbf{x}) &\leq 0, \quad i = 1, \dots, k, \\ f_i(\mathbf{x}) &< 0, \quad i = k + 1, \dots, m, \\ \mathbf{A}_{q \times N} \mathbf{x} &= \mathbf{y}. \end{aligned} \quad (\text{A12})$$

The weaker constraint qualifications (A12) imply that strong duality reduces to feasibility when both the inequality and the equality constraints are linear.

7. Schur complement

Let \mathbf{X} be a square Hermitian matrix partitioned as

$$\mathbf{X} = \begin{bmatrix} \mathbf{A} & \mathbf{B} \\ \mathbf{B}^H & \mathbf{C} \end{bmatrix}, \quad (\text{A13})$$

where \mathbf{A} is also square Hermitian. If $\det \mathbf{A} \neq 0$ then the matrix

$$\mathbf{S} = \mathbf{C} - \mathbf{B}^H \mathbf{A}^{-1} \mathbf{B} \quad (\text{A14})$$

is called the Schur complement of \mathbf{A} in \mathbf{X} .

A useful property related to the Schur complement is that if $\mathbf{A} \succ 0$ then $\mathbf{X} \succeq 0$ if and only if $\mathbf{S} \succeq 0$.

APPENDIX B: BOUNDED TRIGONOMETRIC POLYNOMIALS

This section presents useful results for bounded trigonometric polynomials and their roots as presented in Ref. 37.

1. Trigonometric polynomials

Let $\mathbf{a}(\omega) = [1, e^{j\omega}, \dots, e^{j\omega(L-1)}]^T$ be a $L \times 1$ basis vector for trigonometric polynomials of degree $L-1$ with $\omega \in [-\pi, \pi]$. A (causal) trigonometric polynomial can be written in terms of the basis vector as

$$H(\omega) = \sum_{l=0}^{L-1} h_l e^{-j\omega l} = \mathbf{a}(\omega)^H \mathbf{h}, \quad (\text{B1})$$

where $\mathbf{h} = [h_0, \dots, h_{L-1}]^T \in \mathbb{C}^L$ is the vector of the polynomial coefficients.

2. Non-negative trigonometric polynomials

Let $R(\omega) = |H(\omega)|^2 = H(\omega)H(\omega)^H$. From Eq. (B1), the non-negative trigonometric polynomial $R(\omega)$ has the form

$$R(\omega) = \sum_{k=-(L-1)}^{L-1} r_k e^{-j\omega k}, \quad (\text{B2})$$

where $r_k = \sum_{l=0}^{L-1-k} h_l h_{l+k}^*$ for $k \geq 0$ and $r_{-k} = r_k^*$, i.e., the coefficients are conjugate symmetric thus $R(\omega)$ is Hermitian. Equivalently, the coefficients r_k can be calculated as the sum of the k th diagonal elements of the autocorrelation matrix $\mathbf{Q}_{L \times L} = \mathbf{h}\mathbf{h}^H$ as

$$r_k = \sum_{i=1}^{L-k} \mathbf{Q}_{i,i+k}. \quad (\text{B3})$$

3. Bounded trigonometric polynomials

Let two polynomials $H(\omega)$ and $B(\omega)$ fulfill the inequality

$$|H(\omega)| \leq |B(\omega)|, \quad \forall \omega \in [-\pi, \pi], \quad (\text{B4})$$

which implies $|H(\omega)|^2 \leq |B(\omega)|^2, \forall \omega \in [-\pi, \pi]$. Defining $R_H(\omega) = |H(\omega)|^2$ and $R_B(\omega) = |B(\omega)|^2$ as in Eq. (B2), yields $R_H(\omega) \leq R_B(\omega)$. From Lemma 4.23 in Ref. 37, $R_H(\omega) \leq R_B(\omega)$ implies $\mathbf{Q}_H \preceq \mathbf{Q}_B$, where $\mathbf{Q}_H = \mathbf{h}\mathbf{h}^H$ and $\mathbf{Q}_B = \mathbf{b}\mathbf{b}^H$ are the autocorrelation matrices of the coefficient vectors $\mathbf{h} = [h_0, \dots, h_{L-1}]^T$ and $\mathbf{b} = [b_0, \dots, b_{L-1}]^T$ of the polynomials $H(\omega)$ and $B(\omega)$, respectively. Through a Schur complement (see Appendix A 7), $\mathbf{Q}_B - \mathbf{h}\mathbf{h}^{-1}\mathbf{h}^H \succeq 0$ is equivalent to semidefinite matrix

$$\begin{bmatrix} \mathbf{Q}_B & \mathbf{h}_{L \times 1} \\ \mathbf{h}_{1 \times L}^H & 1 \end{bmatrix} \succeq 0. \quad (\text{B5})$$

Let the polynomial $H(\omega)$ have amplitude uniformly bounded for all $\omega \in [-\pi, \pi]$ such that, $|H(\omega)| \leq \gamma$, where $\gamma \in \mathbb{R}_+$ is a given positive real number. As a special case of the results for bounded trigonometric polynomials in Eqs.

(B4), (B5), with $|B(\omega)| = \gamma$, Theorem 4.24 and corollary 4.25 in Ref. 37 states that the inequality $|H(\omega)| \leq \gamma$ can be approximated by two linear matrix inequalities

$$\begin{aligned} \begin{bmatrix} \mathbf{Q}_{L \times L} & \mathbf{h}_{L \times 1} \\ \mathbf{h}_{1 \times L}^H & 1 \end{bmatrix} &\succeq 0, \\ \sum_{i=1}^{L-j} \mathbf{Q}_{i,i+j} &= \begin{cases} \gamma^2, & j = 0 \\ 0, & j = 1, \dots, L-1. \end{cases} \end{aligned} \quad (\text{B6})$$

The latter constraint follows from the autocorrelation matrix of the constant polynomial $R_B(\omega) = \gamma^2$.

The results for bounded trigonometric polynomials can be used in relation to the ℓ_∞ -norm, since setting an upper bound for the maximum amplitude of a polynomial implies that the polynomial has amplitude uniformly bounded for all $\omega \in [-\pi, \pi]$,

$$\begin{aligned} \|H\|_\infty &= \max_{\omega \in [-\pi, \pi]} |H(\omega)| \leq \gamma, \\ |H(\omega)| &\leq \gamma, \quad \forall \omega \in [-\pi, \pi]. \end{aligned} \quad (\text{B7})$$

4. Roots of real non-negative trigonometric polynomials

For a bounded trigonometric polynomial $|H(\omega)| \leq 1$, we can construct a polynomial

TABLE I. MATLAB code for Sec. IV.

Given $\mathbf{y} \in \mathbb{C}^M, d, \lambda$
Solve dual problem with CVX (Ref. 23), Eq. (23)

```
1: cvx_solver sdpt3
2: cvx_begin sdp
3:   variable S(M+1, M+1) hermitian
4:   S >= 0;
5:   S(M+1, M+1) == 1;
6:   trace(S) == 2;
7:   for j = 1 : M-1
8:     sum(diag(S, j)) == S(M+1-j, M+1);
9:   end
10:  maximize(real(S(1 : M, M+1)' * y))
11: cvx_end
12: c = S(1 : M, M+1);
```

Find the roots of P_+ , Eq. (26)

```
13: r = conv(c, flipud(conj(c)));
14: r(M) = 1 - r(M);
15: roots_P = roots(r);
```

Isolate roots on the unit circle, Eq. (27)

```
16: roots_uc = roots_P (abs(1-abs(roots_P)) < 1e-2);
17: [aux,ind] = sort(real(roots_uc));
18: roots_uc = roots_uc(ind);
19: t = angle(roots_uc(1:2:end))/(2 * pi * d / lambda);
```

Amplitude estimation, Eq. (28)

```
20: A_T = exp(1i * 2 * pi * d / lambda * [0:(M-1)]' * t');
21: x_CS_dual = A_T \ y;
```

$$P(\omega) = 1 - |H(\omega)|^2 = 1 - R(\omega), \quad (\text{B8})$$

which is by definition real-valued and non-negative, thus it cannot have single roots on the unit circle. The degree of the polynomial $P(\omega)$ is $2(L-1)$. Therefore, the polynomial $P(\omega)$ has at most $L-1$ distinct roots on the unit circle. At a root, ω_0 , we have $P(\omega_0) = 0$ and subsequently $|H(\omega_0)| = 1$.

APPENDIX C: IMPLEMENTATION IN MATLAB

The algorithm in Table I for the implementation of the method described in Sec. IV is an adaptation of the code by Fernandez-Granda in Ref. 17.

APPENDIX D: DUAL PROBLEM WITH NOISE

In the case that the measurements Eq. (13) are contaminated with additive noise $\mathbf{n} \in \mathbb{C}^M$ such that $\|\mathbf{n}\|_2 \leq \epsilon$, the primal problem of atomic norm minimization (15) is reformulated to problem (32) or equivalently

$$\min_x \|x\|_{\mathcal{A}} \text{ subject to } \begin{cases} \mathbf{y} = \mathcal{F}_M x + \mathbf{n}, \\ \|\mathbf{n}\|_2 \leq \epsilon. \end{cases} \quad (\text{D1})$$

The Lagrangian for Eq. (D1) is formulated by augmenting the objective function with a weighted sum of the constraints

$$L(x, \mathbf{c}, \xi) = \|x\|_{\mathcal{A}} + \text{Re}[\mathbf{c}^H (\mathbf{y} - \mathcal{F}_M x - \mathbf{n})] + \xi(\mathbf{n}^H \mathbf{n} - \epsilon^2), \quad (\text{D2})$$

where $\mathbf{c} \in \mathbb{C}^M$ are the dual variables related to the equality constraints, $\mathbf{y} - \mathcal{F}_M x - \mathbf{n} = 0$, and $\xi \in \mathbb{R}^+$ is a Lagrange multiplier related to the inequality constraint, $\|\mathbf{n}\|_2 - \epsilon \leq 0$.

The dual function $g(\mathbf{c}, \xi)$ is the infimum of the Lagrangian, $L(x, \mathbf{c}, \xi)$, over the optimization variable x ,

$$\begin{aligned} g(\mathbf{c}, \xi) &= \inf_x L(x, \mathbf{c}, \xi) \\ &= \text{Re}[\mathbf{c}^H \mathbf{y} - \mathbf{c}^H \mathbf{n}] + \xi(\mathbf{n}^H \mathbf{n} - \epsilon^2) \\ &\quad + \inf_x (\|x\|_{\mathcal{A}} - \text{Re}[\mathbf{c}^H \mathcal{F}_M x]). \end{aligned} \quad (\text{D3})$$

Minimizing over the unknown noise $\mathbf{n} \in \mathbb{C}^M$

$$\frac{\partial g(\mathbf{c}, \xi)}{\partial \mathbf{n}} = -\mathbf{c} + 2\xi \mathbf{n} = 0, \quad (\text{D4})$$

yields the optimal noise vector, $\mathbf{n}_0 = \mathbf{c}/(2\xi)$. The dual function evaluated at \mathbf{n}_0 is

$$\begin{aligned} g(\mathbf{c}, \xi)|_{\mathbf{n}_0} &= \text{Re}[\mathbf{c}^H \mathbf{y}] - \frac{\mathbf{c}^H \mathbf{c}}{2\xi} + \xi \left(\frac{\mathbf{c}^H \mathbf{c}}{4\xi^2} - \epsilon^2 \right) \\ &\quad + \inf_x (\|x\|_{\mathcal{A}} - \text{Re}[\mathbf{c}^H \mathcal{F}_M x]). \end{aligned} \quad (\text{D5})$$

Further, maximizing over the dual variable ξ ,

$$\frac{\partial g(\mathbf{c}, \xi)|_{\mathbf{n}_0}}{\partial \xi} = \frac{\mathbf{c}^H \mathbf{c}}{4\xi^2} - \epsilon^2 = 0, \quad (\text{D6})$$

we obtain the optimal value for the dual variable $\xi_0 = \|\mathbf{c}\|_2/(2\epsilon)$.

Finally, the dual function evaluated at the optimal values \mathbf{n}_0 and ξ_0 becomes

$$g(\mathbf{c})|_{\mathbf{n}_0, \xi_0} = \text{Re}[\mathbf{c}^H \mathbf{y}] - \epsilon \|\mathbf{c}\|_2 + \inf_x (\|x\|_{\mathcal{A}} - \text{Re}[\mathbf{c}^H \mathcal{F}_M x]), \quad (\text{D7})$$

and the dual problem is formulated by maximizing the dual function, $g(\mathbf{c})|_{\mathbf{n}_0, \xi_0}$, over the dual variables $\mathbf{c} \in \mathbb{C}^M$ similarly to the process detailed in Sec. IV C,

$$\begin{aligned} \max_{\mathbf{c}} g(\mathbf{c})|_{\mathbf{n}_0, \xi_0} &\equiv \max_{\mathbf{c}} \text{Re}[\mathbf{c}^H \mathbf{y}] - \epsilon \|\mathbf{c}\|_2 \\ \text{subject to } &\|\mathcal{F}_M^H \mathbf{c}\|_{\infty} \leq 1. \end{aligned} \quad (\text{D8})$$

¹M. Elad, *Sparse and Redundant Representations: From Theory to Applications in Signal and Image Processing* (Springer, New York, 2010), pp. 1–359.

²S. Foucart and H. Rauhut, *A Mathematical Introduction to Compressive Sensing* (Springer, New York, 2013), pp. 1–589.

³D. Malioutov, M. Çetin, and A. S. Willsky, “A sparse signal reconstruction perspective for source localization with sensor arrays,” *IEEE Trans. Signal Process.* **53**(8), 3010–3022 (2005).

⁴G. F. Edelmann and C. F. Gaumond, “Beamforming using compressive sensing,” *J. Acoust. Soc. Am.* **130**(4), 232–237 (2011).

⁵A. Xenaki, P. Gerstoft, and K. Mosegaard, “Compressive beamforming,” *J. Acoust. Soc. Am.* **136**(1), 260–271 (2014).

⁶C. F. Mecklenbräuker, P. Gerstoft, A. Panahi, and M. Viberg, “Sequential Bayesian sparse signal reconstruction using array data,” *IEEE Trans. Signal Process.* **61**(24), 6344–6354 (2013).

⁷H. Krim and M. Viberg, “Two decades of array signal processing research: The parametric approach,” *IEEE Signal Proc. Mag.* **13**(4), 67–94 (1996).

⁸W. Mantzel, J. Romberg, and K. Sabra, “Compressive matched-field processing,” *J. Acoust. Soc. Am.* **132**(1), 90–102 (2012).

⁹P. A. Forero and P. A. Baxley, “Shallow-water sparsity-cognizant source-location mapping,” *J. Acoust. Soc. Am.* **135**(6), 3483–3501 (2014).

¹⁰C. Yardim, P. Gerstoft, W. S. Hodgkiss, and J. Traer, “Compressive geoaoustic inversion using ambient noise,” *J. Acoust. Soc. Am.* **135**(3), 1245–1255 (2014).

¹¹Y. Chi, L. L. Scharf, A. Pezeshki, and A. R. Calderbank, “Sensitivity to basis mismatch in compressed sensing,” *IEEE Trans. Signal Process.* **59**(5), 2182–2195 (2011).

¹²M. F. Duarte and R. G. Baraniuk, “Spectral compressive sensing,” *Appl. Comput. Harmon. Anal.* **35**(1), 111–129 (2013).

¹³H. Yao, P. Gerstoft, P. M. Shearer, and C. Mecklenbräuker, “Compressive sensing of the Tohoku-Oki Mw 9.0 earthquake: Frequency-dependent rupture modes,” *Geophys. Res. Lett.* **38**(20), 1–5, doi:10.1029/2011GL049223 (2011).

¹⁴H. Yao, P. M. Shearer, and P. Gerstoft, “Compressive sensing of frequency-dependent seismic radiation from subduction zone megathrust ruptures,” *Proc. Natl. Acad. Sci. U.S.A.* **110**(12), 4512–4517 (2013).

¹⁵W. Fan, P. M. Shearer, and P. Gerstoft, “Kinematic earthquake rupture inversion in the frequency domain,” *Geophys. J. Int.* **199**(2), 1138–1160 (2014).

¹⁶V. Chandrasekaran, B. Recht, P. A. Parrilo, and A. S. Willsky, “The convex geometry of linear inverse problems,” *Found. Comput. Math.* **12**(6), 805–849 (2012).

¹⁷E. J. Candes and C. Fernandez-Granda, “Towards a mathematical theory of super-resolution,” *Comm. Pure Appl. Math.* **67**(6), 906–956 (2014).

¹⁸H. L. Van Trees, *Optimum Array Processing (Detection, Estimation, and Modulation Theory, Part IV)* (Wiley-Interscience, New York, 2002), Chap. 1–10.

¹⁹H. C. Song, S. Cho, T. Kang, W. S. Hodgkiss, and J. R. Preston, “Long-range acoustic communication in deep water using a towed array,” *J. Acoust. Soc. Am.* **129**(3), 71–75 (2011).

²⁰D. H. Johnson and D. E. Dudgeon, *Array Signal Processing: Concepts and Techniques* (Prentice Hall, Englewood Cliffs, NJ, 1993), pp. 1–512.

- ²¹R. G. Baraniuk, "Compressive sensing," *IEEE Signal Proc. Mag.* **24**(4), 118–121 (2007).
- ²²J. A. Tropp, "Just relax: Convex programming methods for identifying sparse signals in noise," *IEEE Trans. Inf. Theory* **52**(3), 1030–1051 (2006).
- ²³M. Grant and S. Boyd, CVX: Matlab software for disciplined convex programming, version 2.0 beta. <http://cvxr.com/cvx>, September 2013.
- ²⁴S. Boyd and L. Vandenberghe, *Convex Optimization* (Cambridge University Press, New York, 2004), pp. 1–684.
- ²⁵E. J. Candes, "The restricted isometry property and its implications for compressed sensing," *C. R. Math. Acad. Sci.* **346**(9), 589–592 (2008).
- ²⁶J. J. Fuchs, "Sparsity and uniqueness for some specific under-determined linear systems," in *IEEE International Conference on Acoustics, Speech, and Signal Processing, ICASSP'05* (IEEE, New York, 2005), Vol. 5, pp. 729–732.
- ²⁷G. Tang, B. N. Bhaskar, P. Shah, and B. Recht, "Compressed sensing off the grid," *IEEE Trans. Inf. Theory* **59**(11), 7465–7490 (2013).
- ²⁸E. J. Candes and C. Fernandez-Granda, "Super-resolution from noisy data," *J. Fourier Anal. Appl.* **19**(6), 1229–1254 (2013).
- ²⁹J. Capon, "High-resolution frequency-wavenumber spectrum analysis," *Proc. IEEE* **57**(8), 1408–1418 (1969).
- ³⁰R. Schmidt, "Multiple emitter location and signal parameter estimation," *IEEE Trans. Antennas Propag.* **34**(3), 276–280 (1986).
- ³¹R. Kumaresan and D. W. Tufts, "Estimating the angles of arrival of multiple plane waves," *IEEE Trans. Aerosp. Electron. Syst.* **19**(1), 134–139 (1983).
- ³²R. Kumaresan, "On the zeros of the linear prediction-error filter for deterministic signals," *IEEE Trans. Acoust., Speech, Signal Process.* **31**(1), 217–220 (1983).
- ³³A. Barabell, "Improving the resolution performance of eigenstructure-based direction-finding algorithms," in *IEEE International Conference on Acoustics, Speech, and Signal Processing, ICASSP'83* (IEEE, New York, 1983), Vol. 8, pp. 336–339.
- ³⁴B. D. Rao and K. V. S. Hari, "Performance analysis of root-MUSIC," *IEEE Trans. Acoust., Speech, Signal Process.* **37**(12), 1939–1949 (1989).
- ³⁵S. U. Pillai and B. H. Kwon, "Forward/backward spatial smoothing techniques for coherent signal identification," *IEEE Trans. Acoust., Speech, Signal Process.* **37**(1), 8–15 (1989).
- ³⁶B. D. Rao and K. V. S. Hari, "Effect of spatial smoothing on the performance of MUSIC and the minimum-norm method," *IEEE Proc. Radar and Signal Process.* **137**(6), 449–458 (1990).
- ³⁷B. Dumitrescu, *Positive Trigonometric Polynomials and Signal Processing Applications* (Springer, Dordrecht, Netherlands, 2007), Chap. 4.3.

Additional Papers

PAPER **F**

Single and multiple snapshot compressive beamforming

Authors:

Peter Gerstoft, Angeliki Xenaki and Christoph F. Mecklenbräuer

Submitted to:

Journal of the Acoustical Society of America, 2015.

Single and multiple snapshot compressive beamforming

Peter Gerstoft^{a)}

Scripps Institution of Oceanography, University of California San Diego, La Jolla, California 92093-0238

Angeliki Xenaki

Department of Applied Mathematics and Computer Science, Technical University of Denmark, Kgs.Lyngby, 2800 Denmark

Christoph F. Mecklenbräuer

Christian Doppler Lab, Inst. of Telecommunications, TU Wien, Gusshausstr. 25/389, 1040 Vienna, Austria

(Dated: March 8, 2015)

For a sound field observed on a sensor array, compressive sensing (CS) reconstructs the direction-of-arrivals (DOAs) of multiple sources using a sparsity constraint. The DOA estimation is posed as an underdetermined problem expressing the acoustic pressure at each sensor as a phase-lagged superposition of source amplitudes at all hypothetical DOAs. Regularizing with an ℓ_1 -norm constraint renders the problem solvable with convex optimization, while promoting sparsity resulting in high-resolution DOA maps. Here, the sparse source distribution is derived using maximum a posteriori estimates for both single and multiple snapshots. CS does not require inversion of the data covariance matrix and thus works well even for a single snapshot resulting in higher resolution than conventional beamforming. For multiple snapshots, CS outperforms conventional high-resolution methods, even with coherent arrivals and at low signal-to-noise ratio. The superior resolution of CS is demonstrated with vertical array data from the SWelEx96 experiment for coherent multi-paths.

PACS numbers: 43.60.Pt, 43.60.Jn, 43.60.Fg

I. INTRODUCTION

Direction-of-arrival (DOA) estimation refers to the localization of several sources from noisy measurements of the wavefield with an array of sensors. Thus, DOA estimation is expressible as a linear underdetermined problem with a sparsity constraint enforced on its solution. The compressive sensing^{1,2} (CS) framework asserts that this is solved efficiently with a convex optimization procedure which promotes sparse solutions.

In DOA estimation, CS achieves high-resolution acoustic imaging³⁻⁵, outperforming traditional methods⁶. Unlike the subspace DOA estimation methods^{7,8} which also offer super-resolution, DOA estimation with CS is reliable even with a single snapshot⁹⁻¹¹.

For multiple snapshots, CS has benefits over other high-resolution beamformers^{3,4}: 1) It does not require the arrivals to be incoherent. 2) It can be formulated with any number of snapshots, in contrast to, e.g., the Minimum Variance Distortion-free Response (MVDR) beamformer. 3) Its flexibility in the problem formulation enables extensions to sequential processing, and on-line algorithms¹⁰. We show here that CS obtains higher resolution than MVDR, even in scenarios which favor classical high-resolution methods.

In ocean acoustics, CS has found several applications in matched field processing^{12,13} and in coherent passive fathometry for inferring the depths of sediment interfaces and their number¹⁴. Various wave propagation phenomena from a single source (refraction, diffraction, scatter-

ing, ducting, reflection) lead to multiple partially coherent arrivals received by the array. These coherent arrivals are a problem for high-resolution beamformers.

We use least squares optimization with an ℓ_1 -norm regularization term, also known as the least absolute shrinkage and selection operator (LASSO)¹⁵, to formulate the DOA estimation problem. The LASSO formulation complies with statistical models as it provides a maximum a posteriori (MAP) estimate, assuming a Gaussian data likelihood and a Laplacian prior distribution for the source acoustic pressure^{16,17}. The LASSO is known to be a convex minimization problem and solved efficiently by interior point methods.

In the LASSO formulation, the reconstruction accuracy depends on the choice of the regularization parameter which controls the balance between the data fit and the sparsity of the solution. We indicate that the regularization parameter can be found from the properties of the LASSO path^{18,19}, i.e., the evolution of the LASSO solution versus the regularization parameter.

We address the limitations of CS which affect reconstruction quality such as basis mismatch²⁰ which occurs when the DOAs do not coincide with the look directions of the angular spectrum. Grid refinement^{3,21} alleviates basis mismatch at the expense of increased computational complexity, especially in large two-dimensional or three-dimensional geo-acoustic inversion problems as e.g. seismic imaging²²⁻²⁴. More importantly, grid refinement causes increased coherence between the steering vectors (basis coherence) which induces bias in the estimate.

^{a)}Corresponding author. Electronic mail: gerstoft@ucsd.edu

II. SINGLE SNAPSHOT DOA ESTIMATION

For simplicity, we assume plane wave propagation, i.e., the sources are in the far-field of the array, and narrowband processing with a known sound speed. Considering the one-dimensional problem with a linear array (ULA) of sensors and the sources residing in the plane of the array, the location of a source is characterized by the direction of arrival of the associated plane wave, $\theta \in [-90^\circ, 90^\circ]$, with respect to the array axis.

The propagation delay from the i th potential source to each of the M array sensors is described by the steering (or replica) vector,

$$\mathbf{a}(\theta_i) = \frac{1}{\sqrt{M}} \left[1, e^{j \frac{2\pi d}{\lambda} \sin \theta_i}, \dots, e^{j \frac{2\pi d}{\lambda} (M-1) \sin \theta_i} \right]^T, \quad (1)$$

where λ is the wavelength and d the intersensor spacing.

Discretizing the half-space of interest, $\theta \in [-90^\circ, 90^\circ]$, into N angular directions the DOA estimation problem can be expressed as a signal reconstruction problem with the linear model,

$$\mathbf{y} = \mathbf{A}\mathbf{x} + \mathbf{n}, \quad (2)$$

where $\mathbf{y} \in \mathbb{C}^M$ is the complex-valued data vector from the measurements at the M sensors, $\mathbf{x} \in \mathbb{C}^N$ is the unknown vector of the complex source amplitudes at all N directions on the angular grid of interest and $\mathbf{n} \in \mathbb{C}^M$ is the additive noise vector. The sensing matrix,

$$\mathbf{A} = [\mathbf{a}(\theta_1), \dots, \mathbf{a}(\theta_N)], \quad (3)$$

maps the signal \mathbf{x} to the observations \mathbf{y} and has as columns the steering vectors, Eq. (1), at all look directions.

The components of \mathbf{x} can be modeled as having a deterministic magnitude with uniformly random phase, or as complex Gaussian with zero mean.

In the following, the noise is generated as independent and identically distributed (iid) complex Gaussian. The array signal-to-noise ratio (SNR) is used, defined as,

$$\text{SNR} = 10 \log_{10} \frac{\mathbb{E} \{ \|\mathbf{A}\mathbf{x}\|_2^2 \}}{\mathbb{E} \{ \|\mathbf{n}\|_2^2 \}} \quad (\text{dB}). \quad (4)$$

The problem of DOA estimation is to recover the set of non-zero components in the source vector $\mathbf{x} \in \mathbb{C}^N$, given the sensing matrix $\mathbf{A}_{M \times N}$ and an observation vector $\mathbf{y} \in \mathbb{C}^M$. Even though there are only a few sources $K < M$ generating the acoustic field, we are interested in a fine resolution on the angular grid to achieve precise localization such that $M \ll N$ and the problem in Eq. (2) is underdetermined. A way to solve this ill-posed inverse problem is constraining the possible solutions with prior information.

Traditional methods solve the problem in Eq. (2) by seeking the solution with the minimum ℓ_2 -norm which provides the best data fit (ℓ_2 -norm regularized least squares),

$$\hat{\mathbf{x}}_{\ell_2}(\mu) = \arg \min_{\mathbf{x} \in \mathbb{C}^N} \|\mathbf{y} - \mathbf{A}\mathbf{x}\|_2^2 + \mu \|\mathbf{x}\|_2^2. \quad (5)$$

The regularization parameter, $\mu \geq 0$, controls the relative importance between the data fit and the ℓ_2 -norm of the solution. The minimization problem in Eq. (5) is convex with analytic solution, $\hat{\mathbf{x}}_{\ell_2}(\mu) = \mathbf{A}^H (\mathbf{A}\mathbf{A}^H + \mu \mathbf{I}_M)^{-1} \mathbf{y}$, where \mathbf{I}_M is the $M \times M$ identity matrix. However, it aims to minimize the energy of the signal through the ℓ_2 -norm regularization term rather than its sparsity, hence the resulting solution is non-sparse.

Conventional beamforming (CBF)⁷ is related to the ℓ_2 solution for large μ . From Eq. (5):

$$\hat{\mathbf{x}}_{\text{CBF}} = \lim_{\mu \rightarrow \infty} (\mu \hat{\mathbf{x}}_{\ell_2}(\mu)) = \mathbf{A}^H \mathbf{y}. \quad (6)$$

In principle, CBF combines the sensor outputs coherently to enhance the signal at a specific look direction from the ubiquitous noise. CBF is robust to noise but suffers from low resolution and the presence of sidelobes.

Since \mathbf{x} is sparse (there are only $K \ll N$ sources), it is appropriate to seek for the solution with the minimum ℓ_0 -norm, which counts the number of non-zero entries in the vector, to find a sparse solution. However, the ℓ_0 -norm minimization problem is a non-convex combinatorial problem which becomes computationally intractable even for moderate dimensions. The breakthrough of CS^{1,2} came with the proof that for sufficiently sparse signals, $K \ll N$, and sensing matrices with sufficiently incoherent columns the ℓ_0 -norm minimization problem is equivalent (at least in the noiseless case) to its convex relaxation, the ℓ_1 -norm minimization problem^{25,26}. By replacing the ℓ_0 -norm with the convex ℓ_1 -norm, the problem can be solved efficiently with convex optimization even for large dimensions^{27–29}.

For noisy measurements, Eq. (2), the ℓ_1 -norm minimization problem is formulated as

$$\hat{\mathbf{x}}_{\ell_1}(\epsilon) = \arg \min_{\mathbf{x} \in \mathbb{C}^N} \|\mathbf{x}\|_1 \text{ subject to } \|\mathbf{y} - \mathbf{A}\mathbf{x}\|_2 \leq \epsilon, \quad (7)$$

where ϵ is the noise floor. The estimate $\hat{\mathbf{x}}_{\ell_1}(\epsilon)$ has the minimum ℓ_1 -norm while it fits the data up to the noise level. The problem in Eq. (7) can be equivalently written in an unconstrained form with the use of the regularizer $\mu \geq 0$,

$$\hat{\mathbf{x}}_{\text{LASSO}}(\mu) = \arg \min_{\mathbf{x} \in \mathbb{C}^N} \|\mathbf{y} - \mathbf{A}\mathbf{x}\|_2^2 + \mu \|\mathbf{x}\|_1. \quad (8)$$

The sparse signal reconstruction problem in Eq. (8) is a least squares optimization method regularized with the ℓ_1 -norm of the solution \mathbf{x} and provides the best data fit (ℓ_2 -norm term) for the sparsity level determined by the regularization parameter μ . The optimization problem in Eq. (8) is also known as the least absolute shrinkage and selection operator (LASSO) since the ℓ_1 regularizer shrinks the coefficients of \mathbf{x} towards zero as the regularization parameter μ increases¹⁵. For every ϵ there exists a μ so that the estimates in Eq. (7) and Eq. (8) are equal.

Once the active DOAs are recovered, by solving Eq. (7) or equivalently Eq. (8), the unbiased complex source amplitudes are determined from,

$$\hat{\mathbf{x}}_{\text{CS}} = \mathbf{A}_\alpha^+ \mathbf{y}, \quad (9)$$

where $^+$ is the pseudoinverse of \mathbf{A}_α with columns solely the active steering vectors (directions of non-zero components).

III. MAP ESTIMATE VIA LASSO

We use the LASSO formulation, Eq. (8), to solve the DOA estimation problem in favor of sparse solutions. The choice of the (unconstrained) LASSO formulation over the constrained formulation, Eq. (7), allows the sparse reconstruction method to be interpreted in a statistical Bayesian setting, where the unknowns \mathbf{x} and the observations \mathbf{y} are both treated as stochastic (random) processes, by imposing a prior distribution on the solution \mathbf{x} which promotes sparsity^{15–17}.

Bayes theorem connects the posterior distribution $p(\mathbf{x}|\mathbf{y})$, of the model parameters \mathbf{x} conditioned on the data \mathbf{y} , with the data likelihood $p(\mathbf{y}|\mathbf{x})$, the prior distribution of the model parameters $p(\mathbf{x})$ and the marginal distribution of the data $p(\mathbf{y})$,

$$p(\mathbf{x}|\mathbf{y}) = \frac{p(\mathbf{y}|\mathbf{x})p(\mathbf{x})}{p(\mathbf{y})}. \quad (10)$$

Then, the maximum a posteriori (MAP) estimate is,

$$\begin{aligned} \hat{\mathbf{x}}_{\text{MAP}} &= \arg \max_{\mathbf{x}} \ln p(\mathbf{x}|\mathbf{y}) \\ &= \arg \max_{\mathbf{x}} [\ln p(\mathbf{y}|\mathbf{x}) + \ln p(\mathbf{x})] \\ &= \arg \min_{\mathbf{x}} [-\ln p(\mathbf{y}|\mathbf{x}) - \ln p(\mathbf{x})], \end{aligned} \quad (11)$$

where the marginal distribution of the data $p(\mathbf{y})$ is omitted since it is independent of the model \mathbf{x} .

Based on a complex Gaussian noise model with iid real and imaginary parts, $\mathbf{n} \sim \mathcal{CN}(\mathbf{0}, \sigma^2 \mathbf{I})$, the likelihood of the data is also complex Gaussian distributed $p(\mathbf{y}|\mathbf{x}) \sim \mathcal{CN}(\mathbf{A}\mathbf{x}, \sigma^2 \mathbf{I})$,

$$p(\mathbf{y}|\mathbf{x}) \propto e^{-\frac{\|\mathbf{y} - \mathbf{A}\mathbf{x}\|_2^2}{\sigma^2}}. \quad (12)$$

Following³⁰, we assume that the coefficients of the solution \mathbf{x} are iid and follow a Laplacian-like distribution (for complex random variables). The corresponding prior is

$$p(\mathbf{x}) \propto \prod_{i=1}^N e^{-\frac{\sqrt{(\text{Re } x_i)^2 + (\text{Im } x_i)^2}}{\nu}} = e^{-\frac{\|\mathbf{x}\|_1}{\nu}}. \quad (13)$$

The LASSO estimate, Eq. (8), can be interpreted as the maximum a posteriori (MAP) estimate,

$$\hat{\mathbf{x}}_{\text{MAP}} = \arg \min_{\mathbf{x}} [\|\mathbf{y} - \mathbf{A}\mathbf{x}\|_2^2 + \mu \|\mathbf{x}\|_1] = \hat{\mathbf{x}}_{\text{LASSO}}(\mu), \quad (14)$$

where $\mu = \sigma^2/\nu$. The Laplacian-like prior distribution encourages sparse solutions since it concentrates more mass near 0 and in the tails.

IV. MULTIPLE-APSHOT DOA ESTIMATION

Even though for moving sources it befits to solve one optimization problem for each snapshot sequentially, for stationary scenarios, the sensor data statistics can be aggregated across snapshots to provide a more stable estimate. In the multiple-snapshot scenario,

$$\mathbf{Y} = \mathbf{A}\mathbf{X} + \mathbf{N}, \quad (15)$$

where, for L snapshots, $\mathbf{Y} = [\mathbf{y}(1), \dots, \mathbf{y}(L)]$ and $\mathbf{N} = [\mathbf{n}(1), \dots, \mathbf{n}(L)]$ are $M \times L$ matrices with the measurement and noise vectors per snapshot as columns, respectively, and \mathbf{X} is the $N \times L$ signal with the complex source amplitudes at the N DOAs per snapshot as columns. For stationary sources the matrix $\mathbf{X} = [\mathbf{x}(1), \dots, \mathbf{x}(L)]$ exhibits row sparsity, i.e., it has a constant sparsity profile for every column, since the few existing sources are associated with the same DOA for all snapshots.

The multiple-snapshot LASSO problem³¹ can be derived from Bayes theorem by imposing a Laplacian-like prior on the ℓ_2 -norm of each row of the matrix \mathbf{X} , $p(\mathbf{x}^{\ell_2}) \propto \exp(-\|\mathbf{x}^{\ell_2}\|_1/\nu)$, Ref.3, and assuming an iid complex Gaussian distribution for the data likelihood $p(\mathbf{Y}|\mathbf{X}) \propto \exp(-\|\mathbf{Y} - \mathbf{A}\mathbf{X}\|_{\mathcal{F}}^2/\sigma^2)$,

$$\begin{aligned} \hat{\mathbf{X}} &= \arg \max_{\mathbf{X}} p(\mathbf{Y}|\mathbf{X})p(\mathbf{X}) \\ &= \arg \min_{\mathbf{X} \in \mathbb{C}^{N \times L}} \|\mathbf{Y} - \mathbf{A}\mathbf{X}\|_{\mathcal{F}}^2 + \mu \|\mathbf{x}^{\ell_2}\|_1. \end{aligned} \quad (16)$$

where the Frobenius norm $\|\cdot\|_{\mathcal{F}}$ for a matrix $\mathbf{F} \in \mathbb{C}^{M \times L}$ is defined as $\|\mathbf{F}\|_{\mathcal{F}}^2 = \sum_{i=1}^M \sum_{j=1}^L |f_{i,j}|^2$ and the regularizer \mathbf{x}^{ℓ_2} is the vector obtained from the ℓ_2 -norm of the rows of the matrix \mathbf{X} . The processing performance can be improved by doing an eigenvalue decomposition of \mathbf{X} and retaining just the largest signal eigenvalues; see Refs.3, 4. The smaller eigenvalues contain mostly noise so this improves processing. However, this eigenvalue decomposition is not done here as this has features similar to forming a sample covariance matrix.

Once the active steering vectors have been recovered, the unbiased source amplitudes are estimated for each snapshot, similar to the single snapshot case, Eq. (9),

$$\hat{\mathbf{X}}_{\text{CS}} = \mathbf{A}_\alpha^+ \mathbf{Y}, \quad (17)$$

If desired, an average power estimate $\mathbf{x}_{\text{CS}}^{\ell_2}$ can be obtained from the ℓ_2 -norm of the rows of $\hat{\mathbf{X}}_{\text{CS}}$, with the i th element squared of $\mathbf{x}_{\text{CS}}^{\ell_2}$ being the source power estimate at θ_i .

For reference, the CBF and MVDR use the data sample covariance matrix,

$$\mathbf{C} = \frac{1}{L} \mathbf{Y}\mathbf{Y}^H. \quad (18)$$

The beamformer power for CBF and MVDR respectively is then,

$$P_{\text{CBF}}(\theta) = \mathbf{w}_{\text{CBF}}^H(\theta) \mathbf{C} \mathbf{w}_{\text{CBF}}(\theta) \quad (19)$$

$$P_{\text{MVDR}}(\theta) = \mathbf{w}_{\text{MVDR}}^H(\theta) \mathbf{C} \mathbf{w}_{\text{MVDR}}(\theta), \quad (20)$$

where the corresponding weight vectors are given by,

$$\mathbf{w}_{\text{CBF}}(\theta) = \mathbf{a}(\theta) \quad (21)$$

$$\mathbf{w}_{\text{MVDR}}(\theta) = \frac{\mathbf{C}^{-1}\mathbf{a}(\theta)}{\mathbf{a}^H(\theta)\mathbf{C}^{-1}\mathbf{a}(\theta)}. \quad (22)$$

The power estimates $P_{\text{CBF}}(\theta_i)$, $P_{\text{MVDR}}(\theta_i)$, and the corresponding i th squared component of $\mathbf{x}_{\text{CS}}^{\ell_2}$ are thus comparable. Note that since the MVDR weights in Eq. (22) involve the inverse of the sample covariance matrix, MVDR requires a full rank \mathbf{C} , i.e., $L \geq M$ snapshots.

V. REGULARIZATION PARAMETER SELECTION

The choice of the regularization parameter μ in Eq. (8), also called the LASSO shrinkage parameter, is crucial as it controls the balance between the sparsity of the estimated solution and the data fit determining the quality of the reconstruction.

For large μ , the solution is very sparse (with small ℓ_1 -norm) but the data fit is poor. As μ decreases towards zero, the data fit is gradually improved since the corresponding solutions become less sparse. Note that for $\mu = 0$ the solution in Eq. (8) becomes the unconstrained least squares solution.

A. The LASSO path

As the regularization parameter μ evolves from ∞ to 0, the LASSO solution in Eq. (8) changes continuously following a piecewise smooth trajectory referred to as the solution path or the LASSO path^{18,19}. In this section, we show that the singularity points in the LASSO path are associated with a change in the sparsity of the solution and can be used to indicate an adequate choice for μ .

We obtain the full solution path using convex optimization to solve Eq. (8) iteratively for different values of μ . We use the cvx toolbox for disciplined convex optimization which is available in the Matlab environment. It uses interior point solvers to obtain the global solution of a well-defined optimization problem²⁷⁻²⁹.

Let $L(\mathbf{x}, \mu)$ denote the objective function in Eq. (8),

$$L(\mathbf{x}, \mu) = \|\mathbf{y} - \mathbf{A}\mathbf{x}\|_2^2 + \mu\|\mathbf{x}\|_1. \quad (23)$$

The value $\hat{\mathbf{x}}$ minimizing Eq. (23) is found from its subderivative,

$$\partial_{\mathbf{x}}L(\mathbf{x}, \mu) = 2\mathbf{A}^H(\mathbf{A}\mathbf{x} - \mathbf{y}) + \mu\partial_{\mathbf{x}}\|\mathbf{x}\|_1, \quad (24)$$

where the subdifferential operator $\partial_{\mathbf{x}}$ is a generalization of the partial differential operator for functions that are not differentiable everywhere (Ref.29 p.338). The subgradient for the ℓ_1 -norm is the set of vectors,

$$\partial_{\mathbf{x}}\|\mathbf{x}\|_1 = \{\mathbf{s} : \|\mathbf{s}\|_{\infty} \leq 1, \mathbf{s}^H\mathbf{x} = \|\mathbf{x}\|_1\}, \quad (25)$$

which implies,

$$\begin{aligned} s_i &= \frac{x_i}{|x_i|}, & x_i &\neq 0 \\ |s_i| &\leq 1, & x_i &= 0, \end{aligned} \quad (26)$$

i.e., for every active element $x_i \neq 0$ of the vector $\mathbf{x} \in \mathbb{C}^N$, the corresponding element of the subgradient is a unit vector in the direction of x_i . For every null element $x_i = 0$ the corresponding element of the subgradient has magnitude less than or equal to one. Thus, the magnitude of the subgradient is uniformly bounded by unity, $\|\mathbf{s}\|_{\infty} \leq 1$.

Denote,

$$\mathbf{r} = 2\mathbf{A}^H(\mathbf{y} - \mathbf{A}\hat{\mathbf{x}}), \quad (27)$$

the beamformed residual vector for the estimated solution $\hat{\mathbf{x}}$. Since Eq. (23) is convex, the global minimum is attained if $\mathbf{0} \in \partial_{\mathbf{x}}L(\mathbf{x}, \mu)$ which leads to the necessary and sufficient condition

$$\mu^{-1}\mathbf{r} \in \partial_{\mathbf{x}}\|\mathbf{x}\|_1. \quad (28)$$

Then, from Eq. (26) and Eq. (28), the coefficients $r_i = 2\mathbf{a}_i^H(\mathbf{y} - \mathbf{A}\hat{\mathbf{x}})$ of the beamformed residual vector $\mathbf{r} \in \mathbb{C}^N$ have amplitude such that,

$$\begin{aligned} |r_i| &= \mu, & \hat{x}_i &\neq 0 \\ |r_i| &\leq \mu, & \hat{x}_i &= 0, \end{aligned} \quad (29)$$

i.e., whenever a component of $\hat{\mathbf{x}}$ becomes non-zero, the corresponding element of the beamformed residual hits the boundary identified with the regularization parameter, $\|\mathbf{r}\|_{\infty} \leq \mu$.

The above is used for formulating a solution procedure where the values of μ for different sparsity levels are indicated by the dual solution \mathbf{r} , solving the dual problem³². For large μ , the solution $\hat{\mathbf{x}} = \mathbf{0}$ is trivial and $\mathbf{r} = 2\mathbf{A}^H\mathbf{y}$ in Eq. (27). Decreasing μ , a first component of \mathbf{x} becomes active when the corresponding component of \mathbf{r} hits the boundary, $\mu = 2|\mathbf{A}^H\mathbf{y}|$. Inserting this solution into Eq. (27) gradually indicates the value of μ for which a second component becomes active. This way we follow the LASSO path towards less sparse solutions and lower μ as detailed in Ref. 32.

For multiple snapshots, the beamformed residuals become

$$\mathbf{R} = 2\mathbf{A}^H(\mathbf{Y} - \mathbf{A}\hat{\mathbf{X}}), \quad \mathbf{r}_i = \sqrt{\sum_{j=1}^L |\mathbf{R}_{ij}|^2}. \quad (30)$$

The values of μ when changes in sparsity appear are obtained similarly to the single snapshot case.

The dual method has been used to estimate the solution path of the real-valued¹⁸ and the complex-valued³² generalized LASSO problems. The generalized LASSO uses the ℓ_1 -norm to enforce structural or geometric constraints on the solution by replacing the sparsity constraint $\|\mathbf{x}\|_1$ with $\|\mathbf{D}\mathbf{x}\|_1$ for a structured matrix \mathbf{D} . The generalized formulation performs well in certain applications, e.g., recovery of continuous sources by promoting block sparsity³³ and DOA tracking for moving sources by an adaptive update of a diagonal weighting matrix \mathbf{D} which reflects the evolution of the source probability distribution¹⁰.

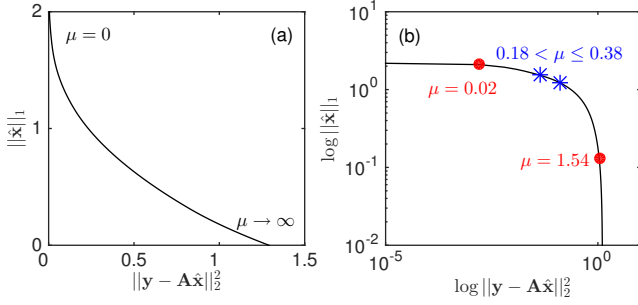


FIG. 1. (Color online) The data error $\|\mathbf{y} - \mathbf{A}\hat{\mathbf{x}}\|_2^2$, describing the goodness of fit, versus the ℓ_1 -norm in (a) linear scale and (b) log-log scale for the estimated solution $\hat{\mathbf{x}}$ for different values of the regularization parameter μ in the LASSO problem Eq. (8) for sparse DOA estimation.

B. Regularization parameter selection via the LASSO path

The LASSO performance in DOA estimation is evaluated by simulations starting with a large μ and subsequently decreasing its value. We consider a uniform linear array (ULA) with $M = 20$ omnidirectional sensors and intersensor spacing $d = \lambda/2$. Three sources are simulated at DOAs $[-5, 0, 20]^\circ$ with corresponding magnitudes $[1, 0.6, 0.2]$. The sensing matrix \mathbf{A} in (3) is defined on the coarse angular grid $[-90^\circ:5^\circ:90^\circ]$. The noise variance in (4) is chosen such that SNR=20 dB.

The trade-off between regularization term $\|\hat{\mathbf{x}}\|_1$ and the data fit $\|\mathbf{y} - \mathbf{A}\hat{\mathbf{x}}\|_2^2$ in the LASSO estimate, Eq. (8), for a range of values of μ is depicted in Fig. 1. The relevant values of μ for the LASSO path are found between the two dots in Fig. 1(b), i.e. $1.54 > \mu > 0.02$. For these values of μ , the importance shifts from favoring sparser solutions for large μ towards diminishing the model residual's ℓ_2 -norm for smaller μ . From inspecting Fig. 1(b), it is difficult inferring the value of μ which results in the desired sparsity level. The LASSO path offers a more insightful method to determine the range of good values of μ (contained within the asterisks in Fig. 1(b)) as explained below.

Figure 2 shows (a) the sparsity level $\|\hat{\mathbf{x}}\|_0$ of the LASSO solution, (b) the properties of the LASSO path and (c) the corresponding residual vector versus the regularization parameter μ . Since the interest is on sparse solutions $\hat{\mathbf{x}}$, it is natural inspecting the LASSO path for decreasing values of μ , i.e., interpreting Fig. 2 from right to left.

For large values of μ (e.g., $\mu = 2$) the problem in Eq. (8) is over-regularized, forcing the trivial solution $\hat{\mathbf{x}} = \mathbf{0}$ (Fig. 2(b)), thus $\|\hat{\mathbf{x}}\|_0 = 0$ (Fig. 2(a)). In this case, the slopes for all components $|r_i|$ are zero (Fig. 2(c)) since $|r_i| = |2\mathbf{a}_i^H \mathbf{y}| < \mu$ for all $i \in [0, \dots, N]$ which is independent of μ .

The first non-zero component of $\hat{\mathbf{x}}$ appears at $\mu = \max_i |2\mathbf{a}_i^H \mathbf{y}| = 1.76$ and remains active for $\mu \leq 1.76$ (Fig. 2(b)) increasing the sparsity level to $\|\hat{\mathbf{x}}\|_0 = 1$ (Fig. 2(a)). The corresponding component $|r_i| = |2\mathbf{a}_i^H (\mathbf{y} - \mathbf{a}_i \hat{x}_i)|$ (Fig. 2(c)) is equal to μ for $\mu \leq 1.76$.

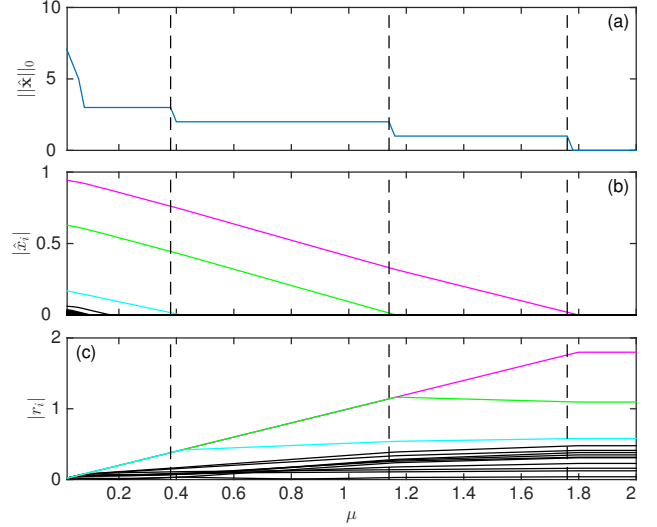


FIG. 2. (Color online) The LASSO path versus μ for three sources and SNR=20 dB. (a) Sparsity level of the estimate $\hat{\mathbf{x}}$. (b) Paths for each component of the solution $\hat{\mathbf{x}}$. (c) Paths for each component of the beamformed residual $|\mathbf{r}| = 2|\mathbf{A}^H (\mathbf{y} - \mathbf{A}\hat{\mathbf{x}})|$.

The other components r_j change slope at the singular point $\mu = 1.76$, since now $|r_j| = |2\mathbf{a}_j^H (\mathbf{y} - \mathbf{a}_i \hat{x}_i)| < \mu$ for all $j \in [0, \dots, N]$, $j \neq i$. For $\mu \leq 1.14$, $\|\hat{\mathbf{x}}\|_0 = 2$ (Fig. 2(a)) as $\hat{\mathbf{x}}$ acquires a second non-zero component (Fig. 2(b)) and the corresponding component $|r_i|$ becomes equal to μ (Fig. 2(c)). Similarly, the estimated solution has a third non-zero component for $\mu \leq 0.38$.

For $\mu \leq 0.18$, $\hat{\mathbf{x}}$ has many non-zero components (Figs. 2(b),(c)) and its sparsity level increases abruptly (Fig. 2(a)). For such low values of μ the importance shifts to the data fitting term (ℓ_2 -norm term) in the regularized problem, Eq. (8), and $\hat{\mathbf{x}}$ includes many non-zero noisy components gradually reducing the data error.

The specific values of μ at which an element of $\hat{\mathbf{x}}$ becomes active are denoted as the singular points in the piecewise smooth LASSO path. At a singular point, some component of \mathbf{r} hits the boundary μ , i.e. $|r_n| = \mu$ for some index n . Thus, the properties of the LASSO path indicate the selection of the regularization parameter μ . For example, for a predefined sparsity level K a good choice of μ is found by decreasing μ until the K th singular point at the LASSO path.

Owing to the piecewise smooth nature of the LASSO path, there is a range of μ which give the same sparsity level (i.e., between two singular points). In principle, the lowest μ in this range is desired as it gives the best data fit. Though, any value of μ which achieves the desired sparsity suffices as once the active DOAs are recovered, the unbiased amplitudes are determined from Eq. (9).

Figure 3 shows the unbiased solution, Eq. (9), along with the corresponding beamformed residual for 4 sparsity levels or values of μ .

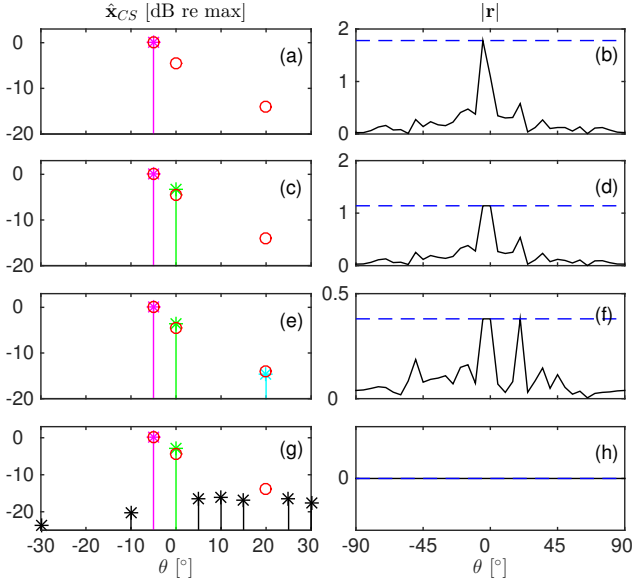


FIG. 3. (Color online) The unbiased estimate $\hat{\mathbf{x}}_{CS}$ (\star) for the signal \mathbf{x} (o) and the corresponding beamformed residual vector for (a)–(b) $\mu = 1.76$, (c)–(d) $\mu = 1.14$, (e)–(f) $\mu = 0.38$, and (g)–(h) $\mu = 0$ (corresponding to dashed lines in Fig. 2),

VI. BASIS MISMATCH AND COHERENCE

A. Reconstruction under basis mismatch

In Sec. V.B, the LASSO path is numerically evaluated on a coarse angular grid and the solution vector has only $N = 37$ components. In this case, the 5° grid spacing suffices for the signal \mathbf{x} to appear sparse in the selected DFT basis, Eq. (3), since the DOAs at $[-5, 0, 20]^\circ$ coincide with angular grid points.

When the DOAs do not coincide with angular grid points, \mathbf{x} may not appear sparse in the selected DFT basis. In this case, basis mismatch^{20,21} between the assumed sensing matrix, Eq. (3), and the actual DOAs degrades the performance of the LASSO reconstruction.

The LASSO path under basis mismatch is demonstrated in Fig. 4(a) for the setting in Sec. V.B by dislocating the DOA -5° to -3° (“off-grid”) while retaining the coarse grid with spacing 5° . Interpreting Fig. 4(a) for decreasing values of μ (leftwards), the first non-zero component \hat{x}_i appears for $\mu \leq 1.8$ (Fig. 4(a)) which corresponds to the component at 0° DOA, Fig. 4(b). The corresponding component of the residual hits the boundary line at $\mu = 1.8$, Fig. 4(c). The maximum of the residual $\mu = \max|2\mathbf{A}^H\mathbf{y}| = 1.8$ occurs at a different direction than in Fig. 3 due to the off-grid source at -3° . At $\mu = 1.62$, the estimate acquires a second active component (Fig. 4(a)) at -5° , Figs. 4(d)–(e), approximating the actual source at -3° on the coarse grid. At $\mu = 0.34$, two components become active simultaneously (Fig. 4(a)), one corresponding to the source at 20° and the other corresponding to an artifact at -10° due to the off-grid source at -3° , Figs. 4(f)–(g). Thus, the LASSO reconstruction is inaccurate under basis mismatch.

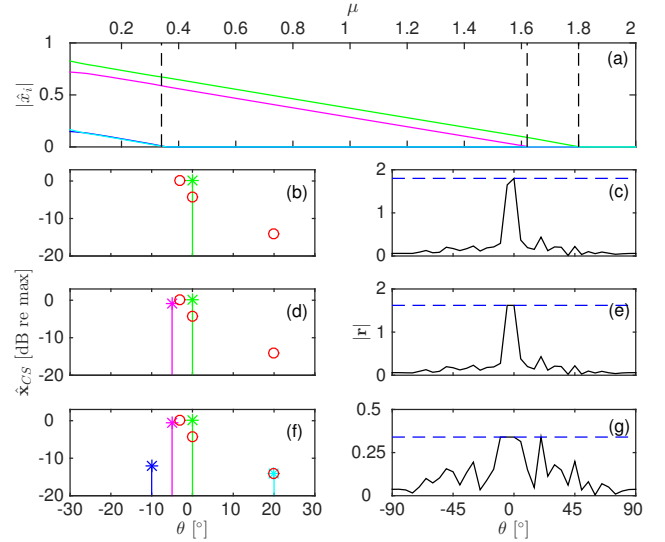


FIG. 4. (Color online) The LASSO path versus regularization parameter μ for $K = 3$ sources at $[-3, 0, 20]^\circ$ with magnitudes $[1, 0.6, 0.2]$ on the coarse angular grid with a ULA with $M = 20$ sensors and intersensor spacing $d = \lambda/2$ and SNR = 20 dB. (a) Paths for each component of the solution, $\hat{\mathbf{x}}$. The unbiased estimate $\hat{\mathbf{x}}_{CS}$ (\star), true signal (o), and the corresponding residual vector \mathbf{r} for (b)–(c) $\mu = 1.8$, (d)–(e) $\mu = 1.62$, and (f)–(g) $\mu = 0.34$ (indicated with dashed lines).

B. Bias due to basis coherence

To overcome basis mismatch and increase precision in the LASSO reconstruction, a finer angular grid is required. However, angular grid refinement also causes higher coherence among steering vectors, Eq. (1), and the problem in Eq. (2) becomes increasingly underdetermined. Then, numerical difficulties when solving the LASSO minimization, Eq. (8), may cause significant loss of accuracy and the numerical solution might not exhibit the desired sparsity. Further, this allows the numerical solution path to be discontinuous with respect to μ . For smaller μ , components in the estimate $\hat{\mathbf{x}}$ can be either activated (become non-zero) or annihilated and the residual components can hit the boundary, or leave the boundary¹⁸.

This is shown in Fig. 5 for a refined angular grid with spacing 1° to avoid basis mismatch. For $\mu > 1.68$, there is an active component (Fig. 5(a)) at -2° which is a spurious DOA (instead of the actual at -3°) and is annihilated for $\mu \leq 0.88$. For $\mu \leq 1.68$, a second component becomes activate (Fig. 5(a)) corresponding to the DOA at -3° ; see Figs. 5(b)–(c). At $\mu = 0.98$, a third component becomes active corresponding to a noise artifact at -1° , Figs. 5(d)–(e), and is annihilated for $\mu \leq 0.66$. At $\mu = 0.84$, the component at 0° becomes active (Fig. 5(a)) while the spurious component at -2° has been annihilated, Figs. 5(f)–(g). Further decreasing μ , a spurious component at -4° appears for $\mu \leq 0.62$ and at $\mu = 0.38$ a component at 21° is activated (Fig. 5(a)) resulting in a more accurate DOA estimate, Figs. 5(h)–(i). For $\mu \leq 0.38$ all four components at $[-4, -3, 0, 21]^\circ$ remain

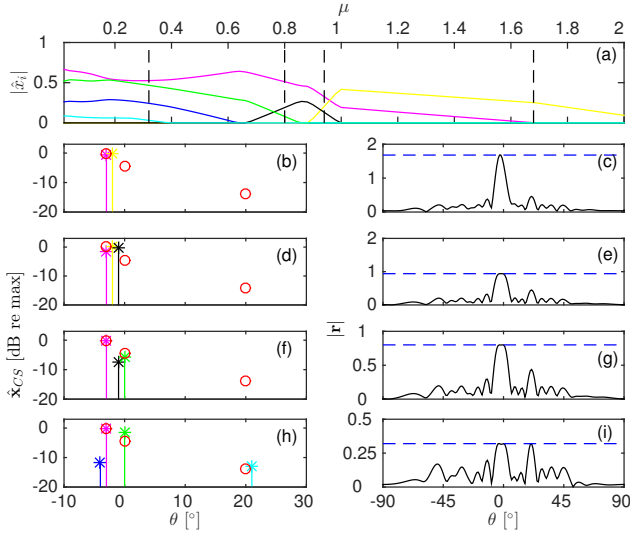


FIG. 5. (Color online) The LASSO path with the configuration as in Fig. 4 but for the refined angular grid $[-90:1:90]^\circ$ which resolves basis mismatch but introduces increased ambiguity in the solution. (b)–(c) $\mu = 1.68$, (d)–(e) $\mu = 0.94$, (f)–(g) $\mu = 0.8$ and (h)–(i) $\mu = 0.32$.

active, while other noisy components become active contributing to the estimated solution for $\mu \leq 0.26$ (omitted in Fig. 5).

Consequently, improved precision from angular grid refinement comes at the expense of increased basis coherence which causes bias in the estimates (cf. the source at 21° instead of the true DOA at 20° in Fig. 5(h)) and noisy artifacts depending on the noise realization (cf. the spurious source at -4° in Fig. 5(h)).

VII. DOA ESTIMATION ERROR EVALUATION

If the source DOAs are well separated with not too different magnitude, the DOA estimation for multiple sources using CBF and CS turns out to behave similarly. They differ, however, in their behavior whenever two sources are closely spaced. The same applies for MVDR under the additional assumptions of incoherent arrivals and sufficient number of snapshots, $L \geq M$. The details are of course scenario dependent.

For the purpose of a quantitative performance evaluation with synthetic data, the estimated, $\hat{\theta}_k$, and the true, θ_k^{true} , DOAs are paired with each other such that the root mean squared DOA error is minimized in each single realization. After this pairing, the ensemble root mean squared error is computed,

$$\text{RMSE} = \sqrt{\mathbb{E} \left[\frac{1}{K} \sum_{k=1}^K (\hat{\theta}_k - \theta_k^{\text{true}})^2 \right]}. \quad (31)$$

CBF suffers from low-resolution and the effect of sidelobes for both single and multiple data snapshots, thus the simple peak search used here is too simple. These

problems are reduced in MVDR for multiple snapshots and they do not arise with CS,

In the following simulation study, we consider an array with $M = 20$ elements and intersensor spacing $d = \lambda/2$. The DOAs for plane wave arrivals are assumed to be on a fine angular grid $[-90^\circ:0.5^\circ:90^\circ]$. The regularization parameter μ is chosen to correspond to the K th largest peak of the residual in Eq. (27) using the procedure in Sec V.A. Note that panel c in Figs. 6–9 shows the simulation results versus array SNR defined in Eq. (4).

A. Single Snapshot

In the first scenario, we consider a single snapshot case with additive noise with $K = 2$ well-separated DOAs at $[2, 75]^\circ$ with magnitudes $[13, 10]$, see Fig. 6. A third weak source is included in the second scenario very close to the first source: Thus, $K = 3$ and the source DOAs are $[-3, 2, 75]^\circ$ with magnitudes $[4, 13, 10]$, see Fig. 7. The synthetic data is generated according to Eq. (2).

For the first scenario, the CS diagrams in Fig. 6a show DOA estimation with small variance but indicate a bias towards endfire, as for the true DOA 75° the CS estimate is 76° . Towards endfire the main beam becomes broader and absorbs more noise power. The CBF spectra Fig. 6a are characterized by a high sidelobe level but for the two well-separated similar-magnitude sources this is a minor problem. Nevertheless, this indicates in which way the CBF performance is fragile.

Using Monte Carlo simulations, we repeat the CS inversion for 1000 realizations of the noise in Fig. 6b. The RMSE increases towards the endfire directions. This is to be expected as the main beam becomes wider and this results in a lower DOA resolution⁴. Since the sources are well-separated in this scenario, CS and CBF perform similarly with respect to RMSE.

Repeating the Monte Carlo simulations at several SNRs gives the RMSE performance of CS and CBF in Fig. 6b. Their performance is about the same since the DOAs are well-separated.

In the second scenario, the CBF cannot resolve the two closely spaced sources with DOAs $[-3, 2]^\circ$. They are less than a beamwidth apart as indicated in Fig. 7a. Sidelobes cause a few DOA estimation errors at -65° in the CBF histogram Fig. 7b. Since CS obtains high resolution even for a single snapshot, it performs much better than CBF Fig. 7c.

B. Multiple Snapshot

In the multiple snapshot scenarios, the CBF and MVDR use the data sample covariance matrix Eq. (18) whereas CS works directly on the observations \mathbf{X} Eq. (16). The sample covariance matrix is formed by averaging L synthetic data snapshots. A source's magnitude is considered invariant from snapshot to snapshot. The source's phases are independent realizations sampled from a uniform distribution on $[0, 2\pi)$.

Due to the weak performance of MVDR in scenarios with coherent arrivals⁷, we assume incoherent arrivals in the simulations although not needed for CS. For CS we use Eq. (16) with a similar choice of regularization parameter μ as for the single snapshot case.

Using the same setup as in Fig. 7, but estimating the source DOAs based on $L = 50$ snapshots gives the results in Fig. 8. At SNR = 0 dB the diagrams in Fig. 8a show that CS localizes the sources well, in contrast to the CBF and MVDR which is also indicated in the histograms in Fig. 8b. The RMSE in Fig. 8c, shows that CBF does not give the required resolution even for high SNR. MVDR performs well for SNR > 10 dB, whereas CS performs well for SNRs down to 2.5 dB.

In a third scenario, the weak broadside sources are moved closer with DOAs defined as $[-2, 1, 75]^\circ$. Fig. 9 gives about the same DOA estimates for CBF, as it is already at its maximum performance. MVDR fails for SNR < 20 dB, which is 10 dB higher than the corresponding value in Fig. 8c. Contrarily, CS fails only for SNR < 2.5 dB in both cases (Figs. 8c and 9c). Note how MVDR completely misses the weak source at -2° in Figs. 9c, but CS localize it with a larger spread. Thus, as the weak source moves closer to the strong source, CS degrades slower than MVDR in terms of RMSE. This is a good indication of its high-resolution capabilities.

Figure 10 shows the estimated power at the one realization in Fig. 8a of $L = 50$ snapshots inverted simultaneously. We emphasize the scale of the problem. Equation (15) has $20 \cdot 50 = 100$ equations to determine $361 \cdot 50 = 18050$ complex-valued variables at 361 azimuths and 50 snapshots observed on 20 hydrophones. The sparsity constraint is crucial here. One reason why CS performs better than MVDR is that for each snapshot it estimates a different complex amplitude. MVDR just gives the average power across all snapshots.

VIII. EXPERIMENTAL RESULTS

The high-resolution performance of CS both in single- and multiple-snapshot cases is validated with experimental data in a complex multi-path shallow-water environment and it is compared with conventional methods, namely CBF and MVDR.

The data set is from the shallow water evaluation cell experiment 1996 (SWellEx-96) Event S5^{34,35} collected on a 64-element vertical linear array. The array has uniform intersensor spacing 1.875 m and was deployed at water-depth 216.5 m spanning $94.125 - -212.25$ m. During the Event S5, from 23:15–00:30 on 10-11 May 1996 west of Point Loma, CA, two sources, a shallow and a deep, were towed simultaneously from 9 km southwest to 3 km northeast of the array at a speed of 5 knots (2.5 m/s). Each source was transmitting a unique set of tones.

Here, we are interested in the deep source towed at 54 m depth while at the vicinity of the closest point of approach (CPA) which was 900 m from the array and occurred around 00:15, 60 min into the event. The deep source signal submitted a set of 9 frequencies [112, 130, 148, 166, 201, 235, 283, 338, 388] Hz at approximately

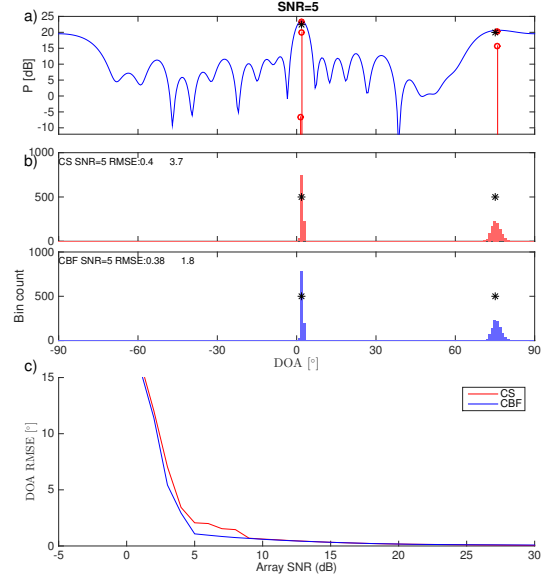


FIG. 6. (Color online) Single snapshot example for 2 sources at DOAs $[2, 75]^\circ$ and magnitudes $[13, 10]$. At SNR = 5 dB a) spectra for CBF, CS (o) and unbiased CS (o, higher levels), and b) CS histogram based on 1000 Monte Carlo simulations, and c) CS and CBF performance versus SNR. The true source positions (*) are indicated in a) and b).

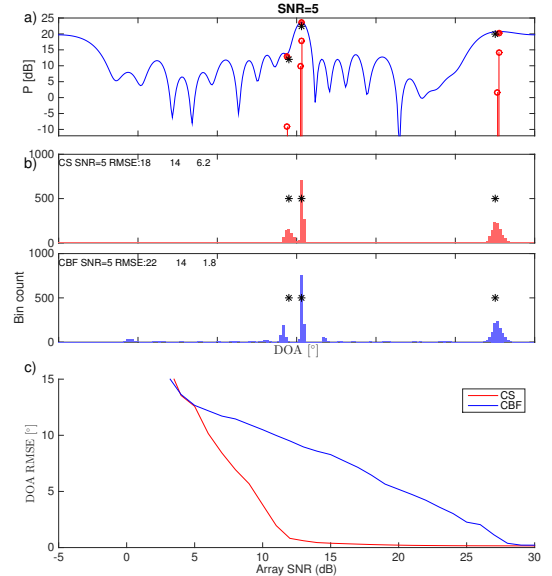


FIG. 7. (Color online) As Fig. 6 but for 3 sources at DOAs $[-3, 2, 75]^\circ$ and magnitudes $[4, 13, 10]$.

158 dB *re* 1 μ Pa. The processed recording has duration of 1.5 min (covering 0.5 min before and 1 min after the CPA) sampled at 1500 Hz. It was split into 87 snapshots of 2^{12} samples (2.7 s) duration, i.e., with 63% overlap.

Figure 11 shows the multiple-snapshot CBF spatial spectrum, Eq. (20), over the 50-400 Hz frequency range. Arrivals are detected not only at the transmitted tonal frequencies of the deep source but also at several other

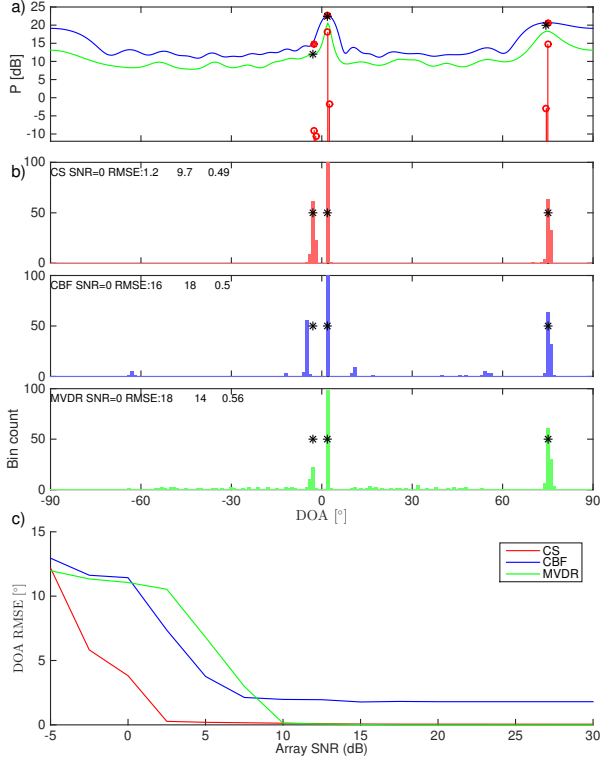


FIG. 8. (Color online) Multiple $L = 50$ snapshot example for 3 sources at DOAs $[-3, 2, 75]^\circ$ with magnitudes $[4, 13, 10]$. At SNR = 0 dB a) spectra for CBF, MVDR, and CS (o) and unbiased CS (o, higher levels), and b) CS histogram based on 100 Monte Carlo simulations, and c) CBF, MVDR, and CS performance versus SNR. The true source positions (*) are indicated in a) and b).

frequencies corresponding to the shallow source tonal frequencies, weaker deep source frequencies, and the acoustic signature of the tow-ship.

Single-snapshot processing with CBF and CS at the deep source tonal set, Fig. 12, indicates the presence of several multipath arrivals which are adequately stationary along the snapshots at the CPA. Due to the significant sound speed variation it is not straightforward to associate the reconstructed DOAs with specific reflections. The CBF map comprises 6 significant peaks but suffers from low resolution and artifacts due to sidelobes and noise. To choose the regularization parameter in the LASSO formulation for CS reconstruction, we solve iteratively Eq. (8) as described in Sec. V.B with initial value $\mu = \max(2\mathbf{A}^H \mathbf{y})$, until the obtained estimate has a sparsity level of 6. The CS reconstruction results in improved resolution due to the sparsity constraint and significant reduction of artifacts in the map.

Combining the data from all the snapshots and processing with CBF, MVDR, and CS, as in Sec. VII.B, reveals that MVDR fails to detect the coherent multipath arrivals; see Fig. 13. Again the peaks of CBF and CS are consistent but CS offers improved resolution.

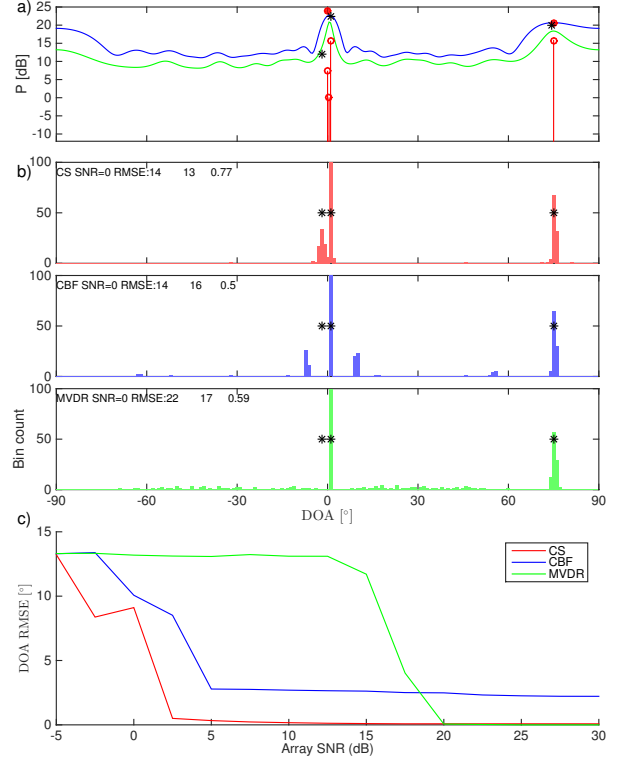


FIG. 9. (Color online) As Fig. 8 but with closer spaced sources $[-2, 1, 75]^\circ$.

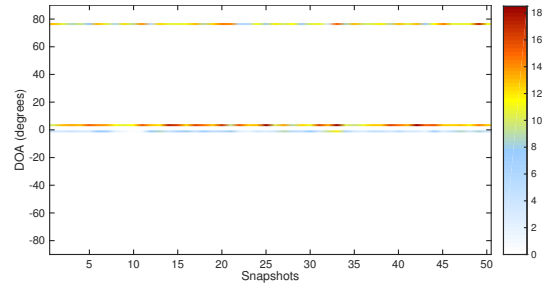


FIG. 10. (Color online) Power (linear) for the multiple snapshot case across azimuths and snapshots for one noise realization at SNR = 0 dB for the scenario with DOAs $[-3, 2, 75]^\circ$.

IX. CONCLUSION

The estimation of multiple directions-of-arrival (DOA) is formulated as a sparse signal reconstruction problem. This is efficiently solvable using compressive sensing (CS) as a least squares problem regularized with a sparsity promoting constraint. The resulting solution is the maximum a posteriori (MAP) estimate for both the single and multiple-snapshot formulations. The regularization parameter balances the data fit and the solution's sparsity. It is selected so that the solution is sufficiently sparse providing high-resolution DOA estimates. A procedure to find an adequate choice for the regularization parameter is described whereby the DOAs are obtained.

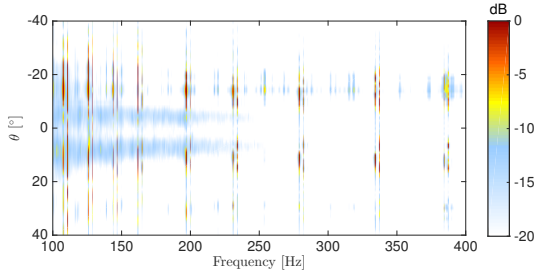


FIG. 11. (Color online) Spatial CBF spectrum across frequency at the source's closest point of approach to the array.

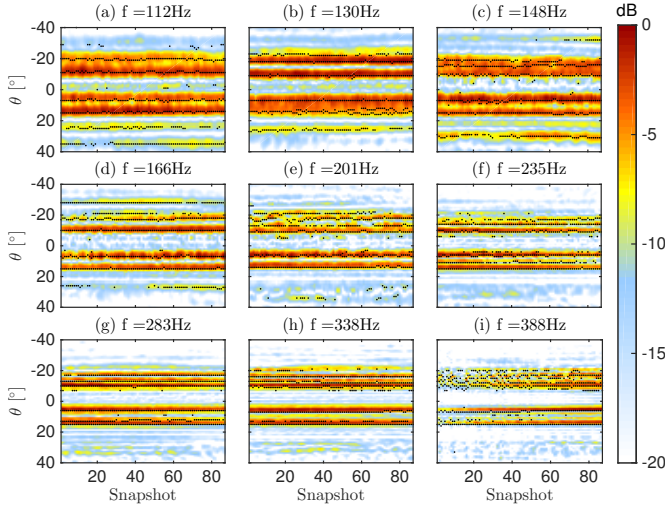


FIG. 12. (Color online) Single-snapshot reconstruction at the transmitted frequencies with CS (dots) and CBF (background color).

CS provides high-resolution acoustic imaging even with a single snapshot. The performance evaluation shows that for single snapshot data, CS gives higher resolution than CBF. For multiple snapshots, CS provides higher resolution than MVDR and the relative performance improves as the source DOAs move closer together.

The real data example indicates that CS is capable of resolving multiple coherent wave arrivals, e.g. stemming from multipath propagation.

X. ACKNOWLEDGMENT

This work was supported by the Office of Naval Research, Grant Nos. N00014-11-1-0439 and a MURI, as well as FTW Austria's "Compressed channel state information feedback for time-variant MIMO channels".

¹ M. Elad. *Sparse and redundant representations: from theory to applications in signal and image processing*, pages 1–359. Springer, New York, 2010.

² S. Foucart and H. Rauhut. *A mathematical introduction to compressive sensing*, pages 1–589. Springer, New York, 2013.

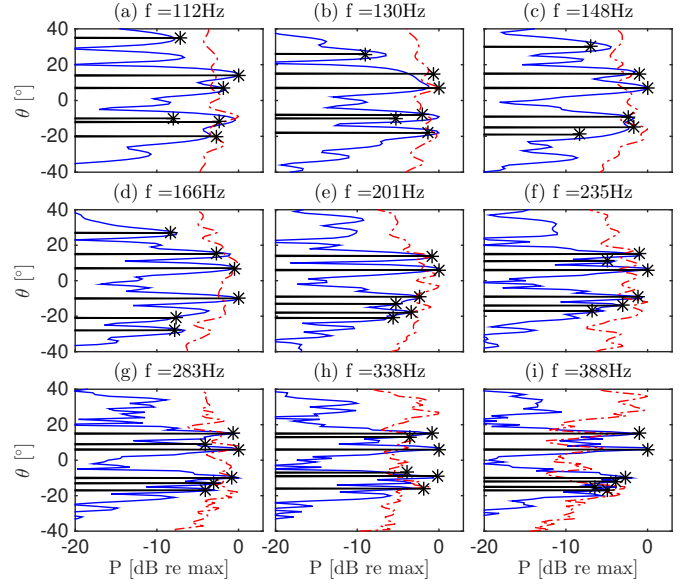


FIG. 13. (Color online) Multiple-snapshot reconstruction at the transmitted frequencies with CS (*), CBF (solid) and MVDR (dashed).

- ³ D. Malioutov, M. Çetin, and A. S. Willsky. A sparse signal reconstruction perspective for source localization with sensor arrays. *IEEE Trans. Signal Process.*, **53**(8):3010–3022, 2005.
- ⁴ A. Xenaki, P. Gerstoft, and K. Mosegaard. Compressive beamforming. *J. Acoust. Soc. Am.*, **136**(1):260–271, 2014.
- ⁵ A. Xenaki and P. Gerstoft. Grid-free compressive beamforming. *J. Acoust. Soc. Am.*, **137**:XXX–XXX, 2015.
- ⁶ H. Krim and M. Viberg. Two decades of array signal processing research: the parametric approach. *IEEE Signal Proc. Mag.*, **13**(4):67–94, 1996.
- ⁷ H.L. Van Trees. *Optimum Array Processing (Detection, Estimation, and Modulation Theory, Part IV)*, chapter 1–10. Wiley-Interscience, New York, 2002.
- ⁸ R. Schmidt. Multiple emitter location and signal parameter estimation. *IEEE Trans. Antennas Propag.*, **34**(3):276–280, 1986.
- ⁹ G. F. Edelmann and C. F. Gaumond. Beamforming using compressive sensing. *J. Acoust. Soc. Am.*, **130**(4):232–237, 2011.
- ¹⁰ C. F. Mecklenbräuker, P. Gerstoft, A. Panahi, and M. Viberg. Sequential Bayesian sparse signal reconstruction using array data. *IEEE Trans. Signal Process.*, **61**(24):6344–6354, 2013.
- ¹¹ S. Fortunati, R. Grasso, F. Gini, M. S. Greco, and K. LePage. Single-snapshot DOA estimation by using compressed sensing. *EURASIP J. Adv. Signal Process.*, **120**(1):1–17, 2014.
- ¹² W. Mantzel, J. Romberg, and K. Sabra. Compressive matched-field processing. *J. Acoust. Soc. Am.*, **132**(1):90–102, 2012.
- ¹³ P. A. Forero and P. A. Baxley. Shallow-water sparsity-cognizant source-location mapping. *J. Acoust. Soc. Am.*, **135**(6):3483–3501, 2014.
- ¹⁴ C. Yardim, P. Gerstoft, W. S. Hodgkiss, and Traer J. Compressive geoacoustic inversion using ambient noise. *J. Acoust. Soc. Am.*, **135**(3):1245–1255, 2014.
- ¹⁵ R. Tibshirani. Regression shrinkage and selection via the

- lasso. *J. Roy. Statist. Soc. Ser. B*, **58**(1):267–288, 1996.
- ¹⁶ M. Yuan and Y. Lin. Efficient empirical bayes variable selection and estimation in linear models. *J. Amer. Statist. Assoc.*, **100**(472):1215–1225, 2005.
- ¹⁷ T. Park and G. Casella. The Bayesian lasso. *J. Amer. Statist. Assoc.*, **103**(482):681–686, 2008.
- ¹⁸ R. Tibshirani and J. Taylor. The solution path of the generalized lasso. *Ann. Stat.*, **39**(3):1335–1371, 2011.
- ¹⁹ A. Panahi and M. Viberg. Fast candidate points selection in the lasso path. *IEEE Signal Proc. Lett.*, **19**(2):79–82, 2012.
- ²⁰ Y. Chi, L. L. Scharf, A. Pezeshki, and A. R. Calderbank. Sensitivity to basis mismatch in compressed sensing. *IEEE Trans. Signal Process.*, **59**(5):2182–2195, 2011.
- ²¹ M. F. Duarte and R. G. Baraniuk. Spectral compressive sensing. *Appl. Comput. Harmon. Anal.*, **35**(1):111–129, 2013.
- ²² H. Yao, P. Gerstoft, P. M. Shearer, and C. Mecklenbräuker. Compressive sensing of the Tohoku-Oki Mw 9.0 earthquake: Frequency-dependent rupture modes. *Geophys. Res. Lett.*, **38**(20):1–5, 2011.
- ²³ H. Yao, P. M. Shearer, and P. Gerstoft. Compressive sensing of frequency-dependent seismic radiation from subduction zone megathrust ruptures. *Proc. Natl. Acad. Sci. U.S.A.*, **110**(12):4512–4517, 2013.
- ²⁴ W. Fan, P. M. Shearer, and P. Gerstoft. Kinematic earthquake rupture inversion in the frequency domain. *Geophys. J. Int.*, **199**(2):1138–1160, 2014.
- ²⁵ E. J. Candès and M. B. Wakin. An introduction to compressive sampling. *IEEE Signal Proc. Mag.*, **25**(2):21–30, 2008.
- ²⁶ R. G. Baraniuk. Compressive sensing. *IEEE Signal Proc. Mag.*, **24**(4):118–121, 2007.
- ²⁷ M. Grant and S. Boyd. CVX: Matlab software for disciplined convex programming, version 2.0 beta. <http://cvxr.com/cvx>, September 2013.
- ²⁸ M. Grant and S. Boyd. Graph implementations for non-smooth convex programs. In V. Blondel, S. Boyd, and H. Kimura, editors, *Recent Advances in Learning and Control*, Lecture Notes in Control and Information Sciences, pages 95–110. Springer-Verlag Limited, London, 2008.
- ²⁹ S. Boyd and L. Vandenberghe. *Convex optimization*, pages 1–684. Cambridge university press, New York, 2004.
- ³⁰ Z. He, S. Xie, S. Ding, and A. Cichocki. Convolutional blind source separation in the frequency domain based on sparse representation. *IEEE Trans. Audio, Speech, and Language Proc.*, **15**(5):1551–1563, July 2007.
- ³¹ D. Wipf and B. Rao. An empirical bayesian strategy for solving the simultaneous sparse approximation problem. *IEEE Trans. Signal Process.*, **55**(7):3704–3716, 2007.
- ³² C. F. Mecklenbräuker, P. Gerstoft, and Zöchmann E. Beamforming of the residuals is the lasso’s dual. *IEEE Trans. Signal Process.*, 2015.
- ³³ R. Tibshirani, M. Saunders, S. Rosset, J. Zhu, and K. Knight. Sparsity and smoothness via the fused lasso. *J. Roy. Statist. Soc. Ser. B*, **67**(1):91–108, 2005.
- ³⁴ N. O. Booth, P. A. Baxley, J. A. Rice, P. W. Schey, W. S. Hodgkiss, G. L. D’Spain, and J. J. Murray. Source localization with broad-band matched-field processing in shallow water. *IEEE J Oceanic Eng.*, **21**(4):400–411, 1996.
- ³⁵ G. L. D’Spain, J. J. Murray, W. S. Hodgkiss, N. O. Booth, and P. W. Schey. Mirages in shallow water matched field processing. *J Acoust. Soc. Am.*, **105**(6):3245, 1999.

PAPER **G**

Sparse acoustic imaging with a spherical array

Authors:

Efren Fernandez-Grande and Angeliki Xenaki

Submitted to:

Euronoise 2015, Maastricht, Netherlands, 31 May-3 June 2015.



Sparse acoustic imaging with a spherical array

Efren Fernandez-Grande

Acoustic Technology, Department of Electrical Engineering, DTU - Technical University of Denmark,
B. 352, DK-2800 Kgs. Lyngby, Denmark

Angeliki Xenaki

Department of Applied Mathematics and Computer Science, DTU - Technical University of Denmark,
B. 303b, DK-2800 Kgs. Lyngby, Denmark

Summary

In recent years, a number of methods for sound source localization and sound field reconstruction with spherical microphone arrays have been proposed. These arrays have some useful properties, e.g. omni-directionality, robustness, compensable scattering, etc. This paper proposes a plane wave expansion method based on measurements with a spherical microphone array, solved in the framework provided by Compressive Sensing. The proposed methodology results in a sparse solution, i.e. few non-zero coefficients, and it is suitable for both source localization and sound field reconstruction. In general the method provides fine spatial resolution and is robust to noise (the noisy components are naturally suppressed). The validity and performance of the proposed method is examined, and some of its underlying assumptions are addressed.

PACS no. 43.60.+d, 43.58.+z

1. Introduction

Spherical microphone arrays are commonly used for analysing complex sound fields, e.g., localise sound sources in a given space [1–6], reconstruct the sound field near a source to examine how it injects energy into the medium [7–12], or capture complex acoustic scenes for subsequent reproduction with an array of loudspeakers [13, 14]. In recent years, spherical array processing is becoming increasingly popular for room acoustic applications. Unlike other common configurations [15], spherical arrays are omnidirectional, and therefore particularly well-suited in situations where sound waves impinge on the array from multiple directions, e.g. in environmental noise measurements, or in enclosed spaces such as rooms, vehicle interiors, etc.

Spherical microphone arrays have extensively been used for sound source localization and direction-of-arrival estimation. Recent studies have also examined the use of spherical arrays for the reconstruction of sound fields [7–12]; these methods use a spherical harmonic expansion to provide a representation of the sound field, used for extrapolating it to a different area than measured. A method was recently proposed that uses an elementary wave expansion to represent

the measured sound field (using point sources), and solves for the corresponding coefficients via a matrix inversion, without explicit numerical integration on the sphere [11, 12].

This study proposes a method based on an elementary wave expansion that promotes a sparse solution to the problem (i.e. few non-zero coefficients), which aims at an optimal representation of the measured data, and results in greater spatial resolution and robustness to noise. The problem is formulated in the framework provided by Compressive Sensing (CS) [18]. Compressive Sensing makes use of the fact that signals that are sparse in some domain can be reconstructed perfectly, even with an apparently under-sampled set of observations, by means of solving an l_1 - minimization convex problem [17–19]. The proposed method consists of formulating an elementary wave expansion where the measured data is expanded in a basis of choice - plane waves in the present study, although also applicable to other wave functions. Then the problem is solved via l_1 - minimization, instead of the conventional l_2 - minimization (i.e., Least Squares), using convex optimization.

The focus of the present paper is to examine the proposed Compressive Sensing approach for spherical array processing, and discuss the potential benefits and limitations compared to the conventional least-squares approach.

2. Theory

2.1. Theoretical background

Let there be a rigid spherical array of radius a immersed in a sound field. The array consists of M microphones that are flush-mounted on the surface of the rigid-sphere. The sound pressure measured by the sensors can be expanded into plane waves arriving from every possible direction Ω_0 ,

$$p_t(a, \Omega_m) = \iint_{\Omega_0} -\frac{A(\Omega_0)}{(ka)^2} \times \sum_{n=0}^{\infty} \sum_{m=-n}^n \frac{4\pi j^{n+1}}{h'_n(ka)} Y_n^m(\Omega_m) Y_n^m(\Omega_0)^* d\Omega_0. \quad (1)$$

The summation over m and n corresponds to expanding a plane wave incident on a rigid sphere into spherical harmonics. The functions $h_n^{(2)}(x) = j_n(x) - jy_n(x)$, are the spherical Hankel functions of the second kind (note that the sign convention chosen is $e^{j\omega t}$ with j the imaginary unit), and $j_n(x)$ and $y_n(x)$ are the spherical Bessel functions of the first and second kind [20]. Their derivative is represented by $j'_n(x)$ and $y'_n(x)$. We express the angular dependency as $\Omega \equiv (\theta, \phi)$, and $d\Omega \equiv \sin\theta d\theta d\phi$, so that the integration over the sphere is $\iint_{\Omega}(\cdot)d\Omega \equiv \int_0^{2\pi} \int_0^\pi (\cdot) \sin\theta d\theta d\phi$. Lastly, $Y_n^m(\Omega)$ are the spherical harmonics defined as in Ref. [20].

Equation 1 can be discretised and expressed as a sum of L plane waves (instead of the continuous expansion expressed by the integration over Ω_0)

$$p_t(a, \Omega_m) = \sum_{l=1}^L -\frac{A_l}{(ka)^2} \sum_{n=0}^{\infty} \sum_{m=-n}^n \frac{4\pi j^{n+1}}{h'_n(ka)} \times Y_n^m(\Omega_m) Y_n^m(\Omega_0)^*. \quad (2)$$

Alternatively, the wave expansion can be formulated in terms of point sources instead of plane waves. The measured pressure is expanded into a continuum of sources distributed over positions \mathbf{r}_0 , associated with the integration surface S that can be chosen arbitrarily (it does not need to be spherical or even separable)

$$p_t(a, \Omega_m) = \iint_{S_0} -\frac{j\rho c U(\mathbf{r}_0)}{a^2} \sum_{n=0}^{\infty} \sum_{m=-n}^n \frac{h_n(kr_0)}{h'_n(ka)} \times Y_n^m(\Omega_m) Y_n^m(\Omega_0)^* dS, \quad (3)$$

where U is the surface velocity on S . In practice, the surface S can be placed either inside the source under study, or in general outside the domain in which the sound field is reconstructed, to prevent the singularities. If the distribution of sources is discretised,

$$p_t(a, \Omega_m) = \sum_{l=1}^L -\frac{j\rho c Q_l}{a^2} \sum_{n=0}^{\infty} \sum_{m=-n}^n \frac{h_n(kr_0)}{h'_n(ka)} \times Y_n^m(\Omega_m) Y_n^m(\Omega_0)^*. \quad (4)$$

This approach based on a point source expansion (Eq. 4), is appropriate for the reconstruction of sound fields, because the decay of the acoustic field is modeled via the spherical spreading of the point sources. Contrarily, the former approach using plane waves (Eq. 2), is better suited for sound source localization where no extrapolation of the sound field is involved, but just aims at determining the direction from which sound waves impinge on the array, or sound field analysis. This is due to the fact that a (propagating) plane wave expansion basis cannot model decaying functions in a straightforward manner; evanescent waves should then be included.

2.2. Method

It is possible to express Eq. (2), i.e. the total sound pressure on the sphere, in matrix form, by conducting the summation over n and m

$$\mathbf{p} = \mathbf{H}\mathbf{x}, \quad (5)$$

noting that the summation should be truncated at N , to satisfy $ka < N$, depending on the number of microphones and size of the sphere [9]. The vector $\mathbf{p} \in \mathbb{C}^M$ contains the sound pressure measured at a discrete set of M points on the sphere, and the matrix \mathbf{H} of dimensions $M \times L$ is the transfer matrix between the amplitude of the waves and the measured pressure. The amplitude of the waves corresponds to the vector $\mathbf{x} \in \mathbb{C}^L$, i.e., the unknown coefficients of the expansion. This problem is ill-posed, and most often under-determined ($M < L$). Therefore the solution to Eq. (5) needs to be calculated via a regularized inversion of the problem.

In a general sense, the problem formulated in Eq. (5) can be cast as an optimization problem of the form

$$\min_{\mathbf{x}} \|\mathbf{x}\|_p \quad \text{subject to } \mathbf{p}_t = \mathbf{H}\mathbf{x} \quad (6)$$

where $\|\cdot\|_p$ represents the vector norm,

$$\|\mathbf{x}\|_p = \left(\sum_i x_i^p \right)^{1/p}. \quad (7)$$

The choice of p -norm in the coefficient vector will promote different solutions to the problem.

The l_2 -norm leads to the ‘conventional’ least-squares minimisation problem. This problem has the well-known closed form analytical solution (including a regularisation term λ),

$$\mathbf{x} = \mathbf{H}^H (\mathbf{H}\mathbf{H}^H + \lambda \mathbf{I})^{-1} \mathbf{p}. \quad (8)$$

which has many non-zero components. The superscript H denotes the Heremitian transpose or conjugate transpose, \mathbf{I} is the identity matrix and λ the regularization parameter for the Tikhonov regularization [10, 21]. When the regularization parameter is

zero, the inversion corresponds to a matrix pseudo-inverse.

On the other hand, the choice of the l_0 -pseudo norm in Eq. (6), defined as $\|\mathbf{x}\|_0 = \#\{i|x_i \neq 0\}$, promotes sparse solutions since, by definition, it minimises the number of non-zero entries in the vector. This norm is in fact a count of the non-zero elements of the vector. However, the l_0 -norm minimisation is a combinatorial problem which often becomes intractable.

It can be shown [17] that for sufficiently sparse problems, the l_0 -norm minimisation problem is equivalent to the l_1 -norm problem. The choice of the l_1 -norm promotes sparsity on the solution, i.e., a small number of non-zero coefficients, while it leads to a convex optimisation problem that can be solved efficiently.

In the presence of noise, the l_1 minimisation problem is reformulated as,

$$\min_{\mathbf{x}} \|\mathbf{x}\|_1 \quad \text{subject to } \|\mathbf{H}\mathbf{x} - \mathbf{p}\|_2 \leq \varepsilon. \quad (9)$$

where ε is the noise floor. Alternatively, the problem can be formulated in an unconstrained form by introducing a regularisation parameter λ which determines the weight of the l_1 -norm penalty.

One important aspect of the l_1 minimization solution is the incoherence between the columns of the sensing matrix \mathbf{H} , since this is a guarantee of the equivalence between the l_0 and l_1 minimization problems. The coherence between the columns of \mathbf{H} can be described by the maximum of the non-diagonal elements of the Gram matrix

$$\mu(\mathbf{H}) = \max_{\{i \neq j\}} |\mathbf{H}^H \mathbf{H}|. \quad (10)$$

This is also connected to the restricted isometry property (RIP) condition, $(1 - \delta_s)\|\mathbf{x}\|_2^2 \leq \|\mathbf{H}\mathbf{x}\|_2^2 \leq (1 + \delta_s)\|\mathbf{x}\|_2^2$, which is frequently found in the literature.

The obtained vector $\tilde{\mathbf{x}}$ yields the amplitudes of the waves used in the expansion, and thus it is sufficient for estimating the direction of arrival of the waves. Nonetheless, if the aim were to reconstruct the sound-field elsewhere than measured, it is possible to extrapolate the wave expansion to reconstruct/predict the sound-field elsewhere: a reconstruction matrix \mathbf{H}_s is defined (analogous to the one in Eq. 2 or 4) that relates the obtained expansion coefficients $\tilde{\mathbf{x}}$ to the desired reconstruction points in the medium \mathbf{r}_s $\mathbf{p}_s = \mathbf{H}_s \tilde{\mathbf{x}}$, with the reconstructed pressure $\mathbf{p}_s \in \mathbb{C}^K$, and using a vector \mathbf{r}_s instead of the \mathbf{r}_0 in Eq. (4). Alternatively, one can choose a reconstruction matrix based on the propagation of plane waves or point sources in free-space, thus compensate for the scattering of the array, and reconstruct the incident pressure as if the array was not present - see Ref. [12]).

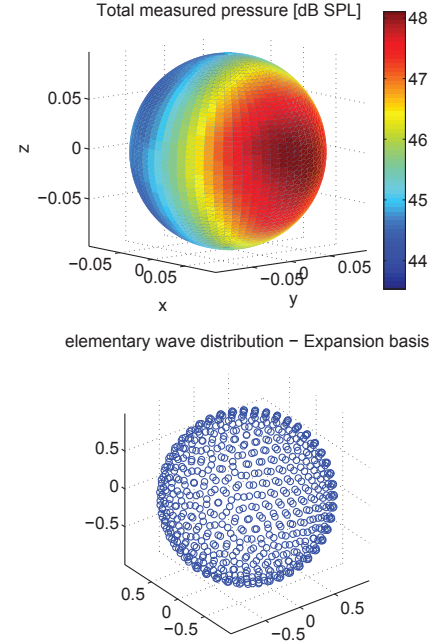


Figure 1. Top: Sound pressure on the spherical array; Bottom: Plane wave model: Distribution of waves used to model the soundfield - each circle corresponds to a direction (total of 650 waves).

3. Results

The proposed methodology and its numerical properties are examined through a simulation example. The method consists of the plane-wave expansion described in Eqs. (1) (2) and (5); the aim is to examine the solution obtained with the proposed CS methodology (Eq. 9), and to compare it with the conventional least-squares solution (Eq. 8).

The study consists of a point source located 6 m away from the array surface, a rigid spherical array of 50 microphones, near-uniformly distributed over its surface, that can sample up to 5 orders of spherical harmonics [9]. The pressure on the array surface at 500 Hz is shown in Fig. 1 (top). Normally distributed noise is added to the simulated measurements with a signal-to-noise ratio (SNR) of 25 dB. A plane wave expansion of 650 waves is considered, and shown in Fig. 1 (bottom). The waves are distributed over an equal solid angle spacing; the distribution of the waves has been determined based on a Thomson problem, that considers equally charged particles on a sphere, and are therefore uniformly distributed over the surface of the sphere.

Figure 2 shows the solution of the problem based on the conventional least-squares solution Eq. (8), and Figure 3 shows the proposed compressive sensing solution based on Eq. (9). The top row of both figures shows the recovered pressures by each of the techniques, making it apparent that both approaches can successfully explain the measured data. The center

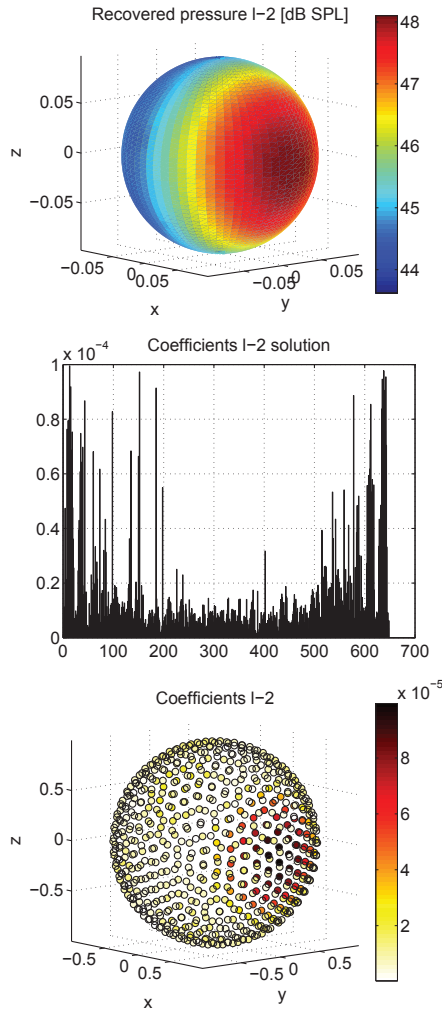


Figure 2. Spherical wave incident on a spherical array, expanded into plane waves (Eq. 2). Solution based on the l_2 -norm - least squares (Eq. 8); Top: Recovered sound pressure; Mid: coefficients based on l_2 minimization; Bottom: Coefficients ordered by their direction of arrival.

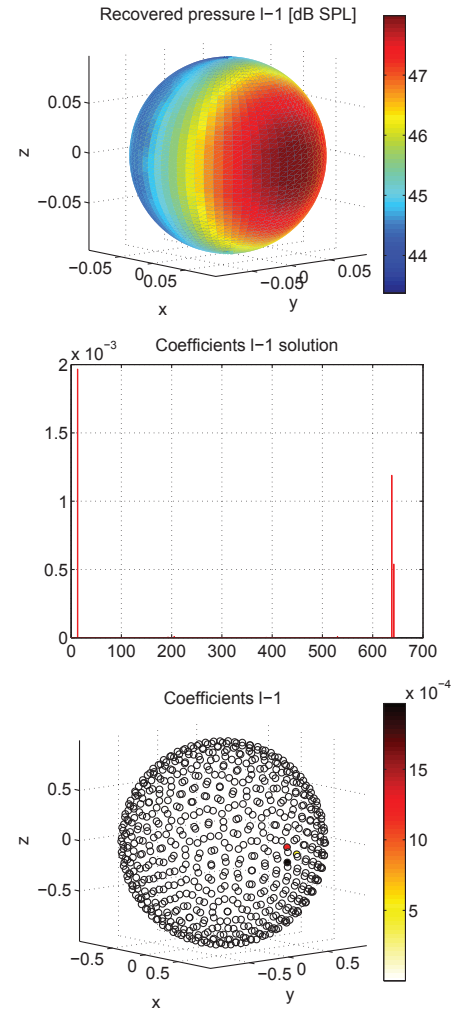


Figure 3. Spherical wave incident on a spherical array, expanded into plane waves (Eq. 2). Solution based on the l_1 -norm - Compressive Sensing (Eq. 9); Top: Recovered sound pressure; Mid: coefficients based on l_1 minimization; Bottom: Coefficients ordered by their direction of arrival.

row shows the coefficients of the two methodologies (without any particular ordering), showing that the set of coefficients obtained by the two approaches is significantly different, particularly regarding the sparsity of the solution. In the l_2 least-squares approach (Fig. 2, mid.) all of the coefficients are non zero, whereas the proposed CS method returns only three non-zero coefficients (Fig. 3, mid.), indicating that the measured data can be explained optimally with a minimal number of entries in the expansion. The bottom plots of the figures show the coefficients of the two approaches and the corresponding direction of incidence of the plane waves used in the model (i.e. incoming direction of the waves used in the expansion). The least squares solution corresponds to a conventional beam-former output [4, 5], with its characteristic limited spatial resolution (main-lobe and side-lobes). The CS solution essentially uses three coefficients, detecting

the direction of arrival of the spherical wave, where the source is located, with optimal accuracy.

All in all, it is apparent that although the recovered sound pressure by the two methods is virtually identical, the differences in the coefficients are notorious. Several aspects to consider about the Compressive Sensing approach / l_1 - solution: i) the spatial resolution is enhanced and approaches an ideal delta function, ii) noise is naturally suppressed; it is evident how the sparsity constrain acts as a regularization mechanism robust to noise, since the recovered coefficients are those that span the signal, and not the measurement noise; iii) lastly, the resulting solution is based on only a few terms of the expansion, which also has the useful implication that an over-determined system of equations can be solved with only the relevant expansion terms, for better quantitative accuracy.

This study focuses on the description of the proposed methodology, and examines a single source case to provide an initial insight on its performance, and some of the numerical properties of the solution. Further studies will focus on sensitivity to noise, multiple sources and complex sound fields, as well as sources of larger spatial extent.

4. CONCLUSIONS

This study proposes and examines a method that makes use of the framework provided by Compressive Sensing for spherical array processing. The solution is obtained via l_1 -minimization, which imposes sparsity on the solution, i.e. requires that few coefficients are non-zero. The results show that the method makes it possible to identify the direction of arrival of the waves with almost ideal spatial resolution and accuracy. This is the case provided that the coherence of the matrix columns is sufficiently low. In a general sense, the results indicate that it is possible to accurately represent the measured data with minimum number of coefficients. This gives the method a promising perspective for its use on direction of arrival estimation, sound field reconstruction and sound field analysis.

Acknowledgement

This work was supported by the Danish Council for Independent Research (DFF), under the individual postdoctoral grant FTP/12-126364.

References

- [1] Jens Meyer and Gary Elko. A highly scalable spherical microphone array based on an orthonormal decomposition of the soundfield. In *Acoustics, Speech, and Signal Processing (ICASSP), 2002 IEEE International Conference on*, volume 2, pages II-1781–II-1784, May 2002.
- [2] B Rafaely. Analysis and design of spherical microphone arrays. *Speech and Audio Processing, IEEE Transactions on*, 13(1):135–143, 2005. ISSN 1063-6676.
- [3] Munhum Park and Boaz Rafaely. Sound-field analysis by plane-wave decomposition using spherical microphone array. *J. Acoust. Soc. Am.*, 118(5):3094–3103, 2005.
- [4] Karim Haddad and Jo/rngen Hald. 3d localization of acoustic sources with a spherical array. *Acoustics '08 Paris. Vol 123*, 123(5):3311–3311, 2008.
- [5] Elisabet Tiana-Roig, Finn Jacobsen, and Efren Fernandez-Grande. Beamforming with a circular array of microphones mounted on a rigid sphere (L). *J. Acoust. Soc. Am.*, 130(3):1095–1098, 2011.
- [6] A. Pereira and Q. Leclere. Improving the equivalent source method for noise source identification in enclosed spaces. *Proceedings of ICSV 18, Rio de Janeiro, Brazil, 10-14 July 2011*, art. 055010, 2011.
- [7] E.G. Williams, N. Valdivia, and P. C. Herdic. Volumetric acoustic vector intensity imager. *J. Acoust. Soc. Am.*, 120(4):1887–1897, 2006.
- [8] E.G. Williams and K. Takashima. Vector intensity reconstructions in a volume surrounding a rigid spherical microphone array. *J. Acoust. Soc. Am.*, 127(2):773–783, 2010.
- [9] Finn Jacobsen, Guillermo Moreno-Pescador, Efren Fernandez-Grande, and Jo/rngen Hald. Near field acoustic holography with microphones on a rigid sphere (I). *The Journal of the Acoustical Society of America*, 129(6):3461–3464, 2011.
- [10] Alba Granados, Finn Jacobsen, and Efren Fernandez-Grande. Regularised reconstruction of sound fields with a spherical microphone array. *Proceedings of Meetings on Acoustics*, 19(1):055010, 2013.
- [11] Efren Fernandez-Grande. Reconstruction of arbitrary sound fields with a rigid-sphere microphone array. *166th Acoust. Soc. Am. meeting San Francisco, 2-6th December*, 134(5):3998–3998, 2013.
- [12] Efren Fernandez-Grande and Tim Walton. Reconstruction of sound fields with a spherical microphone array. In *Proceedings of Inter-noise 2014*, 2014.
- [13] T.D. Abhayapala and Darren B. Ward. Theory and design of high order sound field microphones using spherical microphone array. In *Acoustics, Speech, and Signal Processing (ICASSP), 2002 IEEE International Conference on*, volume 2, pages II-1949–II-1952, May 2002.
- [14] Marton Marschall and Jiho Chang. Sound-field reconstruction performance of a mixed-order ambisonics microphone array. *Proceedings of Meetings on Acoustics*, 19(1):055007, 2013.
- [15] Efren Fernandez-Grande, Finn Jacobsen, and Quentin Leclere. Sound field separation with sound pressure and particle velocity measurements. *The Journal of the Acoustical Society of America*, 132(6):3818–3825, 2012.
- [16] B. Rafaely, B. Weiss, and E. Bachmat. Spatial aliasing in spherical microphone arrays. *Signal Processing, IEEE Transactions on*, 55(3):1003–1010, March 2007.
- [17] Michael. Elad. *Sparse and redundant representations : From theory to applications in signal and image processing*. Springer, New York, Ch. 1, 2010. ISBN 9781441970107.
- [18] E. J. Candes and M. B. Wakin. An introduction to compressive sampling. *IEE Signal Proc. Mag.*, 25: 21–30, 2008.
- [19] Angeliki Xenaki, Peter Gerstoft, and Klaus Mosegaard. Compressive beamforming. *The*

Journal of the Acoustical Society of America, 136
(1):260–271, 2014.

- [20] Earl G. Williams. *Fourier Acoustics - Sound Radiation and Nearfield Acoustic Holography*. Academic Press, 1999.
- [21] Per Christian Hansen. *Rank-Deficient and Discrete Ill-Posed Problems: Numerical Aspects of Linear Inversion*. SIAM monographs on mathematical modeling and computation. SIAM, 1998. ISBN 9780898714036.

